



Tofani, Francesca (2020) Thermal-AFM under aqueous environment. PhD thesis.

<https://theses.gla.ac.uk/81653/>

Copyright and moral rights for this work are retained by the author

A copy can be downloaded for personal non-commercial research or study, without prior permission or charge

This work cannot be reproduced or quoted extensively from without first obtaining permission in writing from the author

The content must not be changed in any way or sold commercially in any format or medium without the formal permission of the author

When referring to this work, full bibliographic details including the author, title, awarding institution and date of the thesis must be given

Enlighten: Theses

<https://theses.gla.ac.uk/>
research-enlighten@glasgow.ac.uk

Thermal-AFM under aqueous environment

Francesca Tofani

Submitted in fulfilment of the requirements for
the Degree of Doctor of Philosophy

School of Engineering
College of Science and Engineering
University of Glasgow



September 15, 2020

*For You,
The most Kind, Beautiful, Generous, Strong and Funny Person I have ever known.
My Best friend, my entire world.
I miss you every minute.
Thank you, Mummy!*

Abstract

The aim of this thesis is to describe the work developing and demonstrating the use of Scanning Thermal Microscopy (S_{Th}M) in an aqueous electrically conductive environment for the first time. This has been achieved by using new instrumentation to allow conventional S_{Th}M probes to measure and manipulate the temperature of non-biological and biological samples. For the latter, the aqueous environment is crucial to allow in-vitro experimentation, which is important for the future use of S_{Th}M in the life sciences. S_{Th}M is known to be a powerful technique able to acquire simultaneous topographic and thermal images of samples. It is able to measure the microscopic thermal properties of a surface with nanoscale spatial resolution. However, S_{Th}M has traditionally been limited to use in vacuum, air and electrically inert liquids. The aqueous Scanning Thermal Microscopy (a-S_{Th}M) described in this thesis is an entirely novel technique that opens up a new field for thermal-AFM.

The first challenge addressed in this work was the adaptation of a commercial Multimode Nanoscope IIIa AFM to permit electrical access to a S_{Th}M probe completely immersed in aqueous solutions. By employing a newly designed probe holder and electronic instrumentation, the probe could then be electrically biased without inducing electrochemical reactions. This approach permitted conventional microfabricated thermal probes to be operated whilst fully immersed in water.

This innovation allowed S_{Th}M measurements under deionized (DI) water to be performed on a simple solid sample (Pt on Si₃N₄) and the results compared with in-air scans and accurate 3D Finite Element (FE) simulations. Once the validity of the technique was proven, its performance was investigated, including crucially the limit of its thermal-spatial resolution; this was investigated using nanofabricated solid samples (Au on Si₃N₄) with well-defined features. These results were compared to the FE model, allowing an understanding of the mechanisms limiting resolution to be developed. In order to demonstrate the advantages granted by the water's superior thermal conductivity compared to air or other liquids, non-contact thermal images were also acquired using the same samples.

The final part of this thesis was focused on extending S_{Th}M into the biological area; a completely new field for this technique. New results are presented for soft

samples: I-collagen gel and collagen fibrils, which were thermally manipulated using a self-heated SThM probe. This successfully demonstrated the possibility of using heat to alter a biological sample within a very well localised area while being operated for long time in an aqueous environment. The difference in force response originated from the AFM scans with different levels of self-heating further proved the robustness of the technique. Finally, the technique was employed to study MG-63 living cells: The SThM probe was left in contact with each cell for a pre-determined period of time, with and without self heating. The results demonstrated that only the heated cells, directly beneath the probe tip died, tallying with the highly localised temperature gradient predicted by FE analysis.

Author Declaration

I declare that, except where explicit reference is made to the contribution of others, the substance of this thesis is the result of my own work and has not been submitted for any other degree at the University of Glasgow or any other institution.

Acknowledgement

Completing a PhD is not always an easy walk across a plain field. In some cases, it can be as difficult as climbing a mountain. It can be characterised by uncertainty and isolation not always related directly to the aim of the research. For this reason, I would like to firstly convey my sincere gratitude to my supervisor Dr Phillip Dobson, for his constant support, for his trust and patience, motivation, and immense experience. He is not only an excellent researcher but also a person I can always count on and a very good friend. Without Phil I would never have completed this thesis.

At the same time, my gratitude goes also to my second supervisor, Professor Johnathan Weaver for his guidance, suggestions and support on several aspects of my research. He was always able to make me laugh even during some difficult moments when all the experiments appeared to fail.

I would also like to thank Professor Huabing Yin for giving me the opportunity to join her team during my last part of PhD, and for offering the complete access to her laboratory and research facilities. Without this precious support it would not be possible to obtain some of the results achieved.

I thank my group, in particular, Zarina Umatova, Rory Lambert, Lukas Avilovas. You folks supported my everyday research with stimulating discussions and gave me support during the never-ending working days when we were struggling in the lab together before deadlines, but also for all the fun we have had in the last four years. Also, I thank all the technicians of the James Watt Nanofabrication Centre, without their work and support I would not be able to complete this research.

Last but not least my Family; my Mum, the most important person of my life, for being so strong and for always thinking about my future. My Dad for supporting me with his love via skype calls during some of the hardest period of this adventure. My partner Daniele for his help and support during this hard time and the latest arrival, my daughter Maria Aurora for having completely messed up my life but also for giving me the strength to continue.

Table of contents

DISSERTATION OUTLINE	10
CHAPTER 1: INTRODUCTION TO MICROSCALE THERMOMETRY	24
1.1 MOTIVATIONS OF THE RESEARCH	24
1.2 THERMOMETRY TECHNIQUES	26
1.2.1 INFRARED THERMOGRAPHY (IRT)	26
1.2.2 RAMAN THERMOMETRY	28
1.2.3 FLUORESCENCE BASED THERMOMETRY	31
1.2.4 THERMOREFLECTANCE THERMOMETRY	33
1.2.5 INTERFEROMETRY THERMOMETRY	34
1.2.6 THERMOCOUPLES AND ELECTRICAL RESISTANCE DEVICES	35
1.2.7 SCANNING THERMAL MICROSCOPY (STHM)	39
1.3 SUMMARY	52
CHAPTER 2: THERMOMETRY IN WATER	54
2.1 CALORIMETRY	55
2.2 INFRARED THERMOGRAPHY (IRT)	56
2.3 RAMAN THERMOMETRY	59
2.4 FLUORESCENT THERMOMETRY	62
2.5 MICRO-FABRICATED THERMOMETERS or THERMAL ELECTRICAL THERMOMETERS	66
2.6 SCANNING PROBE MICROSCOPY (SPM)	71
2.6.1 ATOMIC FORCE MICROSCOPY (AFM)	72
2.6.2 SCANNING THERMAL MICROSCOPY (SThM) IN LIQUID	76
2.7 MICRO-THERMAL STUDIES IN AQUEOUS ENVIRONMENTS: LIVING CELLS	81
2.8 SUMMARY	82
2.9 AIMS AND OBJECTIVES	83
CHAPTER 3: NEW INSTRUMENTS AND APPROACHES EMPLOYED	85
3.1 COMMON LIMITATIONS OF SThM PROBES	85
3.2 THERMO-ELECTROCHEMISTRY	89

3.3 SThM SET-UP EMPLOYED IN THIS WORK.....	90
3.4 NEW HOLDER DESIGN AND REALISATION	92
3.5 NUMERICAL MODELLING OF THE SThM PROBE.....	95
3.6 A REALISTIC a-SThM PROBE MODEL.....	99
3.7 MODELLING STRATEGY	100
3.8 MATERIAL PROPERTIES	105
3.9 FINITE ELEMENT MESH STUDY	107
3.10 CONCLUSIONS.....	108
CHAPTER 4: SOLID SAMPLES → PT/SI ₃ N ₄ & AU/SI ₃ N ₄	110
4.1 INTRODUCTION	110
4.2 SAMPLE DESIGN AND PREPARATION	110
4.3 PROBE CALIBRATION (EXPERIMENT + MODEL).....	123
4.4 AIR/WATER SCAN AND ANALYSIS.....	132
4.5 CONCLUSIONS	150
CHAPTER 5: CONTACT AND NOT IN CONTACT a-SThM ON SOLID SAMPLES.....	152
5.1 INTRODUCTION AND MOTIVATION	152
5.2 FEASIBILITY STUDY OF NON-CONTACT THERMAL MEASUREMENT	152
5.3 NON-CONTACT THERMAL MEASUREMENTS.....	160
5.4 AIR/WATER RESOLUTION COMPARISON	173
5.5 CONCLUSIONS	191
CHAPTER 6: BIOLOGICAL SAMPLES.....	193
6.1 INTRODUCTION AND MOTIVATION	193
6.2 I-COLLAGEN.....	193
6.2.1 COLLAGEN GEL SAMPLE PREPARATION.....	197
6.2.2 COLLAGEN GEL EXPERIMENT	197
6.2.3 COLLAGEN FIBRILS PREPARATION AND RESULTS.....	202
6.3 MG-63 LIVING CELLS	211
6.3.1 INTRODUCTION	211
6.3.2 EXPERIMENTAL METHOD AND RESULTS	213

6.4 CONCLUSION	219
CHAPTER 7: FINAL REMARKS	221
7.1 SUMMARY AND CONCLUSIONS	222
7.2 FUTURE WORK.....	223
APPENDICES	225
A. DESIGN OF PT/Si ₃ N ₄ DEVICES	225
B. a-STHM ELECTRONIC SCHEMATIC AND CODE	228
C. LIFT-OFF PROCESS.....	234
D. HERTZ FIT TOOL FOR ELASTIC MODULUS CALCULATIONS	236
E. LIVING CELLS SAMPLE PREPARATION.....	237
REFERENCES	241

DISSERTATION OUTLINE

The work within this thesis is organised in seven chapters; each chapter covering a different aspect of the work carried out as summarised below. The exception to this format is the concluding chapter, which is focused on a general summary, results achieved and discussion of possible future developments.

In **Chapter 1** an introduction of the most used thermometry techniques is presented, showing their main advantages and disadvantages. For each technique, basic working principles and applications are discussed with emphasis on their performance.

Chapter 2 is dedicated to a literature review concerning thermometry in water, the SPM methodology with an emphasis on SThM in air and liquid (Figure 1). Working principles and electronic background of the technique are discussed in detail. In addition, several examples of applications and their associated limitations are introduced.

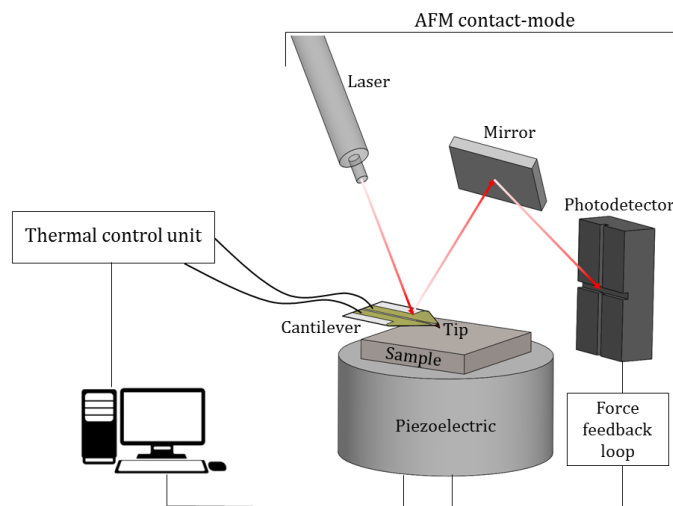


Figure 1 SThM setup.

In **Chapter 3** the design of a novel probe holder and the improved electronics required for the successful development of a-SThM, are presented. A complete 3-D model of the commercial SThM probe used (Figure 2), as well as the modelling strategy employing commercial FE software (COMSOL Multiphysics), is shown. Modelling and meshing approaches are explained, and the technical and engineering design challenges are documented.

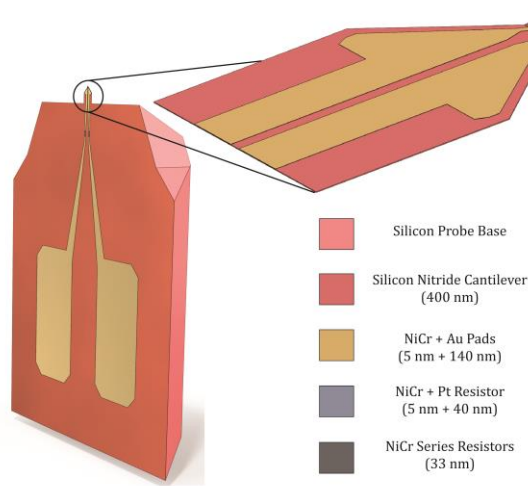


Figure 2 3-D model of the commercial thermal probe.

Chapter 4 is dedicated to the initial evaluation of the newly developed a-SThM on solid samples. The design of the samples and the probe calibration are presented as well as a full comparison between air and two different liquid environments (Figure 3). Detailed finite element simulations are presented for validation and identifying possible further improvement of the underwater technique.

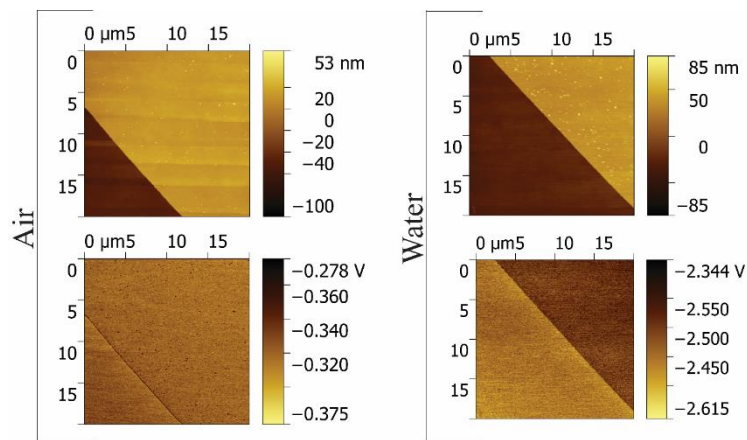


Figure 3 SThM height images and thermal images of Pt/Si₃N₄ sample in air and water.

Chapter 5 describes the use of out-of-contact a-SThM, employing it on solid samples under various liquids. Simultaneous force-distance and temperature distance curves in air and water are reported (Figure 4). The results are used to show that true underwater non-contact thermal scans can be achieved.

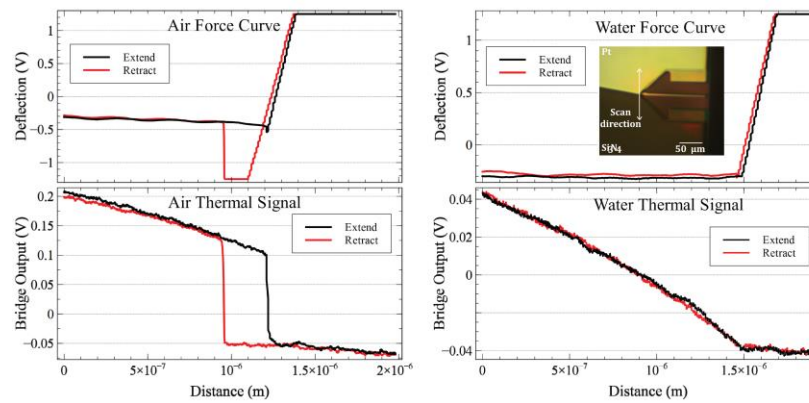


Figure 4 Comparison between SThM force curves and thermal signals in air and water.

In **Chapter 6**, a sample consisting of I-collagen is used to evaluate the use of a-SThM to probe biological samples. The results are validated against FE-predicted thermal behaviour of the probe and sample (Figure 5). a-SThM is then applied to live cells immersed in a biologically benign medium. Sample preparation and experimental results are detailed and the ability of SThM to modify live biological tissues, allowing cell manipulation is discussed.

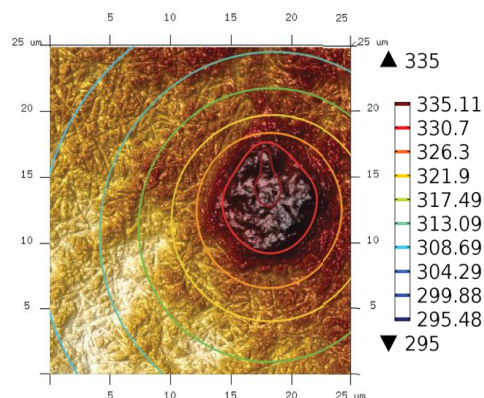


Figure 5 FE simulation of I-collagen fibrils surface temperature contour on top of the imprint left by the self-heated SThM probe.

Chapter 7 is the conclusion of this dissertation, including final considerations as well as detailing the achievements obtained. By discussing the results presented in previous chapters an accurate consideration is outlined regarding possible future work in this area.

List of Figures

Figure 1 SThM setup.

Figure 2 3-D model of the commercial thermal probe.

Figure 3 SThM height images and thermal images of Pt/Si₃N₄ sample in air and water.

Figure 4 Comparison between SThM force curves and thermal signals in air and water.

Figure 5 FE simulation of I-collagen fibrils surface temperature contour on top of the imprint left by the self-heated SThM probe.

Figure 6 Schematic of a bolometer.

Figure 7 Raman spectra of LiNbO₃ acquired at 27 °C (red), 50 °C (blue), 75 °C (brown), 100 °C (navy), 125 °C (green), and 150 °C (black). The spectra are all plotted with same intensity scale [35].

Figure 8 Schematic of the Stokes peak shift during absorption and emission process [38].

Figure 9 Schematic of an interferometer.

Figure 10 Thermocouple circuit schematic representation.

Figure 11 Different schematics of resistance temperature device circuits [49].

Figure 12 Schematic representation of passive and active mode for SThM probe, where R_{int} is the thermal resistance of solid-solid contact, R_{cant} is the thermal resistance of the entire cantilever, R_{conv} is the thermal resistance between the cantilever and the environment against thermal convection, R_{gap} is the thermal resistance between the cantilever and the sample [69].

Figure 13 Contour showing the thermal resistance against the width and length of gold wires with both the length and width varying [70].

Figure 14 (a) Schematic diagram of a Wheatstone bridge for SThM measurements. Two fixed resistors R and a variable resistor R_a to balance the probe's resistance. The applied voltage is V_{in} and the thermal signal proportional to the probe temperature comes from the difference between A and B. (b) Schematic representation of the entire SThM system.

Figure 15 Completed 2 (a) and 4 (b) terminal resistance SThM probes [104].

Figure 16 a) Probe heats up and subsequently b) bends up causing a loss of contact.

Figure 17 Schematic representation of tip artefacts induced with SThM. On a concave surface, a rounded tip with apex radius " r " will not conform to the surface, hence, thermal contact is not ideal, and a lower temperature is measured. On a convex surface, contact is ensured and the temperature is measured correctly.

Figure 18 Schematic representation of thermal artefact caused by the heat transfer coefficient of air along with the sample.

Figure 19 Thermal scan over a heated Johnson noise standard device (not to scale). Note that the heater appears hottest, with the area surrounding the membrane appearing the coolest. The heat spreader and sensor regions appear uniformly hot, with some cooling at the right due to thermal loading by the electrical leads connected to the device (341 K). Adapted *from* [90].

Figure 20 Time-resolved thermal imaging of lipase-catalysed, contained in microchannels (diameter around 600 microns), enantioselective acylation of 1-phenylethanol, 2. Colours correspond to the following temperatures. (a) At time zero; black (12.5-13.5 °C), purple (15-16 °C), pink (17-18 °C), orange (18.5-19.5 °C). (b) After 60 s; orange (18.5-19 °C), yellow (19.5-20 °C), white (20.5 °C), grey (21.4-21.6 °C) [112].

Figure 21 Water molecule absorption spectrum.

Figure 22 Schematic diagram of the micro-Raman spectroscopy system [122]

Figure 23 The left panel depicts the luminescence spectra of the T sensitive (CdTe QDs-LDH)₃₀ QDs ultrathin film in the T range 296–353 K (inset: the emission position or intensity as a function of T, respectively). The right panel shows the reversible fluorescence response of eight consecutive cycles [138].

Figure 24 Schematic representation of the B-DNA and Z-DNA structures [139].

Figure 25 Photo of visible nanothermometer. Samples contained 5 mM of ODN9 in 20 mM sodium cacodylate buffered (pH 7.0) 3.5 M NaClO₄. The photo was taken under UV (365 nm) irradiation [140].

Figure 26 Schematic representation of the sensing area of the micropipette probe [150].

Figure 27 Fabrication procedure of the micro-thermocouple probe: (a) A glass micropipette with a tip diameter of 1 μ m and a length of 50 mm is coated with a Ni film (50 nm) by ion-sputtering. (b) DLC (50 nm) is deposited using a plasma-enhanced chemical vapour deposition method. (c) The tip (1 μ m) is cut off by a

focused ion beam (FIB). (d) Constantan (50 nm) is deposited by ion-sputtering. (e) DLC (50 nm) is deposited. (f) The terminal of each layer is produced at the end opposite the probe tip. (g)-(i) The scanning electron micrographs of the probe [151].

Figure 28 (a) SEM image of a patterned PDMS sheet. The 56.0-fL chambers had STD of 1.63 in volume. (b) Optical microscope view of integrated microheater and micro thermosensor on a glass plate. (c) Schematics of the temperature-controlled microchamber array [152].

Figure 29 a) Diagram representing the AFM working principle alongside with the schematic representation of b) contact mode and c) tapping mode.

Figure 30 AFM force-deflection curve.

Figure 31 Heat transfer mechanisms between probe and sample and associated thermal network, where R_t , R_{ts} and R_s represent the thermal resistance of the tip, interface tip/sample and sample respectively.

Figure 32 Schematic representation of a dielectric inserted into a two-plates capacitor subjected to an electric field E and voltage difference U [216].

Figure 33 Wiring diagram showing connections between potentiostat, electrolysis cell and 100 kHz AC heating unit. The working electrode was a 25 μm platinum wire of ca. 24 mm in length [106].

Figure 34 Schematic illustrating the experimental setup of an active mode SThM probe scanning a sample of two different thermal conductivities (Pt and Si_3N_4). The probe forms a Wheatstone bridge with R_1 , R_2 and R_3 . T_1 and T_2 are transformers used for exciting and measuring the output of the bridge.

Figure 35 Photograph of the holder (a) and the electronic instrumentation (b) integrated into commercial Multimode Nanoscope IIIa AFM.

Figure 36 Multimode Nanoscope IIIa AFM head (with newly developed SThM stage).

Figure 37 Probe's holder for AFM scanning in liquid designed with SolidWorks.

Figure 38 CAD assembly of the complete AFM liquid cell with designed o-ring, glass window, commercial probe, probe PCB and the stage with the sample (a). Assembled 3D printed holder including PVC tubes to inject the liquid inside the cell. SThM probe is electrically connected to the probe PCB inserted in an internal cavity with an angle of 8° , and connected by two small wires to the Wheatstone bridge PCB (b).

Figure 39 Drawings of the newly designed SThM probe holder for Multimode AFM.

Figure 40 Thermal propagation mechanisms for a varying mean free path of the heat carriers and the characterization length of the material. (a), (b) and (c) represents diffusive, ballistic and diffusive-ballistic thermal transport respectively (reproduced by [1]).

Figure 41 CAD of the KNT thermal probe with the material used.

Figure 42 2D drawing of KNT thermal probe.

Figure 43 Finite element solution of the temperature field [K] for the entire probe a), and for the cantilever b).

Figure 44 Schematic representation of the SThM probe with (a) the associated materials and (b) the applied boundary conditions.

Figure 45 a) Four terminals probe station measurements, b) pattern for thin-film material thermal conductivity experiment.

Figure 46 Maximum temperature against the number of elements within the model.

Figure 47 Model and mesh of the University of Glasgow probe.

Figure 48 Pt/Si₃N₄ Device fabrication process.

Figure 49 L-Edit pattern of the devices.

Figure 50 Quarter of silicon wafer with 30 platinum devices (a), and the optical microscope pictures of the three different heaters with their resistances after the metal lift-off (b).

Figure 51 Surrogate heater device and KNT SThM probe.

Figure 52 Electrical behaviour of the probe in air and flutec pp3. The curves a and b show the current against voltage for every device, as well as their average and error bars, without evidence of failure. C and d show the associated resistance against voltage.

Figure 53 Electrical behaviour of the probe in DI water, current against voltage shows the exact moment of the failure.

Figure 54 Schematic representation of electromigration mechanisms in a conductive material under a constant electrical potential E (direction given by the blue arrow). The electrons flux (direction of the flux given by red vector) is limited by Pt ions generating the scattering of electrons (black arrows).

Figure 55 Pourbaix diagram for the nickel-water system, indicating the E/pH regions of thermodynamic stability of various dissolved and solid species and the regions of “corrosion immunity”, “passivation”, and “active corrosion” [173].

Figure 56 Representative SThM sacrificial heaters failure.

Figure 57 Calibration setup for measuring the temperature coefficient of resistance (TCR) of the probe in air, flutec PP3 and DI water.

Figure 58 Temperature plots of a passively heated probe vs resistance in the air (a), flutec PP3 (b) and water (c).

Figure 59 Plots of probe temperature rise caused by probe self-heating due to the AC voltage applied in Air (a), in Flutec PP3(b) and in Water (c).

Figure 60 Rayleigh number calculated for a varying a) thermal gradient and b) a varying characteristic length.

Figure 61 Full-probe FEA showing temperature distribution in air environment during the calibration, strong thermal localisation can be identified at the probe tip.

Figure 62 FE simulation of the temperature contour distribution of a typical Si₃N₄ cantilever with Au leads and Pd thermal sensing element heated by Joule Heating, where each isothermal line corresponds to a change of 2 K (e) in air, flutec and water.

Figure 63 Temperature distributions along the path A-A' of Figure 62 for different environments (air, flutec, water) considered in the numerical analyses.

Figure 64 Total heat flux magnitude generated by the Joule effect during numerical analyses in air and water environments.

Figure 65 SThM height images (a), (c) and thermal images (b), (d) of Pt on Si₃N₄ in air and in water.

Figure 66 Comparison between Pt/Si₃N₄ cross-sections in air and water (red and black line in thermal images).

Figure 67 Comparisons between SThM repeated measurements in air (a, c) and water (b, d), showing the better thermal coupling obtained in water. Comparison of voltage signal between air (e) and water (f) along with two precise paths crossing the interface.

Figure 68 Thermal images for a long-time scan in the air at time 0 (a), 5 minutes (b), 10 minutes (c), 15 minutes in the end at 20 Minutes(d) and a closer view (e).

Figure 69 Sequence of equally timely-spaced thermal images for a 20 minutes scan in water with new probe.

Figure 70 SEM images of a standard SThM tip acquired with two different angles: at 0° (a) and 40° tilted probe (b) and a schematic side and frontal views representation of the cantilever tip with the accumulated material(c).

Figure 71 3D model built in SolidWorks of the standard cantilever and tip on a Pt/Si3N4 sample.

Figure 72 Schematic representation of an interface between different surfaces in COMSOL, where each circle is a node.

Figure 73 Plots of the average temperature of the probe during a line scan in the air (a) and in water (b) for the chosen solid/solid heat transfer coefficients ($h = 10^7 - 10^{10} \text{ W(m}^2\text{K}^{-1}\text{)}$). Arrows point the corresponding vertical axis.

Figure 74 Temperature of the heater and sample during the simulated SThM scan of dissimilar materials at a) 20 μm , b) 35 nm and c) 20 μm from the interface in water.

Figure 75 Temperature of the heater and sample during the simulated SThM scan of dissimilar materials at a) 20 μm , b) 35 nm and c) 20 μm from the interface in air.

Figure 76 Schematic representation of methodology for average temperature calculation, a) finite element model in COMSOL, b) example of nodal temperature contour and c) the average temperature.

Figure 77 Schematic of the meniscus between the probe and sample [63].

Figure 78 Comparison between SThM force curves (a), (b), (c) and thermal signals (d), (e), (f) over Si3N4/Pt sample in air, in water and flutec PP3..

Figure 79 COMSOL MULTIPHYSICS 3D model of the probe in contact with Si3N4 sample. Increase of the temperature of the probe in contact with the sample and surface temperature distribution of Si3N4 in the air (a) and in water (b).

Figure 80 COMSOL MULTIPHYSICS 3D model of the probe in contact with Si3N4 sample. Total heat flux magnitude and heat flux vectors of the probe and the heated extension of the sample Si3N4 in the air (a-b) and in water (c-d) respectively (The vectors magnitude **is not** normalised to a single maximum value).

Figure 81 Plot of the average temperature of the probe versus its distance from Si in air, flutec PP3 and water (left vertical axis for Air and Flutec PP3 and right vertical axis for Water).

Figure 82 Plot of approach thermal signal of probe versus its distance from Si₃N₄/PI sample in air, flutec PP3 and water.

Figure 83 Lift mode profiles.

Figure 84 SThM of PI on Si₃N₄ in water showing AFM height images (a-d), thermal images in contact (b-e) and thermal images out-of-contact (c-f) with probe distant from the surface of 0.5 μm and 1.5 μm .

Figure 85 SThM of PI on Si₃N₄ in flutec PP3 showing AFM height images (a-d), thermal images in contact (b-e) and thermal images out-of-contact (c-f) with probe distant from the surface of 0.5 μm and 1.5 μm .

Figure 86 SThM of Au on Si₃N₄ in water showing AFM height images (a), thermal images in contact (b) and thermal images out-of-contact with probe distant 1.5 μm from the surface (c) and zoom in of the associated picture within the red circle, showing a thermal artefact.

Figure 87 Cross sections through 3D FE simulation of typical Si₃N₄ cantilever with Au leads and Pt thermal sensing element heated by Joule Heating. The global simulation images (a) show the difference of cantilever temperature distribution (black rectangles) between water and the other two environments. Zoomed view of the tip in contact with Si and out-of-contact (0.5 μm and 1.5 μm) in air (b) flutec PP3 (c) and water (d).

Figure 88 Temperature along the probe apex, on the path A-A', when performing SThM (simulation) in Air, Flutec PP (left vertical axis) 3 and water (right vertical axis) in out-of-contact at 1.5 μm from the sample.

Figure 89 Temperature along the probe apex, on the path A-A', when performing SThM (simulation) in Air, Flutec PP (left vertical axis) 3 and water (right vertical axis) in-contact with the sample.

Figure 90 In contact SThM simulations results showing the probe temperature for air and water environment (a and b). The local temperature of the sample's surface is shown in c and d for air and water environments respectively.

Figure 91 Out of contact SThM simulations results showing the probe temperature for air and water environment (a and b). The local temperature of

the sample's surface is shown in c and d for air and water environments respectively.

Figure 92 COMSOL MULTIPHYSICS 3D model of the probe in out of contact with Si₃N₄ sample. Total heat flux magnitude and heat flux vectors of the probe and the sample Si₃N₄ in the air (a-b) and in water (c-d) respectively.

Figure 93 Design of the pattern (a) and optical microscope image of the Au/Si₃N₄ sample surface after lift-off (b).

Figure 94 SThM cantilever on a sample and the scan direction highlighted by a white arrow.

Figure 95 AFM topographic images and thermal images showing the same sample scanned by a standard SThM probe in air (a), (b) and water (c), (d). In the rectangle on the right is reported an enlarged topographic (e) and thermal (f) image in air and topographic (g) and thermal (h) under water and, where a 1 x 1 μm² square is clearly visible.

Figure 96 Thermal signal intensity in a) air and b) water along the path where the signal is taken.

Figure 97 Thermal images of Au/Si₃N₄ sample in air (a) and water (b), obtained by averaging the signal over a 40x20 px area. Trace and retrace plot of the cross sections showing the differences in both the environments with the topographic artefact present in air (c).

Figure 98 Boltzmann sigmoid function plot and parameters.

Figure 99 Comparison of experimentally measured curves of thermal intensity for SThM in air and in DI water across Au-Si₃N₄ boundary and associated fit (R² = 0.99712 for water and R² = 0.93812 for air).

Figure 100 SEM images of a misaligned (a) and a standard (b) thermal heater of the probe.

Figure 101 Probe 3D CAD model (a), thermal field for the standard KNT probe (b), the newly designed probe (c) and the simulated thermal scan achieved by using these two probes and the associated fit(d).

Figure 102 Different design attempts a, b, c and thermal fields for SThM probes with one cut-out at the heater level (d), at the cantilever level (e), in both the areas (f) and of the new design without any cut-out (g).

Figure 103 (a) CAD model of the newly designed probe, FEA temperature distribution of a thermal probe with a newly designed smaller heater (b) and with the standard heater (c).

Figure 104 Plot achieved by the underwater simulations with these two probes scanning across a Pt/Si₃N₄ sample compared with the experimental curve.

Figure 105 Simulated thermal scan plot for standard probe (green line), small heater (red) and the small-asymmetrical design (blue).

Figure 106 Evolution from a single chain precursor to the fibre [279].

Figure 107 Force curves and their derivatives obtained when a hot probe touches I-collagen gel for 2 min (a) and 5 min (b). The curve are compared with those of a glass sample (c).

Figure 108 Icon AFM picture (a), topographic height images in tapping mode and 3-D plots of imprints left by a heated probe on gelatinized I-collagen on glass slide (b).

Figure 109 Schematic representation of the tip-sample interaction and subsequent material softening during a constant force indentation.

Figure 110 Contact stress at the area of contact between two spheres subjected to a force F .

Figure 111 Force curves and their derivatives obtain when a probe, cold at the beginning, touches I-collagen fibrils for 0 min, 2 min, 5 min and 7 min (a), compared with those of a glass sample (b).

Figure 112 Stiffness curves for the glass and collagen against heating time in water.

Figure 113 Icon AFM picture (a), topographic height image, (b) section plot on the highlighted path and (c) deflection image.

Figure 114 Topographic height (a) and deflection (b) images of an imprint left by a heated probe on I-collagen fibrils. 3-D plot with FE simulation of the surface temperature contour on top of the imprint (c).

Figure 115 Optical microscope images of a single MG63 cell left in contact with a hot SThM probe (2 min) and lifted up.

Figure 116 Optical microscope images of a single MG63 cell left in contact with a cold SThM probe (for 10 min) and lifted up.

Figure 117 Finite element mesh of the probe/cell/substrate model, the surrounding environment is not shown for sake of clarity.

Figure 118 COMSOL Multiphysics analysis results showing the temperature generated by the probe using a current of 0.0047 A in a water environment.

Figure 119 Temperature predicted by COMSOL MULTIPHYSICS joule heating simulations during the contact with a hot probe and extracted for MG63 cell.

Figure 120 Resistors design. The total length (l) of the heaters is respectively (a) $l = 1290 \mu\text{m}$, (b) $l = 1630 \mu\text{m}$, and (c) $l = 1210 \mu\text{m}$.

Figure 121 Resistors design. The total length (l) of the heaters is respectively (a) $l=410\mu\text{m}$, (b) $l=340\mu\text{m}$, and (c) $l=287\mu\text{m}$.

Figure 122 Electrical schematic of the a-SThM setup.

Figure 123 Lift-off process steps: I. Preparation of the substrate II. Deposition of the sacrificial stencil layer III. Patterning the sacrificial layer (ex. etching), creating an inverse pattern IV. Deposition of the target material V. Washing out the sacrificial layer together with the target material on its surface VI. Final pattern.

Figure 124 Hertz fit output example.

Figure 125 2D representation of the thermal probe pushing the cell nucleus on the prepared sample.

Figure 126 Optical microscope image of the deposited cell used during the experiment.

List of Tables

Table 1 Boundary conditions used in the FE model for different environments.

Table 2 Estimated thermal and electrical conductivity for thin film materials used in an a-SThM probe.

Table 3 Fitting outcome for data in water.

Table 4 Fitting outcome for data in air, with truncated data.

CHAPTER 1: INTRODUCTION TO MICROSCALE THERMOMETRY

In this chapter, the research background and motivation for investigating SThM in a liquid environment are discussed. In addition, other thermometry techniques are introduced.

1.1 MOTIVATIONS OF THE RESEARCH

The measurement and accurate control of temperature have been fundamental tools in the fields of science and engineering ever since the work of pioneers such as Celsius and Fahrenheit in the 18th century [2]. Despite this maturity, modern applications continue to challenge the technology of temperature measurement by pushing it into ever more demanding scenarios. A good example of this is thermal measurement at the nano-scale with its requirements for both temperature accuracy and high spatial resolution. Modern applications can require sub-100 nm spatial resolution and sub 0.1K temperature resolution [3], [4]), a challenging combination for conventional thermometry methods.

The drive to develop advanced thermometry techniques has been largely led by the rapid evolution of research at sub-micrometre scales, where conventional thermometers are ineffective. Adapting to these new requirements is more complex than simply decreasing the size of conventional tools. Handling of miniaturised conventional thermometers is often impossible due to their extreme delicacy; this means that they are often integrated onto the object being measured (e.g. using microfabrication) or that specialised micromanipulation techniques must be employed [5]. Microfabricated thermocouples, for example, need to be connected to external instrumentation, often by wire bonding. This introduces an additional thermocouple junction, compromising their performance. Small Resistance Temperature Detectors (RTDs) are extremely sensitive to current flow due to their small cross-sectional area (resulting in large current density) [6]. As a consequence, they can self-heat or even be destroyed if specialist low current measurement approaches are not employed.

Advanced nanofabrication methods have permitted the production of an increasing number of nanoscale devices and structures based around new materials such as nano semiconductor devices [7], carbon nanotubes [8] , nanowires [9], superlattices [10] and graphene [11], which have found their

applications in practical work [12]. For example, carbon nanotubes have been used for their excellent electrical properties demonstrating great electron field emission capabilities[13]. Graphene's high conductivity and high carrier mobility, combined with its relatively high optical transmittance, have been exploited in transparent conductive films [14]. Nanowires have opened new possibilities for realising nanosensors known as "electronic noses" capable of identifying chemical substances in the air by exploiting the quasi-one-dimension electronic transport and ability to densely pack arrays of nanowires [15]. These are just some applications of such new nano-materials, all of which require accurate knowledge of the effect of the temperature on the material being developed. The elastic instability induced by rising the temperature may cause the failure of integrated circuits or microelectronic devices. Thermal expansion is a fundamental property of nanomaterials directly related to temperature changes. Experimental results show that the thermal expansion coefficient of nanocrystalline materials are larger than those of their polycrystalline counterparts, a behaviour which depends on temperature and is influenced by size [16]. Furthermore, nano-devices can be operated at a higher current density due to their enhanced cooling granted by their large surface to volume ratio [17]. However, the exact magnitude of this cooling is hard to predict as interfacial heat transfer coefficients can only be determined experimentally [18]. This means that although nano-sensors can be pushed harder without failing, measurement of their self-heating is required for their operating conditions to be optimised.

The wide variety of application areas means that there are an equally large range of micro/nanoscale temperature measurement techniques available: from conventional technologies such as thermocouples and thermal resistance devices adapted to the nanoscale [19], to remote optical approaches such as infrared thermometry [20], Raman [21], fluorescence [22], thermoreflectance [23] and interferometry [24]. Therefore, a clear understanding of the merits and drawbacks of each method is desirable for selecting an appropriate technique. In the following section, the working principles of these measurement methods will be listed according to the signal generated.

1.2 THERMOMETRY TECHNIQUES

1.2.1 INFRARED THERMOGRAPHY (IRT)

Infrared thermography is used to determine the temperature of a body by measuring its radiation intensity, considering it as a black body. A black body is an object capable of absorbing all electromagnetic radiation colliding with it across the entire spectrum of wavelengths. At the same time, this body emits energy at a maximum potential rate at any given temperature. However, in nature, no object behaves fully as a black body, but the underlying concept expressed by Planck's law that a blackbody radiator emits distinct and predictable radiation depending on its temperature is crucial for the functioning of IRT, and still applicable to all objects in nature. Any surface above absolute zero Kelvin emits radiation. The intensity of the radiation emitted by the body can be expressed as follows:

$$I(\lambda, T) = \frac{2\pi hc^2}{\lambda^5 \left(e^{\frac{hc}{\lambda K_B T}} - 1 \right)} \quad (1)$$

where λ is the wavelength, h is the Planck's constant (6.626×10^{-34} Js), c the speed of the light (299,792.458 m/s) and K_B is the Boltzmann's constant ($1.38066503 \times 10^{-23}$ J/K). IRT sensors operate by measuring the magnitude and peak wavelength of emitted radiation, making the technique capable of measuring surface temperatures from cryogenic to over 6000K.

The foundation of IR thermometry can be associated with the discovery of infrared radiation by William Herschel in the early 1800s [25], followed by the first "heat picture" taken in 1840 by his son Sir John Herschel [26]. This was obtained by the differential evaporation of a thin film of oil exposed to a heated surface. However, until the 19th century, no further improvement in this field was achieved [27]. The first step forward in IR thermal imaging was associated with the development of the bolometer by Samuel Langley. This sensitive device was able to detect the heat loss from cattle at 400 meters [28].

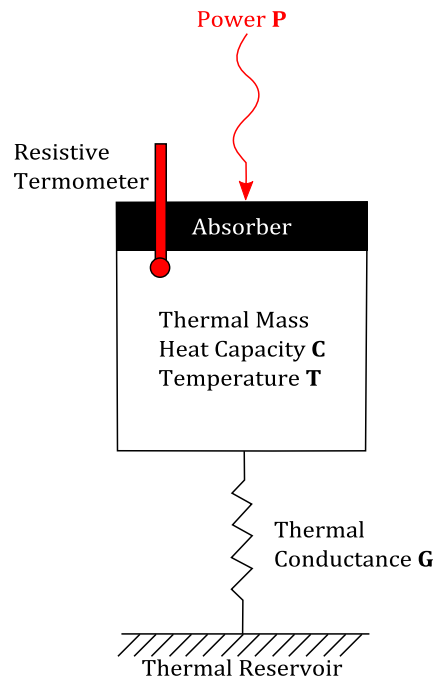


Figure 6 Schematic of a bolometer.

A bolometer (Figure 6) is composed of an absorbing element, usually a thin foil of metal connected to a thermal reservoir via a thermal link, which is kept at a constant temperature. The incident radiation tends to increase the thin foil temperature generating a difference in temperature between the foil and the reservoir. Consequently, the measuring speed of the device is directly related to the ratio between the heat capacity of the absorbing element and the thermal conductance on the thermal link [29]. To measure the change in temperature the change of electrical resistance within the thin foil is commonly used. However, a simpler approach involves attaching a resistive thermometer directly to the absorbing element. The first bolometers were based on metal, without any cooling system to keep the thermal reservoir at a constant temperature. Depending on the type of bolometer and its application, the cooling system can range from a simple heat sink that dissipates the heat accumulated by the reservoir through to a complex cryogenic system used for example in space imaging applications [30].

This concept was heavily developed in the 20th century, mainly due to demand from the military. Between the 1950s and 1990s devices became more portable, more accurate and less expensive, even for scientific applications. This permitted the simplification of thermal-cameras and infrared detectors, which decreased in size and weight by operating without complex cooling systems [28].

Infrared thermometry nowadays is applied to several areas from engineering to medical fields for the rapid evaluation of the temperature of bodies. Despite the immediate availability of this technique, it has limitations. These include a low spatial resolution of around 3 microns due to the diffraction limit of the infrared optical wavelength. Furthermore, radiation from the surrounding environment must be controlled and minimised to obtain accurate measurements. This significantly increases the difficulties of deploying such systems in environments with several sources of heat.

1.2.2 RAMAN THERMOMETRY

Raman spectroscopy [31], [32], named in honour of its inventor, C.V. Raman, who along with K.S. Krishnan published the first paper on it, is a spectroscopy technique based on an optical signal, in particular on the inelastic scattering of monochromatic light.

The Raman process is based on inelastic scattering where scattered light exhibits a decrease in energy and frequency [33], as opposed to elastic scattering (known as Rayleigh scattering) in which the scattered photons from atoms or molecules have the same energy as photons impacting the material. This type of scattering is not common and represents only a small fraction of the scattering process of photons. This process makes the Raman effect different from processes such as the fluorescence, where a photon is emitted from a high energy state. In addition, the Raman effect can be observed at any frequency of incident light with no resonant effect. This is important for the practical application of Raman spectroscopy in general since the Raman peaks are well separated by the excitation frequency. This concept can be applied to study molecules by measuring the ratio between the intensity of incident and scattered photons, which corresponds to the excitation energy of the molecule.

Therefore, Raman spectroscopy is a well-established analytical technique for identifying chemical compounds, characterizing chemical bonding and solid-state structure of materials. However, it is less known for its use as a thermal sensor despite being a valid technique for measuring temperature when other more direct approaches are not practical. Its working principle is based on the peak shift in the Raman bands when the analyzed material is affected by a change in temperature.

The shift in the Raman bands is caused by the behavior of phonons within the material. Theoretically, the vibrational and rotational excitations measured by Raman spectroscopy arise from perfectly harmonic independent oscillators (phonons) at the very well-defined spectrum. However, the excitation of phonons are not fully harmonic and also depends on interaction with other phonons and electrons [34]. Therefore, when the shift in the Raman band is significant enough to be resolved, the peak position can provide an accurate measurement of the temperature.

There are two possible approaches to measure the temperature using Raman spectroscopy. When a narrow Raman band is available, the peak position will significantly shift with the increase or decrease of temperature. This is because an increase in temperature will enhance the bond length decreasing the energy of the vibrational mode. As mentioned previously, this vibration can be associated with the harmonic oscillation with a fixed force constant. The vibrational magnitude of molecules is dictated by temperature that stretches the bonds of the atoms, reducing the repulsion force and so the potential energy. Conversely, a decrease in temperature will increase the energy of the vibrational mode by shortening the bond length. This change in bond length will affect the vibrational force constant (that for a harmonic oscillator can be assumed to be a linear Hook's spring constant), which will consequently affect the Raman peak position producing the shift (Figure 7).

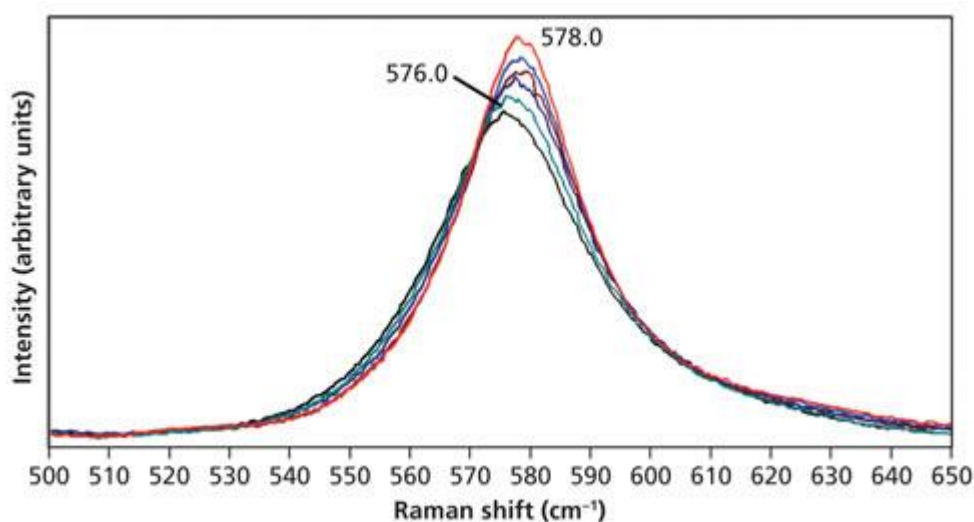


Figure 7 Raman spectra of LiNbO₃ acquired at 27 °C (red), 50 °C (blue), 75 °C (brown), 100 °C (navy), 125 °C (green), and 150 °C (black). The spectra are all plotted with same intensity scale [35].

When no narrow Raman band is available, it is possible to measure the signal strengths of a specific Raman band at the Stokes and anti-Stokes positions [36], calculating the temperature based on a Boltzmann distribution of the base and first excited state populations.

The Stokes shift consists of the re-emission of a photon that has a lower energy (longer wavelength) than the incident radiation. Its origin can be found in two processes; vibrational relaxation and solvent reorganisation. The process of relaxation and re-equilibrium of both excited and ground state is very fast, in the order of femtoseconds. However, the surrounding solvent does not react and re-organise so quickly, leading to a delayed re-equilibrium [37]. These two processes of re-organisation are the cause of Stokes shift depicted in Figure 8. Conversely, the anti-Stokes shift that corresponds to the emission of photons at higher energy than those impacting. The additional energy is caused by dissipation of thermal phonons [38].

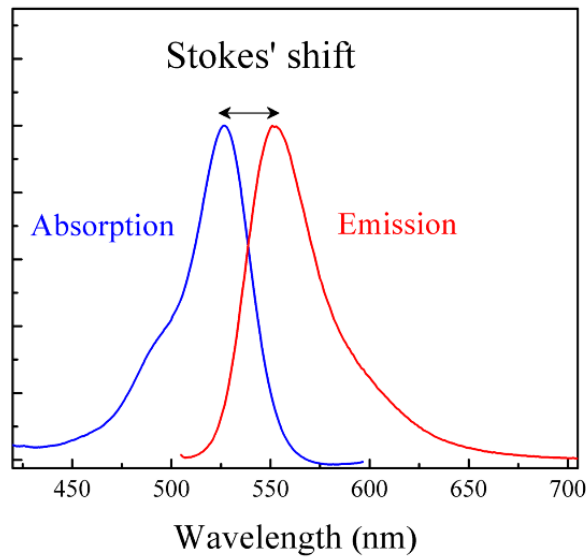


Figure 8 Schematic of the Stokes peak shift during absorption and emission process [38].

The expression most frequently used [39] to describe this relationship is shown in equation (2)

$$\frac{J_{AS}}{J_S} = \frac{(V_l + V_v)^4}{(V_l - V_v)^4} \exp\left(\frac{-hV_v}{kT}\right) \quad (2)$$

where T is the temperature, k is Boltzmann's constant, h is Planck's constant, V_l is the frequency of the laser, V_v is the frequency of the vibrational mode (Raman band position), and the Stokes (J_S) and anti-Stokes (J_{AS}). Raman scattering strengths are based on energy detection of the signals. In the case where the

spectrum is obtained using an energy-based approach equation (2) is recommended.

Typically, as mentioned previously, Raman scattering is less probable than Rayleigh scattering, resulting in a weaker signal that is difficult to separate from the more intense Rayleigh scattered laser light. For this reason, a photomultiplier tube is connected via optical fibre to the sample chamber to amplify and enhance the signal produced by Raman scattering.

One of the benefits of Raman thermometry is that the sample can be directly measured without preparation and the technique is not invasive. However, disadvantages include the fact that this technique can only be used on materials that have a clear Raman response and the processing velocity of the peaks generated by the sample is limited by its surface properties. In addition, this technique is more suitable for temperature changes in the order of 5 K, due to the weak nature of the inelastic scattering [40] affecting the overall accuracy of the method. Finally, the spatial resolution is limited by the spot size of the laser adopted for generating the Raman scattering on the sample, and it is typically around 0.5 microns in a good optical system.

1.2.3 FLUORESCENCE BASED THERMOMETRY

Fluorescence is a widely studied mechanism that can be observed in nature consists of the emission of light by a material that has previously absorbed incident radiation. More specifically fluorescence is the result of the change of energy state of an electron, which drops from an excited high energy state S_1 to its ground state S_0 . This emission process produces heat, in the form of infrared radiation, and a photon with associated energy expressed by $E=h\nu_{fe}$, where h is the Planck's constant and ν_{fe} fluorescence emission frequency [41]. The photon emitted by the fluorescence mechanism usually has a longer wavelength (Stokes shift), hence lower energy with respect to the incident radiation. Any fluorescence process is characterised by a typical emission frequency, which can be affected by the temperature. This change in frequency enables a fluorescent compound to be used as a thermometer.

There are several types of fluorescent thermometers, each works depending on different principles including fluorescence intensity [42], quantum yield [43], fluorescence lifetime [44], peak wavelength [42], and fluorescence anisotropy [45]. As explained for IR thermometry, all objects and so every luminescent

molecule exhibits a temperature dependent radiative emission. This is due to the Boltzmann distribution and the electronic band system of the material considered. The dependency between luminescence and temperature can be summarized by a non-radiative transition constant (k_{nrt}). This constant is related to the temperature by:

$$k_{nrt} = e^{-\frac{\Delta E}{kT}} \quad (3)$$

where ΔE is the energy gap between the lowest energy level of the excited state and a non-radiative decay level and k is the Boltzmann constant [46].

Luminescence intensity follows Parker's law [47] that depends linearly on the intensity of the exciting source I_0 (usually a laser), the quantum yield factor Γ (that goes from 0 to 1), a geometrical factor associated with the experimental setup ε , the penetration depth of the laser δ , the absorbance α and finally concentration of the luminophore c_{lum}

$$I_p = I_0 \cdot \Gamma \cdot \varepsilon \cdot \delta \cdot \alpha \cdot c_{lum} \quad (4)$$

The luminophore is defined as an atom or a functional group of a chemical substance responsible for its luminescence response [47]. Theoretically, the temperature should affect only the quantum yield, which is the ratio between the emitted photons and those excited – making a measure of intensity change a measure of temperature change in an otherwise stable system. However, it has indirect effects via other practical aspects such as the background luminescence of the sample.

In order to achieve accurate measurements, luminescence thermometers are not based on single-wavelength intensity [46]. This is because a single wavelength can easily be affected by external light excitation from the surrounding environment. To cancel this effect, a second emitting source is used. The first approach considers the use of a second source that can take the form of a reference dye. However, it is not capable of solving the background fluorescence, the light scattering and the reflection issues. The reference dye is excited using the same wavelength used for the main measurement but should generate a well-distinguished emission wavelength. The second approach requires the use of two emission wavelength probes, which will produce two independent emission bands and their ratio will be used as a reference signal.

Another way of calculating the temperature consists of directly measuring the quantum yield, which is given by

$$QY = \frac{\Gamma}{\Gamma + k_{nrt}} \quad (5)$$

where Γ represents the emissivity rate of the luminophore, which decreases with increasing temperature (k_{nrt}). Similarly, fluorescence lifetime, which is defined as the average time during which the electron stays in the excited state, can be used. The lifetime is related to temperature by the following relationship

$$\tau = \frac{1}{(\Gamma + k_{nrt})} \quad (6)$$

The use of luminescence thermometry has been developed for a great number of applications, especially in the biological field. The range of operating temperatures is from 77 K up to 525 K, with sensitivities that can reach up to 0.08 K⁻¹ [46]. However, there are drawbacks such as the measurement spot size, which is fixed by the luminophore size and is typically in the order of microns. In addition, the detection of the signal depends on the optical probe and read-out process, adding complexity to the system.

1.2.4 THERMOREFLECTANCE THERMOMETRY

Thermoreflectance thermometry is based on the ability to detect the variation of reflectivity ($\Delta R/R$) of the surface of a sample due to the associated change in temperature at the surface (ΔT). A linear relationship can be established between the variation of reflectivity and the change in temperature:

$$\frac{\Delta R}{R} = C_{TR} \Delta T \quad (7)$$

where C_{TR} is the thermoreflectance coefficient, with this linear relationship being valid for small temperature changes [48]. The constant C_{TR} is usually in the range of 10⁻⁵ up to 10⁻³ K⁻¹. When this coefficient is known, a simple measurement of change in reflectivity can give the temperature change. However, C_{TR} is dependent on the specimen material and the wavelength of incident light. In addition, the specific measurement apparatus can have a severe impact on the accuracy of the method. This accuracy is dictated by the capability of the optical sensor to measure small differences in reflectivity of the surface under study. This can lead to a drift in the temperature measurement and a subsequent low degree of accuracy, which is detrimental in a field where high thermal resolution is

required. For these reasons, a measurement calibration process must be undertaken before performing each measurement. C_{TR} is temperature dependent, even at moderate temperatures (around ambient temperature), and its dependency increases at high-temperature, eventually becoming nonlinear. Predicting the dependence of a material's C_{TR} on temperature is challenging since it is governed by a combination of electron transition, optical absorption, phonon integration and light polarisation [49].

The main advantage of this technique is the fact that it can work at wavelengths much smaller than other optical methods such as infrared thermometry, permitting spatial resolution down to 100 nm [49]. However, the measurements are highly dependent on the specific sample and the calibration process to identify the reflectivity constant. This makes accurate measurements a non-trivial task since values are not only dependent on temperature and material, but also on surface finish, leading to a significant risk of inaccurate measurements [48].

1.2.5 INTERFEROMETRY THERMOMETRY

Interferometry is a non-invasive technique that uses superimposed electromagnetic waves to obtain information through their interference. This mechanism consists of the interaction between two waves, which by constructive or disruptive interference, generate a new wave with greater or lower amplitude. Usually, interferometry regards the interaction between correlated waves, due to originating from the same source or because they have a similar frequency. The technique employs two light beams, one passing away from the region of interest, and the other going across it (Figure 9).

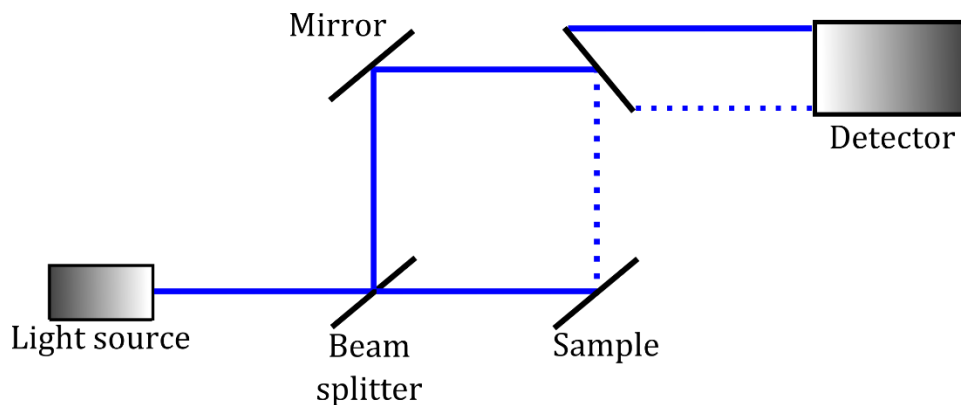


Figure 9 Schematic of an interferometer.

The difference in the path and the interaction with the object produce a distortion in the wavefront ultimately resulting interference at the detector [50]. In thermal measurements, this distortion is caused by a change in the reflective coefficient and local deformation caused by thermal expansion.

Interferometry measures both the refractive index (α) variation and the thermal expansion (β) of a sample, and using the following relationship this information can be used to derive the temperature change:

$$\alpha = \frac{1}{n_t} \frac{dn_t}{dT}, \beta = \frac{1}{h_t} \frac{dh_t}{dT} \quad (8)$$

where n_t is the reflectivity and h_t the linear coefficient of thermal expansion. Despite spatial resolution as high as 100 nm, the interaction of the beam with the sample can cause many problems impacting on the accuracy of the measurements. The accuracy of this class of instruments is affected by the quality of the signal between the sample and the detector[49]. The reflected radiation originated from other sources and the unknown reflectivity of a sample are some of the most common issues of this technique.

In addition, the surface finish and any material mismatch (when more than one material is present) can decrease the accuracy of this method whilst, at the same time, increasing the complexity of the measurement.

1.2.6 THERMOCOUPLES AND ELECTRICAL RESISTANCE DEVICES

Among all the methods currently employed for measuring temperature, thermocouples are one of the most common, least expensive and simple approaches. Thermocouples work through the Seebeck effect, which describes the production of an electromotive force across a circuit when two different conductors are exposed to a thermal gradient [49]. This electromotive force modifies the well-known Ohm's law by redefining the current density as:

$$J = \sigma(-\nabla V + E_{emf}) \quad (9)$$

where σ is the conductivity of the material, V is the electrical potential and E_{emf} is the electromotive force. In thermocouples, the current density is considered to be equal to zero since the system is supposed to be at steady state. The electromotive force is a function of the temperature gradient and the Seebeck coefficient, which is dependent on the material and temperature. Assuming steady-state conditions ($J = 0$), it is possible to calculate the potential without

knowing the conductivity of the material. This is fundamental for the use of thermocouples, that can measure temperature by measuring the difference of potential generated by the thermal gradient.

Effective thermocouples can be fabricated using several types of conductive material, including noble metals, base metals, refractory metals and even non-metals [35]. Common metals include copper, nickel, chromium and the alloy Constantan (Nickel + Chromium), and can operate over a temperature range between -268 up to 2000 °C. Figure 10 describes the formation of a thermocouple circuit. Initially, Figure 10a, two conductors (A and B) are in contact and T_1 is greater than T_2 . This causes the formation of an electromotive force. In Figure 10b a third conductive material is included and will be affected only if a thermal gradient occurs. A change in the position of conductor C is depicted in Figure 10c and d. This improvement allows local measurement of the temperature gradient, where both A and B are connected to C creating 2 distinct junctions. In order to obtain a useful measurement, T_2 must be known. This can either be achieved through independent measurement of T_2 or by keeping it constant, for example by using a Peltier cooler or a water bath.

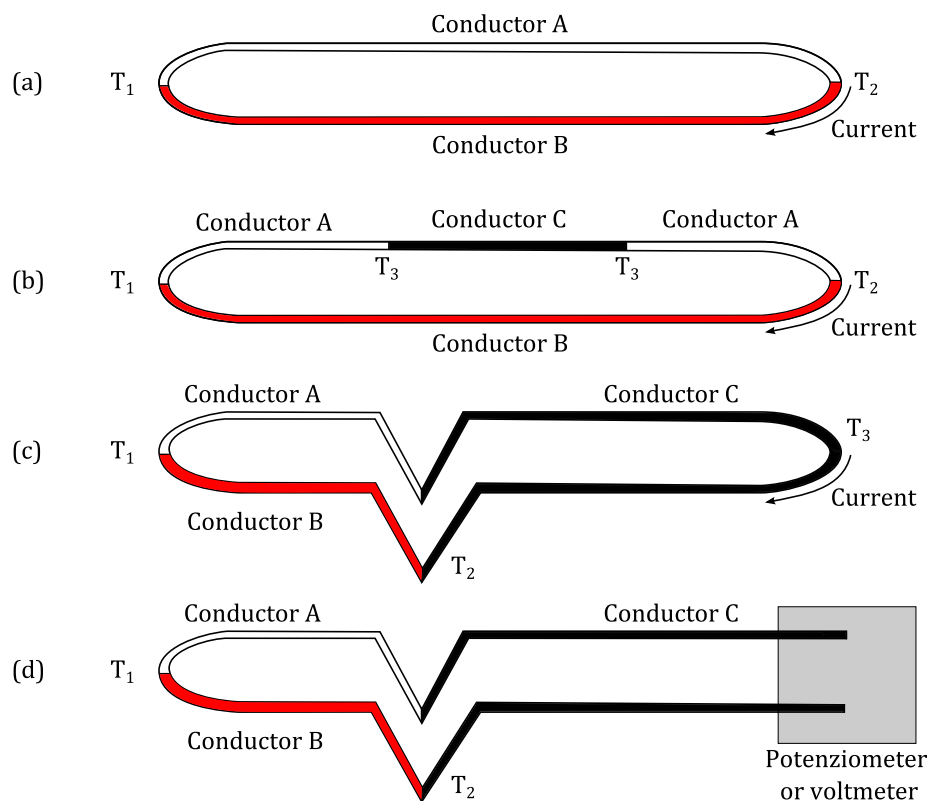


Figure 10 Thermocouple circuit schematic representation. Conductor A in contact with Conductor B with T_1 greater than T_2 (a). A third conductive material (Conductor C) is included in the circuit and will be affected only if a thermal gradient occurs (b). A change in the position of Conductor C is shown (c and d).

The main advantage of this measuring method is its simplicity and low cost, but if poorly implemented, for example if the thermocouple wire does not exhibit ideal behaviour (e.g. due to electron surface scattering in the wires, poor contact at junctions or high wire resistance, all of which are problems associated with the very thin wires used for fast thermal response), it can be associated with low accuracy and a spatial resolution that depends entirely on the thermocouple dimensions. This low accuracy is caused by multiple factors like cable specification, spurious intermediate junctions, cold junction temperature measurement, voltmeter sensitivity, and cable drift. Cables can also be affected by high-temperatures or stresses that alter the thermocouple material properties. Drift can be observed, especially at high-temperature, when annealing of the material that makes the thermocouple is present, again resulting in a change of its properties [49].

Another way to measure temperature is by using electrically conductive material to form resistance temperature devices (RTD). RTDs use the change in material resistivity to determine the temperature and require a power source to be operated. In theory the resistance of a metallic material changes linearly with temperature, however, this is not true for all materials, for example, the resistance of tungsten has a power-law trend with temperature. The dependence of resistivity with temperature can be explained by looking at the atomic level. Thermal vibration in solids is associated with phonons. When a current of electrons flows in the conductor they can interact with phonons, resulting in scattering and hence electrical resistance. However, when the temperature increases, so do the thermal vibrations, increasing the number of collisions between electrons and phonons. The effect associated with this increase in collisions is an increase in electrical resistance [51].

Theoretically, any metal can be used as a thermometer, but due to stability, manufacturing, operation and cost issues, the choice is typically limited to copper, gold, nickel, platinum and silver [49]. A variety of options for measuring temperature-induced changes in resistance are shown in Figure 11.

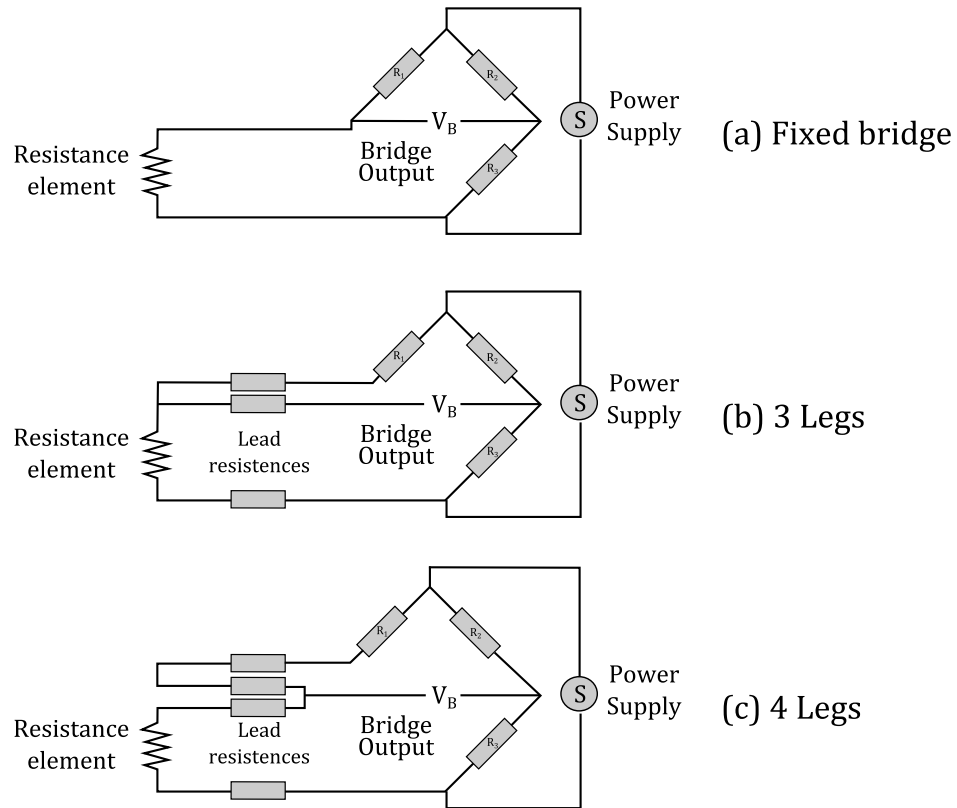


Figure 11 Different schematics of resistance temperature device circuits [49].

One of the most common is depicted in Figure 11a, where a fixed bridge configuration is shown. In this configuration the resistance R_1 is adjusted until the current flow across the bridge output is zero. The principal drawback of this type of circuit is the inaccuracy generated by the intrinsic resistance of the wires connecting the bridge to the resistance element that is not balanced. In Figure 11b and c, improvements to the fixed bridge are shown. In this 3-leg RTD circuit, the wire resistance of the central leg is common to the two other parts of the bridge, reducing the lead wire resistance and so the error. The 4-leg variation gives the best performance by assigning a lead to each end of the probe, connecting the power supply to the two remaining leads and allowing the measurement of the voltage from the resistance element and the leads at the same time [49]. Platinum-based RTDs or Standard Platinum Resistance Thermometers (SPRT) are considered as a standard for defining and measuring temperature in controlled environmental conditions. This class of RTD are manufactured using high purity platinum with a coefficient of resistance of $3.987 \times 10^{-3} \text{ K}^{-1}$ at room temperature, with the device being assembled in a way that ensures it is strain-free. The temperature sensible part of the device consists of a coil of thin gauge wire [52]. However, for hostile industrial applications, this type of design would not survive the operating conditions for long. For this reason,

Industrial Platinum Resistance Thermometers (IPRT) have the platinum wire encapsulated in a ceramic matrix. In addition, the sensing element is often protected from the environment by a super nickel alloy sheath. IPRTs have an achievable accuracy in the order of ± 0.01 and ± 0.2 °C over a range of temperature of 0-300 °C.

RTDs are categorised into five different classes, from the most sensitive to thermal change (1/10 DIN) to the least (Class C). The most commonly used in industrial applications are class A and B where the respective accuracy is temperature-dependent and it is defined as $\pm 0.15 + 0.002|T|$ and $\pm 0.3 + 0.005|T|$ [52]. Finally, as with thermocouples, their spatial resolution is fixed and related to the dimensions of the device, although values between 1 and 10 microns have been demonstrated [53].

1.2.7 SCANNING THERMAL MICROSCOPY (STHM)

One highly promising method to measure temperature that can employ either thermocouples or RTDs is Scanning Thermal Microscopy (SThM) [54], [55]. This is a form of Scanning Probe Microscopy (SPM) that employs a nanofabricated thermocouple or resistance temperature detector (RTD) at the very end of an otherwise conventional Atomic Force Microscopy (AFM) probe. Both SPM and AFM techniques will be discussed in detail in the following chapter (Section 2.6). SThM works by placing the probe tip in contact with the sample, and the tip temperature is then measured as it is modified by tip-sample heat transfer. This results in a technique that inherits high thermal and spatial resolution (mK, nm) and the straightforward operation and interpretation of conventional electrical thermal sensors, providing simultaneous measurement of surface topography and temperature. The measure of the temperature is obtained from the well-established electrical interrogation of calibrated sensors (thermocouple or RTD). It also offers additional advantages, such as active (probe-as-heater) or passive (probe-as-thermometer) operation for the same probe and instrument as well as simultaneous force (AFM) and thermal actuation/sensing. These last points are particularly important for its use in thermal-mechanical studies, e.g. micro-thermal analysis (μ TA) [56]. Moreover, the system is flexible and can be adapted to measure either the temperature distribution or the thermal properties [57] of

the sample by simply modifying the degree of self-healing experienced by the thermal sensor.

The history of SThM can be traced back to Scanning thermal profilometry, proposed by Williams *et al.*[58], that consists of a coaxial wire that contains a thin-film thermocouple at the end of a conventional scanning tunnelling microscopy (STM) tip. In these experiments, the thermocouple probe was mounted on a piezoelectric actuator and heated. As it was brought closer to the surface to be scanned, heat transfer between the tip and the sample through the surrounding gas-cooled the tip. To preserve a constant tip-sample gap, a feedback control system was used to move the piezoelectric actuator and maintain a user-specified thermocouple temperature. However, in this system, any temperature changes on the scanned surface could appear as features on the topographic image thus making it difficult to separate temperature from topographic variations.

Weaver *et al.* [59] modified an STM by introducing a tunnelling thermometer in order to measure optical absorption of thin metal films with 1 nm spatial resolution. This technique used the STM tip to form a thermocouple junction with the substrate itself. By changing the frequency of an incident laser beam to heat a gold film, the absorption spectrum of gold was reproduced. Ultimately the purpose was to perform optical absorption spectroscopy at nanometer scales to identify chemical species. This experiment also allowed the STM to be employed to measure the thermoelectric tunnelling voltage due to optical absorption.

However, temperature-measuring scanning probes had limited use in attempts to perform simultaneous thermal and topographic imaging of biased electronic devices and interconnects. Such samples can contain dissimilar materials - insulators, semiconductors and metals on their surface making it impossible for STM to be used. In addition, a biased device can have surface potential variations making it more difficult to use an STM under constant external bias.

To solve some of these problems M. Nonnenmacher and H. K. Wickramasinghe [60] introduced a new SThM system based on the measurement of contact potential between a metallic tip and a thin metal film on the sample surface. To improve their technique, they also made use of the tunnelling thermocouple, formed by the tip of their (AFM) probe contacting the metal covering the sample;

therefore, topographic and thermal images could be obtained simultaneously but via separate channels.

The major advantage of this method was the improved feedback control of the z-piezo actuator; based on force measurement and, in contrast to the STM technique, independent of electrical measurements such as thermovoltage. This phenomenon occurs if the tip and sample of a scanning tunnelling microscope (STM) are at different temperatures. When this happens, a voltage can be generated between them. This thermovoltage is similar to the well-known thermoelectric Seebeck effect: both of which are caused by the different broadenings of the fermi distributions and the different densities of states (DOSs) of tip and sample. This DOS is linked to both temperature gradients between tip and sample as well as their chemical properties and, if neither the tip or the temperature change during the experiment, chemically different areas of the sample can be distinguished. The combination of this effect with AFM permitted mechanical contact between the sample and tip to be kept constant during the scan. Sample temperature change or variations in tip-sample thermal conductivity were imaged by the thermal sensor located on the probe tip. However, one limitation with this technique stemmed from its use of contact potential, so requiring the substrate surface to be without an external bias making it incompatible with the imaging of biased electronic devices.

To circumnavigate these issues, A. Majumdar *et al.* [61] developed a new AFM based technique in 1993. This method offered the ability to simultaneously image surface topography and temperatures of biased devices. In this approach, the traditional AFM probe was replaced by a thermocouple made of two wires of dissimilar metals. A piece of aluminium foil was stuck to the wires to form a reflector for the laser used by AFM for detecting cantilever deflection. When the tip was scanned across the sample, the topographic image was obtained by standard AFM operation. However, because the thermocouple at the tip was in contact with the sample during scanning, the local temperature was also measured simultaneously. Hence, temperature structure correlation was possible, which was critical for probing electronic devices. These thermocouple probes were typically made of chromel and alumel because these materials had sufficiently low melting points for the probe/thermocouple tip to be formed using capacitive discharge during manufacture of the probe. However, soft sensor

materials posed the problem of tip deformation under contact. This problem was solved by attaching a small piece of diamond, 20 μm in diameter, on the thermocouple junction, with the hardness of diamond preventing any tip deformation, whilst efficiently spreading heat to the thermocouple junction.

Another, commonly used probe, based on a similar fabrication principle but using an RTD instead of a thermocouple is commonly named 'the Wollaston probe' [62], and has proved itself useful in a large number of applications. The Wollaston probe is composed by a V-shaped Pt90/Rd10 wire of about 75 μm in diameter, which makes up the 'cantilever' of the AFM probe. The probe tip, with a diameter of 5 μm and a total length of 200 μm is fabricated by removing (etching) the silver shell from a Wollaston wire. Due to this fabrication procedure of Wollaston wire, the wire at the tip is characterised by a grooved surface. This ensures direct contact only between the grooves and the sample surface. The equivalent curvature radius of an individual groove was estimated at about 300 nm [63]. This probe has proved popular for local thermal analysis to investigate the thermal-micromechanical properties of materials due to its ability to reach higher self-heated temperatures than other, microfabricated probes. However, the Wollaston probe has a limited spatial resolution (around 1 micron [64]) as dictated by the dimensions of the probe wires that form the AFM tip.

In an attempt to improve on double-wire thermocouple probes, Nakabeppu *et al.* [65], presented a single-wire thermocouple AFM probe fabricated by depositing a thin metal film of gold on a sharpened nickel wire. The key issue with this approach was the size of the thermocouple junction, which could only be controlled to fall in the range of 0.3–5 μm as it was primarily dictated by the viscosity and surface tension of the varnish layer separating the wire and deposited thin film. This varnish insulated the wire from the thin film over most of its length, but surface tension caused it to retract from the top and bottom of the sharpened nickel wire leaving it exposed for the subsequent gold deposition and hence thermocouple junction formation.

To controllably improve the resolution of thermocouple SThM probe junctions to the sub-0.1- μm range, Zhou *et al.* [66] and Mills *et al.* [67] presented batch fabricated SThM thermal probes. This represented a novel technique based on direct-write electron beam lithography (EBL) at the apex of micromachined atomic force microscope tips. A silicon substrate was micromachined to form

pyramidal tips. The substrate was then coated with silicon nitride and patterned using EBL to form cantilever and tip with a radius of ~ 30 nm. A thermocouple, made of two overlapping thin film wires of gold (25 nm thick) and palladium (50 nm thick), was designed through separate levels of EBL and metal lift-off. Finally, the silicon substrate was etched away, leaving the silicon nitride cantilever with a Au-Pd thermocouple on the tip. The biggest advantage of this kind of probe was that an imaging spatial resolution of sub-50 nm could be achieved. Furthermore, the optimised fabrication process, allowed thermal probes to be batch fabricated – more than 300 probes on a single wafer, allowing probes to be manufactured in a more economical and controllable way. However, the sensitivity of the thin-film thermocouples was far lower than their bulk equivalent, resulting in lower signal-to-noise. One important point to note is that the fabrication procedure presented permitted the flexibility to produce RTD based probes (detailed later in this section) by employing a simple material change, whilst leaving the majority of the fabrication process unchanged.

RTD based SThM has proven to be an extremely popular nano-thermal technique in recent years due to its relative ease of use and flexibility; as already stated it can be considered as operating in one of two modes, active or passive [55], distinguishing by whether or not the SThM probe is heated above the ambient temperature. When employing an RTD SThM probe in passive mode, minimal electrical current is passed through the probe and temperature measurements with negligible self-heating can be achieved [68]. In this way, SThM offers an ideal tool for measuring sample temperature at the nanoscale with high spatial resolution. In active mode (used in this thesis), the RTD SThM probe acts as both a heat source and a thermometer to measure the thermophysical properties of the sample such as thermal conductivity [55]. In this case, a larger electrical current is passed through the probe, resulting in a significant Joule heating. When an SThM probe is heated and approaches a surface, part of the Joule heating power flows into the sample, with a magnitude dependent upon the tip-sample thermal contact and the sample's thermal resistance (Figure 12).

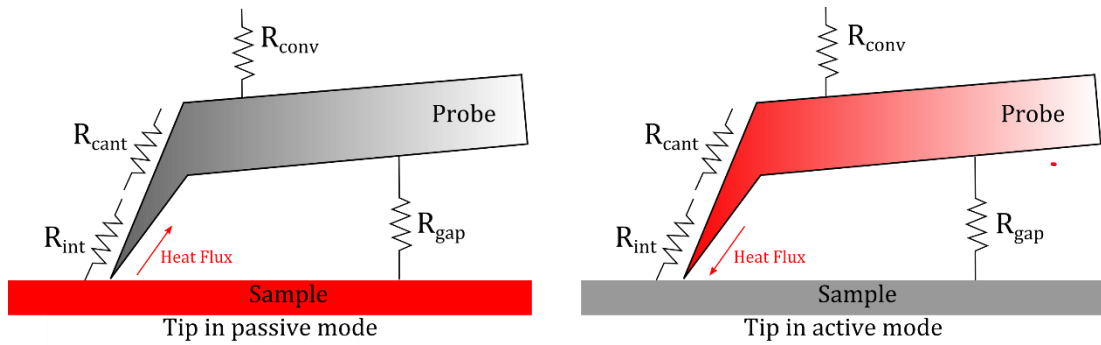


Figure 12 Schematic representation of passive and active mode for SThM probe, where R_{int} is the thermal resistance of solid-solid contact, R_{cant} is the thermal resistance of the entire cantilever, R_{conv} is the thermal resistance between the cantilever and the environment against thermal convection, R_{gap} is the thermal resistance between the cantilever and the sample[69].

However, interpretation of this data is non-trivial, and it has been demonstrated that an object can only be treated as a half-space if its thermal resistance is suitably close to that of a bulk sample. This is often not the case for nano-features, whose geometry heavily influences their ability to conduct heat. For example, when considering a commercially available KNT (Kelvin Nanotechnology) SThM probe, whose material properties and geometry will be discussed in the following chapter, only thin-film gold features above micrometre sizes could be treated as a half-space (red shadowed area in Figure 13) [70].

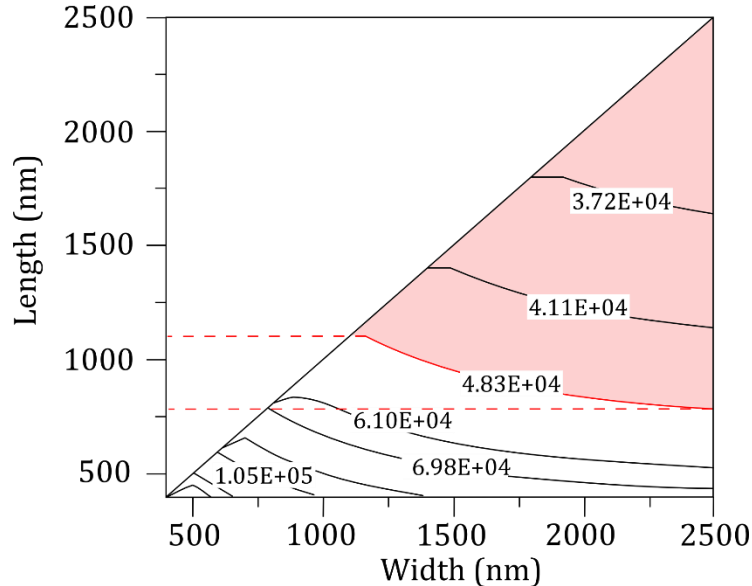


Figure 13 Contour showing the thermal resistance against the width and length of gold wires with both the length and width varying [70].

The practical implementation of RTD based SThM can be described as follows: If the tip RTD of the SThM probe is made from pure metal, this temperature change will cause a variation in its electrical resistance. A Wheatstone direct current (DC) or alternating current (AC) bridge can be used to sensitively monitor this resistance change as described previously. When there is a change in sample

thermal resistance the heat flux from the tip to the sample changes and hence the temperature of the probe changes. This will modify the probe's electrical resistance, which in turn will cause a change in the output of the electrical bridge. This is measured and input into the scanning control computer to form the thermal image. A diagram of the basic SThM together with the Wheatstone bridge is shown in Figure 14.

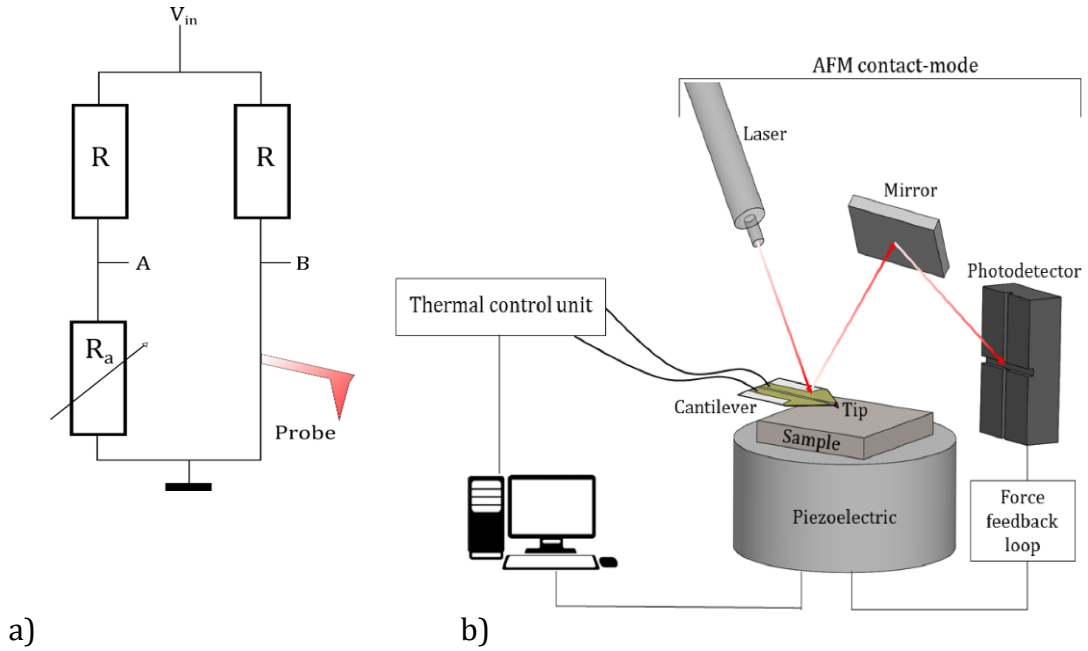


Figure 14 (a) Schematic diagram of a Wheatstone bridge for SThM measurements. Two fixed resistors R and a variable resistor R_a to balance the probe's resistance. The applied voltage is V_{in} and the thermal signal proportional to the probe temperature comes from the difference between A and B . (b) Schematic representation of the entire SThM system.

For both active or passive mode measurements to be made quantitative, it is necessary to use calibration to link the output of the probe to the thermal properties or temperature of the sample. As the output of the probe instrumentation takes the form of an electrical signal, it is essential to have a solid understanding of the electrical characteristics of a probe. The function of a resistance-element based SThM probe is dictated by its temperature coefficient of resistance (TCR). This represents the change of electrical resistance (R) as a function of the temperature variation ($T - T_0$) through the following relationship:

$$R(T) = R(T_0)(1 + \alpha(T - T_0)) \quad (10)$$

where R is the resistance of the metallic sensor changing with temperature from T_0 to T , and α is the temperature coefficient of resistance (TCR), with units of K^{-1} . Accurate knowledge of this value permits conversion of probe electrical

resistance into temperature with minimum error. In addition, the stability of the resistive thermal sensor is also important, particularly when operating at a high (self-heated) temperature [71]. If this information is not taken into account, overheating the probe can result in significant drifts of resistance when undertaking long experiments, reducing the reliability of results.

In recent years, the probes developed at the University of Glasgow have become one of the most popular thermal probes worldwide, due to their availability and flexible working modes. They employ a thermal resistive sensor which is located at the very end of the probe and is made from a thin film of palladium or platinum. These probes were first described in 1998 when Mills *et al.* [67] introduced the first batch fabricated thermal probes and were subsequently improved in 2007 by Dobson *et al.* [72]. Figure 15 shows two complete thermal resistance probes (two and four terminals) in which a palladium resistor is located at the extremity of the sharp tip at the end of thin silicon nitride cantilevers.

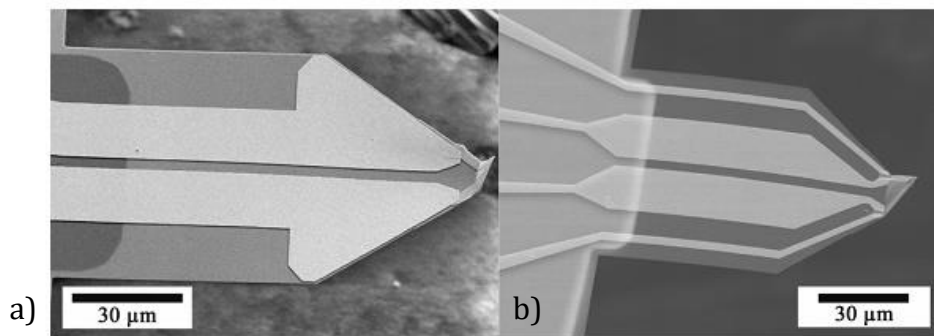


Figure 15 Completed 2 (a) and 4 (b) terminal resistance SThM probes [104].

Electrical connection to the resistor is achieved by Au wires running the length of the cantilever to pads on the probe body. As the thermal sensor is a resistor it is important to minimize the resistive contribution from these wires, limiting the probe thermal response to regions of the sample close to the tip. This was achieved through either one of two different methods:

Two terminal resistance measurements are more convenient for some SThM instrumentation, especially transformer-coupled bridge systems, as will be described in chapter 3. In this case, the width of the two wires is maximized so that they have the smallest possible resistance, subject to the constraints imposed by the cantilever size.

Alternatively, four terminal measurement of the tip resistance gives the most direct localization of the sensitive area, making the resistance of the wires and

any variation in that resistance due to variations in cantilever temperature inconsequential. One major problem was presented by the use of either of these probes on biased, electrically conductive devices. If scanned in contact over a conductor, current flow between the tip and sample could become large enough to destroy the thin film tip resistor. However, if an insulating coating was employed on the tip to prevent this, the difference of potential between the tip and sample generated an electrostatic force causing mechanically destructive scans for even low potential differences (10 V). To solve this problem, a circuit was employed where the SThM probe was inserted into a bridge circuit located locally on the AFM probe holder. RF transformers were then used on the input and output of the bridge to achieve passive electrical isolation from the DC current flow [72]. This innovation is something that was subsequently adapted for the work presented in this thesis.

Another well-known class of thermal probes used for SThM is based around the use of doped silicon (DS), which was proposed and designed by King et al [73] and based on the IBM millipede [74]. The DS probe is often used as a higher resolution version of the classical Wollaston probe as the DS probe greatly improves on its resolution, whilst maintaining the ability to self-heat to high temperatures.

The design of the DS probe consists of a U-shaped single crystal silicon cantilever. Essential to its function is the fact that it has different doping applied to the legs and to the end of the U cantilever. The two legs are highly doped to increase their conductivity, conversely, the central part has low doping to increase its resistivity. This simple, but effective approach allows for a highly localised active region, where the self-heated temperature can increase up to 1000^oC [75]. Other aspects of the probe are very similar to conventional silicon-based AFM probes. For example, the tip in the centre of the U-shaped cantilever is obtained by oxide sharpening, leading to a radius of curvature at the end of the tip of about 20 nm. The total length of the sharpened tip is about 1 micron, with a cantilever resonant frequency of 50-150 kHz and a spring constant of 1 N/m. The temperature of the DS probe is measured indirectly (i.e. not at the tip) thanks to the temperature dependent resistivity of the central part of the cantilever, which varies from 0.5 k Ω at room temperature to 1 k Ω at 850^oC [76]. The sharpness of the tip of these

probes is also important as it results in a high thermal contact resistance as a result of the small tip-sample contact area [77].

Over the years SThM probes have been employed in many applications where the tip and/or sample are considerably above ambient temperatures [78]. However, under these conditions, SThM probes can suffer from thermally induced cantilever bending [79]. This is particularly disruptive as the AFM component of SThM makes use of cantilever deflection as a way of monitoring tip-sample forces. In 2011 Zhang *et al.* [80] conducted research attempting to reduce this problem. It is well understood that the bending of the cantilever is caused by the different thermal expansion of the layered probe materials. In a typical SThM configuration, metallic wires (often gold) sit on the lower surface (i.e. tip side) of the silicon nitride cantilever. An increase in the temperature of the probe (Figure 16a) will cause the cantilever to bend away from the surface due to gold's greater thermal expansion in comparison to silicon nitride (Figure 16b). This can impact the measurement in a number of ways; for a static probe in contact with a surface, there will be a reduced force between the tip and the sample. If the Z topographic feedback loop is engaged, this deflection is identified by the AFM feedback loop as being due to an increase in the contact force; therefore, the tip will be withdrawn from the sample leading to loss of the tip-sample contact.

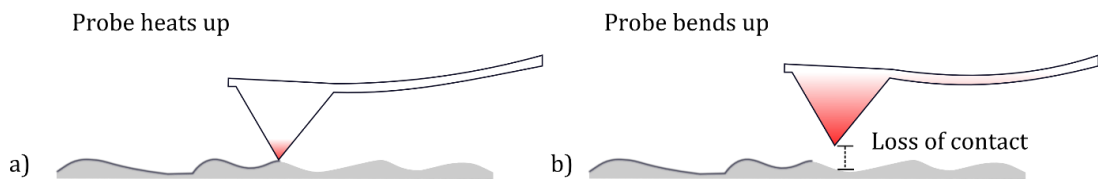


Figure 16 a) Probe heats up and subsequently b) bends up causing a loss of contact.

The opposite problem will occur if the temperature of the probe decreases. Here the cantilever will bend toward the surface and the contact force between the tip and the sample will increase. However, the feedback loop will detect this as a reduction in force and will move the tip down causing false topography signals and possibly damaging tip-sample loads. The first scenario above (probe becoming hotter) is representative of a cold probe approaching a heated sample, or an in-contact heated probe scanning from a sample region of high thermal conductivity to one that is lower. The second scenario (probe becoming cooler) represents a heated probe approaching a cool sample or scanning from a region of low conductivity to one that is higher.

To provide a possible solution to this cantilever thermal bending, the authors designed and fabricated a grooved cantilever using the concept of structural compensation by making the groove with a depth equal to the thickness of the metal layers along the length of the cantilever. In anticipation of a higher attainable operating temperature, the palladium thin-film resistor, used as a thermometer, was replaced with platinum, which has improved high-temperature stability. This new design allowed a drastic reduction in thermal bending demonstrating that the previous sample temperature limit (as low as 64.7 °C on some samples) could be greatly improved.

Over the years, there has been a constant effort to develop advanced techniques and increase the accuracy and the sensitivity of the SThM probe, permitting challenging samples to be imaged. However, it has also been recognised that there are still several factors impeding the truly reliable measurement of the real temperature and accurate thermal properties.

One of them is represented by SThM measurement artefacts [81] visible in many scans. As a consequence, to obtain a clear thermal map and to correctly interpret the signal into reliable thermal properties of a material can be extremely difficult. Great effort has been spent to understand these artefacts, recognising this is essential to progress the understanding of heat transfer mechanisms present in SThM. Artefacts in SThM can be either abrupt or more commonly smooth deviations of the thermal signal captured by the probe due to the signal's strong dependence on probe-sample heat transfer. These deviations may be incorrectly interpreted as temperature or thermal conductivity variations of the sample if they are not appropriately accounted for or eliminated. Artefacts are always associated with the disruption of stable heat transfer paths between the probe and the sample. The most dominant of these are changes in the tip-sample solid-solid contact (topographically induced artefacts) and air conduction (air-conduction artefacts) both of which can result in thermal image distortion.

Topographically induced artefacts are often the most striking when looking at an image and can be explained by sample topography altering the tip-sample contact area (Figure 17).

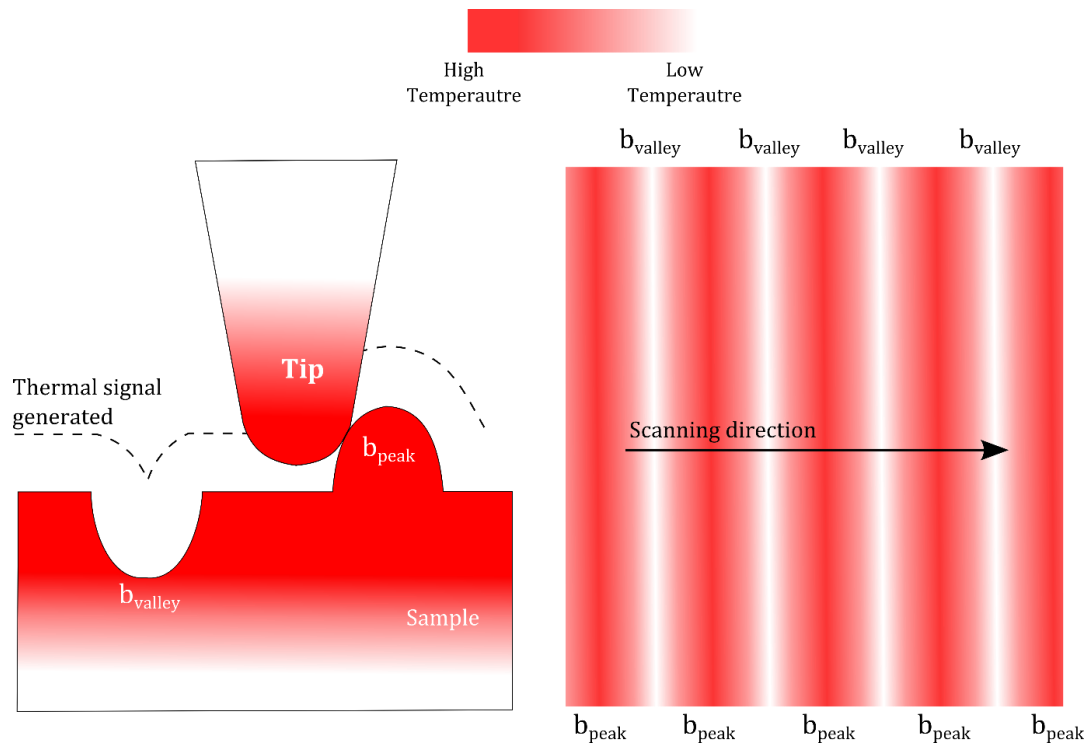


Figure 17 Schematic representation of tip artefacts induced with SThM. On a concave surface, a rounded tip with apex radius "r" will not conform to the surface, hence, thermal contact is not ideal, and a lower temperature is measured. On a convex surface, contact is ensured and the temperature is measured correctly. The schematic thermal image of the sample is characterised by a disomogeneous temperature field, which is not correct and is the result of the sample topography. The red colour refers to high temperature and the white colour indicates low temperature.

One of the first to report a "double-line-like" thermal profile was Soudi *et al.* [82] during the thermal scan, in passive mode, of heated nanowires with 40 – 60 nm diameter in both air and vacuum. They concluded that, when these artefacts occur, the temperature of the nanowire could not be estimated accurately, and only an averaged value could be obtained over a large region. A similar issue has also been reported for thermal scans on soft materials, imposing the necessity to use the thermal scan in conjunction with the topographic image when carrying out analysis [83], [84].

Efforts have been made to obtain real thermal images without artefacts. Cahill *et al.* [85] elaborated a method to remove them from the thermal image via either accurate modelling of the artefacts and removing these from the image or by thermally nulling the probe. Other researchers employed complex post-processing analyses to clean the thermal signal that generates the image [86]. However, this approach is not straightforward for those samples that exhibit both material and topographic variations. To overcome these challenges Menges *et al.* [87] developed a method that uses image post-processing in conjunction with the deterministic calculation of tip-sample heat transfer. A corrected temperature

map could then be achieved by convolving the position-dependence thermal contact resistance into the original temperature map.

Although present in earlier work, so-called topographic peaks and valleys were first described by Luo *et al.* [88] while scanning samples using a nanofabricated thermocouple. The presence of these features is characterised by a sudden decrease and increase in the temperature measured by the probe. Another parameter investigated for its role in SThM artefacts is surface roughness. For example, Gotsmann *et al.* [89], studied the relationship between surface roughness and thermal interface conductance at the atomic scale, under vacuum. In this work, the authors noticed a variation in the thermal signal associated with the change in the number of atom-atom contacts.

Conversely, thermal artefacts that are not associated with the tip-sample thermal contact can be caused by a difference in the heat transfer coefficient between the probe and the surrounding environment, as shown in Figure 18. Importantly, this mechanism varies spatially over the sample and does not always cause an abrupt change in the thermal signal.

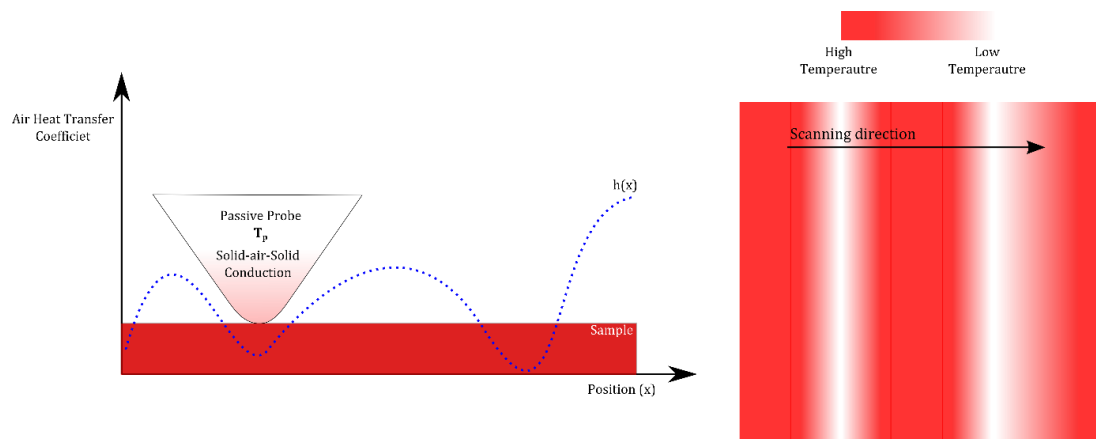


Figure 18 Schematic representation of thermal artefact caused by the heat transfer coefficient of air along with the sample. Measured temperature changes with the change of the film coefficient $h(x)$. Where $h(x)$ is lower the thermal coupling is not ideal and lower temperature is measured. The red colour refers to high temperature and the white colour indicates low temperature.

An example of this mechanism can be found in the thermal image presented by Dobson *et al.* [90]. In this work, a symmetric and uniformly heated membrane generated an asymmetric thermal profile despite being a symmetrical structure (Figure 19). This mechanism is caused by the spatial change of the heat transfer between the sample and probe caused by part of the heater being located below the cantilever (hence heating the cantilever through air-conduction) in the lower part of the image but not in the top part of the image.

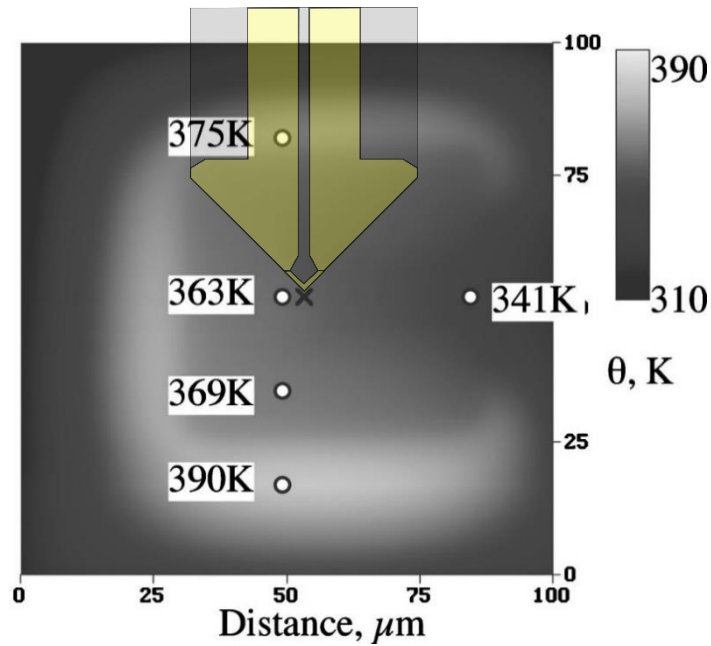


Figure 19 Thermal scan over a heated Johnson noise standard device (not to scale). Note that the heater appears hottest, with the area surrounding the membrane appearing the coolest. The heat spreader and sensor regions appear uniformly hot, with some cooling at the right due to thermal loading by the electrical leads connected to the device (341 K). Adapted from [90].

In order to overcome this thermal artefact, various methods have been investigated. The simplest, but less practical and cost-effective solution is the use of SThM in a vacuum [67]. However, work has been carried out on other scanning procedures, which proved to mitigate the problem to some extent; for example the “double-scan technique” [91] and the “topography correction technique” [92].

1.3 SUMMARY

The techniques introduced can be divided into two distinct types, contact and no-contact thermometry. The latter one has been widely developed and used for monitoring the temperature of samples, which for different reasons should not be altered. Examples can be represented by cells in biological applications or combustions gases where contact thermometry can alter the measurement of fluid’s (gas state) parameters.

Over the last decade, a large number of works have been carried out in the micro/nano thermal analyses field including Raman spectroscopy, adopted in several field of science and engineering, or infrared thermometry that has been used by several researchers thanks to its versatility and simplicity. However, much has been done also in the area of contact thermometry with great emphasis on SThM. This research effort can be divided into two areas, the development of more accurate and sensible probes, and understanding the interaction between

the sample and probe including the effect of the surrounding environment (vacuum [93] or air). Contact techniques like the thermocouples or electrical resistance-based devices are being progressively used more by scientists thanks to the improvements in materials and in more compact designs.

All the techniques introduced in this chapter are generally operated in air or vacuum. However, operating in a liquid environment is important for many specific applications in the area of biology and life science. For this reason, in the next chapter, some of these techniques and others will be introduced paying particular attention on their use in liquid environments.

CHAPTER 2: THERMOMETRY IN WATER

The fundamental importance of temperature to a wide range of disciplines has been described in chapter 1. However, what was not considered was the requirement for thermometry under complicated and challenging conditions. For example, measurements may need to be carried out under liquid [94] or on soft materials [95], both conditions typical in the biomedical and chemical fields. Specifically, temperature plays a crucial role in chemistry where it is fundamental in determining the speed of chemical reactions. This is also highlighted by the classical and well-established Arrhenius' law [96], which relates the rate constant of a chemical reaction to the activation energy and surrounding temperature via an exponential function. In some cases, reactions need an elevated of temperature to commence, but it also determines the speed at which reactions occur and whether they proceed in a forward or reverse direction.

In a related manner, temperature is also fundamental to all aspects of life and can regulate many cellular functions, ranging from gene expression [97] to cell metabolism [98], [99]. Unfortunately, much of our knowledge about thermal effects on cells is based on macroscopic measurements of temperature, which do not permit a detailed study of how highly localised temperature change affects biological activities. Although thermal gradients typically extend over large distances in natural systems, there are some scenarios where highly localised heating can be imposed on biological systems. Examples include hyperthermal-nanoparticle therapies [100], manipulation of cellular development [101] and fundamental studies of biological pathways [102], as well as temperature dependent cellular [103] and biomaterial mechanics [104].

Unfortunately, the mechanism of temperature-induced changes at the subcellular level is poorly understood, despite the fact that temperature governs every biochemical reaction within living cells. This leaves the precise measurement of temperature at the nanometer scale in biologically compatible environments a significant outstanding challenge.

Over the years, a significant number of techniques have been developed to accurately measure both steady state and transient temperature, many of which have been introduced in section 1.2. Within this chapter, particular focus will be given to their use in an aqueous environment as well as the introduction of other relevant approaches.

When undertaking thermal measurement in liquid, each technique presents its own advantages and disadvantages as well as spatial-thermal resolution. If we consider methods beyond simple macro thermometers that can operate in an aqueous environment, two commonly employed techniques described in the literature [49] are calorimetry and IR thermography.

2.1 CALORIMETRY

The very first calorimeter used was developed by Antoine Lavoisier and Pierre-Simon Laplace around the 1782-83, based on the discovery of the latent heat by Joseph Black [105] and used for the measurement of heat generated by several chemical reactions. These measurements can be considered to represent the foundation of modern thermochemistry.

Although an old technique, the method is still commonly used, and over the last fifty years has been employed with success to study the effect of drugs, cellular activity and metabolic heat. The foundation of this technique is its ability to measure the heat generated or absorbed by a sample during a chemical reaction. One of the quantities that is mostly commonly used to characterise a chemical reaction is the Gibbs free energy change, ΔG , that shows if a reaction is thermodynamically favourable (negative) or not (positive). The Gibbs free energy change is a function of two important thermodynamic quantities $\Delta G = \Delta H - T \Delta S$ [106], where ΔH is the enthalpy and ΔS is the entropy of the system. For chemical processes at constant pressure, the enthalpy change (ΔH) is related to the change in internal energy plus the product of the system pressure and the change of volume (volume work) performed by the system. When this is positive, the system undergoes expansion, in the opposing scenario, it is in contraction [106]. This means that such a change in enthalpy can be related to the release or absorption of heat via a chemical reaction or from an external source. At the same time, the change in entropy (ΔS) can be expressed as the ratio between the change in heat transfer to the closed system and its temperature. Entropy is a classical thermodynamic quantity, which is described by the second law of thermodynamics. Since the heat generated from natural reactions flows from hot regions to cold, the change of entropy for a whole system is always positive [106]. Calorimeters offer the possibility to study a chemical reaction in an isolated environment, where external factors such as ambient temperature fluctuations are avoided. Essentially a calorimeter is an insulated chamber where a reaction

can occur with minimum interaction with the outside. This allows the change of temperature associated only with the chemical reaction to be monitored. This has been greatly assisted by the introduction of modern electronic control calorimeters, that can be configured to keep several parameters, such as temperature, pressure or volume constant during measurement if desired.

In the field investigating hyperthermal cancer cell treatment, several researchers [107],[108],[109],[110] have made use of calorimetry as a method to characterise large batches of cells exposed to an increase of temperature. In addition, calorimetry has been used to monitor the heat release caused by protein denaturation as the result of heat treatment [108]. In this field, one of the most commonly used types of calorimetry is differential scanning calorimetry (DSC), which permits the energetic response of chemical compounds such as polymerisation or biological molecules reactions to be studied. The key feature of DSC is its ability to measure the partial heat capacity of a system, that is a fundamental property, which reflects the increase of temperature for a given heat flux [111]. Usually, this type of calorimeter has two chambers, one containing the sample in its liquid environment and the other only the liquid to provide a reference. Measurement is carried out by linearly increasing the amount of heat provided to both chambers in a quasi-adiabatic way. There will be a difference in temperature between the reference and sample chambers due to their different heat capacities. This difference is measured and used for the calculation of molecular partial heat capacity.

Despite the relatively high thermal resolution, calorimetry is by definition limited in terms of spatial and temporal resolution. This is because it is designed to measure a single, global value of the steady-state heat produced by a chemical process, limiting its ability to observe the process over time. In addition, measurements are affected by the sample/sensor interaction that can be poor for some samples, even in the best instruments. One well-known issue is the poor thermal conductivity between the sample and the sensor. This issue causes inaccurate measurements of the time frame of chemical reaction occurring in the calorimeter introducing a temporal measurement error.

2.2 INFRARED THERMOGRAPHY (IRT)

Within the macro-optical techniques available, infrared thermography (IRT) has a significant role due to its wide area of applicability in terms of spatial resolution.

The use of IRT in biology is well-established, not only for the control of large-scale cell cultures and for monitoring the temperature of microfluidic chips [112], but also for monitoring in vivo experiments where knowledge of the global sample temperature is required; for example during hyperthermal cancer treatment [113]. An example of large-scale biological temperature measurement employed on an enzyme reaction [112] is shown in Figure 20. In this experiment, the temperature change was monitored periodically before (Figure 20a) and after the start of a reaction initiated by the addition of vinyl acetate in toluene solution (Figure 20b). The thermal image before the reaction shows low-temperature spots (dark blue) caused by the endothermic process of solvent evaporation. However, after reagent addition, the reaction starts to emit heat and the spots turn to yellow and bright white, indicating a temperature increase.

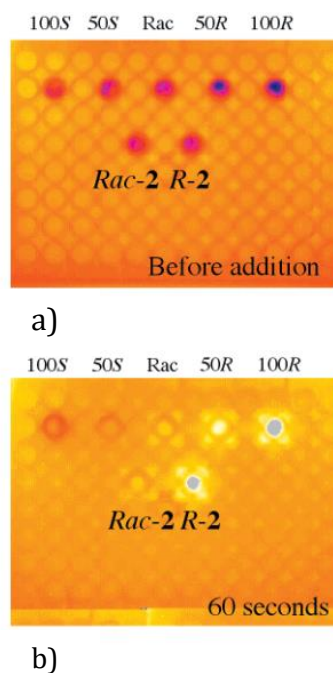


Figure 20 Time-resolved thermal imaging of lipase-catalysed, contained in microchannels (diameter around 600 microns), enantioselective acylation of 1-phenylethanol, 2. Colours correspond to the following temperatures. (a) At time zero; black (12.5-13.5 °C), purple (15-16 °C), pink (17-18 °C), orange (18.5-19.5 °C). (b) After 60 s; orange (18.5-19 °C), yellow (19.5-20 °C), white (20.5 °C), grey (21.4-21.6 °C) [112].

Despite employing the same working principle as introduced in section 1.2, IRT in these scenarios often needs special attention to be given to the calibration process. For example, when the IRT camera is employed to interrogate samples surrounded by a liquid medium [20].

The behaviour of the water molecule in terms of absorption bands in the infrared spectrum depends on whether it is liquid or gaseous. Two types of absorption

spectrum are a possible, rotational and vibrational spectrum. For the water molecule in a liquid state, the rotational spectrum is absent and the only vibration occurs. The liquid water absorption spectrum is shown in Figure 21. Except for a narrow window in the near IR the water is quite strongly absorbing. This behaviour has been documented for several applications, for example, in the study of water rain droplet IR absorption [114] or for its use at the ice point as quasi-blackbody infrared calibration source [115]. This is the behaviour allowed the researchers to measure the average temperature of a small volume of medium contained in the IR transparent channels as shown above (Figure 20).

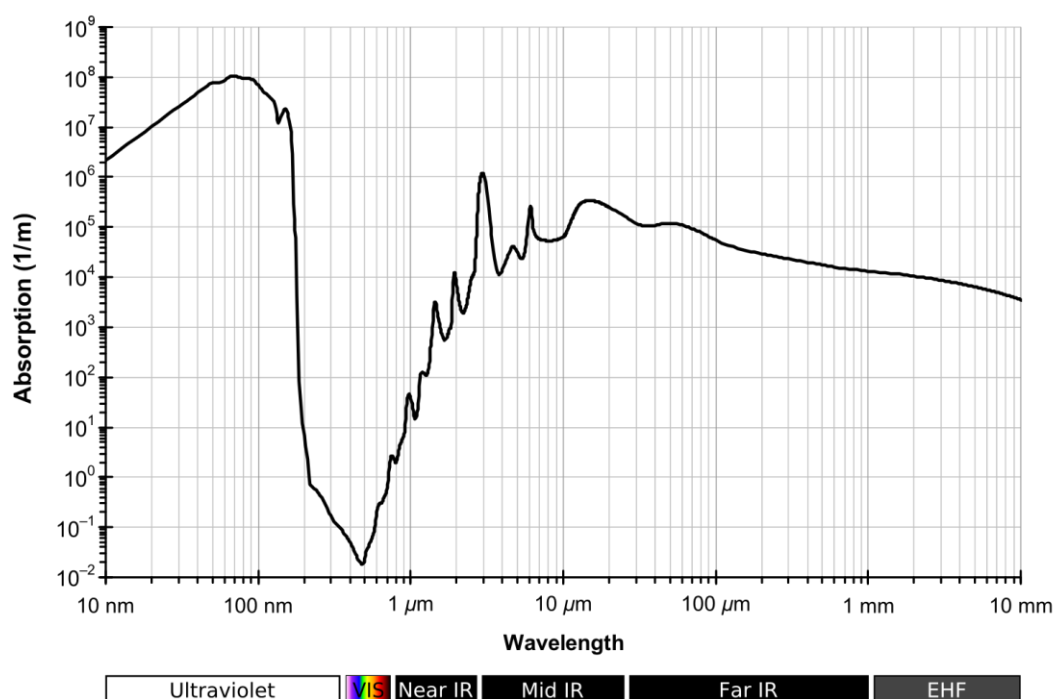


Figure 21 Water molecule absorption spectrum (Wikipedia).

In these cases, it should be remembered that the air/liquid environment undergoes natural convection, decreasing the accuracy of the measurement due to changes in surface temperature that are not related to the chemical reaction occurring within the water environment. In addition, the presence of an air/liquid interface, where evaporation occurs constantly, can hinder the formation of a constant, homogeneous sample temperature required to accurately calibrate the IRT. In order to solve this issue, an accurate calibration procedure must be followed, and attempts have been made to minimize the cost and the time required to achieve this. A typical calibration tool for in-water IRT consists of a controlled temperature water bath, where water is circulated

through a copper diffuser using a pump before returning to a reservoir in a closed cycle. A thermistor is placed close to the water surface and is used as a calibration target, whilst being continuously measured electrically. The IR camera is then focused on the “hot” spot generated via a controlled copper-based heating element, and several repeated measurements of the temperature are recorded. The temperature of the hot spot is controlled in order to be in equilibrium with the water flowing over it, creating a stable reference temperature for IR calibration. This method is superior to many others since it solves the issue of calibration in the presence of an air/water interface since the thermistor is always in water and the surrounding environment flows constantly. The method is also relatively low-cost as no commercial blackbody is required for the calibration procedure [116].

IRT offers several advantages, due to its ability to observe a sample from a distance [117], allowing, for example, the non-invasive study of cell growth [118] or fungal transport [119]. In addition, a real-time, two-dimensional image of the temperature can be obtained and recorded, allowing areas within the image to be compared offline, identifying temperature differences. However, IRT can exhibit artefacts due to the increase in temperature of the sample, which can promote evaporation of the surrounding medium altering the temperature between sample and medium. As an imaging technique, one major advantage offered by IRT is that it does not require the use of harmful illuminating radiation or the addition of contrast dye, making it appropriate for repeated usage with minimal preparation [117]. However, IRT has limited spatial resolution (10 microns [40]), leading to it mainly being used for monitoring a large region of a sample (in the order of millimetres). In addition, IR thermography is limited by its ability to only measure or map surfaces [112, 120] as infrared radiation is only emitted from the surface of a body and not from the inside.

2.3 RAMAN THERMOMETRY

Raman thermometry, (introduced in section 1.2), is particularly useful for applications in a liquid environment, and more particularly in water [121, 122], for example as used in experiments that measure the temperature inside microchannels [123] [122]. Raman thermometry, being a far-field optical technique, does not require instrumentation to be in direct contact with the medium, making it well suited to probe samples in a range of environments. Small

volumes are easily analysed with minimal interaction with the surrounding environment. As introduced previously, Raman thermometry is based on temperature-dependent Stokes/anti-Stokes band intensity ratio [124], which also holds true in water. In contrast to the classical use of the Raman thermometry in air (section 1.2), when working in water the Raman spectrum of O-H vibration modes is used [21]. One type of O-H vibration is the bending mode of hydrogen-bonded water at 170 cm^{-1} , which is a very common vibration mode at such low energy. The other most commonly used mode is the O-H stretching vibration, that takes place in water at $3300\text{-}3400\text{ cm}^{-1}$. The range of detection can vary between systems, but for most instruments lays between $2600\text{ to }4000\text{ cm}^{-1}$ with a resolution of 1 cm^{-1} . For Raman thermometry in water, the incident radiation is nearly fixed to values which are not close to those of absorption in the water. Depth of penetration depends almost exclusively on the target material and the surrounding environment. In all the biological applications, the main advantage is the fact that samples are water-based, and this means that the O-H vibration is a valid target to determine the temperature. However, it worth noting that attention must be paid to the effect of the container's material or medium in the case they are not water-based. For example, most micro-channels used for in situ Raman Thermometry are made of the polymer polydimethylsiloxane (PDMS), which tends to exhibit strong signals from C-H stretching modes around $2900\text{-}3000\text{ cm}^{-1}$, that could cover or disrupt the signal coming from the solution. For this reason, it is normal practice to target the excitation laser as far as possible from the polymer side walls and use borosilicate glass to enclose the channel walls as borosilicate does not emit a signal in the wavelength range of interest. Calibration is also crucial for Raman Thermometry and the intensity of the O-H stretch against temperature needs to be investigated against a reference target. During this procedure, the laser source is targeted at several points within the region of interest (In Raman the volumes interrogated are always very small). This allows a more accurate calibration obtained by using more reference points, but also enables the possibility to measure the signal distribution across the region.

One typical experimental setup used to achieve in situ micro-Raman spectroscopy for temperature monitoring is shown in Figure 22. Here the system consists of a dual grating monochromator, a notch filter and a dual axis (XY) stage

with multi magnification objective lens [122]. The laser source is an Ar-ion laser with a wavelength of 488 nm and a power of 50.0 mW. As the Raman scattering signal is typically weak a photomultiplier tube is employed to measure the signal. The microchamber is filled with water and mounted on the stage, which is computer controlled on y and x-axis, in addition the stage is equipped with a 90x objective lens. An in-situ temperature control system is in place to alter the temperature and calibrate the Raman thermometer (Temperature controller in Figure 22). Two heaters and two sensors are realised via lift-off technique within the micro channel. They are realised via off-axis magnetron sputtering used to deposit 30 nm of Ti and 500 nm of Pt. The electronic system controlling the temperature is composed of an amplification circuit, an AD converted, a DA converted and a power supply. This system regulates the temperature via a sensor and a micro heater, which provides a localised source of heat. The fluid is heated directly in the microchannel while flowing. The smallest laser spot achievable with this set up is about 1 μm and a total of 9 consecutive measurements can be taken. The authors achieved a temperature deviation from -1.4 up to -0.2 $^{\circ}\text{C}$ across 9 equally spaced contact-free measurement points. The combination of the Raman thermometry and its calibration via the microfabricated thermometers granted a very good consistency of the measurements, which however still concentrated on a reduced number of points.

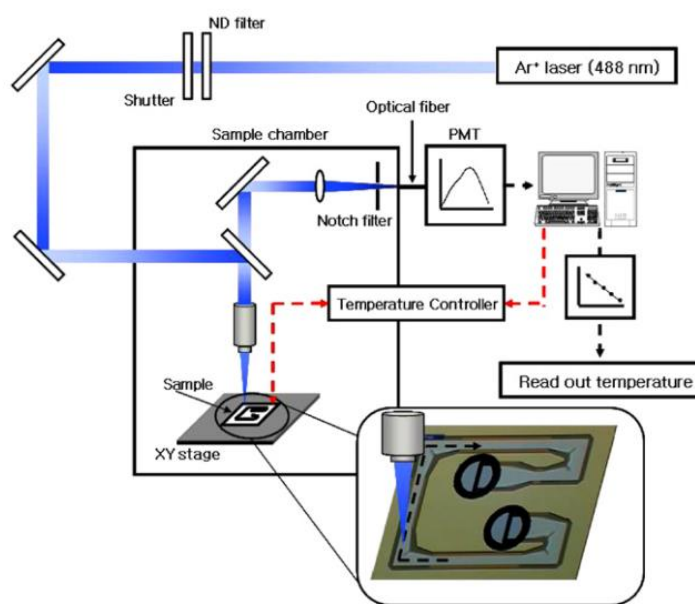


Figure 22 Schematic diagram of the micro-Raman spectroscopy system [122].

As described previously, Raman thermometry in a water environment can provide a measurement of temperature without interfering with the sample and

its medium. This is thanks to the fact that temperature variations can be measured via the temperature-sensitive O-H stretching envelope of the water Raman spectrum, which is strong and free from spectral interference. Due to this feature, systems like that shown above can achieve a precision in temperature measurement of 1 °C and a spatial resolution of 1.5 μm . In addition, thanks to the small volume analysed, the heat generated by the sample tends to increase the temperature of the surrounding medium allowing the sample temperature to be inferred by measurement of the local medium's temperature. It worth remembering that Raman Thermometry is generally a single point measurement but can produce spatially resolved images using an apparatus, such as the one presented in Figure 17. However, thereby adopting this technique it is possible to accurately measure only a single point at time, this is also limited by the long acquisition time, which is around 0.5 points per second [125].

2.4 FLUORESCENT THERMOMETRY

In contrast to luminescent techniques, fluorescent thermometers base their functionality on the use of temperature dependent physical behaviour that can occur even at the quantum level. As detailed in Section 1.2.3 the main driver for the emission of fluorescence radiation is the relaxation of an electron from an excited singlet state to a stable one. The entire process is usually divided into two subprocesses, excitation and emission (fluorescence). Emission is characterised by the production of heat and a photon with energy equal to the product of Planck's constant and the emission frequency.

Currently, a wide range of fluorescent thermometers have been developed based on diverse fluorescent parameters (described in Section 1.2.3) and materials. Those based on small organic molecules and nanomaterials have been widely adopted as fluorescent thermometers working on the nanoscale. Thermometers based on small organic molecules like fluorescence, NBD or rhodamine, which have high quantum yield, have been used by the research community in the past [126]. This class of compounds have precise energy barriers to be overcome before the electron system has enough energy to promote an electron to a higher energy state and subsequent emission. This "on-off" response make them an ideal tool for studying the biological process, where the fluorescent response is reached only when the energy barrier is overcome by a certain threshold of temperature. For example, Rhodamine B, which is widely used in biology for

monitoring the temperature of a biological sample, has a range of operation that starts from 283 K up to 368 K [46]. Consequently, emission starts at well defined, low temperature and the energy (frequency) of the emission changes with the change of temperature of the sample. In the literature, efforts have been described to engineer molecules that have well-defined energy gaps, achieving better control of this process [127]. The precision in activating the emission and generating specific frequencies at particular temperatures improves the accuracy of the measurement. In addition, the use of compound that contain Boron have been widely studied thanks to their interesting photophysical properties induced by the presence of a vacant p-orbital in the Boron atom. A significant aspect of this physical state is the possibility to control this configuration affecting the fluorescent properties of the compound. This can include a more precise on-off threshold or a particular colour emission in conditions desired by the use. These established fluorescent dyes including rhodamine [128] and Eu-TTA [129, 130] have high flexibility. However, the use of organic dyes presents several problems, such as the fact that the chemical environment can influence the intensity profile of the fluorescence. Furthermore, organic dyes have a limited operating life, up to 30 minutes, due to photobleaching, which limits their long-term monitoring ability [131]. Several attempts have been made to eliminate or minimise their sensitivity to the chemical environment by placing the dye molecules in a PDMS matrix [132, 133]. However, since the PDMS matrix has poor thermal conductivity and the thickness surrounding the dye, for this application, is around 30 μm , this causes a significant reduction of accuracy and speed of response.

In recent studies [128] a new organic dye has been developed, borylated arylisoquinoline dye or BAI. This is very attractive due to its intramolecular charge transfer (ICT) properties [134], which describes the ability of large molecule systems to transfer a fraction of charge from two different molecule parts, promoting an electronic transition that generates the desired excited state required for subsequent photon emission [135]. This feature enhances the ability for scientist to create more accurate and application-focused dyes with specific and adjustable excitation and emission frequencies.

In addition, the presence of functionalised carbohydrates in this compound make it well suited for studies in biological systems, where a thermal probe is likely to

interact with the sample [136]. In particular, these groups can be chemically functionalised to accurately target a desired site on the sample. These advantages result in BAI being well suited to and real-time temperature monitoring of biological systems, with a sensitivity of around 0.039 to 0.025 $^{\circ}\text{C}^{-1}$ [137]. However, for long-term or time-lapse measurements, this technique may still have limitations due to the continued presence of photobleaching. This consists of a progressive alteration of the dye, which causes it to fade, resulting in the eventual loss of its effective fluorescence ability.

Luminescence is a property that spans across all the length scales and reaches down into the nanoscale. Several nanoparticles are capable of emitting light and all of them show behaviour with a clear and distinct temperature dependence [46]. One class of engineered nanomaterials that exhibit this behaviour are quantum dots. Quantum dots or DQs are semiconductor particles with a size in the order of few nanometers, capable of emitting radiation in precise frequencies using the same physical principles explained previously.

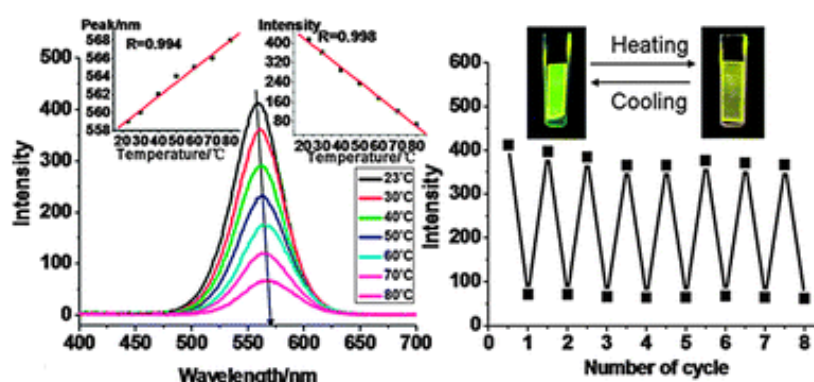


Figure 23 The left panel depicts the luminescence spectra of the T sensitive $(\text{CdTe QDs-LDH})_{30}$ QDs ultrathin film in the T range 296–353 K (inset: the emission position or intensity as a function of T, respectively). The right panel shows the reversible fluorescence response of eight consecutive cycles [138].

Luminescence in QDs tends to decrease as the temperature increases, leading to a widening and red shifting of the emission spectra (as shown in Figure 23). One class of QDs used in the biological field are water-soluble CdTe QDs, which respond to the change of temperature between 77 to 300 K with anti-quenching effect. This behaviour has been investigated and associated with the inter-QDs dipole-dipole interaction [46]. QDs of the CdX class have a relatively short fluorescence lifetime in the order of ns, which tends to degrade with an increase of temperature over 300 K. One of the key advantages of DQs is their stability against photobleaching, as it is shown in Figure 23. This shows that, in contrast

to traditional dyes, the intensity of the emission does not significantly vary over multiple cycles of heating and cooling [138].

One recent innovation in fluorescence thermometry, allowing for very localised temperature measurement in water environments, are DNA molecular beacons[139]. The core principle behind this technique is the thermo-transformable responses of DNA. The change in double-stranded DNA structure from B-DNA to Z-DNA (Figure 24) [139], can be used as a potential DNA based thermometer. The DNA structure can exist in three forms and B-DNA is an ordinary form where the double-helical structure winds to the right in a zigzag pattern. Conversely, Z-DNA, which is less common, has a structure that winds to the left.

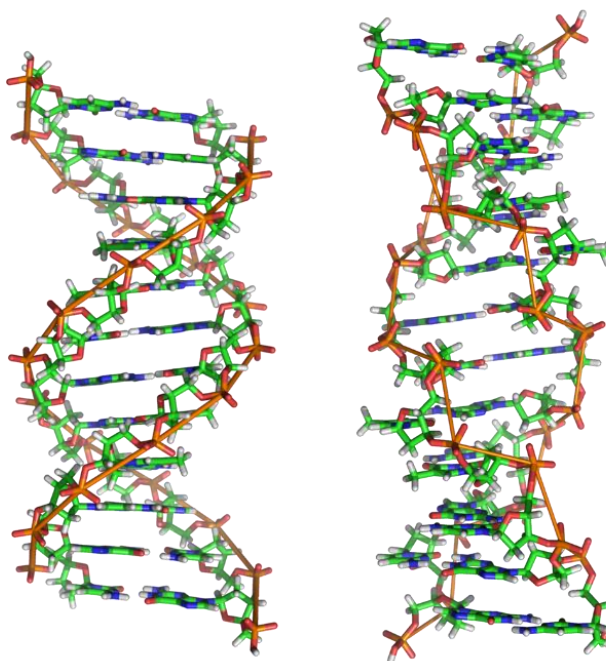


Figure 24 Schematic representation of the B-DNA and Z-DNA structures [139].

The Z-DNA configuration is not thermodynamically favourable but the transition from B to Z can be controlled through environmental conditions [140]. Specifically, it has been demonstrated [141] that a molecular switch indicates an inverted response of the DNA or RNA to thermal stimuli. This concept is the basis for using DNA or RNA as a thermal probe. Depending on the temperature of the surrounding environment, the transition from B to Z-DNA can result in a strong change in fluorescence intensity. Specifically, the fluorescence intensity decreases with an increase of temperature, as shown in Figure 25. It worth underlining that the conformational state (B or Z) is responsible for the on-off

mechanism while the fluorescence generated is also temperature-dependent as described for conventional fluorescent dyes above.

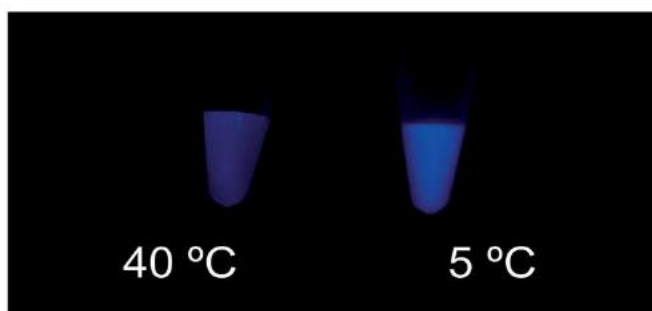


Figure 25 Photo of visible nanothermometer. Samples contained 5 mM of ODN9 in 20 mM sodium cacodylate buffered (pH 7.0) 3.5 M NaClO₄. The photo was taken under UV (365 nm) irradiation [140].

The same physical principle has been exploited for certain messenger RNAs, which change their conformation when subjected to precise temperatures. The above techniques exhibit spatial resolution down to 0.1 microns, and thermal accuracy of 0.045 K⁻¹ up to 0.023 K⁻¹. However, they also suffer from significant systematic errors due to the fluctuation of the fluorescence rate and the optical properties of the surrounding medium [142].

2.5 MICRO-FABRICATED THERMOMETERS or THERMAL ELECTRICAL THERMOMETERS

One of the most straightforward approaches to measuring the temperature in liquid environments and biological samples is the thermocouple, [143, 144]. The spread of this technique is related to the advancement of microfabrication methods, especially lithography and vapour-deposition [77, 145], allowing low-cost, nano-scale, reproducible thermocouples to be produced. The use of microfabricated thermocouples has been integral in realising tools such as built-in temperature sensors for micropipettes and micro-scale lab-on-a-chip [146]. One of the most demanding applications for the accurate and economic measurement of temperature is within biology, where the temperature of micro-reactors [147] or the in-vitro measurement of cells [148] is crucial. These two example applications point to the two main types of deployment for micro-thermocouples: invasive and non-invasive.

One of the most common invasive tools used by cell engineers, for a broad range of tasks, including drug studies and artificial insemination are micropipettes. Consequently, the embedding of a micro-thermocouple probe into the

micropipette is a simple method to extend the functionality of the tool. Micropipettes equipped with an integrated thermocouple can simultaneously introduce reagents to a cell whilst measuring real-time changes in temperature. However, the invasive nature of micropipette based measurements limits the experiment to short analysis periods (around 1.5 seconds [149]).

The original idea of measuring local cell temperature using a modified micropipette was described in the work of Fish et al. [150], employing the design shown in Figure 26.

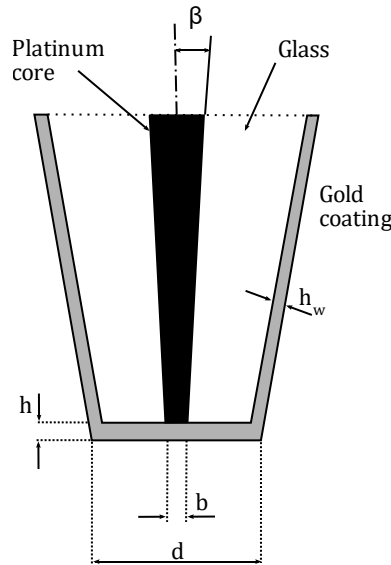


Figure 26 Schematic representation of the sensing area of the micropipette probe [150].

Fish also determined two conditions that must be met to ensure accurate measurement when employing a micropipette-based thermocouple probe. First, the heat flow through the platinum core must be smaller than that from the surrounding medium, in order to minimise the influence of the surrounding environment. This requirement allows the point temperature to be measured accurately, avoiding other heat fluxes that can easily generate unwanted readings. When considering the geometry of a micropipette, this constraint limits the cone angle β as follows:

$$\beta = \lambda_m \frac{d}{(\lambda_{Pt} b)} \quad (11)$$

Where λ_{Pt} is the thermal conductivity of platinum, b is the diameter of the platinum electrode in contact, d is the pipette tip diameter and λ_m is the thermal conductivity of the medium. To satisfy this condition for b/d equal to 0.1 in a water environment, the cone angle must be less than 4.8° . This limit is strictly

related to the materials involved, water for the environment and platinum for the micro-thermometer core.

The second condition determined by Fish is related to the thickness of the gold coating, h (Figure 26), which also affects the thermal conductivity and the associated temperature sensitivity at the tip. To allow the tip to effectively measure the temperature the following condition must be satisfied:

$$2h\lambda_{Au} \geq \lambda_{Pt} \left(\frac{b}{2}\right) \beta \ln\left(\frac{d}{b}\right) \quad (12)$$

where h is the thickness of the gold disk at the end of the tip, λ_{Au} is the thermal conductivity of the gold coating, b and d are geometrical parameters shown in Figure 26. The model used by Fish et al [150] is based on the solution of the heat transfer equation for a metal layer with the shape of a disk, where the heat flows out from the centre. Equation 11 ensures that the gold coating present at the tip will result in a homogenous heat flow across the gold film.

This design is amenable to additional miniaturisation and recently an improvement in spatial resolution (down to 2 μm) and accuracy (± 0.01 $^{\circ}\text{C}$) has been demonstrated [149]. This improvement in thermal sensing capabilities has been useful in several biological studies where analysis at the single cell level is required. This has opened up the possibility to study the individual cellular response to drugs and to laser heat treatment in real-time [149].

The fabrication procedure that allowed such an improvement in the micropipette design and consequently its characteristics is described by Watanabe et al [151]. In brief; the base of the thermocouple is still a glass micropipette as it is shown in Figure 27a. However, a layer of Ni with a thickness of 50 nm is deposited instead of gold. In order to create an electrically insulating film between the layers, 50 nm of Diamond-Like-Carbon (DLC) was then deposited. The end of the probe (the tip) was then etched using FIB, to eliminate the thick layer of DLC and Ni. A thin film of Constantan (Cu: 60% + Ni 40%) was then deposited on the surface of the tip, in contact with the DLC and tip-Ni. Finally, a layer of DLC, acting as an insulator, was deposited encapsulating the entire device. The use of DLC improved both the electrical insulation and the mechanical properties of the probe, especially in the thermocouple junction area.

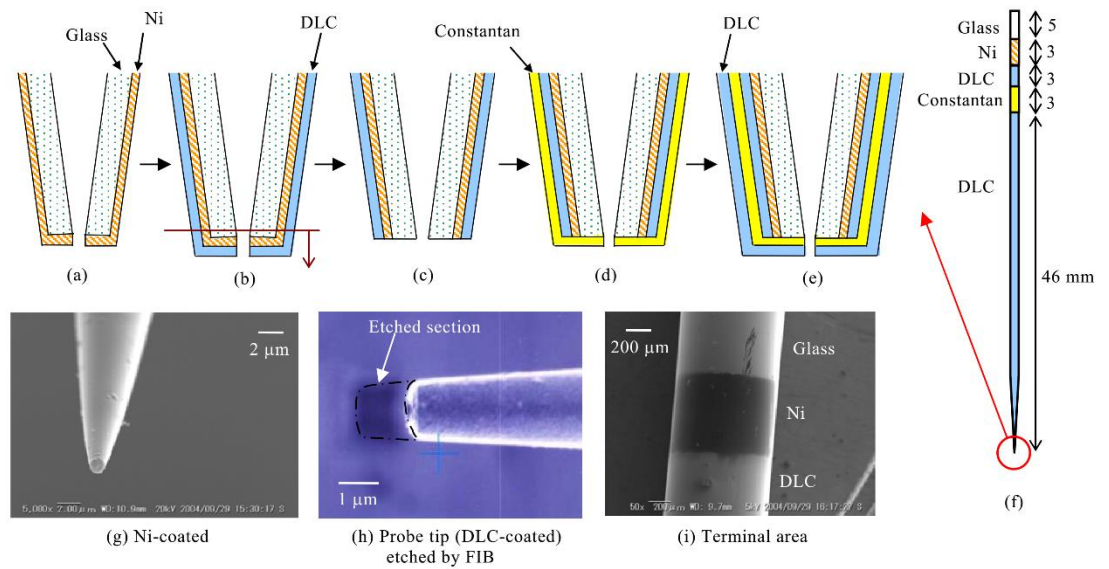


Figure 27 Fabrication procedure of the micro-thermocouple probe: (a) A glass micropipette with a tip diameter of $1\ \mu\text{m}$ and a length of $50\ \text{mm}$ is coated with a Ni film ($50\ \text{nm}$) by ion-sputtering. (b) DLC ($50\ \text{nm}$) is deposited using a plasma-enhanced chemical vapour deposition method. (c) The tip ($1\ \mu\text{m}$) is cut off by a focused ion beam (FIB). (d) Constantan ($50\ \text{nm}$) is deposited by ion-sputtering. (e) DLC ($50\ \text{nm}$) is deposited. (f) The terminal of each layer is produced at the end opposite the probe tip. (g)-(i) The scanning electron micrographs of the probe [151].

In contrast to a micropipette, where the probe penetrates the cell, the non-invasive approach consists of remotely measuring the temperatures changes while a reaction occurs. These types of thermometers do not extend beyond the surface of the cell, therefore avoiding altering its mechanical integrity. This feature has been widely developed especially for lab-on-a-chip applications where temperature control and monitoring are fundamental to maintaining correct experimental parameters. An example of a micro-reactor with an active temperature sensor as it is shown in Figure 28a-b. In this case [152], the micro-chamber temperature is controlled by a separate heater as depicted in Figure 28c. This has the advantage of creating an “isolated” area where more chambers can be heated with the use of a single heater at the same time.

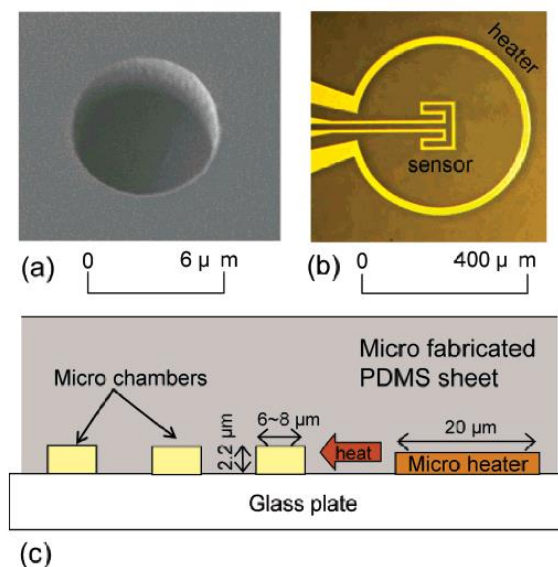


Figure 28 (a) SEM image of a patterned PDMS sheet. The 56.0-fL chambers had STD of 1.63 in volume. (b) Optical microscope view of integrated microheater and micro thermosensor on a glass plate. (c) Schematics of the temperature-controlled microchamber array [152].

The miniaturisation of these devices has a series of advantages. The entire micro-reactor exhibits lower energy consumption when compared to larger reactor systems. It is possible to also integrate different sensors and actuators onto the device, including pH and photoluminescence sensor [153], micro thermocouple and micro-heaters [154, 155]. This enhances the flexibility of the micro-reactor, allowing different parameters to be studied at the same time. Finally, yet importantly these devices are relatively cheap compared to normal scale reactors and sensors and can be mass-produced. However, spatial resolution is much lower than a micropipette-based method, which tends to monitor each cell. Despite this, the approach has no limitation in terms of measurement duration, since the sensor is not in direct contact with the biological sample and the length of the measurement is not dictated by the probe/sample interaction.

However, advances in this area have been recently presented in the literature [156], pushing the boundaries of the micro-fabricated thermocouple. Using low-resolution electron beam lithography and lift-off procedures, a thermocouple with just 2.5- μm -wide electrodes (Au-Ni) has been fabricated on a Si_3N_4 membrane with a thickness of 30 nm. In this work, the authors showed that the newly fabricated thermocouple was capable of sensing heat with great sensibility (around 10.1 $\mu\text{V}/\text{K}$). In order to reach a higher spatial resolution, a nano-thin membrane with sub-micron diameter was used. The device demonstrated usefulness for real-time monitoring, even for small and relatively fast temperature changes up to $\sim 2 \times 10^5$ K/s, measured at a rate of 10 kHz. This is

important when studying complex chemical behaviour, such as the enzymatic activity involved during ATP hydrolysis, which can take place in a very short period depending on the case study. Accuracy and speed of measurement are crucial for processes that are strongly temperature dependent [157]. A similar device is under investigation for use in conjunction with optical microscopy [158], coupling the imaging process [159] with thermal registration from the sample, such as a cell in their medium.

2.6 SCANNING PROBE MICROSCOPY (SPM)

SPM is based on near-field interactions such as Van der Waals forces or tunnelling [81]. From this point of view, SPM represents a powerful technique, allowing nano-scale images to be taken and local properties of materials determined. Scanning probe microscopes are now relatively commonplace in nano-scale research groups within universities and industry. This popularity is due to the fact that SPM has many different uses not just in imaging but also techniques such as nano-manipulation [160, 161]. The different operational modes of a SPM allow versatility to study and image a wide range of samples and properties (examples include confirmation of proteins [162], the structure of intermolecular electronic bonds [163], local nanomechanical properties and adhesion [164], [165], [166], as well as thermal [60] and magnetic [167] properties). The possibility to explore mechanical properties can be integrated, as has been done using the Wollaston probe by [168], with SThM. This method combines the possibility to characterise the mechanical properties of a material while locally increasing the temperature of the sample. This approach has been used in microthermal analysis of polymers [169] for measuring the stiffness of a sample, while temperature changes occur directly in the location where the force is directly applied via Wollaston probe.

The foundation of SPM can be marked by the invention of the scanning tunnelling microscope (STM) in 1982 by G. Binnig and H. Rohrer [170], a revolutionary discovery that won them the Nobel Prize for Physics in 1986. STM is based on the quantum tunnelling principle; when a metal tip is brought near a conducting surface, a voltage difference applied between the two allows electrons to tunnel from the tip to the surface or vice-versa. Since the tunnelling probability is exponentially dependent on the distance between the tip and the specimen, a map of topography can be obtained by measuring the sample height whilst keeping the current constant. In this way is possible to reach resolutions of 0.2

nm. However, to conduct a tunnelling measurement, the sample of interest has to be conductive, meaning STM has somewhat limited use.

2.6.1 ATOMIC FORCE MICROSCOPY (AFM)

In 1986 Binnig, Quate and Gerber proposed a new type of microscope, the atomic force microscope (AFM) [171], nowadays the most commonly used form of SPM. With this technique atomic interaction forces, Van der Waals attraction, are measured by means of a tip connected to a cantilever. By combining this principle with the same sample/probe positioning approaches employed for STM, the topography of the sample can be imaged. To achieve good spatial resolution, a sharp tip is required, with an ideal tip having just a single atom at the very apex and a high aspect ratio. Figure 29a shows a diagram of the atomic force microscope.

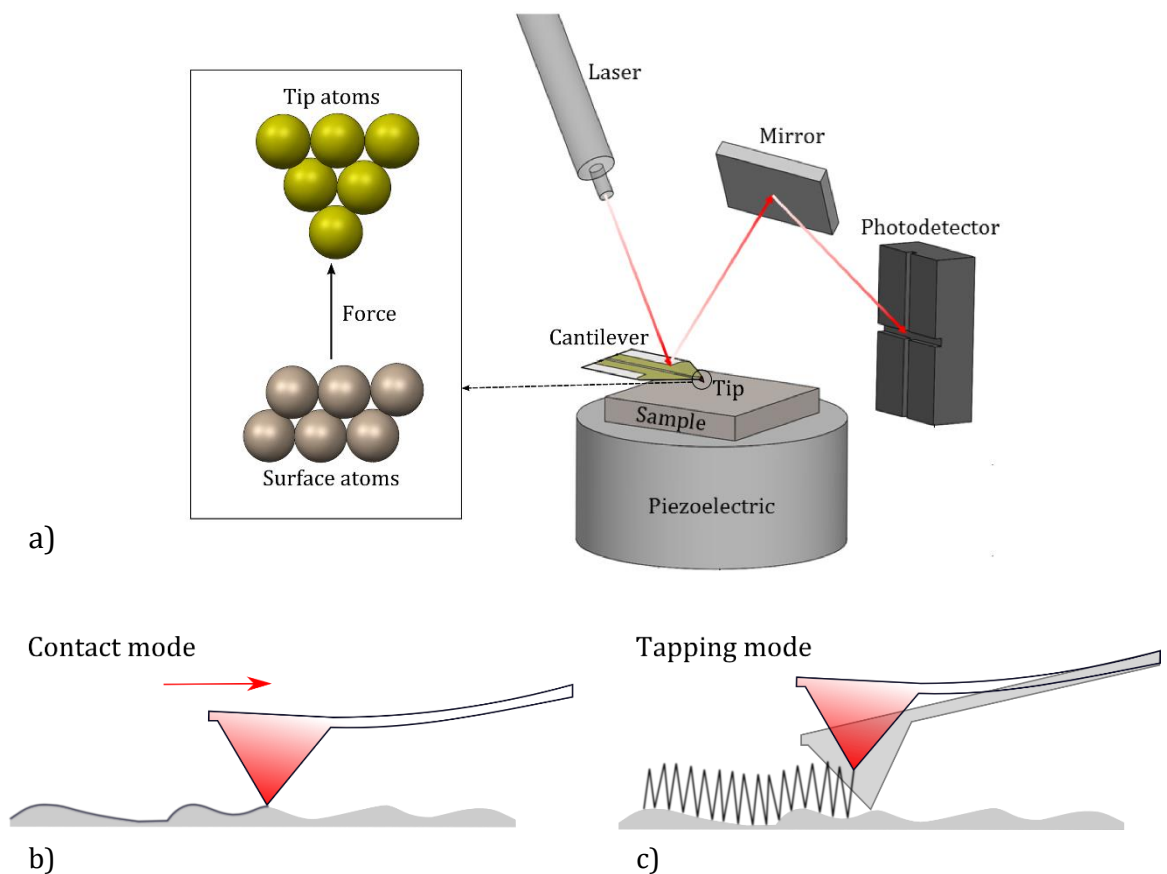


Figure 29 a) Diagram representing the AFM working principle alongside with the schematic representation of b) contact mode and c) tapping mode.

In contact mode, (Figure 29b), the tip is gently brought into contact with the surface which is scanned along an x-y grid. The tip is located at the very end of a cantilever that acts as a spring. As the tip moves over the surface, its deflection is measured by a laser reflected off the top of the cantilever into a photodetector,

often via a mirror. This photodetector typically has four segments allowing both the vertical and lateral deflections to be measured. During scanning, an electronic feedback loop works to maintain a constant force (i.e. cantilever bend) between the probe and sample by moving the sample up or down, adjusting the cantilever height above the surface. To do this the sample (or probe) is attached to a piezoelectric tube. The change in height, required to maintain a constant cantilever deflection, is then used by the computer to recreate the topography of the sample.

It is possible to carry out an experiment studying the deflection of the cantilever and therefore the forces experienced by the probe as it moves into, and away from, contact with a sample. This is achieved by approaching or retracting the probe from the surface whilst monitoring the forces between the probe and sample. The recorded data can then be presented in what is commonly known as force-distance curves [172] (Figure 30).

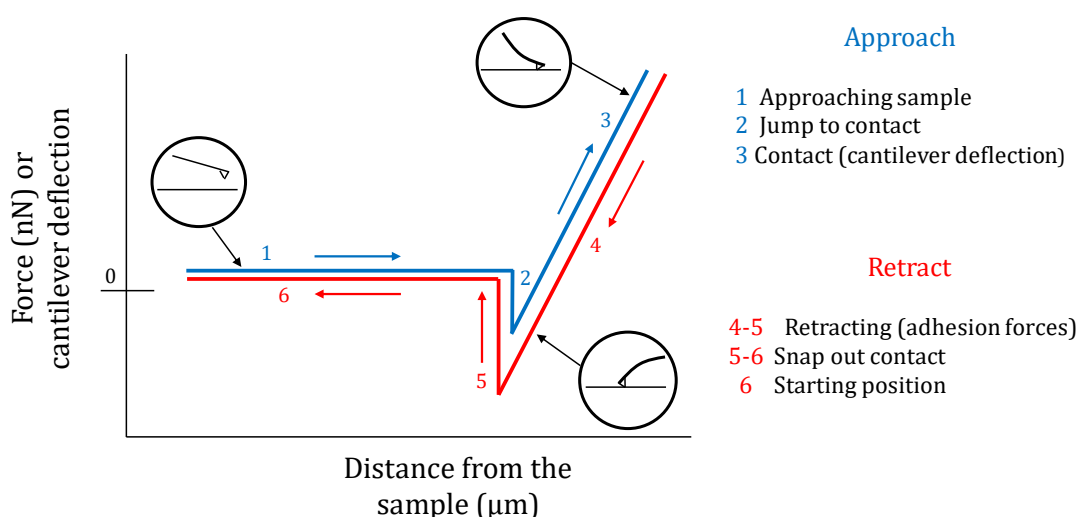


Figure 30 AFM force-deflection curve.

These curves are generated by moving the tip towards (approach) and away (retract) from the surface. At point 1 (Figure 30) the sample moves up and the tip is approaching (but not contacting) the surface, therefore a constant (zero) force is measured. In the air, when the tip is very close to the sample, it starts to experience attractive capillary forces due to the surface water film and jumps to contact (2). As the piezo continues to expand, the tip is then pressed further into the sample causing an increase of the force and the cantilever starts to bend (3). At point 4 the process is reversed; the tip is retracted and the force starts to decrease. Eventually, adhesive forces cause the tip to maintain contact with the

surface even under negative force (5) until it loses contact and returns to its initial, un-bent position (6). These curves can provide useful information about the surface characteristics and mechanical properties of the sample. This mechanical information includes elasticity, visco-elasticity and adhesion, all of which can be extracted from the gradient and hysteresis of force-deflection curves (3, 4 and 5 in Figure 30). With an included hold or dwell time during the force curve (where the probe tip is held at constant force or indentation distance in contact with the surface), it is also possible to extract creep/relaxation behaviour.

In tapping mode (Figure 29c), the cantilever is driven at its resonance frequency oscillating up and down. This oscillation is commonly achieved using a small, separate piezo element located in the cantilever holder. The oscillation's amplitudes range from 10 to 50 nm depending on the setpoint used [173]. The frequency and amplitude of the driving signal are kept constant as long as there is no drift or interaction with the surface. However, when the tip comes close to the surface, Van der Waals and electrostatic forces dampen the oscillations. The amplitude of this oscillation is used as a parameter in the feedback loop that controls the height of the cantilever above the sample. The feedback loop adjusts the height to maintain a set cantilever oscillation amplitude (i.e. constant damping) as the cantilever is scanned over the sample. Since the probe is not permanently in contact with the surface, the lateral friction forces are lower compared to those in contact mode, decreasing the possibility of surface (or tip) damage. For this reason, tapping mode is commonly used to scan soft or poorly adhered samples to minimise the risk of dragging [174].

PeakForce Tapping mode is a novel and promising imaging technique that has been incorporated into several modern AFMs, providing topographic and materials properties data in parallel with other modes such as electrical characterisation. PeakForce Tapping can also simultaneously combine high resolution AFM imaging with quantitative, nanoscale electrical, mechanical, biological, and chemical property mapping. In PeakForce Tapping, the probe is driven away from its resonance frequency, periodically tapping the sample. The pN-level interaction force is measured directly by rapid recording of the deflection of the cantilever. The feedback loop keeps the peak probe-sample interaction force constant, down to 10 pN, in both air and fluid, which is

significantly lower than is typically used with other modes, such as tapping mode (~ 1 nN). In addition to material research, PeakForce Tapping is ideal for measurement of biological samples due to its low imaging forces. It overcomes the many limitations of TappingMode operation in a fluid, such as the need to constantly tune the cantilever. Routine measurements of live-cell mechanical properties are now available with PeakForce Tapping technology. The superior force control maintains tip shape and sample integrity, leading to consistently accurate and high-resolution measurements of even the smallest biological structures, such as double-helix DNA. One particular implementation of PeakForce Tapping is the PeakForce QNM (Quantitative Nano-Mechanical) mode used in this thesis (Chapter 6). PeakForce QNM maps and distinguishes between nanomechanical properties including modulus, adhesion, dissipation, and deformation with nanometer lateral resolution. It is non-destructive to both tip and sample since it directly controls the peak normal force and minimizes the lateral force on the probe. In this AFM mode, the tip engages the sample intermittently without damage, thus eliminating lateral forces. The force between the tip and sample is controlled using a continuous feedback loop. Force curves are generated for each tip oscillation of the area being scanned and are simultaneously used for calculating the modulus and providing a nanoscale map of deformation, adhesion, dissipation and modulus [175]. Recently, the Peak Force QNM technique has been employed to study the nanomechanical properties of soft surfaces such as fibrils [176], polymers [177], living cells [178], nano-bubbles [179], nanocomposites [180].

With normal (i.e. tapping or contact) AFM it is also possible to carry out studies under liquid environments. In this case, sample and probe are submerged in liquid by means of special holders. The use of AFM with the cantilever and sample in aqueous environments is well established and offers many advantages allowing not only physiologically more realistic environments but also better control of the forces that are applied to the sample.

In 1989 Drake et al. [181] used an AFM in water to study biological processes; by imaging crystalline mica, polyalanine and the polymerization of fibrin, the authors showed, for the first time, the potential of the AFM in biology and medicine to revealing the structure of molecules and subtle details of biological processes as they occur in real-time. In the same year, Weisenhorn *et al.* [182]

reported a study showing a comparison between the force curves produced by a tip in contact with a surface in air and water. From these curves, they observed that while in air two transitions were visible, one due to snapping out of contact and the second one due to lifting out from a water meniscus. In water, there was just one transition due to lifting off the surface. This shows that tip-sample forces can be dramatically reduced in water, allowing more gentle scans. Furthermore, the authors observed that AFM in the liquid was able to acquire fast images, just a few seconds per image, with a force of less than $2 \cdot 10^{-9}$ N, making under-liquid AFM a very gentle tool to observe biological and chemical processes in real-time. Following these promising results, in-liquid AFM was used to conduct several studies to image biological structures, such as mammalian cells or DNA [183], [184] and to understand cell mechanics [185]. Researchers were able to investigate living plant cells [186], and red blood cells [187] in a buffer solution. By keeping forces below 5nN even soft and deformable cells could be imaged for several hours without being destroyed [187]. Analysis of force-distance curves for different liquids was compared to air, showing that the forces in a liquid environment are around 10 times less than in air [188].

2.6.2 SCANNING THERMAL MICROSCOPY (STHM) IN LIQUID

The working principle of SThM has been described in section 1.2. However, this is still a limited technique and is not as flexible as basic AFM, for example, one area of research that is largely unexplored is SThM under aqueous environments due to the instruments being unsuited to work underwater. This represents a great frustration as the accurate measurement and manipulation of temperature in aqueous solutions at the nanoscale has been increasingly recognised as a key capability. Experimental studies have already established, showing that there is no intrinsic limit to operating SThM under liquid environments. Immersion SThM [94], that employs electrically insulating liquids, has already identified a number of interesting advantages offered by a liquid environment. These include improved probe-sample contact stability, minimal probe-sample adhesion and improved stability of the tip-sample thermal contact.

However, the use of water as the surrounding liquid has always been impossible due to the immediate failure of conventional SThM probes when placed in this environment. Observations suggest that this is the result of uncontrolled electrochemical reactions occurring at the probe and resulting in corrosion of the

exposed RTD. This is a plausible explanation as the probes are typically biased in the $\sim 1\text{V}$ range during operation and consist of metals (NiCr, Pd, Au) that will undergo electrochemical reactions in water under these conditions [189]. Further extensive discussions on this topic will be given in the following chapter. To achieve SThM underwater, probe encapsulation by isolating the metal layers from the aqueous solutions has been previously proposed [190]. However, the insulating layers isolate the RTD from the object being studied and increase the tip radius, resulting in less accurate temperature measurement, reduced maximum heating temperature applied to the sample and reduced AFM spatial resolution. Furthermore, newly developed probes require characterisation, commercialisation and availability if they are to be adopted by the wider research community.

Although there has been a very little investigation into SThM in liquid environments due to this being highly challenging, its operation in liquid presents several advantages. For example, one detrimental feature that affects SThM measurements in the air is the thin water film that covers most surfaces under ambient conditions due to condensation of humidity [191]. The tip-sample thermal interaction involves many factors, however, solid-to-solid contact, the water meniscus [192] and conduction through the ambient gas are generally considered to dominate over heat transfer through radiation [193], [54], [194]. When an SThM probe contacts the sample under ambient conditions, a microscopic water meniscus forms between the tip and sample due to the capillary forces between the two. The size of this meniscus can vary and is strongly influenced by the humidity and temperature of the environment, as well as the sample and tip materials. This water meniscus forms an effective heat path between the tip and sample, essentially altering the thermal contact area of the tip, reducing the thermal resolution. Air surrounding the tip plays a similar role but its low thermal conductivity greatly reduces its impact in decreasing resolution and sensitivity. Furthermore, when a tip comes into close proximity to a surface covered with water, there is an adhesion force that pulls the tip towards the sample. As described for conventional AFM in the section above, this force can be much larger than the applied forces desired [181], potentially damaging tip or sample.

Luo *et al.* [88] first proposed that the water meniscus dominates heat transfer interactions based upon measurements using a thermocouple probe. Shortly after this work, Gomès *et al.* [195] further explored the water meniscus using Wollaston probes on several materials employing the same theory as Luo and concluded that the degree of meniscus importance depended on the thermal conductivity of the sample. However, their estimations were based on an equation that neglected the thermal resistance provided by the interface between the water meniscus and the tip, which was first realised by Shi *et al.* [191]. They proved that the interface would greatly affect heat transfer through the water meniscus and weaken its contribution. The ambiguity and variability of the meniscus effect seem to require quantitative SThM to be carried out under vacuum conditions, eliminating any surface water, as well as conduction or convection through the air; thereby greatly simplifying the system. For example, thermal sensitivity of SThM thermometry has been reported to be within 0.1 °C of sample temperature [196] in a vacuum. However, a more accessible method to eliminate the water layer whilst remaining in air is to undertake SThM measurements with the probe heated beyond the evaporation point of water [197]. However, this remains a challenge for some probes that cannot easily sustain the heating current required, such as the commercially available 'KNT' Si₃N₄ probe employed by many types of research. It is worth noting that the water meniscus can be removed if the sample is heated to a high temperature (>100 °C). However, this temperature can be challenging to achieve and potentially destructive to the sample or AFM instrument. Heating the probe above 100 °C can have a similar effect locally, but the current required is destructive to microfabricated probes such as KNT. Even if the probe survives, the cantilever thermal bend induced makes approaching and scanning the surface almost impossible.

Following the same logic as aqueous AFM described above, operation of SThM submerged in water environment would eliminate the undesirable and potentially destructive adhesion forces caused by the water meniscus, allowing better control of the tip-sample interaction even at the smallest separations. It would also eliminate the variable extent of the water meniscus, stabilising the tip-sample thermal contact area. Additionally, the elimination of air from the system also simplifies it down to be a two-phase system, making calculations of the

thermal interaction more accessible. Finally, the operation of experiments in aqueous environments is extremely useful in biology and chemistry, opening the possibility to image samples under their native conditions.

Some researchers have undertaken SThM in liquid, whilst avoiding the detrimental effects of an aqueous environment; Tovee *et al.* [94] conducted a study showing that it is possible to make measurements using an SThM fully immersed (iSThM) in dodecane, a low volatility and non-corrosive liquid, benign to SThM sensors. As part of their work, finite element (FE) simulations were employed alongside experiments. These simulations helped them to conclude that a silicon nitride probe with a platinum heater (as employed in subsequent chapters of this thesis) was the most suitable for measurement in the liquid environment due to the localised heat source provided. The approach they employed was to use the same probe to perform measurements in air and in dodecane environments before comparing the results. Images showing the topography of an aluminium and benzocyclobutene (Al-BCB) sample were obtained in both environments. The thermal images showed contrast, attributable to the lower temperature of the probe in contact with the aluminium region. This was a reasonable observation given the great difference in the thermal conductivity of the materials ($k_{Al} = 200 \text{ W m}^{-1} \text{ K}^{-1}$, $k_{BCB} = 0.29 \text{ W m}^{-1} \text{ K}^{-1}$). Voids were visible in the topography signal in both environments but only the in-air thermal signal. The authors claim that this could indicate that measurements made in dodecane enabled better thermal contact between the tip and sample across the whole surface topography. However, it could also be due to the lower spatial resolution of the liquid environment.

This study demonstrated, for the first time, that active heating nanoscale SThM in a fully immersed liquid environment is feasible. iSThM was shown to be sensitive to the local thermal conductivity of materials ranging from polymers (BCB) to metals (Al) and graphite nanoflakes. From FE modelling, the research showed that probe design may play a crucial role for iSThM performance, suggesting that dedicated optimization of probes for iSThM, e.g. changing the geometry of the heater and the probe apex, could significantly improve iSThM resolution and performance. The authors also confirmed that the heat flux between the probe and the sample defined the nanoscale spatial resolution of

iS_ThM and that heat was predominantly conducted through liquid rather solid–solid contact.

The same group started a preliminary investigation of the performances of S_ThM in water using FE simulations [198], however, their experimental technique was still severely limited by its requirement for electrically insulating liquids, ruling out the use of water.

The ability of S_ThM in aqueous environments to enable imaging of biological samples under their native conditions allowed L. Bozec *et al.* [104] to present the first analytical characterization of a biological system using a thermally controlled AFM probe. They conducted a study into the thermomechanical properties of collagen, a good example of a hierarchical biological nanomaterial. Collagen fibres with low hydrothermal stability convert to a gelatin structure when placed in water at room temperature. This is relevant to the storage of parchment fibres, where the avoidance of gelatinization is important, to avoid damage of historically valuable documents.

The authors recorded the behaviour of a sample of hydrated collagen as it experienced a temperature rise. By increasing the temperature of the S_ThM probe, its mechanical deflection remained constant until the start of the transition at 58°C. The main transition appeared at 65°C; corresponding to the well-understood denaturation of collagen into gelatin within a hydrated environment that is caused by the rupture of internal cross-links. This denaturation was characterized by a well-defined, abrupt drop of the AFM deflection signal, which progressively decreased with the increase of temperature. Experiments continued by studying the effect of the temperature rise on dried collagen fibrils and on the dehydrated gelatin, showing that when the probe temperature was increased up to 500°C, a gelatinized area could be seen in the area surrounding the point of the imprint. It should be noted that this imprint size was relatively large (~10 x 20 μm) due to the 5 μm diameter of the (Wollaston) thermal probe used in the experiment.

Although illuminating, this research encountered some technical limitations. The S_ThM probe could not be immersed in water, therefore the sample was kept hydrated in humid air. Even under these conditions, the probe struggled in achieving contact with the sample surface due to the diffuse hydrated surface structure of the gelatin, which exists at the surface of collagen fibrils in aqueous

environments. Furthermore, tip temperatures exceeding 100°C caused water evaporation and drying of the sample before any thermal events could be detected. The introduction of SThM under aqueous environments would assist work of this type by greatly simplifying sample preparation and experimental procedure. In this specific instance, this would result in a better understanding of the biophysics of collagen, the most abundant protein in the human body.

2.7 MICRO-THERMAL STUDIES IN AQUEOUS ENVIRONMENTS: LIVING CELLS

To date, micro-thermal studies in aqueous environments have either employed specifically engineered thermometers [199] or optical methods such as Raman spectroscopy [122], optical absorption [200] and fluorescence-based measurements [40] as described above. In particular, optical approaches typically employ spectroscopy to interrogate naturally present thermo-sensitive molecules or specifically introduced fluorescence molecules/nanoparticle probes within the system. However, despite some promising data, many of these methods suffer from significant limitations. These include low thermal and/or spatial resolution, the necessity to label the sample, systematic errors due to fluctuations in the fluorescence rate or the local chemical environment and the indirect nature of the temperature measurement they offer. This is highlighted in perhaps one of the most debated areas in thermal-biology: the temperature distribution within living cells [42], [201] where theoretical and experimental approaches have failed to agree on the validity and meaning of the experimental results obtained [202], [203], [204]. This means that the measurements obtained are sometimes controversial and there is still a poor understanding of how temperature varies among and within cells.

This is illustrated by the “10⁵ gap issue” proposed by Baffou *et al.* [201]. In their work, they observed a large discrepancy between the temperature rise of a single cell measured using cellular thermometry (a rise of 1 K), compared to that predicted by theoretical calculations (a rise of 10⁻⁵ K). Some groups, e.g. Suzuki *et al.* and Kiyonaka *et al.* [203], [202], claim that this discrepancy may be because the amount of heat production depends on cell type and on their history (stimulated cells show metabolic differences). Both groups also questioned the heat diffusion equation (HDE) used by Baffou *et al.* for the calculations:

$$\Delta T = \frac{P}{kL} \quad (13)$$

where L is the typical size of the heat source, ΔT is the temperature difference (in Kelvin), P is the power of the heat source (in watts) and k is the thermal conductivity of the medium surrounding the heat source (in $W\ m^{-1}\ K^{-1}$). Specifically, they believed that temperature fluctuations measured on the micrometre scale were too large for the HDE to be applied.

Furthermore, to make progress in temperature imaging of single cells, environmental parameters need to be checked and the robustness of intracellular thermosensors tested with respect to environmental parameters. In particular, it is believed that the working medium can drastically affect the heat flux and therefore the point temperature of the cell [205]. The message coming from these discussions may be perfectly summarized by Baffou's phrase: "*Thermal biology is still at its infancy. There is no reliable temperature mapping for cells.*" This is particularly important when considering the development of new thermally-activated drug delivery [206] and localized hyperthermia [207] systems. Localized hyperthermia is a promising treatment for cancers that allow very specific treatment of the patient's tumour via the magnetically or optically induced heating of nanoparticles [208]. However, the effectiveness of these proposed treatments varies significantly as a result of their unknown heating (i.e. equivalent to drug dosing) profile and a poor understanding of the effect localized heat has on cells [209], [210], [211], [212].

2.8 SUMMARY

In this chapter, several methods to measure the temperature of a sample in liquid environments have been presented. The techniques described can be classified into two types, contact and no contact. This latter class has been widely investigated, thanks to its advantage of being non-invasive. Over Raman and infrared, the fluorescent thermometry has been the most developed, also recently, thanks to the use of new no-toxic and photo-bleaching resistant dyes or thanks to the development of new quantum dots. In addition, no contact techniques have been used in several liquid environments.

Conversely, contact methods have been used for measuring thermal properties of materials in several environments, but only a few some preliminary works have been done in the non-conductive liquid environment [198]. A relatively small number of works considered the use of probes like the Wollaston one for specific measurement and thermal-induced modification on the biological

sample[104]. It is worth noting that the use of SThM in the biological field has been recognised as a natural progression of this technique [53] since it would allow a nano-scale accurate measurement of thermal properties in active and/or passive mode. No one currently has designed an efficient apparatus capable of operating in a liquid conductive environment and measuring living samples. Furthermore, in the literature, no specific study has been done to design a new probe to be used in a liquid environment. This latter point is also related to the reduced research work done within the numerical simulation of SThM in a water environment.

In the next chapter the new SThM instrumentation and the solutions adopted to overcome the existing problems, which limited the used of SThM in a conductive aqueous environment, will be discussed.

For the aforementioned reasons, SThM in aqueous environments holds the potential to assist studies in several temperature related fields. One specific example is photothermal therapy for cancer cells. This class of cancer therapy has been under study for decades and has relied on several conventional as well as more advanced techniques to locally increase the cell temperature associated to optical irradiation (usually within the near-infrared region). Currently, most of the experiments in the field monitor cell temperature using fluorescence dyes, confocal and optical microscopes. Having an accurate measurement of the temperature as well as the ability to locally heat cells directly using the SThM probe during experiments represents a great advantage. In particular, these approaches would permit SThM to not only study single-cell response to external heat treatment, monitoring cellular membrane mechanical properties in real-time, but also to selectively impose different levels of heat treatment using the probe itself, whilst simultaneously monitoring cell response in an aqueous environment.

2.9 AIMS AND OBJECTIVES

This thesis aims to develop and demonstrate the use of SThM in an aqueous conductive environment (a-SThM) for the first time.

The objectives of the research are therefore to:

- Develop the hardware and improved electronics needed to implement SThM under aqueous solution using commercially available probes.

- Validate the possibility of aqueous SThM and clearly demonstrate its performance in terms of thermal-spatial resolution in comparison to non-conductive liquid environments and air.
- Demonstrate the feasibility of out-of-contact a-SThM and compare the results with other non-conductive liquids.
- Design and model new probes that could improve the performance of SThM in water.
- Use the instrument to probe and thermally manipulate biological samples.

CHAPTER 3: NEW INSTRUMENTS AND APPROACHES EMPLOYED

3.1 COMMON LIMITATIONS OF SThM PROBES

As mentioned in Chapter 1, conventional SThM probes normally fail immediately if immersed in water and biased. The mechanisms behind this are explored further in Section 3.2. However, the work in this thesis stems from a belief that uncontrolled electrochemical reactions play a fundamental role in this problem. If this is the case, an obvious solution as suggested by Li et al. [213] is the use of a dielectric thin film to encapsulate the probe or part of it. This electrically non-conductive thin film can be based on a polymer like a Polyimide or more commonly SiO_2 or Si_3N_4 and prevents physical contact between the electrically active part of the probe and the water environment. However, this approach, despite its effectiveness, introduces several hidden problems. The first is the added complexity in the design and manufacturing process of the probe. This represents a significant challenge, especially for industries that must produce such devices. The second consideration is the fact that the measurement itself can be severely altered by the presence of an insulation layer that sits between the active region of the probe and the sample. This can be elaborated as follows:

The temperature generated by an SThM probe can be analytically described using a network of thermal resistances, where the cantilever, the sample, their interaction and the working environment are represented by separate thermal resistances [88]. An example that summarises this thermal resistance network is depicted in Figure 31.

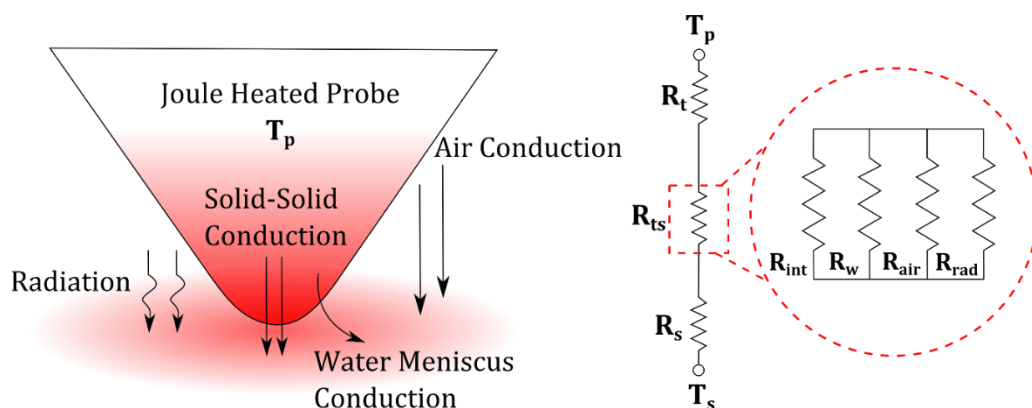


Figure 31 Heat transfer mechanisms between probe and sample and associated thermal network, where R_t , R_{ts} and R_s represent the thermal resistance of the tip, interface tip/sample and sample respectively[1]. R_{ts} is represented as a series of several other resistors R_{int} , R_w , R_{air} and R_{rad} . These represent the thermal resistance associated to the solid-solid contact, the water meniscus, the air conduction and the radiative heat transfer.

The thermal resistance of the contact interface, R_{ts} , is associated with several parameters. It is generally accepted, in air, that solid-to-solid contact (R_{int}), water meniscus (R_w) and air conduction (R_{air}) dominate over heat transfer through radiation (R_{rad}) [54]. In terms of magnitude, there is a significant difference between R_w and R_{air} . By comparing the thermal conductances, it has been observed that the conduction across the water meniscus, in air, is not dominant when using a Wollaston probe. The values of the thermal conductance are lower than $0.2 \mu\text{WK}^{-1}$ which is smaller than the values of the thermal conductance through the air (few μWK^{-1}). It worth mentioning that in this area, results are also highly affected by the environment and by the probe type and design. In water, this completely changes due to the presence of a water medium around the probe. Among all the thermal resistances R_{int} is still the one that dominates in air. R_{int} has been estimated in various works [214] considering a single-asperity contact between the probe and the sample. $R_{int} = \frac{R_b}{\pi b_c^2}$ where R_b is the thermal boundary resistance for bulk materials on macroscopically large areas, having units of $\text{m}^2\text{K}/\text{W}$ and b_c represents the contact radius. Due to the lack of precise data for R_b , which has been studied mainly at low temperatures, values at room temperature for R_{int} can only be said to lay in the range from 1×10^{-9} to $2 \times 10^{-7} \text{m}^2\text{K}/\text{W}$ [215].

If the SThM probe were encapsulated, a new resistance term (or modification of the R_t term) would be required to describe the thermal resistance associated with the insulating film. Although this may appear to be a trivial modification, experience teaches us that this type of interaction will be difficult to quantify. Typically this is due to the different, often unknown, thermal conductivity of thin films, as well as the variable interface resistance that will accompany its interaction with each material of the probe (R_t), surroundings (R_w , R_{air}) and any surface being measured (R_{int}). The importance of this additional resistance is shown in the following equation of the probe temperature when operating in active mode:

$$T_p = \frac{PR_{cant}(R_s+R_c(R_{int},R_t,R_p))}{R_{cant}+R_s+R_c(R_{int},R_t,R_p)} + T_\infty \quad (14)$$

Where P is the Joule heating power of the probe, R_{cant} is the resistance of the cantilever and R_p is associated with the environment and all are independent of the sample considered if the probe and scan conditions remain unchanged. R_{int} ,

which is the interfacial thermal resistance resulting from the solid-solid contact, will vary according to the materials in contact. T_∞ is the ambient temperature and it is considered to be constant. Therefore, including a second coating on the cantilever will increase the complexity of both numerator and denominator.

These changes can only increase the thermal resistance between the probe and sample, decreasing the thermal coupling between them and ultimately affect the thermal resolution of the probe. In addition, the introduction of another material at the probe tip will increase the contact radius (decreasing topographic resolution), unless additional production steps are included to sharpen it.

In addition to the issue of complicated design and thermal model, encapsulating films can completely alter the tip-sample contact force generated in some situations. This is because an SThM probe and sample held at different electrical potentials and separated by a dielectric film would generate an electrostatic force. This is directly related to the dielectric thickness and to the electrical potential difference present. A schematic representation of the geometry of a simple capacitor is depicted in Figure 32. The force generated across a dielectric material with a permittivity ϵ (ϵ_0 of the environment surrounding the capacitor) within a two-plates capacitor is equal to the gradient of the electrical work ($W_{el} = \frac{wd}{2} \left(\frac{U}{d}\right)^2 [\epsilon x + \epsilon_0(l - x)]$) at constant electrical potential U [216].

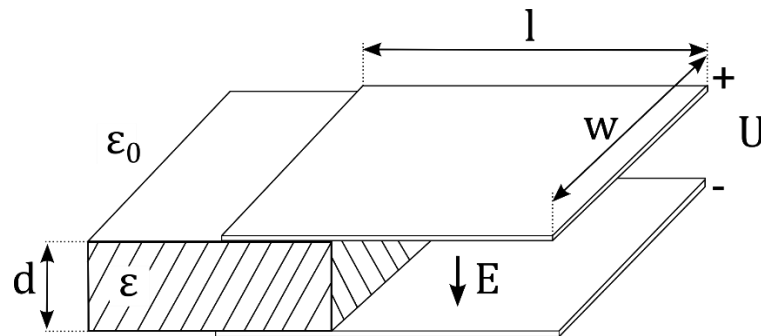


Figure 32 Schematic representation of a dielectric inserted into a two-plates capacitor subjected to an electric field E and voltage difference U [216].

This force between tip and sample is not easily controllable using the normal AFM mechanisms (i.e. cantilever deflection, probe-sample separation control) and could have a destructive effect on the tip or sample. For example, the dielectric strength of Polyimide, a commonly employed encapsulant, is around 0.118 V/nm and for SiO_2 or Si_3N_4 is 1 V/nm. During a-SThM measurements the voltage at the tip can increase with time and temperature due to the change in the probe resistance, as it will show in Chapter 4, within the calibration section. Considering

an averaged value of 4V and using the inverse of the encapsulant dielectric strength is simple to estimate a minimum of 34 nm required to ensure the coating life. This rough estimation shows the nearly impractical use of very thin coatings at modest potentials. If the voltage is increased, to obtain larger temperature differences, the only solution would be to use a thick layer of dielectric material, which would further compromise the SThM tip-sample thermal contact and topographic resolution as described above.

Another problem that originates by using an insulation layer is related to the thermal bending present in bimetallic cantilevers. As described in Section 1.2.7, nanofabricated SThM probes can be severely affected by the thermal bending of the cantilever under certain conditions. Such detrimental behaviour is caused by the mismatch in coefficient of thermal expansion between the main material of the cantilever (e.g. silicon nitride) and electrical connection (e.g. gold). The design of the cantilever uses the presence of gold connections only on one side of the structure. Therefore, a change in temperature will result in the bending of the cantilever. This bending affects the forces on the cantilever, which can be misinterpreted by the measuring system, leading to false signals. Normally, if a constant force is applied between tip and sample the system will keep this constant acting on the applied force. However, the bending behaviour of the cantilever is strongly influenced by the temperature. For example, if the temperature decreases the cantilever of KNT style probes employed in this work naturally bends towards the sample. This signal is processed by the AFM feedback system that will adjust the Z position to alter the applied force. A more severe problem is encountered when the probe is active and heats the sample, or the sample itself is heated. In this case, the feedback loop processes the data considering the probe as overloaded and subsequently reduces the applied force. To do this, the feedback loop will move the tip away from the sample to reduce the force. At a certain temperature, the thermal bending of the cantilever will correspond to a greater force than that controlled by the feedback loop and the sample will be withdrawn from the tip completely, breaking contact between tip and sample. The thermal bending of cantilevers is therefore seen to be an important problem for the practical application of the technique [217]. Unless very carefully layer design is used, the introduction of another material would increase the thermal stresses arising during the measurement. This is clear by

simply observing the difference in coefficient of thermal expansion: Polyimide $14.6 \cdot 10^{-6} \text{ }^\circ\text{C}^{-1}$, Si_3N_4 $3.3 \cdot 10^{-6} \text{ }^\circ\text{C}^{-1}$, Gold $5 \cdot 10^{-6} \text{ }^\circ\text{C}^{-1}$, SiO_2 $5.8 \cdot 10^{-6} \text{ }^\circ\text{C}^{-1}$. This phenomenon is due to the intrinsic thermomechanical behaviour of the cantilever, which is composed in most cases of silicon nitride, and the electrical connections to the sensor made of gold [80]. It is worth noting that when operating at low temperature (less than $47 \text{ }^\circ\text{C}$) accurate calibration procedures of the spring constant against the temperature can solve this issue [218].

3.2 THERMO-ELECTROCHEMISTRY

The challenges of maintaining an electrically active heater in contact with an aqueous solution, whilst controlling/suppressing electrochemical reactions have previously been considered by the electrochemical community. Their approach was to employ an electrolysis cell connected to a potentiostat as shown in Figure 33. The potentiostat is an instrument invented by Hickling in 1942 to measure the difference in electrical potential between the working and reference electrodes [219].

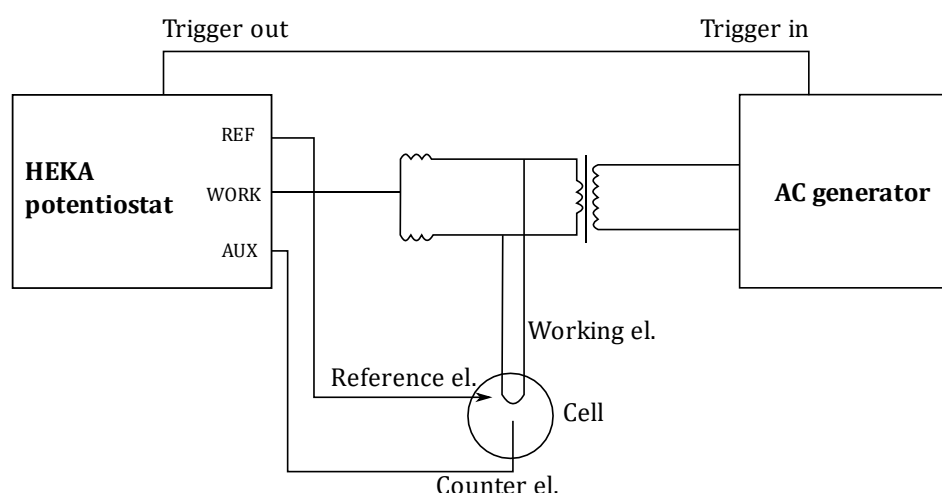


Figure 33 Wiring diagram showing connections between potentiostat, electrolysis cell and 100 kHz AC heating unit. The working electrode was a $25 \mu\text{m}$ platinum wire of ca. 24 mm in length [106].

In this configuration, Joule heating of the working electrode is controlled by the AC generator, coupled through an isolating transformer, whilst electrochemical reactions are independently controlled using the directly connected potentiostat. Using this approach to achieve the localized heating of the electrode leads to a significant number of advantages; the electrode surface temperature can be quickly varied allowing for the sudden change of the experimental conditions. This permits a controllable change in the chemical reaction rate, providing information on kinetic and thermodynamic properties [220]. Heating can also

regenerate the electrode surface (e.g. removing surface contamination) and it is useful to conduct experiments at several temperatures to selectively discriminate substances in electroactive mixtures [221]. Normally noble metals such as platinum or gold are used as thin heated wire electrodes (25 μm in diameter) due to their superior electrochemical and thermal behavior. For example, Platinum is commonly employed in electrochemical oxidation, for detecting the presence of oxygen and of various organic analytes such as methanol or glucose [220].

3.3 SThM SET-UP EMPLOYED IN THIS WORK

Inspired by this electrochemical approach, an a-SThM system capable of measuring temperature and generating localised heating on the nano-scale under aqueous solutions whilst still employing commercially available SThM probes was constructed. The instrumentation was inspired both by the electrochemical systems above and by a system previously employed by the AFM group of The University of Glasgow to enable SThM scanning of active electrical components in the air, without a direct current path forming between the probe and sample [72].

In the configuration employed, the SThM probe was connected in one leg of a Wheatstone bridge biased by a high frequency (2.5MHz) through a small RF transformer (Figure 23). The self-heating of the probe was obtained by measuring the change in signal at the (single) input frequency of 2.5MHz. The 2.5MHz and 5MHz signals have been generated by heating at DC and the slow response of the probe smoothed away the 5MHz signal. The DC change in temperature unbalanced the bridge, causing a change of the resistance of the probe and leading to a large signal at the fundamental 2.5MHz. By increasing the power at 2.5MHz, the temperature of the probe changed giving a measurable change in probe temperature. This results in a change of resistance of the palladium tip, due to its relatively high Thermal Coefficient of Resistance (TCR), leading to a change in the output of the bridge. This output was detected by a lock-in amplifier through another transformer and then compared to a reference signal.

The DC output voltage from the lock-in amplifier was then fed into the AFM control unit via a signal access module, allowing thermal signals to be recorded simultaneously with topographic images using the normal AFM control software.

To quantify the output signal, the initial electrical resistance of the probe (R_p) was obtained *in situ* by balancing the bridge.

The bridge, transformers and connectors were all soldered to the same PCB, directly connected to a sub-PCB onto which the probe was mounted. These two PCBs were positioned as close as possible to one another to minimise capacitance on the probe side of the bridge, decreasing sensitivity to any transient current flow. A basic schematic of the electronic system used for the a-SThM experiments is shown in Figure 34 whilst the full circuit, and the code required to operate the entire electronic apparatus can be found in Appendix B.

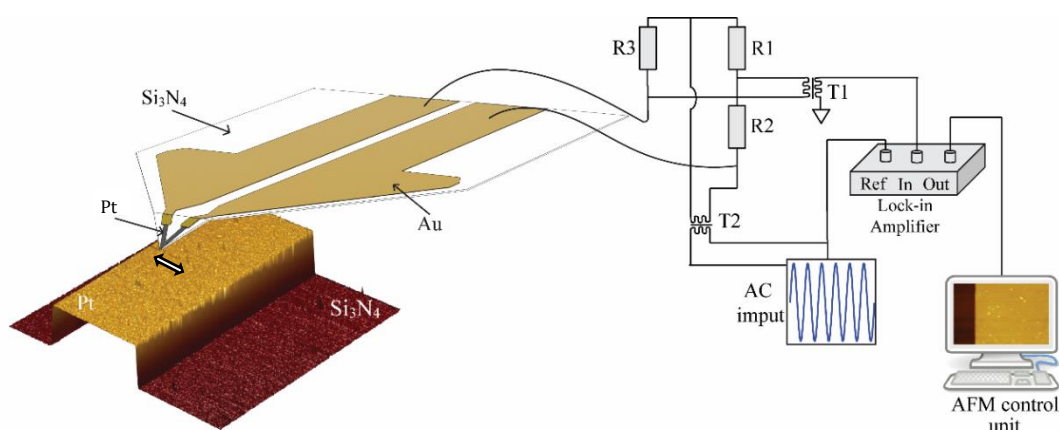


Figure 34 Schematic illustrating the experimental setup of an active mode SThM probe scanning a sample of two different thermal conductivities (Pt and Si₃N₄). The probe forms a Wheatstone bridge with R1, R2 and R3. T1 and T2 are transformers used for exciting and measuring the output of the bridge.

It worth noting that the three resistances (R1, R2 and R3) are set and chosen so that the Wheatstone bridge is balanced considering the known resistance of the probe.

Figure 35 shows a photograph of the holder (a) and the electronic instrumentation (b) integrated into the commercial AFM (Multimode Nanoscope IIIa) that was adapted for aqueous environment measurements.

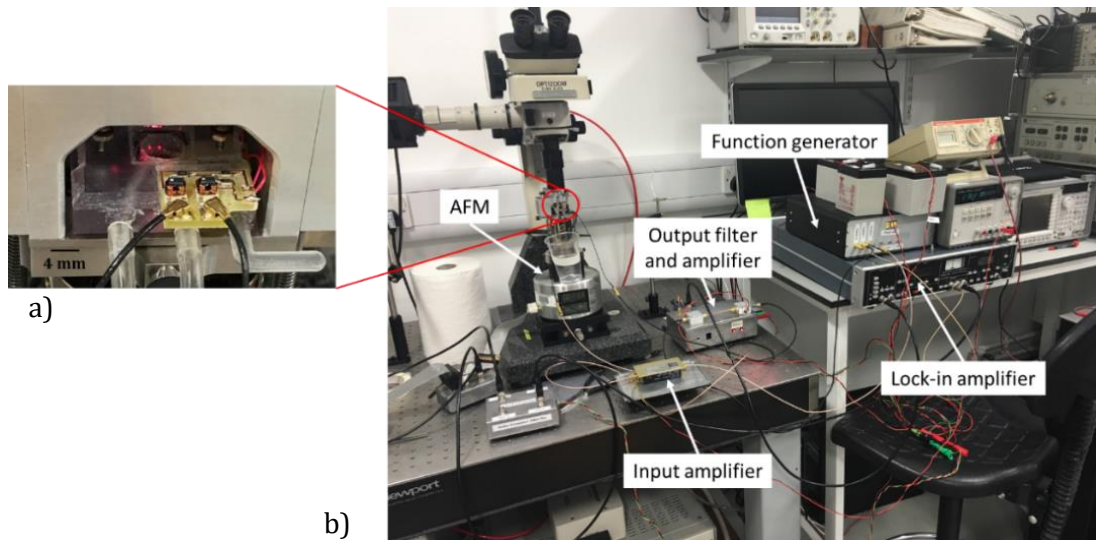


Figure 35 Photograph of the holder (a) and the electronic instrumentation (b) integrated into commercial Multimode Nanoscope IIIa AFM.

3.4 NEW HOLDER DESIGN AND REALISATION

To conduct aqueous-SThM (a-SThM) scans, the AFM probe holder needed to be modified alongside the electronic system. Although the approach is compatible with any liquid-capable AFM, the system employed was a commercial Multimode Nanoscope IIIa AFM (Bruker). The new instrumentation required two independent electrical connections to the probe, allowing the current path required to drive and measure the SThM probe [55]. A fluid cell with these specifications was not available commercially so a new holder, based around a conventional Multimode fluid cell [222] was designed and manufactured using SolidWorks, solid modelling computer-aided design (CAD) software, and 3D Printing (Stratasys Objet30 Prime [223] employing VEROCLEAR RGD810 [224]). Figure 36 shows the Multimode Nanoscope IIIa AFM head indicating the important aspects around which the new holder was designed.

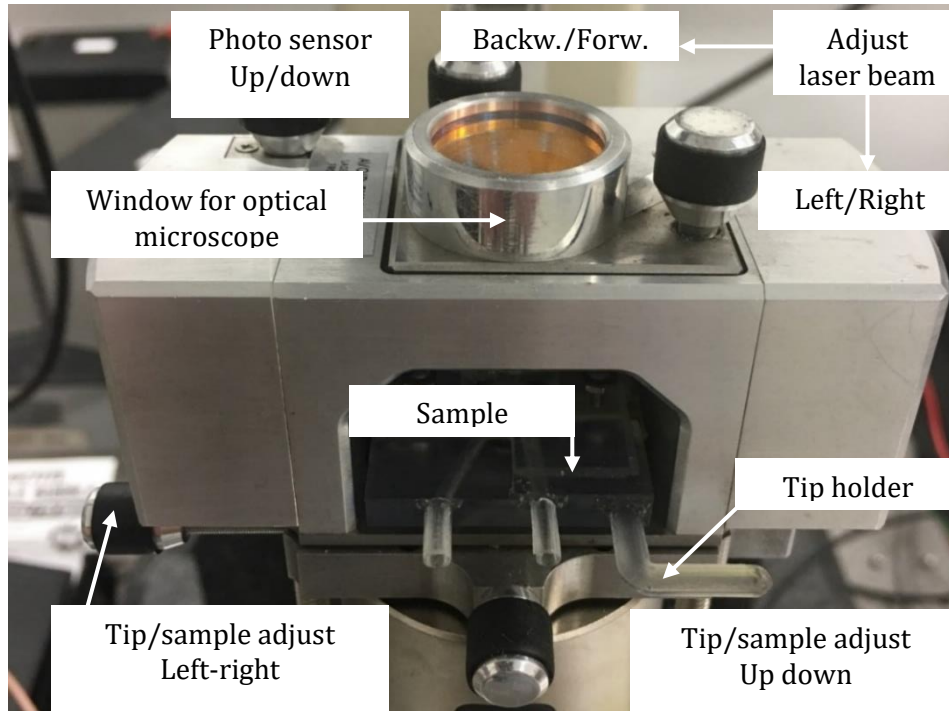


Figure 36 Multimode Nanoscope IIIa AFM head (with newly developed SThM stage).

Beyond the two electrical connections described above, the key requirements of the holder were to permit injection of water onto the probe/sample whilst avoiding leaks or evaporation and still maintaining enough space for the PCB, probe and sample. These were achieved using the same approaches as the commercial fluid cell, with one exception; electrical connection to the probe was made using a small PCB that was fed through the holder at an angle of 8° , and sealed, with the SThM probe attached once this was in place. To avoid leaks, the concept was to employ a rubber O-ring of 8.1 mm of diameter and vacuum grease between the holder and sample whilst an internal cavity accommodated the PCB/probe assembly and sample. An external cut-out housed the Wheatstone bridge PCB near the probe. Finally, two tubes with an external diameter of 3 mm (0.8 mm wall thickness) were designed to inject liquid into the cell whilst allowing air to exit (Figure 37).

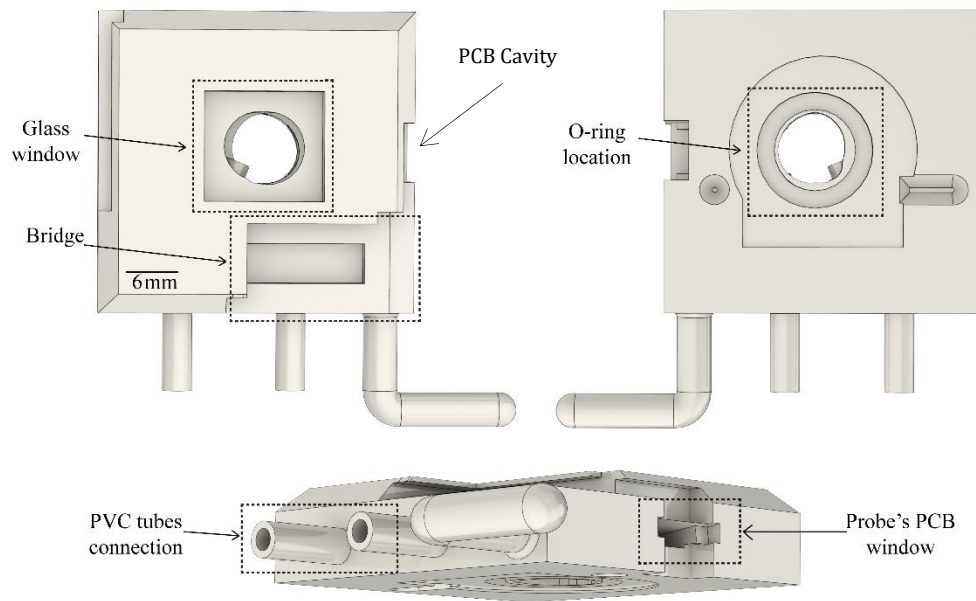


Figure 37 Probe's holder for AFM scanning in liquid designed with SolidWorks.

Furthermore, as the fluid cell was produced from a polymer with non-ideal optical properties, a top window, made from a thin piece of glass (0.4 mm thick) adhered to the holder with epoxy resin, enabled optical access to the probe. This was essential for optical microscopy and cantilever deflection measurements under the liquid. Figure 38 (a and b) shows an assembly of the complete liquid cell, complete with the commercially available SThM probe [225] attached to the probe PCB using epoxy resin adhesive [226] and electrically connected with silver conductive paint [227].

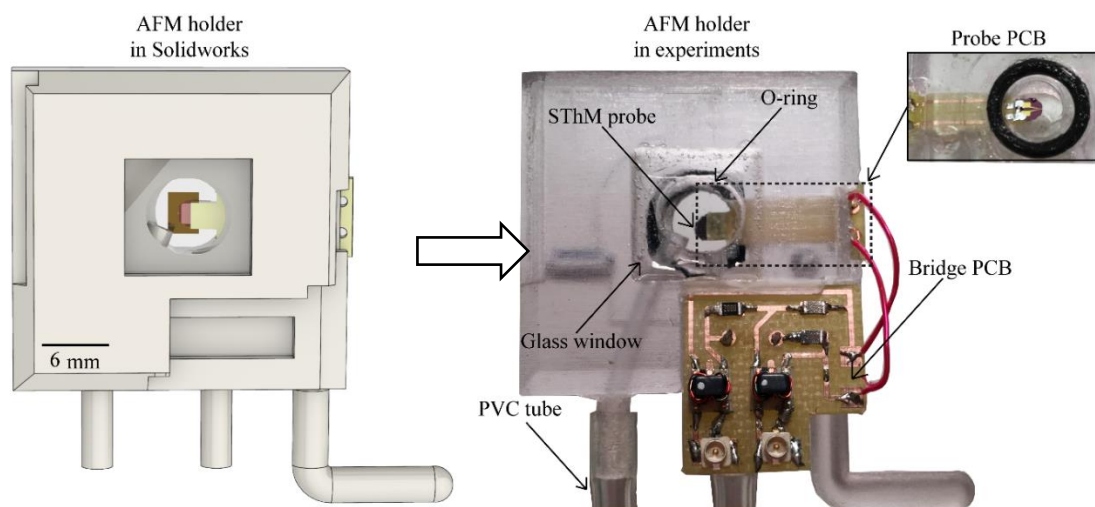


Figure 38 CAD assembly of the complete AFM liquid cell with designed o-ring, glass window, commercial probe, probe PCB and the stage with the sample (a). Assembled 3D printed holder including PVC tubes to inject the liquid inside the cell. SThM probe is electrically connected to the probe PCB inserted in an internal cavity with an angle of 8° , and connected by two small wires to the Wheatstone bridge PCB (b).

Figure 39 shows the detailed design and dimensions (in mm) of the liquid holder used for SThM in aqueous environments.

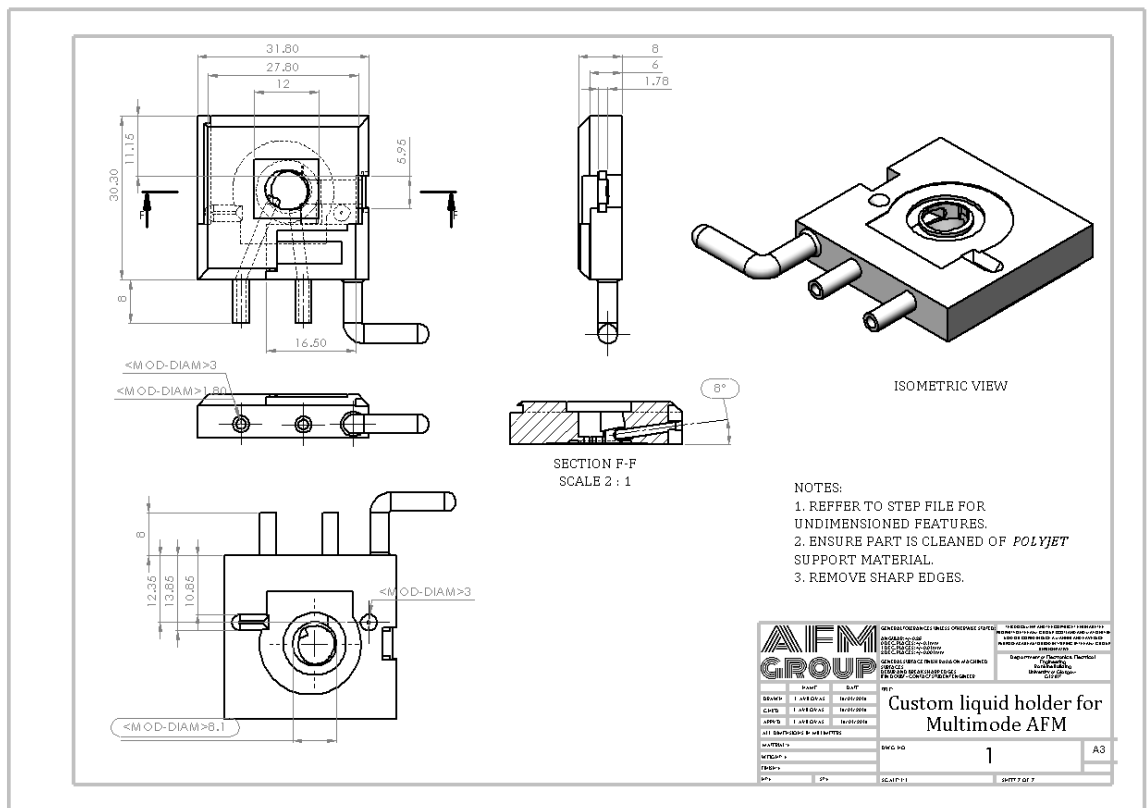


Figure 39 Drawings of the newly designed SThM probe holder for Multimode AFM.

3.5 NUMERICAL MODELLING OF THE SThM PROBE

As already stated in Section 2.2, probe design has come on a long way since the early development of SThM and now probes are often micro-fabricated from Si [73], [228], SiO₂ or Si₃N₄ [67], and produced in batches. They can have varying spring constants and resonant frequencies, like standard AFM cantilevers. The Si₃N₄ thermal probe, microfabricated in the University of Glasgow, was the one chosen for all experiments of this thesis [72].

In the literature, there are two main approaches to simulate an SThM probe, analytical or numerical, and the main difference between these two approaches is the number of degrees of freedom available. In the analytical models a single dimension is adopted and the entire system, including the working environment, is described by a series of resistances forming a thermal resistance network [54]. This approach enables to calculate the temperature of the probe, but not the volume that the probe is measuring/heating.

When using finite element (numerical) models a full 3D [229] or 2D axisymmetric [230] geometry can be used. Having said this, a 3D model is often adopted, despite its high computational cost, due to the complexity of the probe assembly. This type of approach is preferred when the thermal effects of the surrounding media, sample and probe need to be spatially resolved or described with greater accuracy. In addition, many commercial finite element tools offer ‘multi-physics’ to be implemented, permitting several researchers to model SThM probe heat generation by directly simulating the electrical conduction (and hence Joule heating) across the heating element. For example, Tovee *et al.* [229] describe how Ohm’s law can be used to describe electrical transport within the heating element.

In order to predict the temperature field within the model the heat transfer problem needs to be solved accounting for all the heat fluxes and the associated thermal gradients. In most of the commercial finite element software available, the heat transfer process across materials is described by the diffusive heat transport:

$$\rho C_p \frac{\partial T}{\partial t} - \nabla(k\nabla T) = Q \quad (15)$$

where ρ is the density of the material, the CP is the heat capacity, k the thermal conductivity and Q the heat source.

Most of the difficulties associated with simulating SThM heat transfer occurs when describing the very end of the tip and the probe-sample interface, especially for high thermal conductivity samples. Heat transfer can be described through the transport to two different particles: phonons and electrons. Phonons are recognised to play a predominant role in heat conduction for semiconductors and insulators. Conversely, electrons are dominant for metals [231]. However, a single heat transfer process cannot be considered to be unique across all length-scales of an object due to the nature of heat conduction that consists of the interaction between the particles mentioned above. Three typical scenarios are depicted in Figure 40, showing the (a) diffusive, (b) ballistic and (c) diffusive - ballistic heat transport.

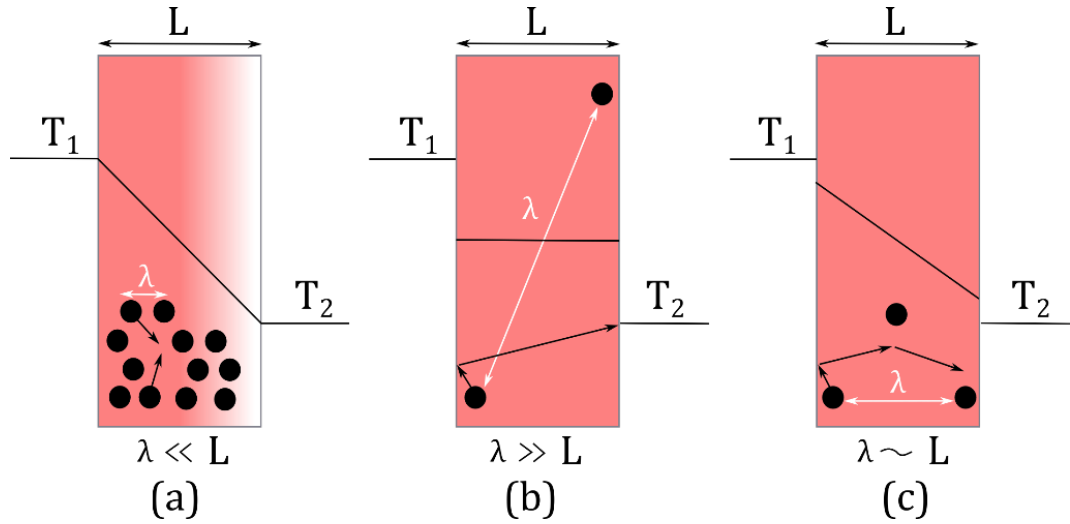


Figure 40 Thermal propagation mechanisms for a varying mean free path of the heat carriers and the characterization length of the material. (a), (b) and (c) represents diffusive, ballistic and diffusive-ballistic thermal transport respectively (reproduced by [1]).

As can be seen in Figure 40(a) a diffusive mechanism, which is typical of macroscopic thermal heat transport, is characterised by a Mean Free Path (MFP), λ , smaller than the characteristic length of the object. The MFP can be described as the mean distance travelled by a particle in motion between subsequent collisions, that cause a change in its moving direction, energy or other physical property [232]. The ratio between MFP and L is known as the Knudsen number (K_n), which, in SThM, is the ratio between the MFP for acoustic phonons and the nanoscale contact dimension L [233]. K_n is a dimensionless number widely used in science and engineering to quantify the compatibility of scale lengths in a problem. When K_n for heat transfer is much smaller than 1, the diffusive mechanism is dominant [234], classical Fourier's law can be used and the heat flux is associated with a thermal gradient across the macroscopic length L. When K_n is larger than 1, the heat carriers will scatter only at the boundaries of the domain (Figure 40, b). In this case, Fourier's law is not in accordance with the physics of the system, and the heat flux (q) is associated with a ballistic mechanism can be described by: $q = \sigma(T_2^4 - T_1^4)$, where σ is the Boltzmann constant, T_2 and T_1 are the temperatures at two point of the system. The existence a temperature gradient is the condition to generate an heat flux. The diffusive to ballistic thermal conductivity coefficient can be expressed as:

$$k_{db} = \frac{k}{2(\pi K_n)^2} [\sqrt{1 + (2\pi K_n)^2} - 1]. \quad (16)$$

From the previous equation, if K_n is much lower than unity, this mathematically implies that heat conductivity during the transition from diffusive to ballistic

(k_{ab}) is equal to the material thermal conductivity (k). Conversely, if K_n is higher than one, ballistic transport with a transition coefficient of conductivity of $k_{ab} = k(\pi K_n)$ can be used [234]. However, a distinct mechanism is difficult to observe in nature. For this reason, a third case must be considered (Figure 40, c), where both diffusive and ballistic transport exist and the ratio between MFP and L is nearly 1. In the model considered in this research work the characteristic length is always larger than the mean free path and the conduction of heat between tip/environment/sample occurs always in presence of thermal gradient. This allows the use of conventional heat transfer equations, readily available in any finite element software. The characteristic length L of the probe used is 50 nm, corresponding to the radius of the tip and it is made by a 40 nm thick Platinum layer. The MFP for Platinum thin film has been experimental and numerically calculated by Fisher et al. [235]. For a 3 nm thin film of Platinum the MFP is around 10 nm, which is five times smaller than the characteristic length L. In addition, the overall dimensions of the probe are several orders above the MFP of the material.

Regarding the heat generated by the resistive heater, two distinct modelling approaches have been employed in the literature. The first one directly calculates the heat flux generated by the Joule's effect, [229, 236]. This approach has the benefit of being more predictive rather than representative since it calculates heat generation for a certain geometry, material and applied current. However, the main difficulty of employing this method is the accurate measurement of the electrical conductivity of the thin-film materials at the apex of the SThM probe.

In the second case, the heat flux is directly imposed in the area of the heater [230]. This approximation is generally valid if the tip is homogenous and does not contain slots or abrupt changes in cross-section resulting in very localised generation of the heat flux. This means that the heat flux will be applied homogeneously without considering any changes in heater geometry, which is not optimal given the complex design of some SThM probe tips.

One final aspect that greatly affects the simulation results is modelling of the environment. Generally, the numerical models described in the literature are largely associated with perfect vacuum or air environments [230, 236, 237]. Conversely, only a few works consider a liquid (non-electrically conductive) environment [94], and no one has considered a liquid (electrically conductive)

environment. However, one common aspect of all models is the fact that only the working environment directly surrounding probe cantilever is considered.

3.6 A REALISTIC a-SThM PROBE MODEL

The Glasgow Si_3N_4 thermal probe has not previously been employed fully submerged in an aqueous environment. As a result, it is essential to create a realistic model of heat transfer between this probe, environment and a surface (sample) to help interpret experimental results. It also offers the possibility of evaluating new probe designs for improved aqueous performance, without requiring the expensive and time-consuming task of fabricating all possible designs. To generate the model an accurate 3D representation of the probe was created using probes dimension taken from lithographic patterns that were then input into SolidWorks CAD software (Figure 41).

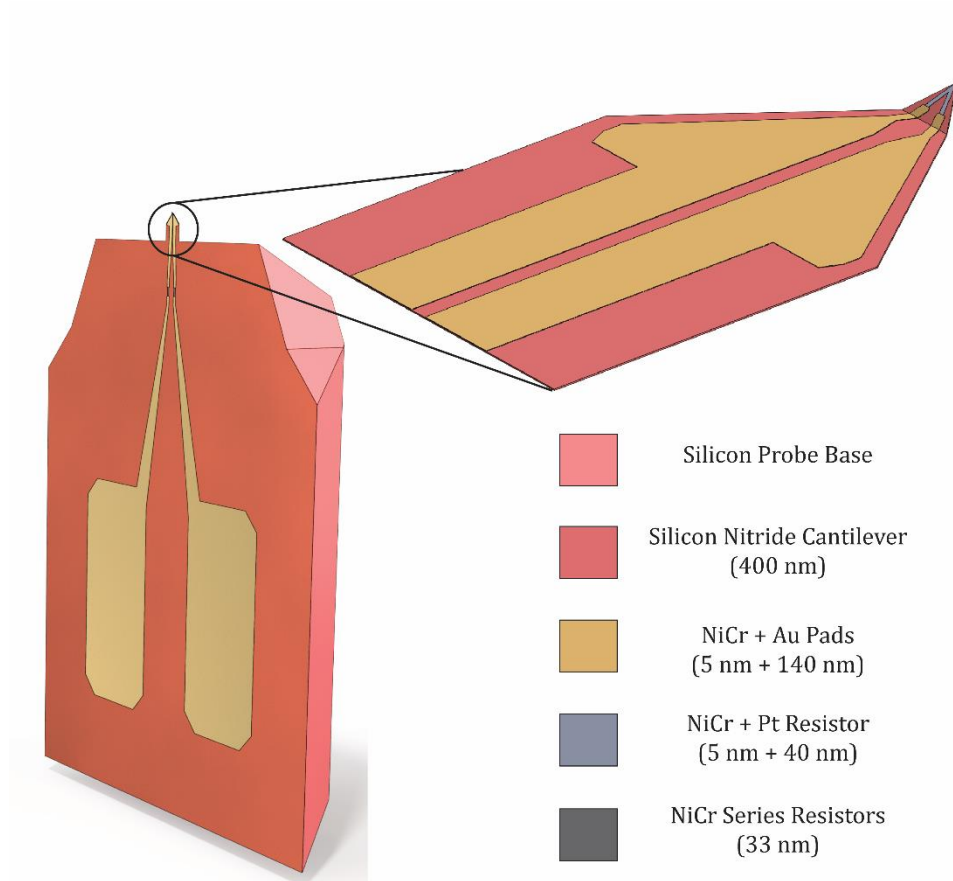


Figure 41 CAD of the KNT thermal probe with the material used.

These probes are identical to commercially available devices that are currently produced by Kelvin Nanotechnology (KNT) [225]. Figure 41 shows the complete CAD model and a close-up of the cantilever section. Features of particular note include the significant size difference between the bulk silicon probe body (2500

μm width, $365 \mu\text{m}$ thick) and the cantilever ($120 \mu\text{m}$ width, $0.4 \mu\text{m}$ thick), as well as the tip with a radius of approximately 50 nm . The two gold pads are clearly visible on the probe body and are used to connect the external circuitry, delivering current to the tip where a thin higher resistance platinum film generates the heat. The commercial SThM probes used in this work include an additional 100Ω series resistance on the body of the probe to protect the tip resistor from damage by Electrostatic Discharge (ESD). Therefore, these limiting resistors have been included in the model (Figure 42, detail C) and the simulations take account of them both thermally and electrically.

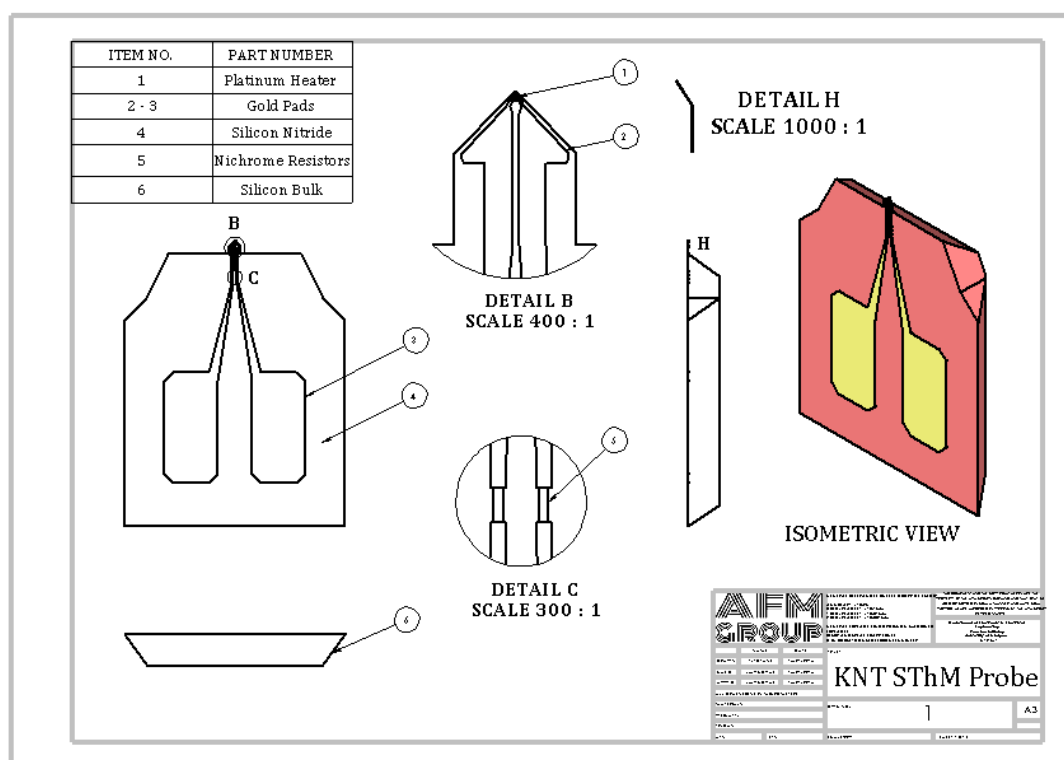


Figure 42 2D drawing of KNT thermal probe.

3.7 MODELLING STRATEGY

Using the geometric model described above, the performance of the probe was then studied using finite element analysis (FEA), a fundamental tool for this thesis. The software used throughout was COMSOL MULTIPHYSICS 5.2 with the “Joule Heating” module, which was employed to simulate the SThM probe in and out of contact with the sample. This approach was used as it most closely resembles the actual experiments, combining both electrical heating and heat transfer in a single simulation. This approach results in a geometrically accurate model, incorporating all material properties and considering Joule heating, together with the different thermal contact conductance coefficients (h) for solid-

solid[238] (tip-sample) and solid-environment interfaces [239], [240] (tip-environment and sample-environment) for both air and water.

Initially, simulations were conducted for two geometries i) the entire probe and ii) only the cantilever region as shown in Figure 43, a and b. In this numerical test, the entire probe was modelled surrounded by an air-based environment as this represents the scenario most commonly employed in Glasgow prior to this work. By comparing the preliminary numerical tests shown in Figure 43, a and b, it can be seen that the changes in temperature were only observed to occur along the cantilever. In addition, the difference in temperature between the two models is so small as to be considered negligible. Therefore, the probe body was eliminated from future simulations and the base of the cantilever held at ambient temperature to reduce the computational cost.

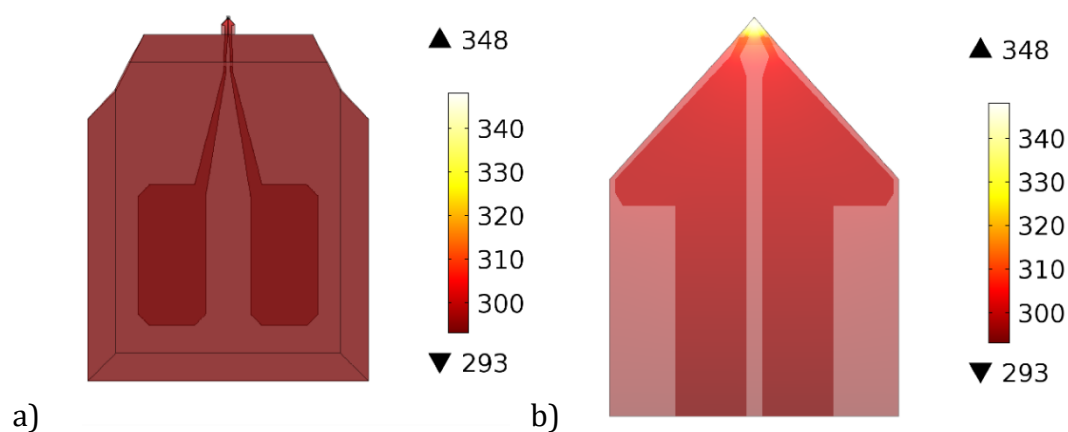


Figure 43 Finite element solution of the temperature field [K] for the entire probe a), and for the cantilever b).

Simulations were carried out using 3D geometry models; a rectangular block, enclosing the cantilever and the sample, was used to simulate the surrounding environment present during the experiments. The materials assigned to the different sections of the cantilever are depicted in Figure 44a. The boundary conditions used to best represent the experimental conditions and system, as shown in Figure 35, were:

	Air	Water
Current applied to one gold pad of the probe	$I = 0.0017 \text{ A}$	$I = 0.0045 \text{ A}$
Temperature of the edges	$T_0 = 293.15 \text{ K}$	$T_0 = 293.15 \text{ K}$
Heat transfer coefficient solid/environment interface	$h = 10^5 \text{ W(m}^{-2}\text{K}^{-1})$	$h = 10^8 \text{ W(m}^{-2}\text{K}^{-1})$
Heat transfer coefficient solid/solid interface	$h = 10^7 - 10^{10} \text{ W(m}^{-2}\text{K}^{-1})$	$h = 10^7 - 10^{10} \text{ W(m}^{-2}\text{K}^{-1})$

Table 1 Boundary conditions used in the FE model for different environments.

The initial temperature boundary conditions of all the subdomains were set to represent a room temperature of 293 K. All the outer boundaries of the air block, sample block and cantilever end were fixed at 293 K, whereas all the inner boundaries were presumed to have temperature continuity. The choice of this outer boundary temperature was taken by considering the ambient temperature present during the experiments, which were conducted in a laboratory with air condition fixed at 293 K. A constant electrical current was applied to one of the gold pads while the other was set to ground, all outer geometrical boundaries were set as electrically insulating. The electrical current of 1.7 mA for air and 4.5 mA for water were applied to the SThM probe as these were observed from the calibration experiments (Section 4.3) to be safe yet high enough to heat the probe $\sim 65^\circ\text{C}$ above T_{amb} . A schematic of the electrical boundary conditions is shown in Figure 44b.

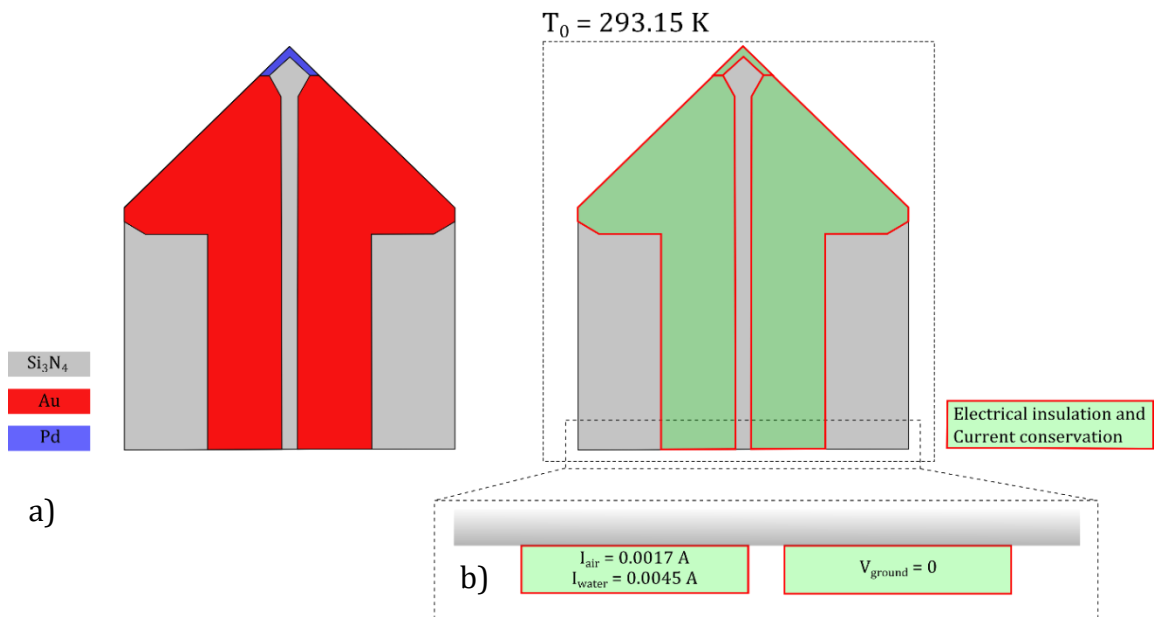


Figure 44 Schematic representation of the SThM probe with (a) the associated materials and (b) the applied boundary conditions.

The values chosen for the heat transfer between solid/environment are based on the literature available [239, 240]. In their research the authors investigated the interfacial heat transport of Au film on a silica substrate, immersed in a solution of water and ethanol. The key points within this work is the importance of the coating film on Au. They demonstrated that the interfacial thermal conductance decreases of nearly 50% when a hydrophobic coating is applied. In this work, due to the design of the KNT probe and the type of sample analysed, no hydrophobic coating is present and a representative value of $100 \text{ MW(m}^{-2}\text{K}^{-1})$ in water, and $0.1 \text{ MW(m}^{-2}\text{K}^{-1})$ [240] in air is considered.

When considering the solid/solid heat transfer a range of values is adopted. This range has been suggested by the literature [241], and also by the difficulty of estimating the accurate coefficient for each material involved. Among the technical difficulty in measuring such quantity for each material system involved, there is also the effect of temperature as demonstrated by Gundrum et al. [241]. In their work the authors for the first time gave a quantitative estimation of the interfacial heat conduction between two different solid materials. In addition, they demonstrated experimentally and with a simple extension of the Wiedemann-Franz law [242] how electrons contribute to the charge and heat transport. In addition, they estimated the contribution given by phonons, which is lower than 10%. For solid-solid the magnitude of the heat conduction coefficient is in the order of $\text{GW(m}^{-2}\text{K}^{-1})$, and due to the large variability, a range in line with several experimental results has been adopted within the numerical simulations.

According to Cahill *et al.* [243], below 50 nm length scale, heat transfer in some media is known to have ballistic characteristics. The dimensions of the system above are between 50 nm and 10's of μm and the mean-free-path (MFP) of heat carriers is generally of 10 nm - 25 nm. Accordingly, for the probes used in this work the Knudsen number (K_n) for heat transfer, discussed in Section 3.5, is $K_n \approx 0.2$. As defined previously this means that diffusive transport dominates over ballistic and the probes are well described by diffusive heat transfer. Hence, the COMSOL diffusive approximation can be applied and reasonable results can be obtained. This is the same approach as has been employed by other researchers [94]. This is possible because COMSOL finite element software is used to solve the

partial derivative equations based on the Fourier's law and conservation of energy, which states:

$$E_m^+ + q_m^{in} = E_m^- + \Delta E_m^{in} \quad (17)$$

where E_m^+ is the energy conducted from outside the medium, q_m^{in} is the heat generated within the medium, E_m^- is the energy conducted to outside the medium and ΔE_m^{in} is the change of internal energy within the medium.

Within this work, the sample and the probe were considered to operate in different environments (air, flutec pp3 and water), which were introduced as finite blocks of material large enough to incorporate the entire model. The block of air/liquid surrounding the probe was designed to be sub-millimetre in size. When considering air, attention was given to heat transfer in gases at the nanoscale, which is known to have a ballistic characteristic at distances below 50 nm. Since only a very small number of the smallest dimensions in this model are in the order of 50 nm or larger, it was not felt to be essential to take these effects into account. This aspect is relevant when considering the impact of convection on the thermal transport. It is well known that convection is associated not only with the heat exchange between a solid and gas but also to the buoyancy force and viscosity of the gas that regulates the process. In addition, the film coefficient that regulates the heat transfer by convection increases with the pressure but is very low at ambient pressure. Due to the dimensions of the sample and the working pressure considered, the convection can be neglected [244]. This can be demonstrated by calculating the Rayleigh number (Ra), which is a dimensionless number related to the ratio between the time scale for thermal transport via diffusion and via convection at a certain speed u . Depending on the magnitude of Ra it is possible to understand how big is the contribution of one of these two mechanisms. This constant can be calculated using the following equation:

$$R_a = \frac{\Delta\rho g L^3}{D \mu} \quad (18)$$

here $\Delta\rho$ is the difference between the material associated to the surface and the air, g is the acceleration of gravity, L is the characteristic length of the system, D is the thermal diffusivity and μ is the dynamic viscosity of the fluid. By considering an approximated Platinum plate, with a length of 50 nm in contact with air the associated $R_a = 7.5 \cdot 10^{-14}$. This means that any mechanism associated with convection at this scale is too slow to have any influence.

In contrast to other environments, the heat flux generated by the probe is easily transported through the liquid environment, due to its relatively high thermal conductivity. The effect of different environments including water and dodecane was studied numerically by Tovee et al [229]. In this work, the authors also discussed the temperature profile generated in vacuum and air, concluding that the main effect of an environment is to provide additional paths for the heat generated by the probe. The presence of water and dodecane cause much less localised heating of the tip, thanks to the enhanced thermal coupling. In this way, the sample is not significantly heated, with very little heat flux into it.

When considering a liquid environment, it has been discovered that the design of the probe plays a significant role in the thermal resolution [94]. In addition, it has been confirmed that the heat flux between the probe and the sample that defines the nanoscale spatial resolution of iSthM is predominantly conducted through liquid rather solid-solid contact. In this work the liquid environment surrounding the probe and sample has dimensions of several hundred microns. These are significantly larger than the sub-micron tip dimensions (50-70 nm). Consequently, the volume of water and its effect on the heat transfer process is considered, and a perfect contact between probe, liquid environment and sample is considered.

3.8 MATERIAL PROPERTIES

Great attention was paid to the material properties employed in the model, in particular estimating the thermal conductivities of the thin films constituting the probe as their properties can differ significantly from bulk materials [245]. This phenomenon has been explained by Goodson and Flik [246, 247] and is caused by the difference in the phonons wavelength and microstructural defect sizes like surfaces, point defects, dislocations, and impurities. The increase in the number of defects and the decrease in dimensions leads to a significant reduction of the mean free path of the heat carriers (phonons and electrons). This results in a lower conductivity (both thermal and electrical) in thin films with respect to the bulk material.

To obtain the thin film values for electrically conducting materials, test samples were produced using the same materials and thickness as SThM probe components. These test structures were then electrically characterised by means of a probe station using the 4-terminal measurements (Figure 45, a). From

a practical point of view, 4-terminal measurements employ two additional probes used for sensing voltage. To achieve this, two probes were positioned on pads A and B with a known current passing between them. The voltage was then measured using two probes on sequential combinations of pads 1, 2, 3 and 4 (Figure 45, b). This permitted resistance measurement to be made for various geometries of sample material without the influence of connecting pads and wires, permitting improved thermal and electrical conductivity calculations [248].

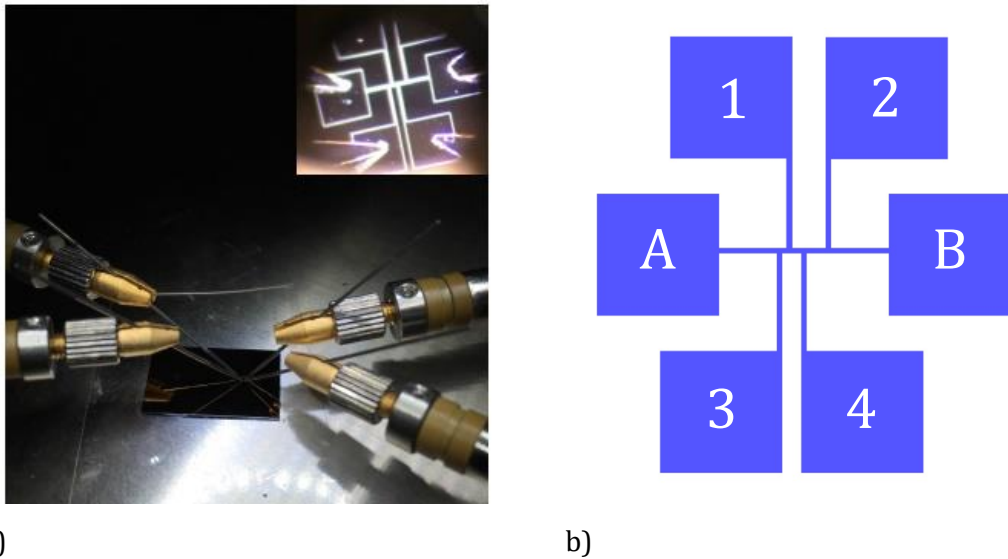


Figure 45 a) Four terminals probe station measurements, b) pattern for thin-film material thermal conductivity experiment.

The main output of the 4-point measurements was the thin film electrical resistance, which was then used to calculate the electrical resistivity. In the case of the metallic thin films, thermal conductivity was approximated by applying the Wiedemann-Franz law, which states that the contribution to the electrical and thermal conductivity of the electrons is linearly proportional to the temperature:

$$K = \sigma \cdot L \cdot T \quad (19)$$

where L is the Lorentz constant ($2.44 \cdot 10^{-8} \text{ W}\Omega\text{K}^{-2}$), T is the ambient temperature and σ is the electrical conductivity. It worth stressing that this approach was not suited to the Si_3N_4 SThM cantilever material. The experimental results obtained, based on the pattern shown in Figure 45b, are reported in Table 2.

Thin Film Material	Thermal Conductivity [W/mK]	Electrical Conductivity [S/m]
Au (140 nm thick)	153	$2.09 \cdot 10^7$
NiCr (5 nm thick)	2	$3.23 \cdot 10^5$
Pt (40 nm thick)	22	$8.9 \cdot 10^6$

Table 2 Estimated thermal and electrical conductivity for thin film materials used in an a-SThM probe.

The thermal conductivity of the Si_3N_4 was taken from the literature: 3 W/mK for films of the same thickness and composition [1], [249], [250]. The silicon wafer ($\sim 390 \mu\text{m}$ thick) was considered to be bulk silicon (130 W/mK) [1].

3.9 FINITE ELEMENT MESH STUDY

As is normal practice when first setting up a finite element model for a new geometry, a series of numerical tests were carried out to understand the impact of model mesh size on the final predicted temperature. For simple cases where only the probe was immersed in the environment the sequential increase of the mesh density on otherwise identical models (depicted in Figure 46) led to a convergent value. As expected, the increase in the number of elements, which correspond in a reduction in element size, improved the overall results at the compromise of computational cost. Figure 47 shows an example mesh of the entire system and a detail of the tip in contact with the surface. Using the terms employed by COMSOL, the mesh used was ‘normal’ for larger areas and ‘extremely fine’ for the smallest features, such as around the tip. The cantilever, whose dimensions and geometry are exactly those of the one used experimentally, was positioned with an angle of 8° from horizontal reflecting its true position during real measurements. When such a complex model needs to be discretised, the main challenge is to cope with different length scales present in the model. It is evident that using a very fine mesh would waste computational power since the remote areas of sample and environment do not require a dense mesh as temperature variation in those locations would be minimal. In this case, the most important feature was considered to be the mesh density around the tip. For this reason, a minimum element averaged size of 15 microns was adopted. The mesh is not constant, but it is made coarser in regions of no interest and extremely fine around the tip with a minimum size down to 2.5 nm. It worth noting that a coarser mesh (less than around 55,000 elements), not only led to a change in temperature but also affected the convergence of the solution. This was

due to the quality of problem discretisation, which is related to the length scale of the problem itself as described above. For this reason, the tip was modelled using a fine mesh, whilst the cantilever employed a coarser mesh, leading to a higher computational efficiency whilst maintaining the quality of the solution. This approach was employed in all COMSOL models of the system used in the rest of this thesis.

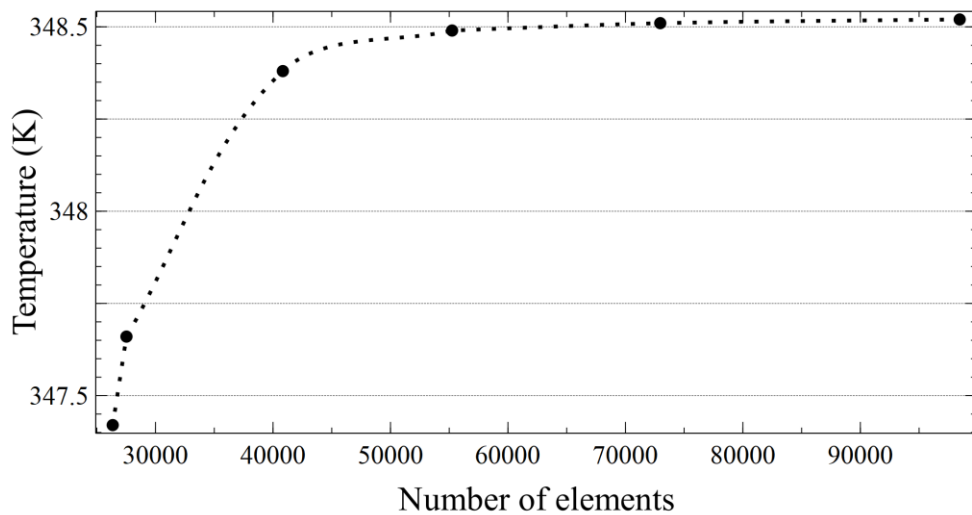


Figure 46 Maximum temperature against the number of elements within the model.

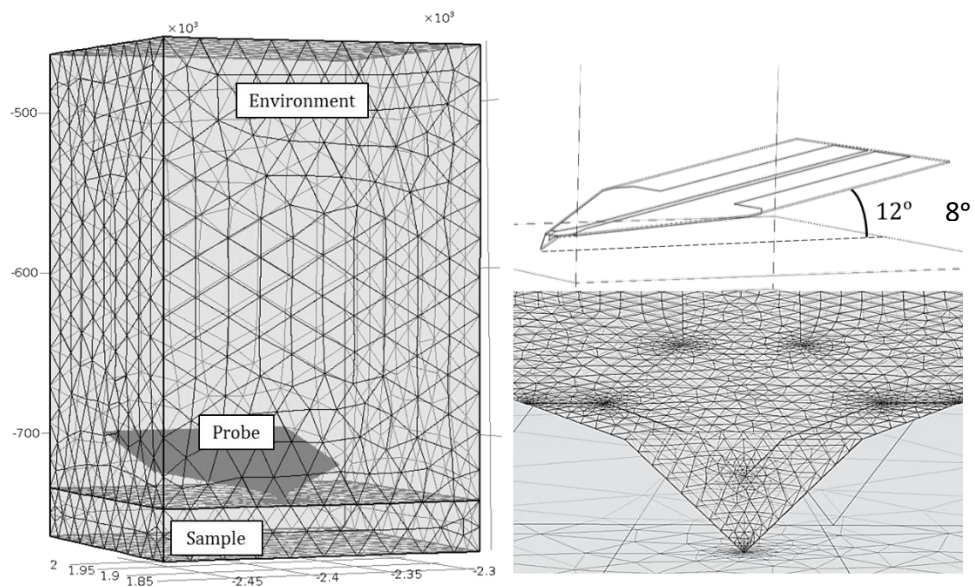


Figure 47 Model and mesh of the University of Glasgow probe.

3.10 CONCLUSIONS

Within this chapter, a detailed description of the technical approaches employed in the rest of this thesis, along with the motivation for their choice was presented.

Importantly, the following, fundamental observations that underlay the remaining chapters can be made:

- 1) It is proposed that electrochemistry is a crucial detrimental mechanism that limits the probe operating in conductive environments and the physical solution to this problem, (e.g. a protective probe coating) is not optimal.
- 2) The set-up for aqueous SThM will involve the implementation of new instrumentation inspired by the thermal-electrochemistry community as well as previous SThM work carried out at Glasgow.
- 3) Due to the specific use of KNT probe, it can be argued that the dominant mechanism involved in the thermal transfer is diffusive, allowing the use of commercial finite element code COMSOL.
- 4) The KNT probe, sample and surrounding environment can be effectively modelled even if the silicon probe body is excluded as long as an appropriately structured mesh is employed.

The knowledge listed above, together with the new instrumentation and holder developed during this work, as described in this chapter forms the basis for the remaining work of this thesis. Most importantly, their efficacy and ability to perform SThM on a large variety of solid and biological samples in aqueous environments will be explored in the subsequent chapters.

CHAPTER 4: SOLID SAMPLES → PT/SI₃N₄ & AU/SI₃N₄

4.1 INTRODUCTION

Within this chapter, initial underwater SThM measurements and the process of probe thermal calibration are presented. In this regard, the first objective was to validate the possibility of aqueous SThM and clearly demonstrate its performance in terms of thermal-spatial resolution in comparison to non-conductive liquid environments and air. These experimental results were then compared with the corresponding FEA analysis to gain further insight into the thermal behaviour of the probe in different environments. The second objective consisted of designing and modelling a new probe to improve and overcome the limitations identified when employing the current KNT design in water.

4.2 SAMPLE DESIGN AND PREPARATION

To demonstrate the detrimental effect of uncontrolled electrochemical reactions on SThM probes, a planar device was designed and fabricated with similar material characteristics (Pt/NiCr/Si₃N₄) and electrical properties to the SThM probes used in Glasgow. The reason for this approach was the fact that SThM probes are a limited resource that are delicate and expensive to produce. Therefore, it was desirable to carry out initial test-to-failure experiments using an equivalent but less valuable sample. These also offered a cheaper, more robust SThM probe surrogate for use in the initial stages of developing the new instrumentation.

The steps used to fabricate the planar Pt/Si₃N₄ sample [251] are listed below and shown in Figure 48:

- I. A quarter of a 3-inch double-side polished silicon wafer, with 50 nm coating of LPCVD silicon nitride (Si₃N₄), was cleaned using acetone for 5 minutes in an ultrasonic bath. After acetone cleaning was completed, the step was repeated using methanol (5 minutes) and then 2-propanol for other 5 minutes. The sample was then dried in a stream of N₂.
- II. Two layers of polymethyl methacrylate (PMMA), having different molecular weights (2010 8% PMMA and 2041 4% PMMA), were spun on top of the wafer (5000 rpm for 60 seconds) with each layer baked for 1 hour at 180 °C.

- III. EBL was used to write the pattern into the PMMA resist (dose 1000 $\mu\text{C}/\text{cm}^2$, beam current 1nA, VRU 2nm) after which the wafer was developed for 30 seconds using an IPA: MIBK 1:1 developer at 23 $^{\circ}\text{C}$, which selectively removed the exposed resist. After that, the sample was immersed in IPA to stop the development and then dried with nitrogen
- IV. After a low power (80 W) O_2 ash of 30 seconds, 5 nm of nichrome (NiCr) and a thin film of platinum (Pt), 50 nm thick, were evaporated on the sample
- V. Metal lift-off (described in appendix C) was realized by immersing the sample in warm acetone (50 $^{\circ}\text{C}$) for ca. 10 minutes. During the process, the liquid was agitated using a pipette to facilitate removal of the platinum. The sample was then washed with IPA and dried with nitrogen.

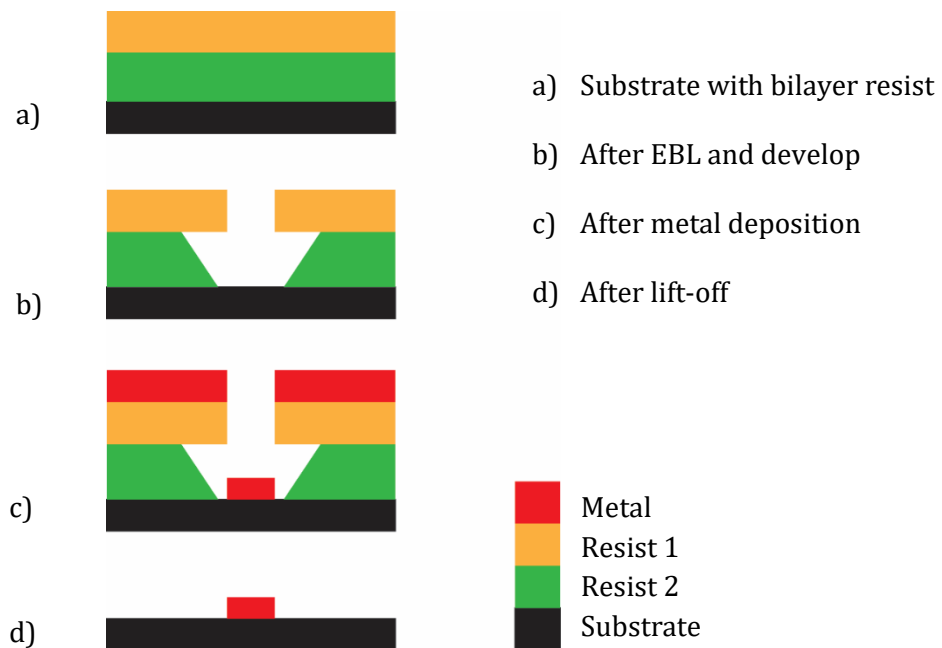


Figure 48 Pt/Si₃N₄ Device fabrication process.

PMMA used in step III is as a versatile polymeric material, able to act as a high-resolution positive resist for e-beam lithography. NiCr (step IV) is an ideal under-layer material, because it has relatively high electrical resistance, is thermally stable and forms an adherent layer of chromium oxide when it is heated for the first time [252]. The pattern was drawn using a CAD package (L-Edit); with consideration to fully exploit the available space on the sample and, at the same time, realize the maximum number of resistors, which were arranged in groups

of three individually addressable heaters close to each other (Figure 49). Another advantage for this layout is that it offers the ability to perform electrical measurement on one device while simultaneously heating another.

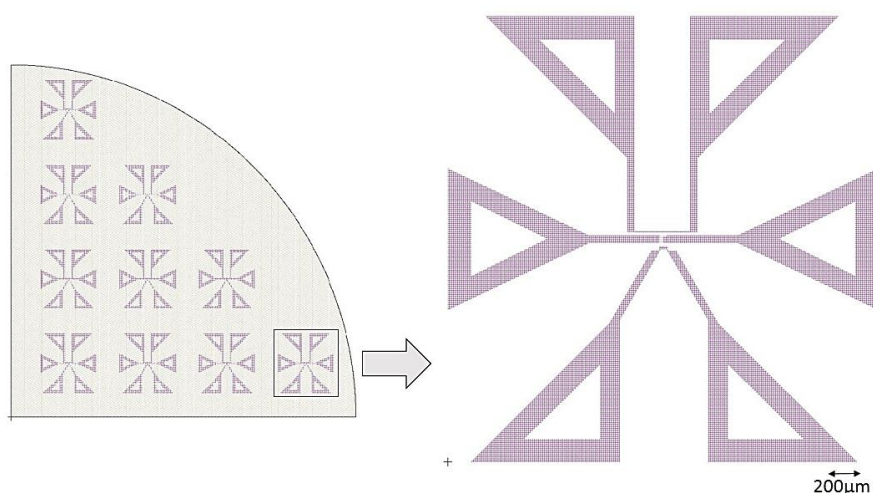


Figure 49 L-Edit pattern of the devices.

Since the SThM probes available within Glasgow have a resistance of about $300\ \Omega$, the lengths and the widths of the test devices were modified to achieve resistance values close to that of probes. With a view towards publicity material, one heater was modelled to form a word; this was chosen to be “CIAO”, meaning “HELLO” in Italian, shown in Appendix A. Figure 50 shows the completed quarter of wafer with thirty platinum devices in 10 groups (a) having a resistance of $299\ \Omega$ (top), $315\ \Omega$ (middle) and $325\ \Omega$ (bottom) respectively as shown in Figure 38 (b).

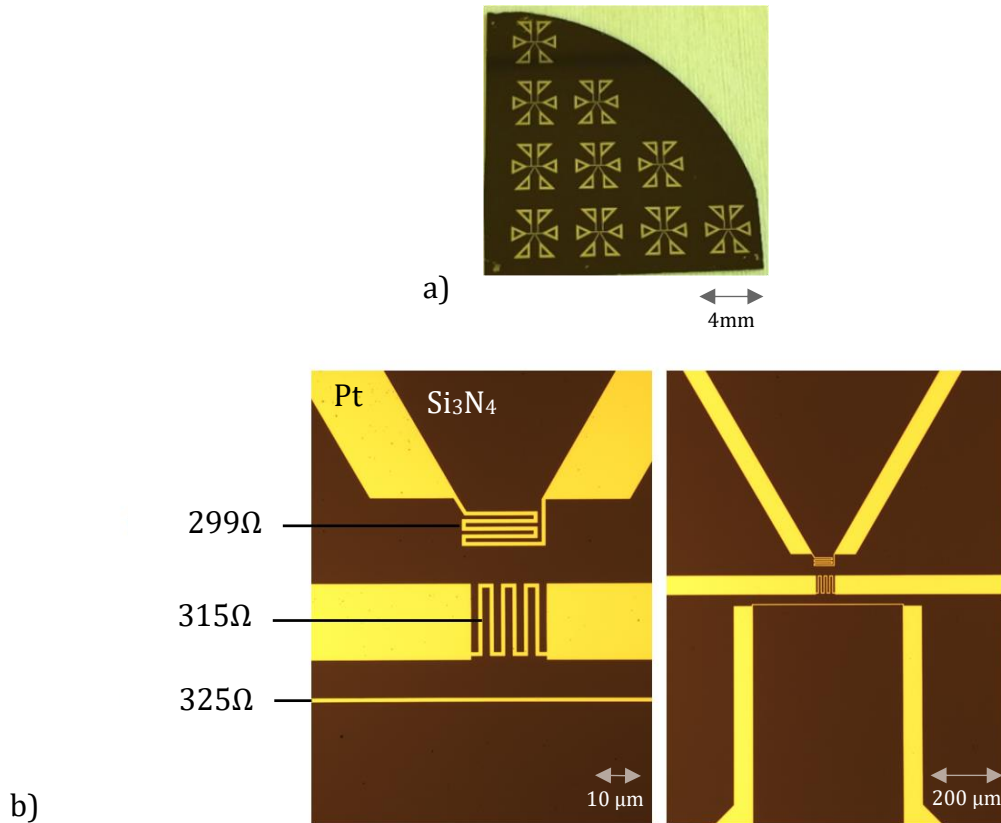


Figure 50 Quarter of silicon wafer with 30 platinum devices (a), and the optical microscope pictures of the three different heaters with their resistances after the metal lift-off (b).

The behaviour of this surrogate device was studied, focusing on its electrical performance with varying bias and at different temperatures. To approximate the performance of a thermal AFM probe the Pt resistor at the extreme end of the cantilever can be considered equivalent to a Pt heater connected to two pads through two wires (Figure 51). The width (hence cross-section) of the pads and the wires on both SThM probes and the surrogate sample are maximised to provide them with the smallest possible electrical resistance. Therefore, by applying a potential difference to the pads, Joule heating was primarily limited to the central, narrow heater. It should be noted that the Pt resistors of both probe and sample shared the same thickness (50 nm) with 5 nm of nichrome as a sticky layer.

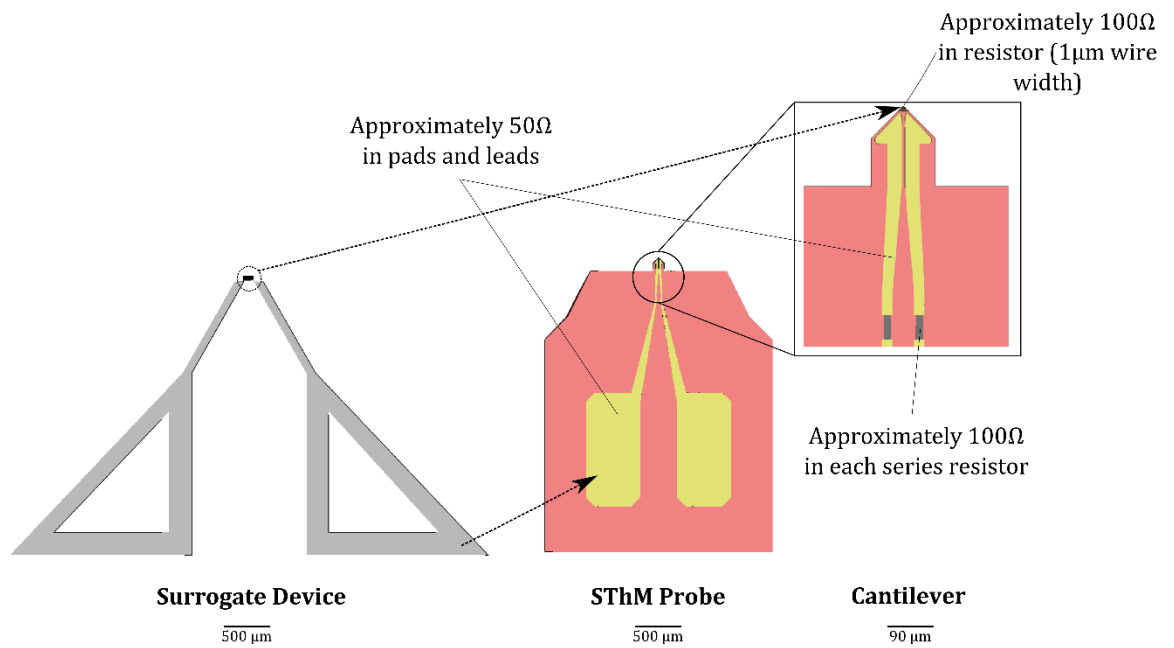


Figure 51 Surrogate heater device and KNT SThM probe.

One important characteristic of resistive SThM probes is their maximum sustainable current as this dictates the maximum temperature they can generate. To make an equivalent measurement on the surrogate samples, a probe station, working in 2-terminal mode, was used to measure the minimum current capable of destroying the resistors in various environments. To achieve this, an increasing potential difference was applied across the pads whilst simultaneously measuring the current passed.

These measurements were repeated on 10 devices to check reproducibility. In air and flutec pp3 (Perfluoro-1,3-dimethylcyclohexane [253]), the resistors were tested up to the limit of the probe station (18 V applied with 50 mA compliance) surviving without displaying irreversible changes in resistance or any damage. Flutec pp3 is a fully-fluorinated, odourless, colourless liquid, chosen because it is nontoxic with an operating temperature range from 70 °C to 102 °C, which is appropriate for the measurements. In addition, it has previously been successfully used to calibrate SThM probes [254], due to its very high electrical resistivity ($10^{15} \Omega\text{m}$) and low viscosity (1.92 mPa·s, just 0.01% of oils which are commonly used as an insulator), making mechanical damage of the probe as it breaks the liquid surface a negligible risk. Figure 52 (a, b) shows the current vs voltage (I-V) curves of all samples tested in air and flutec PP3. It also presents the average of the curves with the error bars based on the standard deviation for each set of measurements. The curves clearly deviate from a linear trend at high

voltages. This is caused by the resistors self-heating through the Joule effect. The non-linearity comes from the fact that the resistor's temperature increases proportionally with power (i.e. the square of voltage). However, the resistance of the platinum, over the operating temperature range, increases linearly with temperature (and hence the square of voltage). This is depicted in Figure 52 (c, d), where the resistance against the voltage as well as the average and error bars are plotted for every device.

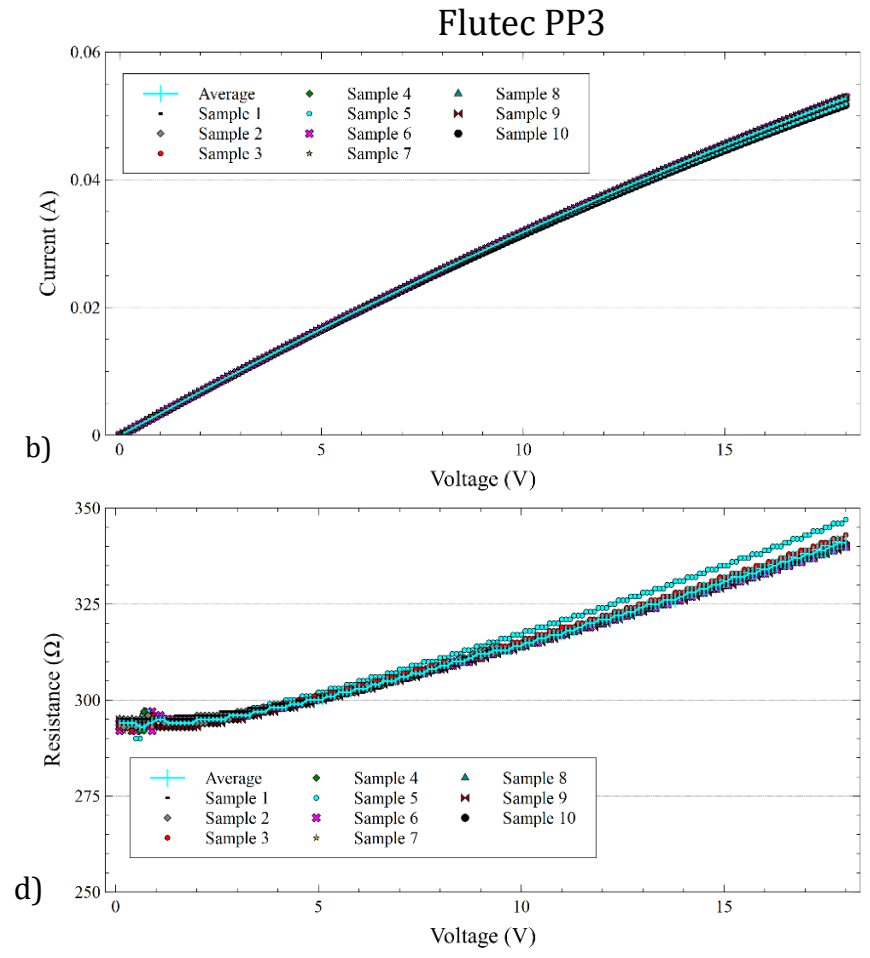
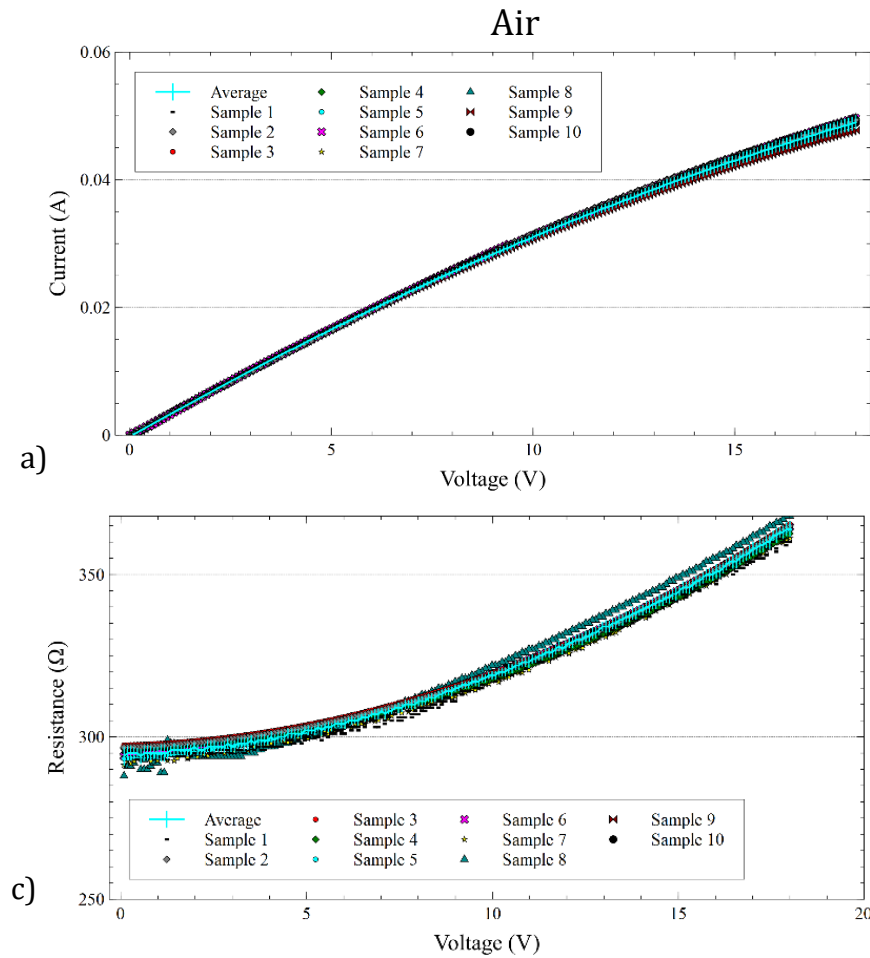


Figure 52 Electrical behaviour of the probe in air and flutec pp3. The curves a and b show the current against voltage for every device, as well as their average and error bars, without evidence of failure. C and d show the associated resistance against voltage.

These devices do significantly differ from SThM probes in that probes can tolerate much lower current ($< 3\text{mA}$) in the same environments [1]. The reason for this behavior is that the probe heater is located on a Si_3N_4 cantilever (essentially a thin membrane), effectively thermally isolating it. As a result, the tip/sample (i.e. heater/sample) thermal conductivity is low, resulting in a higher temperature for the same power applied. Another difference is the dimensions of the heaters on the surrogate sample, which are larger than those on probes, resulting in a lower current density for the same power dissipation. However, the devices do have the same material composition and exhibit most of the same problems as those encountered by the probes, making them very suitable for the study of challenges associated with an aqueous environment.

Rapid failure of biased probes upon immersion in water represents the reason why SThM is still largely limited to electrically benign environments such as air [60], [61] or vacuum [196]. Understanding the failure mechanism is of fundamental importance as this behaviour prevents SThM probes being used in aqueous environments. Possible mechanisms that should be considered are:

- electromigration.
- electrochemistry

To test these possibilities, the surrogate heaters were tested in DI water having a resistivity of $18.2\text{ M}\Omega$. All these devices failed in DI water after a few seconds by the time they reached 8 V with 27 mA compliance which is approximately 100°C . Representative I-V curves of 6 devices, as well as their average and error bars, are shown in Figure 53.

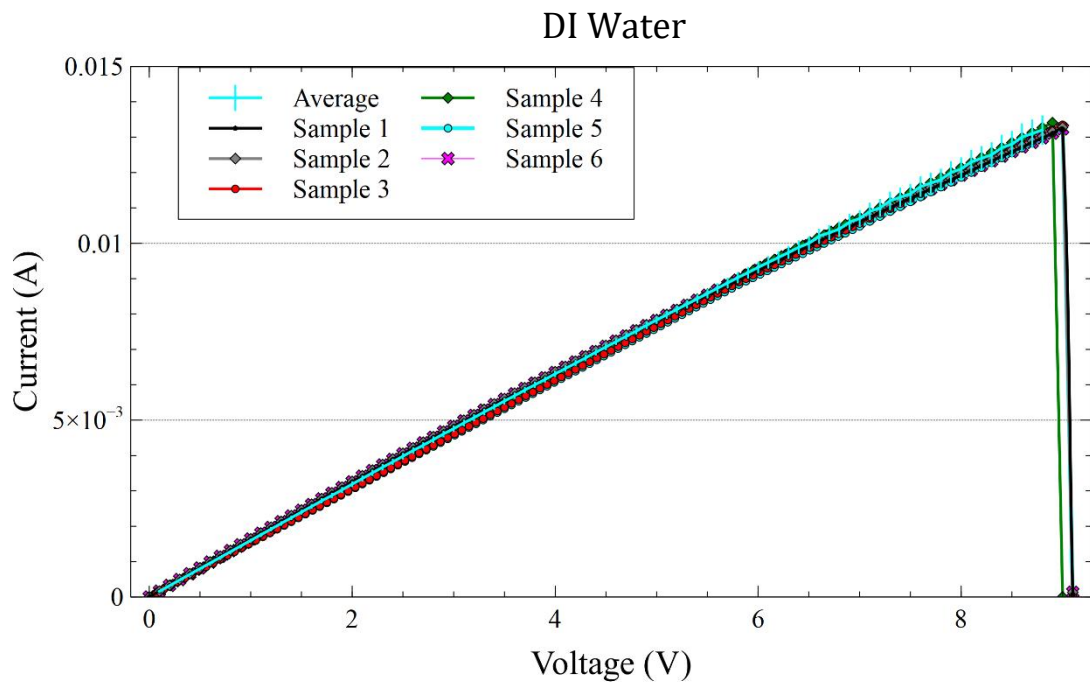


Figure 53 Electrical behaviour of the probe in DI water, current against voltage shows the exact moment of the failure.

It worth noting that 8 V was the potential that caused the instantaneous failure of the surrogate devices in DI water; however failure was occasionally observed at lower voltages (from 5 V). The failure of the resistors (Figure 53) was not observed in the air or in flutec pp3; this strongly indicates that our hypothesis of an electrochemical mechanism has validity. This trend was observed for several geometries despite all working well in the air and in flutec pp3. These observations are also consistent with the belief that the SThM probes used in this study typically fail due to electromigration when used in electrically benign environments. A current density of $3.56 \cdot 10^{10}$ A/m² [1] has been observed as the threshold for heater failure of these SThM probes. This can be compared to the maximum current density sustained by the surrogate sample in air, flutec ($19.5 \cdot 10^{10}$ A/m² calculated from Figure 52b) and the onset of failure in water ($5.34 \cdot 10^{10}$ A/m² calculated from Figure 53). Given such a large difference in sustainable current for identical devices in the two environments, this indicates a mechanism other than electromigration for probe failure in water.

Electromigration [255], [256] occurs when the electrons conducted through a metal conductor interact with the atoms of the metal and scatter. This scattering occurs whenever the electrons encounter an imperfection e.g. an atom that is out of place in the lattice. Due to the scattering of the electrons momentum is

transferred, as shown in Figure 54, diffusing metal atoms and promoting a “flow” of material, eventually inducing a severe defect.

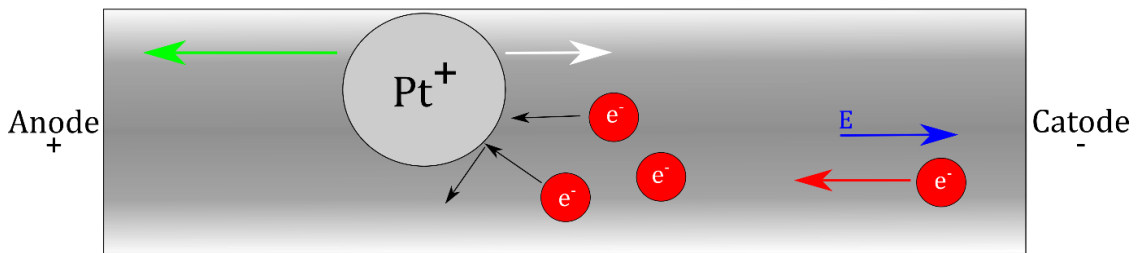


Figure 54 Schematic representation of electromigration mechanisms in a conductive material under a constant electrical potential E (direction given by the blue arrow). The electrons flux (direction of the flux given by red vector) is limited by Pt ions generating the scattering of electrons (black arrows). The green and with arrows depict the displacement direction of the ion, the green one is dominant in this case.

This mechanism is particularly relevant in devices where high current densities and voltages are applied. In addition, its practical manifestation is strongly dependent on the dimensions of the device, becoming a crucial problem for micro and nanodevices [257].

This is because one of the most common failure mechanisms associated with electromigration is the diffusion mechanism. This is typical in homogeneous crystalline structures, due to the uniform lattice of the metal ions. Despite this particularly resistant crystal structure being somewhat immune to momentum transfer, the same is not true at grain boundaries and material interfaces [258] – both abundant features in nano-devices. As a result, there is a strong transfer of momentum between electrons and metal ions in areas that exhibit a weaker bonding force than others. Consequently, electron flow induces the movement of atoms along boundaries causing severe dislocations.

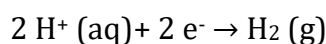
This phenomenon is problematic in narrow metal wires due to the ease in which they can be driven at very high current density. Joule heating accelerates this phenomenon as, by increasing the temperature, the number of atoms out of their original position will increase causing more scattering. In this way, a conductive material can quickly form a breakage, preventing the passage of current. Electromigration can also cause an accumulation of displaced atoms, and material can bridge gaps to other nearby wires, creating an electrical connection through a hillock or whisker (short circuit). It is possible to calculate the average time to failure for a single wire using Black’s model [259]:

$$MTTF = \frac{A}{J^n} e^{\frac{\Delta E}{kT}} \quad (20)$$

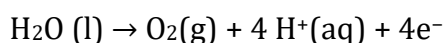
where A is a constant containing the cross-sectional area of the film, J is current density, ΔE is the activation energy, k is the Boltzmann's constant and T is the temperature.

In contrast, electrolysis is an electrochemical phenomenon in which chemical reactions take place through an external difference of applied potential. Therefore, electrical energy is converted into chemical energy. A substance subjected to electrolysis breaks down into its constituent elements. To achieve electrolysis the following conditions are necessary: an electrolyte, two electrodes and a directly applied voltage. When operating, the power supply provides electrons which flow from the cathode, forming anions. The presence of the electrolyte allows these anions to move away from the cathode and towards the anode, whereas cations move away from the anode and towards the cathode. The presence of the potential is crucial to make the nonspontaneous reactions occur. In theory this potential is equal to the potential encountered in the reversed cell reaction. In reality this is not what occurs and usually the minimum potential required is higher. However, if the surrounding environment contains oxidising or reducing species a substantial decrease in potential is observed [260].

In the electrolysis of water [261] (H_2O), hydrogen gas (H_2) and oxygen (O_2) are produced. However, depending on the pH present in the water around the electrodes, and the potential applied, different chemical reactions can occur. For intermediate levels of pH (typical for biological environments) competing reactions at the anode and cathode can take place. At the cathode hydrogen ions (H^+) gain electrons in a reduction reaction leading to the formation of the hydrogen gas:



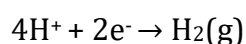
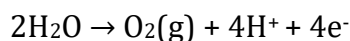
If the pH at the anode is very low (pH = 0 in extreme case), the water molecules undergo electrolysis (at the minimum electrical potential of $E = 1.229 V$ at pH=0), yielding oxygen gas, hydrogen ions and electrons:



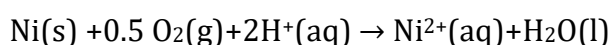
Electrochemical reactions can destroy electrodes either through the dissolution of the reduced/oxidised electrode surface or by generating a corrosive environment that attacks the electrode surface. Beyond electrode corrosion, this is also problematic as electrochemical current makes the accurate measurement

of electrode electrical resistance (i.e. for determining the temperature in SThM) impossible.

A group of materials affected by electrochemical corrosion that are relevant to KNT SThM probes are Nickel and its alloys (exp. Nichrome). Nickel typically has high resistivity and good oxidation resistance [262] and is widely used as thin-film material for micro/nano heaters fabrication [69, 263]. However, as shown in [264] Nickel suffers electrochemical corrosion in water over a wide range of pH (up to 8) and over a range of potentials (from -0.4 V up to 1.7 V). In addition, the pH level of the solution can enhance the corrosion of Nickel or promote the creation of protective oxides (passivation). In most cases where corrosion is relevant, there is not a large concentration of metal ions acting as cathodic reactants. Instead, the electrolysis of water when exposed to a potential difference of 1.23 V leads to:



Within this environment Nickel can be oxidised, for example through the reaction shown:



This type of corrosion mechanism leads to the dissolution of Nickel in an aqueous environment depleting the bulk surface. If Chromium is present, this tends to oxide forming the solid Cr_2O_3 . In both cases, the rate of corrosion is strictly dependent on the concentration of the reacting species, O_2 and H^+ .

These electrochemical reactions are particularly important to this work as NiCr is one of the materials present in the Glasgow SThM probes. In fact, it is probable that the uncontrolled electrochemical reactions occurring at the probe, resulting in the corrosion of Nickel are the reason of probe failure. Platinum is a highly stable metal even under the most aggressive chemical/electrochemical environments. Therefore, it is probable that the corrosion of Nickel in the NiCr adhesion layer is the cause of the breakage. According to the Pourbaix diagram for the Nickel-water system (Figure 55) active corrosion of Nickel in RO water (pH 6 – 7) occurs for stabilized potential between - 0.4 V and 1 V. This is a plausible explanation as the probes are typically biased in the ~1V range during operation and consist of metals (NiCr, Pd, Au) that will undergo electrochemical reactions in water under these conditions [189]. For higher and lower values

there are respectively regions of “passivation” (metal forms a stable coating of oxide) and “corrosion immunity” (metal is thermodynamically stable and the corrosion reaction is unable to occur spontaneously [265]) [264] [266].

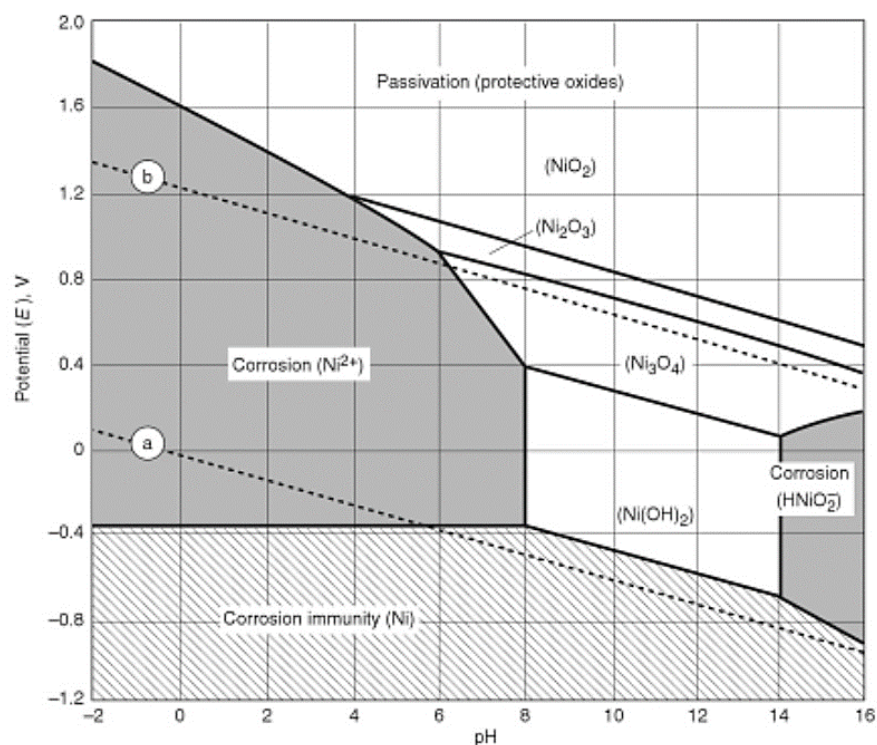


Figure 55 Pourbaix diagram for the nickel-water system, indicating the E/pH regions of thermodynamic stability of various dissolved and solid species and the regions of “corrosion immunity”, “passivation”, and “active corrosion” [173].

This leads to the reasonable explanation that the failure of SThM probes immersed in an aqueous conductive environment is due to the electrochemical corrosion of the NiCr used as an adhesion layer for the thin film Pt resistor. This is corroborated by looking at Figure 56, showing the breakage of the device measured in Figure 53, after operation in DI water using the same instrumentation as conventional SThM. From this image, it is possible to see the breakage of the platinum heater which has become detached from the surface and twisted. The twisted structure is the result of evaporated platinum being extremely stressed, which manifests in tightly curled films when it becomes free standing. This happened in the region of the heaters instead of the triangular pads because corrosion has only progressed a short distance sideways under the device, so only narrow features lift.

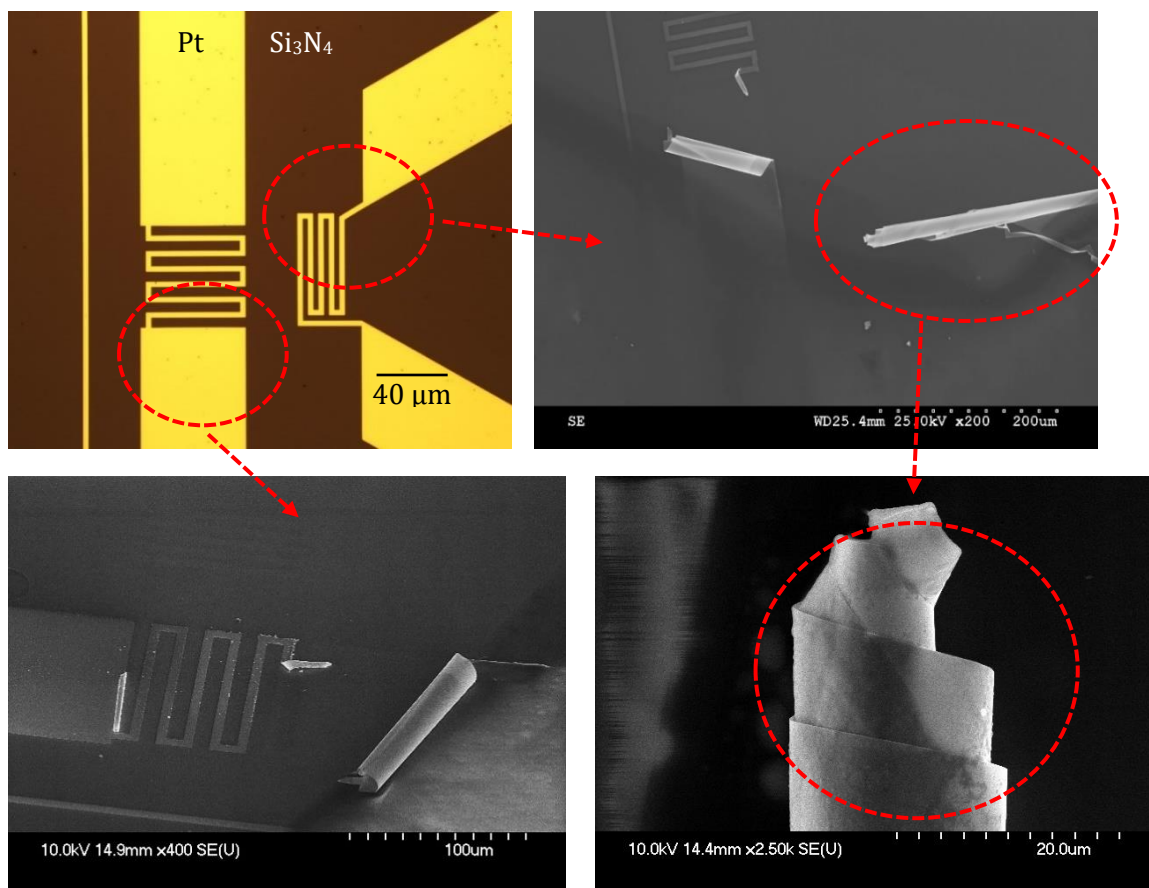


Figure 56 Representative SThM sacrificial heaters failure.

As discussed in section 3.2 the thermo-electrochemistry of the probe is complex and represents a severe limitation for the use of traditional SThM in a conductive liquid. The electrochemical reactions that occur due to the presence of a DC current across the probe can severely damage the probe. Overcoming these difficulties, therefore enabling under-water SThM is an essential aspect of this work. Beyond increasing the capabilities of SThM to include biological or chemical systems, there are benefits to more conventional samples. One example stems from the fact that AFM capillary and contact forces can be greatly reduced in aqueous solutions [182].

4.3 PROBE CALIBRATION (EXPERIMENT + MODEL)

For SThM working either in active or passive mode, calibration of the probe is necessary if quantitative measurements are desired. As already stated in Section 2.2, the change in electrical resistance of a thermal resistance thermometer as a function of changing temperature is represented by its TCR. To determine the TCR, two conditions have to be satisfied: accurate measurement of the resistance, and a stable, well-known temperature that is as uniform as possible along the thermal sensor. The most effective way to achieve these conditions in this work

is through the use of a heat-bath, the temperature of which is independently measured using a small, high-quality thermometer located close to the SThM probe.

This was realised by employing a well-established platform previously exploited with success in air by the AFM Group of the University of Glasgow [254], [1]. Three different environments were chosen: air, flutec pp3 and DI water, reflecting those used in the subsequent experiments. The probe was mounted in its own holder described in Section 3.3 with a 2.1 ± 0.2 mm sized PT100 thermal sensing element attached in close proximity. The sealed holder was positioned on a Peltier thermoelectric module, the temperature of the Peltier was varied (from room temperature to 60°C) and the probe and PT100 resistances measured. It was ensured that before each measurement the signal from the probe and PT100 had stabilised (~ 4 minutes each measurement), indicating a constant temperature had been reached. It was assumed that, given their proximity to each other, the probe and PT100 were at the same temperature, although it is recognised that this assumption is most valid for the liquid environments. The calibration setup, for passively heated probes, is shown in Figure 57. It is essential to note that the measurements performed in water with an actively heated probes were carried out using the electronic setup described in section 3.3, which inhibits the DC current responsible for the electrochemically induced probe failure.

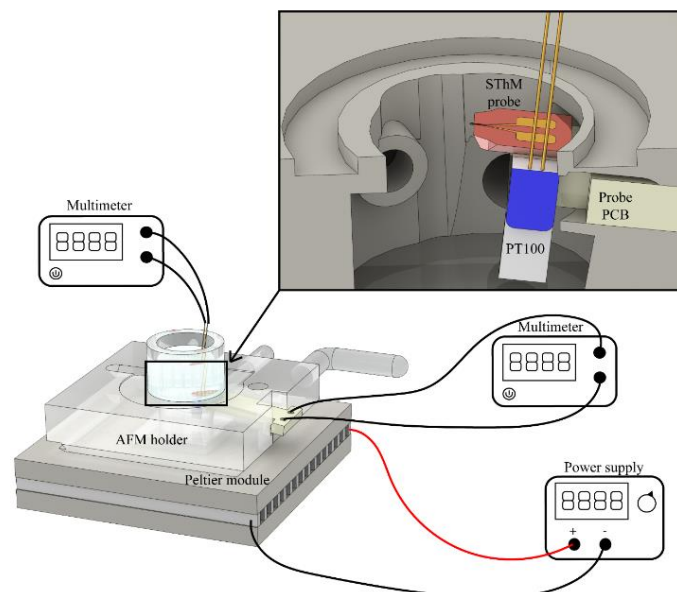


Figure 57 Calibration setup for measuring the temperature coefficient of resistance (TCR) of the probe in air, flutec PP3 and DI water. The power supply power the Peltier module, the PT100 thermocouple is connected to a multimeter and the signal from the probe is measured using a second multimeter.

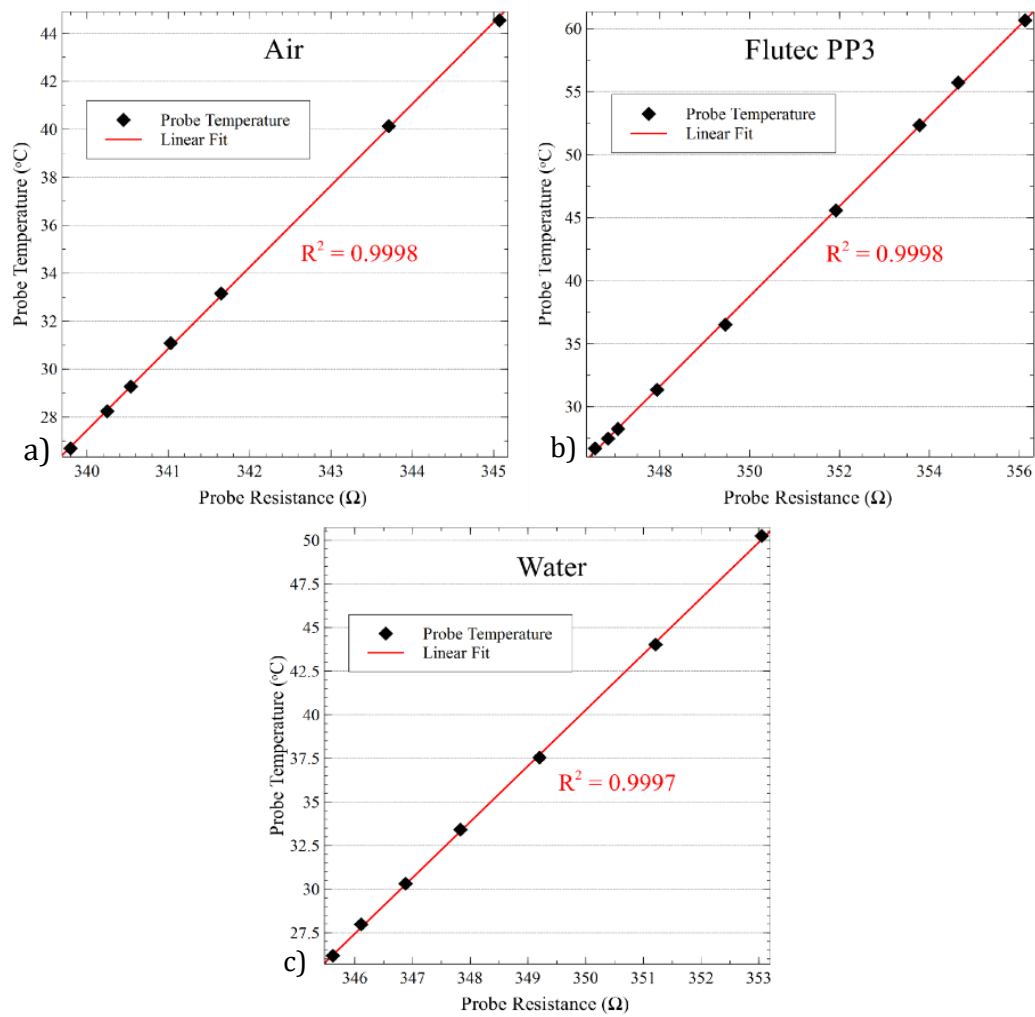


Figure 58 Temperature plots of a passively heated probe vs resistance in the air (a), flutec PP3 (b) and water (c).

The resistance of the probe and its temperature as measured using the PT100 sensor were then recorded and plotted (Figure 58). As the TCR will change marginally with temperature, an averaged TCR over a certain temperature range is usually employed in practical work. To confirm this assumption, the platinum resistance element of the probe was measured for 7 temperatures in air, water temperatures and flutec PP3 as shown in Figure 58. The average TCR was determined and, as expected, variations were within measurement tolerance for all environments: $0.000849 \pm 0.0000137 \text{ K}^{-1}$ for air, $0.000870 \pm 0.0000471 \text{ K}^{-1}$ for flutec and $0.000877 \pm 0.0000417 \text{ K}^{-1}$ for water. The error was calculated as the standard deviation of the 10 values. Those values are close to that described by [1] for the same tip sensor material (platinum) as the probes used in this thesis. This result demonstrates that the probe acts as a good thermometer with a linear response to temperature over the ranges considered in this work. Whilst in the same environment, it was also possible to use the TCR to quantify the self-

heating of the probe, by monitoring its temperature-induced resistance change as an increasing current was supplied and Joule heating occurred (Figure 59).

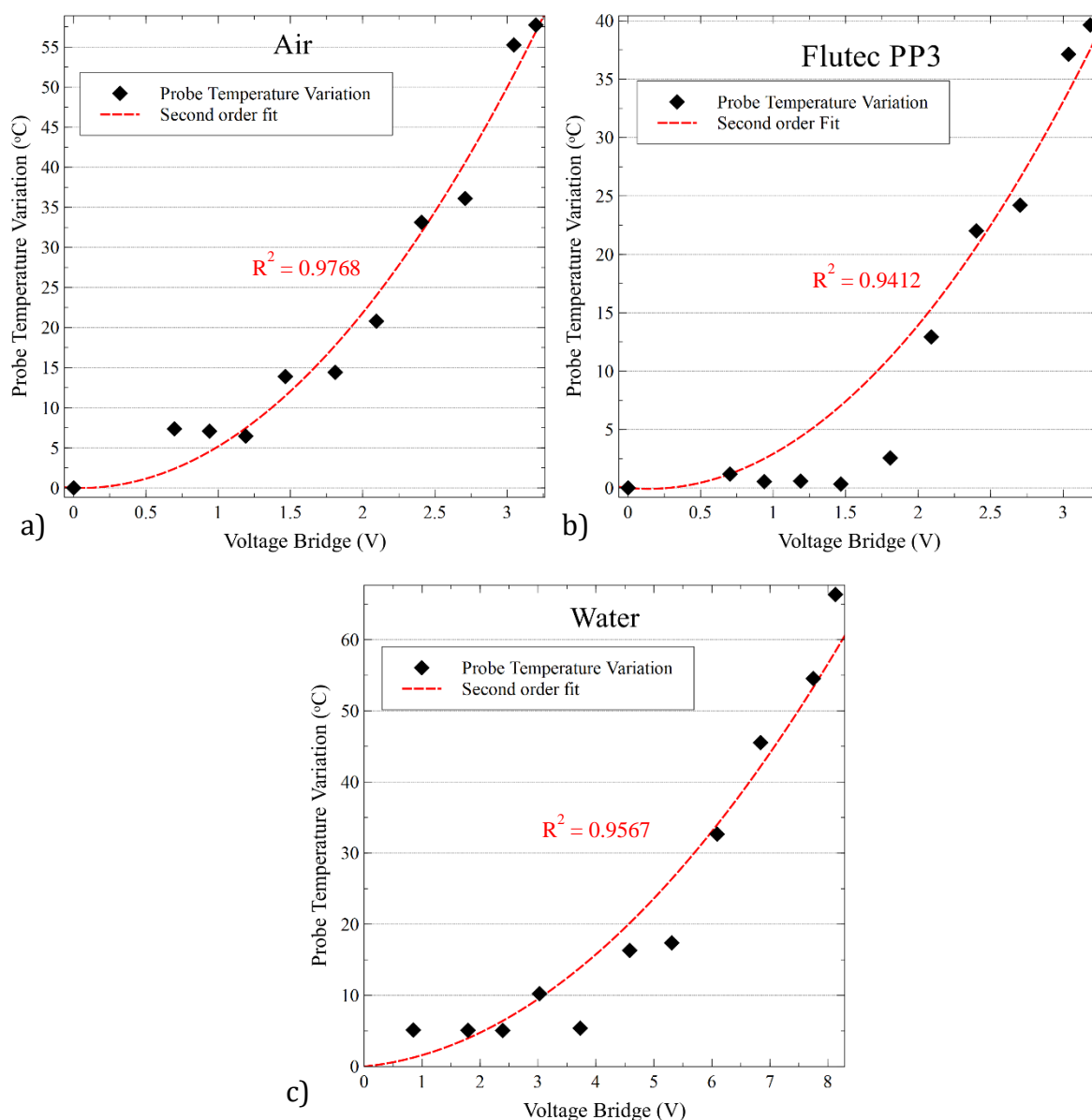


Figure 59 Plots of probe temperature rise caused by probe self-heating due to the AC voltage applied in Air (a), in Flutec PP3(b) and in Water (c).

It worth noting that the second order fit used for the plots has been forced through (0,0) as Joule heating is proportional to input power, which is given by $\frac{V^2}{R}$. The first horizontal part of the plots is not always visible due to the tiny temperature rise at small V being hidden by the scatter in the data.

Even though electrochemical failure had been suppressed by instrumentation, the maximum attainable temperature of the probes employed in this work was still largely dictated by the current density in the tip resistor/heater. If this current density exceeded a critical value, the tip resistor failed due to electromigration as described in section 4.2 above. This maximum sustainable

current varies with the specifics of the experiment as both current type (AC or DC) and probe temperature (influenced by the environment – e.g. vacuum, air or liquid) play a role in dictating the rate of electromigration [71]. With the instrumentation used in this work, the max temperature sustainable by the probe in water was found to be $T_{\text{water}} \sim 85 \text{ }^{\circ}\text{C}$. No significant convection of fluid was observed due to the small mass of water being heated ($<50 \text{ }\mu\text{m}$). This means that the water away from the probe cools to ambient temperature very quickly. It can be demonstrated with an approximated estimate based on the Rayleigh number equation, already reported in Chapter 3. The Rayleigh number has been calculated using water properties at $85 \text{ }^{\circ}\text{C}$ and calculating it for different thermal gradients, from 2 to $30 \text{ }^{\circ}\text{C}$ (Figure 60, a). The volume considered for this case is a cube of $10 \text{ }\mu\text{m}$ edge size. This volume is positioned with its centre on the tip apex, which allows to consider the thermal gradient generated in the immediate vicinity of the probe. The values obtained are very small, with a maximum of 0.01704 , which is well below the literature threshold value of 10^9 [267]. This highlights the significant difference in time scale between the two processes. This limit, however, is general and in microfluids can be lower. Usually this behaviour needs intensive CFD calculations to produce accurate results. However, it is generally recognised that large Rayleigh number (10^3 up to 10^7) [268] is required to have a significant contribution from convection even at this scale.

The convection time scale is much longer than diffusive transport. To evaluate the effect of the volume of water, the same approach has been used fixing the thermal gradient to $30 \text{ }^{\circ}\text{C}$ and changing the characteristic length from 50 nm to $50 \text{ }\mu\text{m}$. In this case, the growth of Ra follows a third-order power law and increases rapidly (Figure 60, b). Based on the geometry of the probe and to the associated numerical analysis a characteristic length of $17.5 \text{ }\mu\text{m}$ can be considered as the worst case. With the conditions introduced the Rayleigh number is well below the convection limit, 0.06123 . Furthermore, these results assume a significant thermal gradient ($30 \text{ }^{\circ}\text{C}$) across a large volume of heated water. This will be further demonstrated in Sections 5.2 and 5.3. For these reasons, it is reasonable to consider the contribution of convection minimal for this specific case.

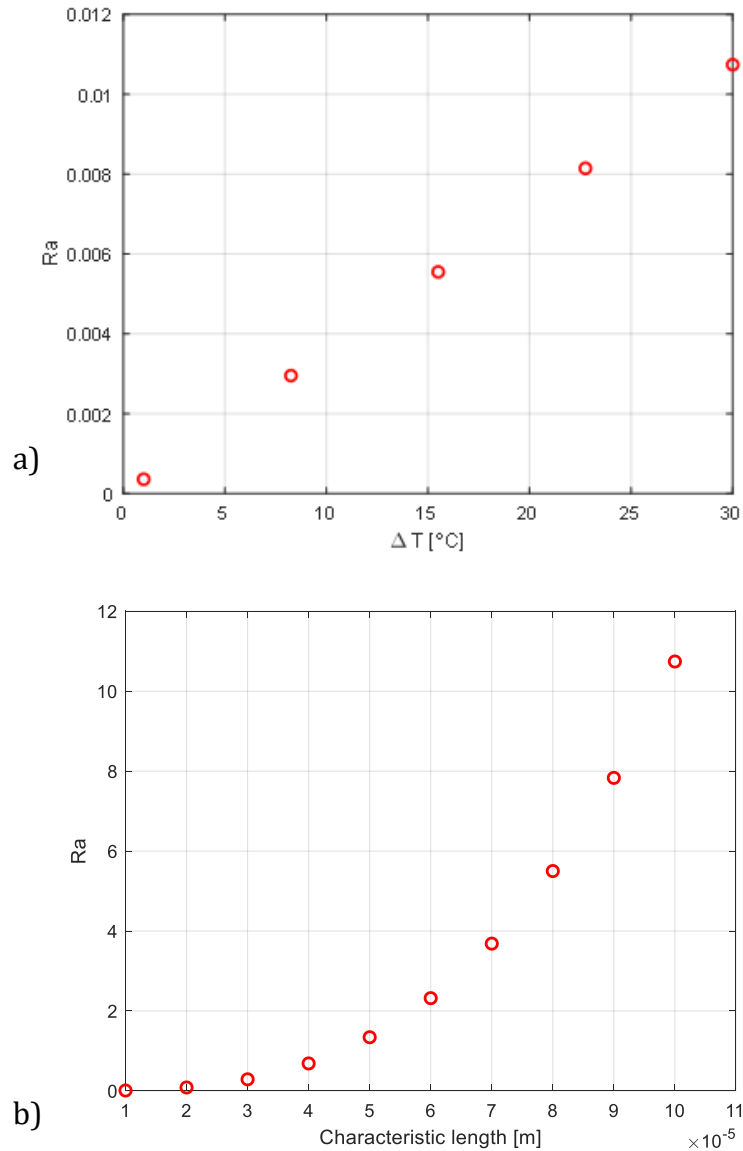


Figure 60 Rayleigh number calculated for a varying a) thermal gradient and b) a varying characteristic length.

This result was corroborated by numerical simulation (COMSOL Multiphysics) that was carried out using the correct probe geometry and materials as described in Chapter 3. In the simulation, the same current as that used for the calibration experiment was applied to one Au pad while the other one was fixed to the ground, and the surrounding environment properties were changed between air, flutec and water. The probe-measured temperature was taken to be the average temperature of the tip resistor in the FEA model. An example of the thermal distribution generated by the model is given in Figure 61 where the simulation considers the SThM probe in the air without any sample. The image shows the (Joule) heated cantilever and the tip fully immersed in air, and it can be clearly

seen that the hot region is mostly localised at the very apex of the probe. Due to the large change of length scale from the pad's region of the cantilever to the probe's apex, the mesh element size changes drastically, as described in Chapter 3. The implementation of this can be seen in Figure 61 where the tip of the probe is surrounded by two cuboid regions. Although this had no impact on probe materials, behaviour or geometry they did allow a gradual and smooth transition in the mesh size to be dictated. The fact that these regions extend outside of the probe itself is important as the mesh of the environment needs to match with the mesh of the probe apex, allowing continuity between the two parts and ensuring mesh quality and solution accuracy. Conversely, if a single transition is used, severe mesh distortion and loss of mesh quality could result, causing a failed simulation.

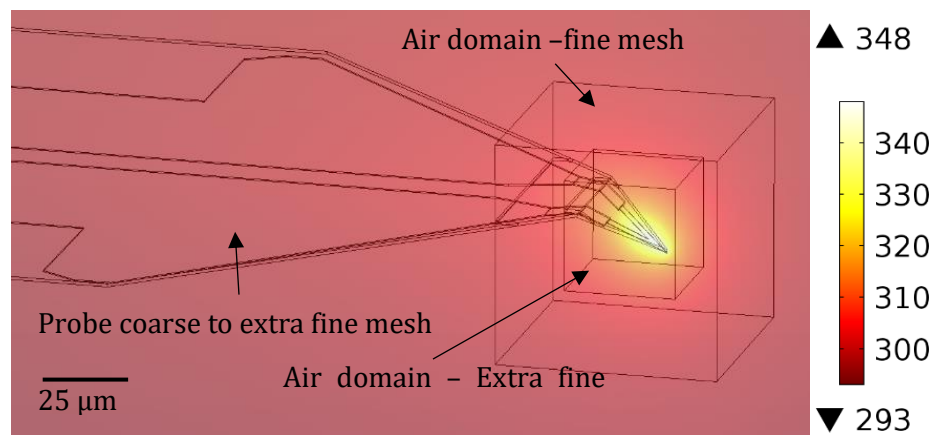


Figure 61 Full-probe FEA showing temperature distribution in air environment during the calibration, strong thermal localisation can be identified at the probe tip.

The FEA analysis was repeated for all experimental environments (air, flutec and water) and the results are shown in Figure 62. In this image, the simulated temperature distributions of the Si_3N_4 SThM probe in free space, all with the same temperature scale (as dictated by the largest T: air) are reported, showing that the extent of the heated region, generated by the self-heated probe, is dictated by the size of its tip RTD.

There are some differences in the heat profile between the three environments. When operating in air the thermal field is very localised and the hottest region corresponds to the very apex area of the tip (Figure 62, a). This behaviour has been widely discussed in the literature and these results are in line with those reported by Tovee et al. [94]. However, when the same simulation is done for a flutec environment (Figure 62, b), an overall decrease in the temperature at the tip is observed, and the thermal field is less localised. A dramatic change in both

maximum temperature and thermal field also occurs when water is considered (Figure 62, c). This progressive change is caused by the increased thermal coupling between the probe and the surrounding environment. This mechanism is directly related to thermal conductivities of the environment considered, which is $0.025 \text{ W m}^{-1} \text{ K}^{-1}$ for air, $0.0611 \text{ W m}^{-1} \text{ K}^{-1}$ for flutec and $0.563 \text{ W m}^{-1} \text{ K}^{-1}$ for water. Water is the most conductive environment tested and due to this characteristic, it allows a larger fraction of the heat generated by the probe to dissipate. This produces a shift of the maximum temperature away from the very end of the tip towards the centre of the heater.

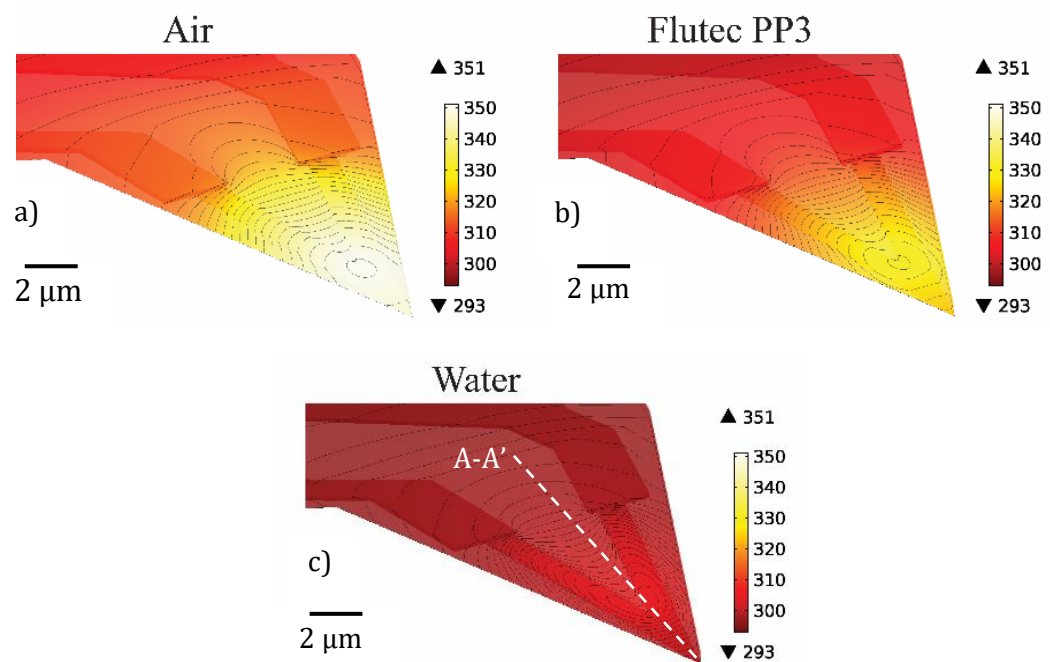


Figure 62 FE simulation of the temperature contour distribution of a typical Si_3N_4 cantilever with Au leads and Pd thermal sensing element heated by Joule Heating, where each isothermal line corresponds to a change of 2 K (e) in air, flutec and water.

Furthermore, in air and flutec the heated region extends along cantilever, as shown in Figure 63, whereas in water the temperature gradient is more localised at the tip. Figure 63 shows the temperature change along the path A-A', where A is the start point and A' is the end located on the tip extremity. The increase in thermal conductivity of the environment tends to decrease the maximum temperature and to homogenise the temperature field across the probe's apex. This is particularly evident for the case where water is considered.

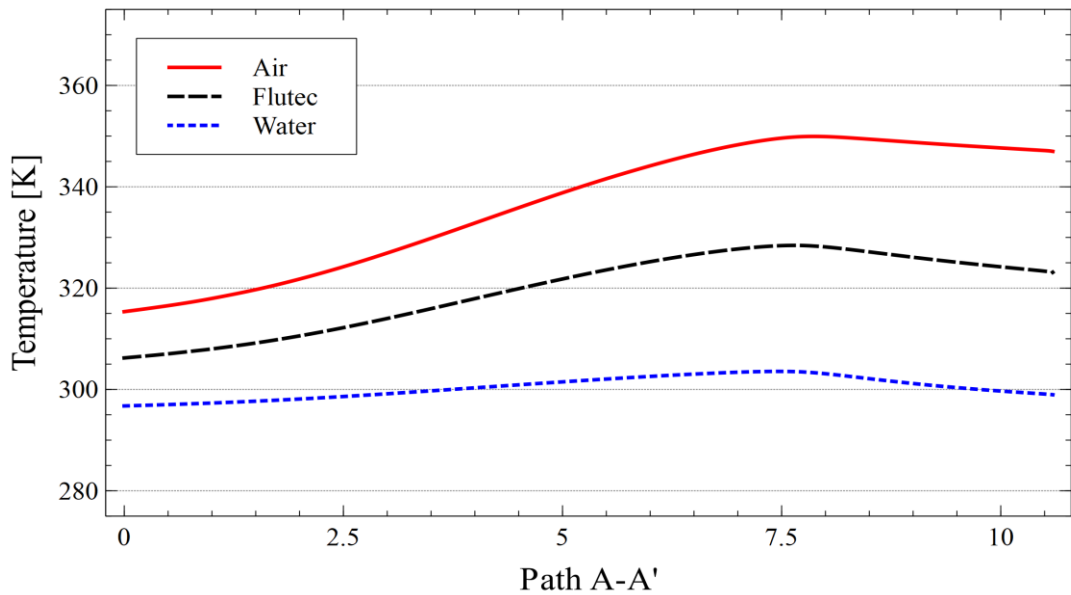


Figure 63 Temperature distributions along the path A-A' of Figure 62 for different environments (air, flutec, water) considered in the numerical analyses.

All of these observations can be explained by the higher thermal conductivity of water compared to air and flutec, which decreases the thermal resistance between the entire probe surface and its surrounding environment. Therefore, the increased heat flow to the surrounding environment in water results in the high-temperature region being restricted to the portion of the heater with the greatest Joule heating. This is highlighted in Figure 64, where the total heat flux magnitude is reported for the two FEA simulations in air and water environments. As expected, in air, the entire apex exhibits a widespread high heat flux, which is associated with a high temperature as shown in Figure 62. In addition, part of the heat flux is also diffusing into the cantilever. Conversely, when operating in water the total heat flux magnitude is largely reduced and is high only in areas close to the heater and nearly zero heat flux flows back into the cantilever.

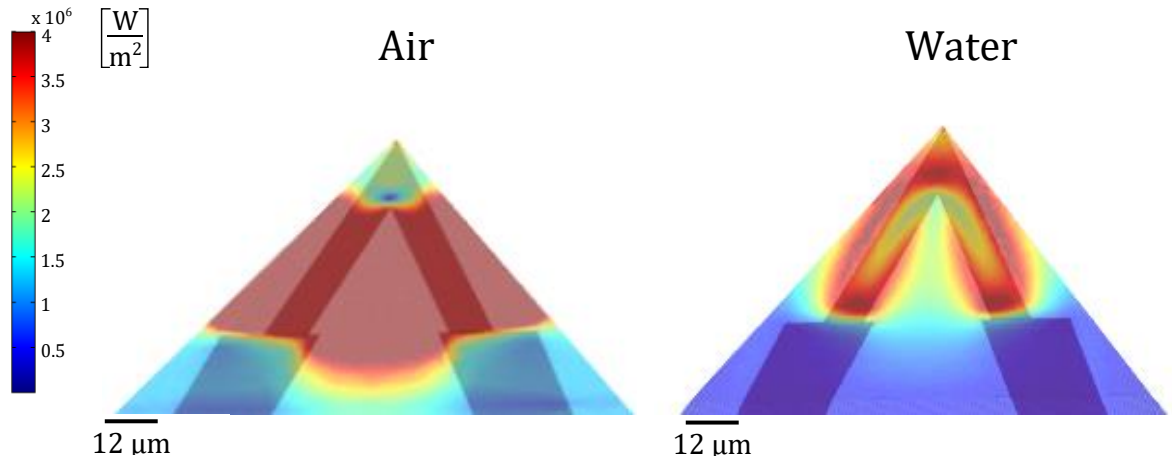


Figure 64 Total heat flux magnitude generated by the Joule effect during numerical analyses in air and water environments.

These simulations lead to the conclusion that although significant probe self-heating is still attainable under aqueous environments, greater heating power will be required to achieve the same temperature rise underwater as in the air. This is entirely expected and is due to the increased thermal conductivity of the surrounding aqueous environment in contrast to air. This is also expected to have an effect on the resolution, which will be assessed in the following section.

It worth noting, that the FEA analyses are based on an accurate CAD model of the KNT probe as-designed, where the material thin films have been characterised (see Section 3.8).

4.4 AIR/WATER SCAN AND ANALYSIS

To investigate the impact of operating an SThM probe underwater, whilst simultaneously testing the new liquid holder and electronic system described in chapter 3, SThM imaging of solid samples was carried out in the air, flutec pp3 and DI water. The sample used has been described in Section 4.2 and consisted of a Pt thin film (50 nm thickness with 5nm of NiCr as an adhesion layer) on a Si₃N₄ coated wafer [251]. Electrical currents of 1.7 mA for air and 4.5 mA for water were applied to the SThM probe as these were observed from the calibration (Figure 58) to be safe and sufficient to heat the probe $\sim 65^{\circ}\text{C}$ above T_{amb} in each environment. The experiment was then conducted by carrying out contact mode imaging of the microfabricated sample using the self-heated probe.

Figure 65 shows the SThM topographic and thermal images taken in air (a and c) and water (b and d). It is possible to see that, by employing the transformer bridge described in chapter 3, the SThM probe remains stable and undamaged for

the duration of the scan. Indeed, no variation in electrical performance was observed throughout the experiment. It can also be seen that, even when submerged in water (Figure 65, d), there is still excellent SThM resolution and thermal contrast between the Pt and Si₃N₄ is clearly visible. All the images have been processed with Gwyddion software using level data by mean plane subtraction, align rows using median of differences method and flattening by fitting a plane through three points.

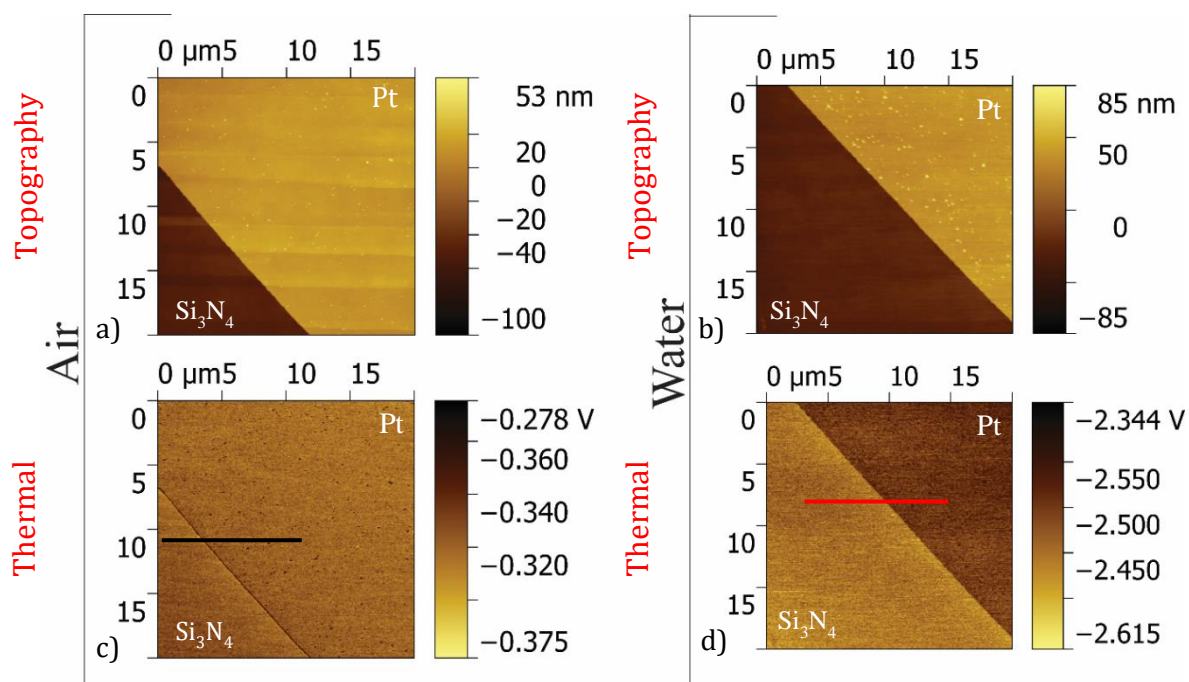


Figure 65 SThM height images (a), (c) and thermal images (b), (d) of Pt on Si₃N₄ in air and in water.

The results presented above in Section 4.3 may lead to the anticipation that enhanced heat dissipation in water dominates the SThM probe signal, resulting in the complete loss of sensitivity. However, this is not the case. In fact, the in-water thermal image exhibits some clear advantages over the one obtained in-air. The first of these is the decrease in thermal signal visible at the edge of the Pt feature in-air SThM image. This thermal artefact can be clearly seen in Figure 66 where trace and retrace cross-section plots, corresponding to the drawn lines on the thermal images of Figure 65, are presented for both air and water. It worth noting that the trace and retrace features do not line up. This is caused by the probe scanning side-to-side (laterally), so the tip twists left and right depending on the scan direction resulting in a small tip displacement between the trace and retrace data.

Cross-Section Pt/Si₃N₄

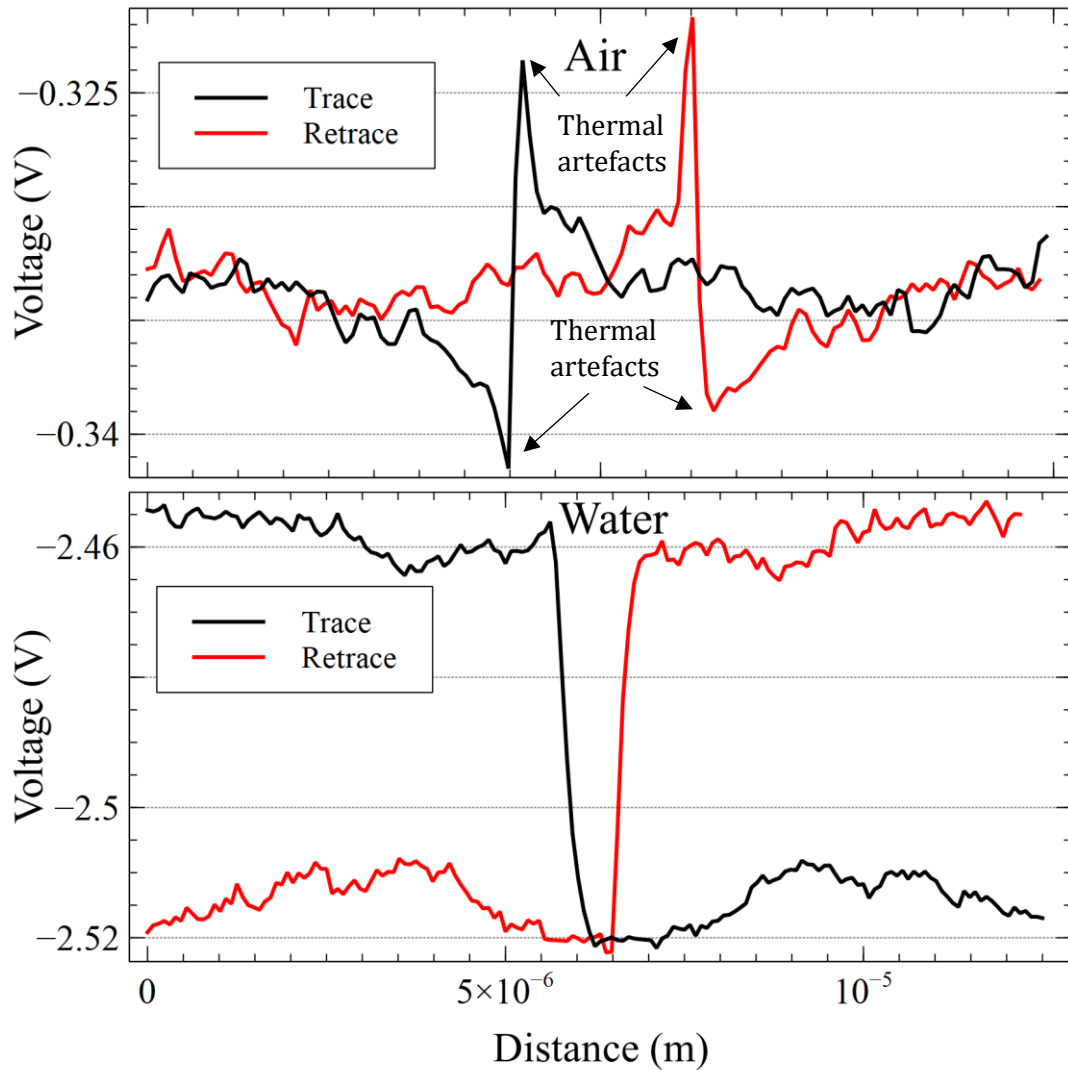


Figure 66 Comparison between Pt/Si₃N₄ cross-sections in air and water (red and black line in thermal images).

The artefact of Figure 66 in air is well understood and is the result of sample topography [269]. The lateral contact at the step edge is still present; the location, size and number of contacts changes as the tip encounters a step. At an edge, the contact area and/or number of contact points increase leading to lower tip temperature and decreased thermal signal. This effect is not visible in water suggesting that thermal coupling between the tip and sample is more stable, even during a scan, resulting in a signal that is less dependent on the local topography (Figure 67).

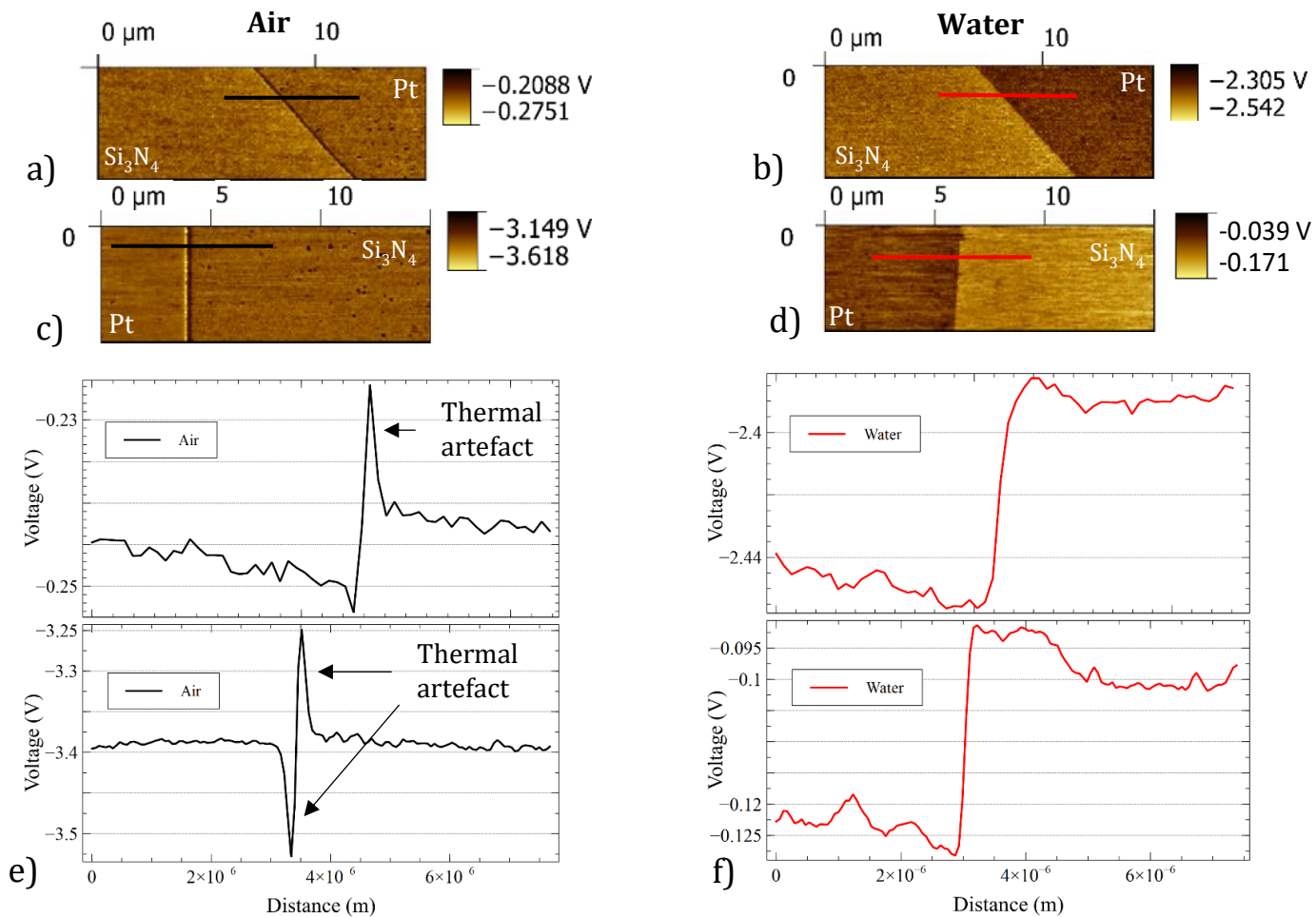


Figure 67 Comparisons between STHM repeated measurements in air (a, c) and water (b, d), showing the better thermal coupling obtained in water. Comparison of voltage signal between air (e) and water (f) along with two precise paths crossing the interface.

The same stable tip-sample thermal contact can also explain the second difference, the fact that the in-water thermal image exhibits less 'noise' than the in-air equivalent, a phenomenon that is explored further in section 4.5 below. This behaviour is highlighted by the voltage signal (Figure 67) measured along the paths shown in Figure 67. Two differences are visible, the first is the signal to noise level, which in the air is clearly higher than in water. In order to better demonstrate this phenomenon and its repeatability, SThM scans were repeated with a different scan direction (Figure 67). In all the cases the scans in water offer better signal to noise and fewer artefacts. The second important difference is the observable contrast at the interface. When measuring in air the signal does have a small transition, conversely, in water a large well-defined transition with a clear slope is present.

Both simulations (Figure 64) and experiments suggest a loss in thermal spatial resolution. In addition, the electrical current needed to obtain good contrast in water for the thermal images is higher when compared to air ($I_{\text{air}}=1.7$ mA $I_{\text{water}}=4.5$ mA). This is mainly due to the heat dissipated into the environment and explainable by the high thermal conductivity of water. In air the heat-flux and the peak in temperature are highly localised at the tip apex. Conduction through air is negligible when compared to the conduction via solid-solid contact. In both experiment and simulations, the thermal conductivity of water enhances the spread of the heat by the probe tip, this has been observed in the simulations and by Tovee *et al.* [94].

In addition, it was observed that while undertaking long duration scans in air, the stability of the signal was poor, particularly when operating the probe at a high, self-heated, temperature ($\sim 65^{\circ}\text{C}$ above T_{amb}) [71]. This resulted in significant drift, reducing the reliability of results. Figure 68 shows in-air thermal images acquired 5 minutes apart from each other (20 minutes in total) with the same probe, illustrating the changes in contrast that were observed.

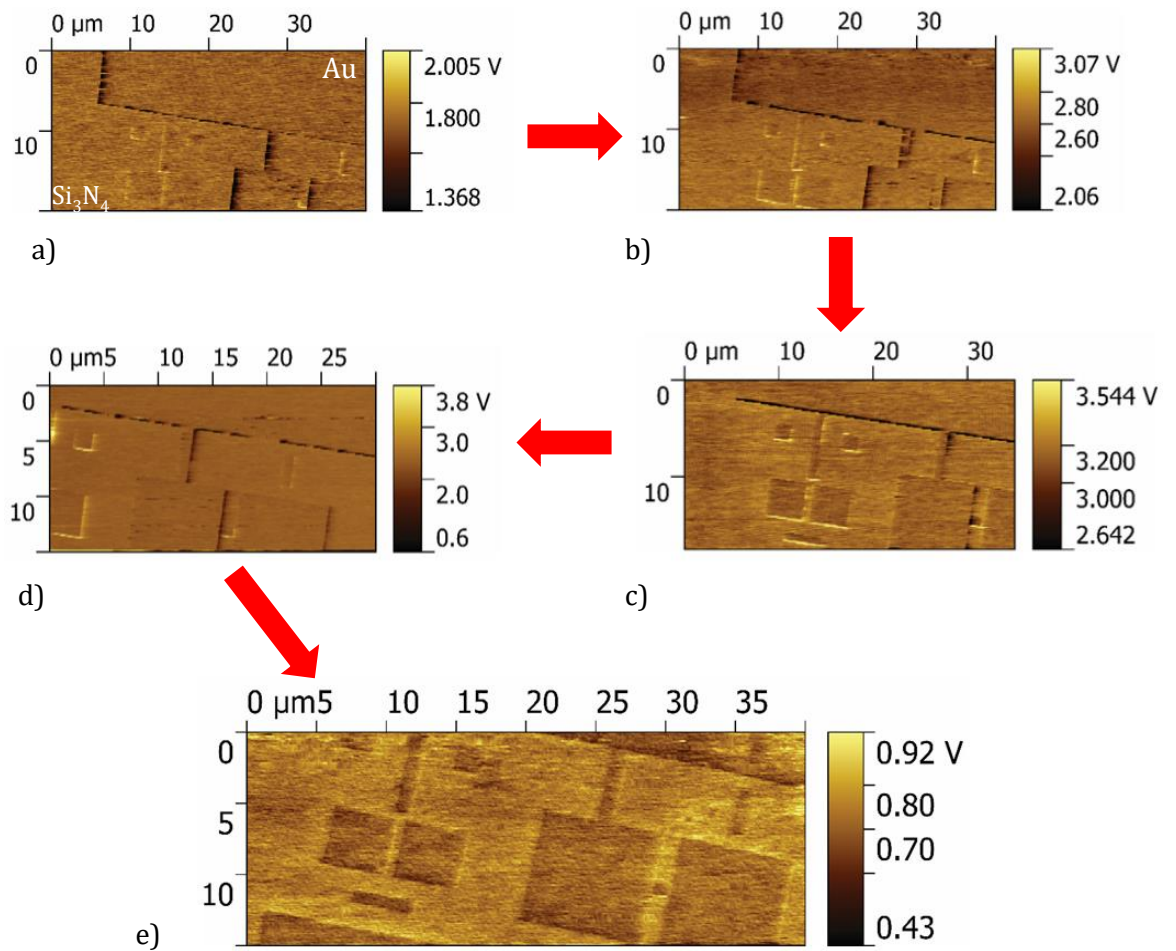


Figure 68 Thermal images for a long-time scan in the air at time 0 (a), 5 minutes (b), 10 minutes (c), 15 minutes in the end at 20 Minutes(d) and a closer view (e).

It is proposed that these are mainly due to the changes to the nature of the tip-surface contact. Conversely, Figure 69 shows the in-water thermal images acquired on the same day using a new probe for an equal scan duration. In this case, the change in contrast is not present and the image contrast remains unaltered.

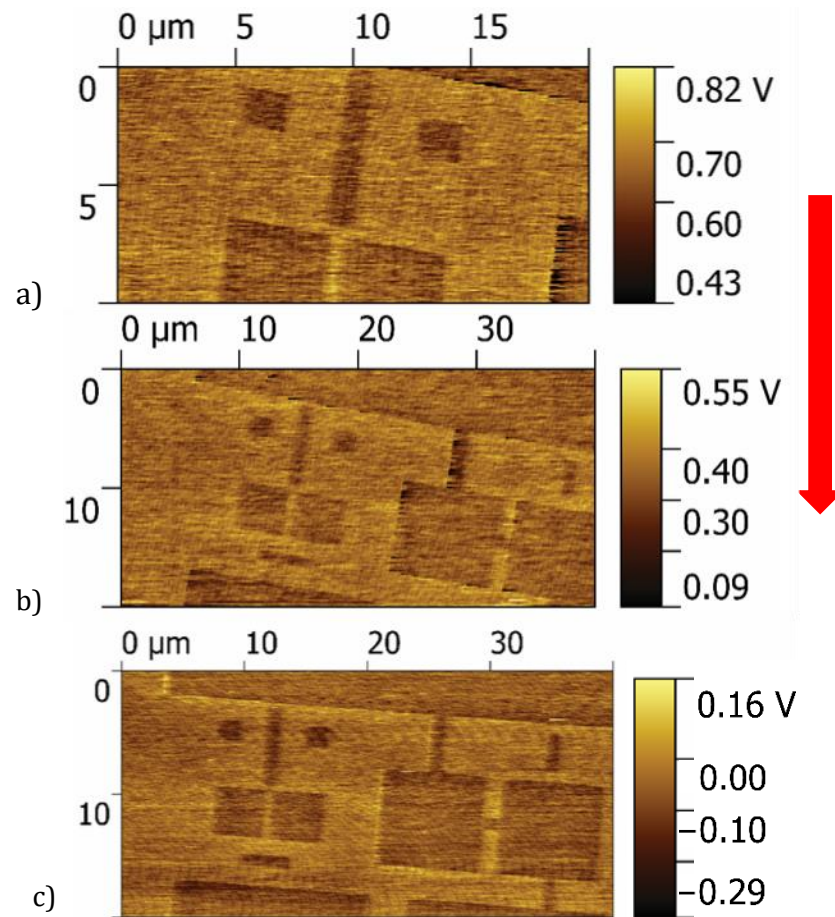


Figure 69 Sequence of equally timely-spaced thermal images for a 20 minutes scan in water with new probe.

It is not unusual to see poor stability in the signal when using the type of SThM probes employed in this work. This is attributable to their tip structure that can change as it stabilises over the first few hours of use. Beyond this time, the thermal image contrast can change as the tip collects and drops contamination from the surface; a common occurrence for AFM probes used in contact mode imaging. Figure 70 shows SEM images (FEI Nova NanoSEM 630 at the JWNC) of a new thermal tip taken with the probe tilted at two angles 0° (Figure 70 , a) and 40° (Figure 70 , b).

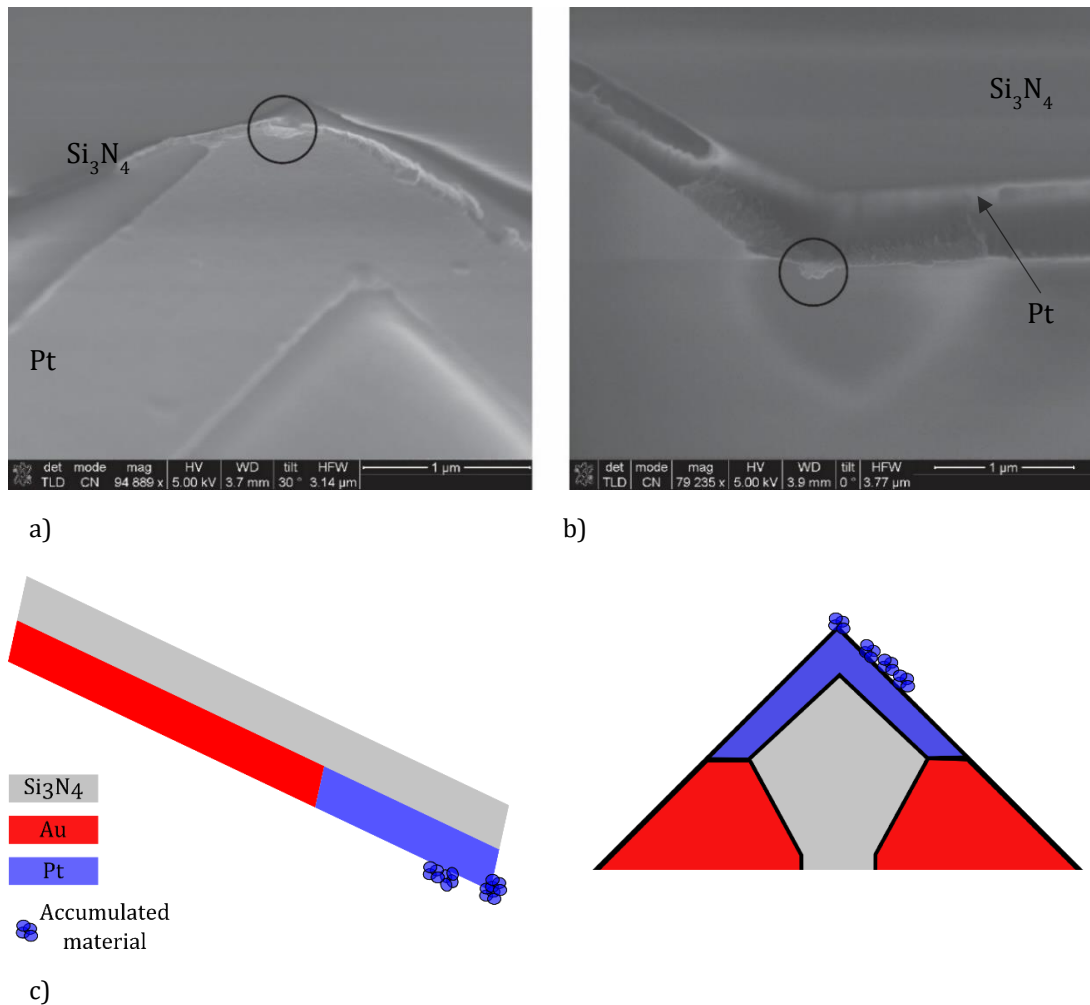


Figure 70 SEM images of a standard SThM tip acquired with two different angles: at 0° (a) and 40° tilted probe (b) and a schematic side and frontal views representation of the cantilever tip with the accumulated material(c).

They show the Pt heater on the Si_3N_4 cantilever with a region of the non-homogeneous surface on the tip apex highlighted by a black circle. Figure 70 , b shows this to be a 'ball' of metal attached at the very end of the tip. This metal is a consequence of the deposition of the Pt tip resistor that is part of the fabrication procedure used in the production of probes. A plausible scenario would be that, after a few in-contact scans, this excess metal would easily be removed, resulting in a change in the solid-solid contact and altering the thermal images. In addition, the removed metal may remain on the sample surface, possibly being picked-up and dropped multiple times during an experiment. Unfortunately, this theory could not be confirmed as the holder used (described in chapter 3) requires the use of epoxy adhesive to attach the SThM probe making it impossible to remove for SEM inspection post-scanning. However, in her thesis, Z. Umatova [270] demonstrated this progressive tip-altering process first identified by Killgore et al [271]. In her work, Umatova investigated different types of probes including a

conventional 'Olympus' design AFM probe and the KNT SThM probe. In both cases, several tests were conducted across several days, with the probe repeatedly entering into contact with and retracting from a membrane designed to study the thermal conductivity between the tip and the sample. In both probes, a drastic change in the thermal conductivity between initial and subsequent contact was observed. The reason for this change was identified as the physical changes that occur during the scanning process. It is well known that sharp Si AFM tips become blunted and broken during a scan. However, when investigating the KNT probes, Umatova identified metal accumulation and loss on the extremity of the tip associated with the metal flaking off the tip, similar to that illustrated in Figure 70. These changes resulted in the variation of thermal conductance between the tip and sample that she observed in her experiments. This study demonstrated that every AFM/SThM probe tends to change after being brought into contact with a surface, leading to a change in thermal conductance. As a consequence, the mechanism proposed above to explain the instability observed in Figure 68 is plausible. Even if the probe thermal conductance changes, the heat bath calibration of the probe is still valid as it generates a TCR in an isothermal environment. Since there is no heat flow without a temperature gradient, the contact resistance is irrelevant and subsequent measurements will always correctly report the average tip temperature, as TCR is stable. However, changing tip-sample resistance means that the tip temperature cannot be accurately linked back to the sample temperature or conductivity (depending on the mode). In the best scenario, the tip contact will remain stable throughout the experiment, allowing the tip-sample contact resistance to be assumed constant, but this is not guaranteed. At the very least, it will result in a noisy signal as the probe scans. For temperature measurement, thermal nulling is the only reliable solution: if tip and the sample are isothermal, there is no heat flow and the contact resistance is irrelevant. For conductivity scans, variability is known to be a significant problem and is one of the main reasons why quantitative SThM conductivity measurements are extremely hard.

Interestingly, the fact that the images obtained in-water, as shown in Figure 55, do not display the same instabilities is surprising. Therefore, a deeper understanding of the mechanisms was sought by comparing these experimental

results with the numerical model. The idea behind the simulations was to reproduce features of a thermal scan using FE analyses. Specifically, a probe was simulated in contact with a surface, moving laterally between two different solids, whilst surrounded by the different environments described in the experiments above. This model was then used to investigate the impact of changes in the tip-sample contact material for the different surrounding fluids. The model used for the numerical simulation was the same as described in Section 3.4, with the tip having a contact radius of 50 nm. The simulated probe was brought into contact with a surface consisting of two rectangular blocks thermally connected to each other, representing a sample of two dissimilar materials (Pt and Si₃N₄) as shown in Figure 71.

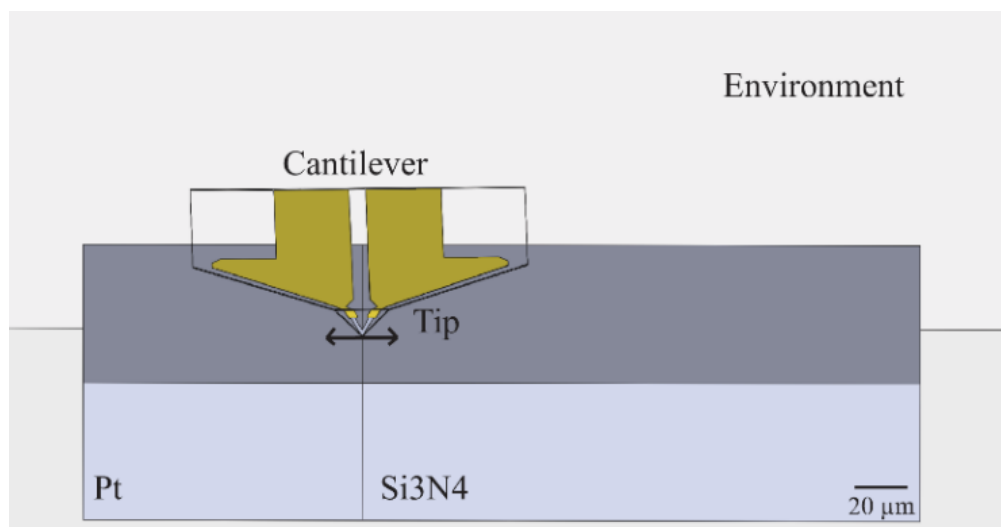


Figure 71 3D model built in SolidWorks of the standard cantilever and tip on a Pt/Si₃N₄ sample.

As described previously, a block, enclosing the cantilever and sample, was introduced to simulate the surrounding environment (air or water). An electrical current of 1.7 mA and 4.5 mA, for air and water respectively, was applied to one Au pad of the probe as these were equivalent to the values employed in the experiment. The other pad was fixed to electrical ground. The initial temperature of all the subdomains, the environment block, sample block and the cantilever end were set to 293.15 K (room temperature). Simulations were repeated for different thermal contact conductance coefficients (h), representing both the solid-solid contact and solid-liquid contact conductance, were used as reported in Table 1 (Chapter 3, section 3.7), representing potential 'limit cases' as identified in the literature [238]. The heat transfer conditions were applied to all appropriate surfaces (tip-sample, probe-fluid and fluid-sample). For simplicity, the mesh of the different parts was merged allowing simplification of the

calculations (i.e. a mechanical interface with friction etc. was not required). Figure 72 shows how the nodes of the mesh are all connected across the interface forming a single body. In this case, the heat conductance between surface A and B is implemented by applying an appropriate heat conductance coefficient at the boundary between surface A and B. Different thermal conductance coefficients were assigned within COMSOL between each set of domains (Surface A/ Surface B for example). The heat transfer coefficient solid/environment interface was chosen to be $h = 10^5 \text{ W(m}^{-2}\text{K}^{-1})$ or $h = 10^8 \text{ W(m}^{-2}\text{K}^{-1})$ for solid/air and solid/water respectively. The heat transfer coefficient used for the solid/solid interface was $h = 10^7 - 10^{10} \text{ W(m}^{-2}\text{K}^{-1})$ for the parametric study.

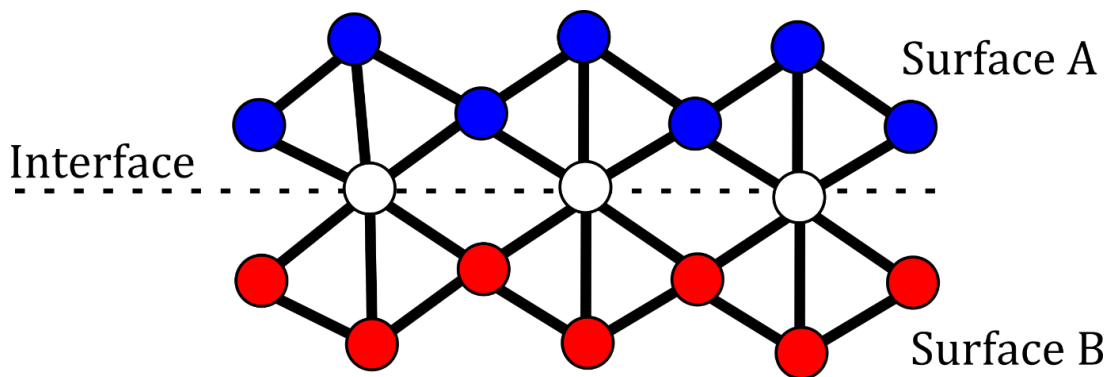


Figure 72 Schematic representation of an interface between different surfaces in COMSOL, where each circle is a node.

Several simulations were performed, focusing on when the probe was close to the region of interface between the two substrate materials. The probe tip-contact was moved from the material with high thermal conductivity (Pt: $71.6 \text{ [W/(m}\cdot\text{K)]}$) to the one with low thermal conductivity (Si_3N_4 : $3.0 \text{ [W/(m}\cdot\text{K)]}$). From every simulation, the average value of the tip resistor steady-state temperature was extracted and plotted. In this way a temperature vs scan-distance plot was generated. Figure 71 shows the 3D model used for these simulations with the tip 'scanning' the Pt/ Si_3N_4 sample. The zero μm x-axis point in the plots (Figure 73, a and b) represents the Pt- Si_3N_4 interface, with negative values corresponding to the Pt region, while positive values are the Si_3N_4 . In Figure 73, a the simulated probe temperatures are shown using two Y axes (left and right). It should be noted that the full y-axis scale is around 7 K on the left-hand axis and 1 K on the right-hand axis. This clearly illustrates the impact that varying the solid-solid heat transfer coefficient has on the magnitude of the signal detected. However, once superimposed (by scaling both signals to the same full magnitude) the data slopes at the interface match perfectly. In both cases, the

transition that is associated with scanning the probe from one material to the other is effectively instantaneous with the abrupt change in temperature, characteristic of a thermal scan in air. Conversely, the same simulation under water is shown in Figure 73, b, where a single vertical axis is used for both solid-solid heat transfer coefficients. This highlights a possible reason for the stability of SThM in water, which appears to be nearly independent of the change in solid-solid heat transfer coefficient, whilst remaining sensitive to the thermal conductivities of the two sample materials. However, this is also associated with a much less abrupt transition as the probe scans from one material to the other, as will be discussed later in this chapter.

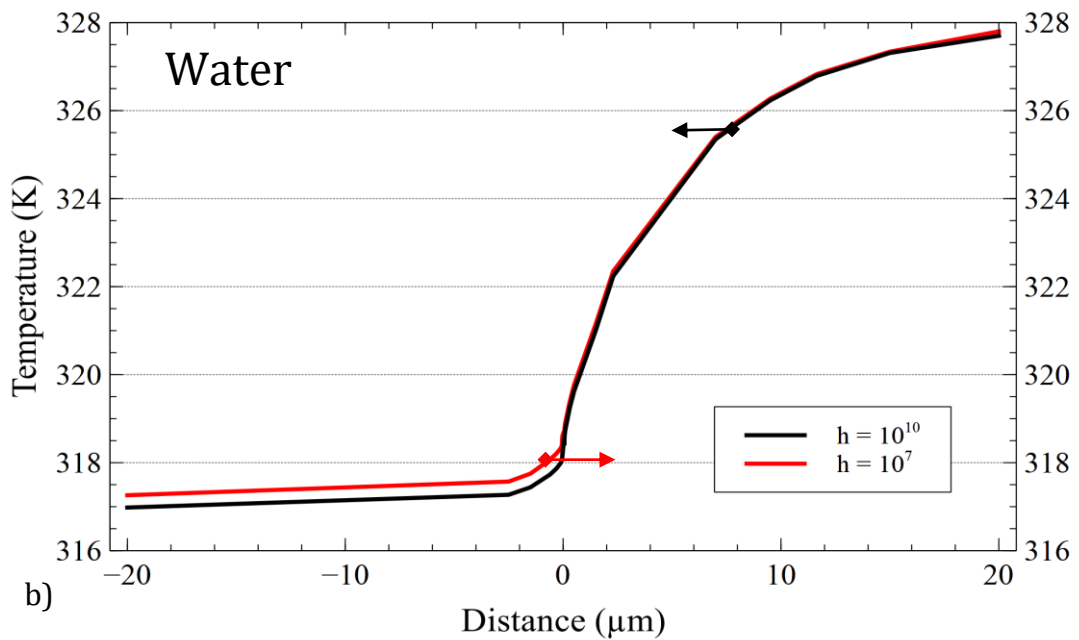
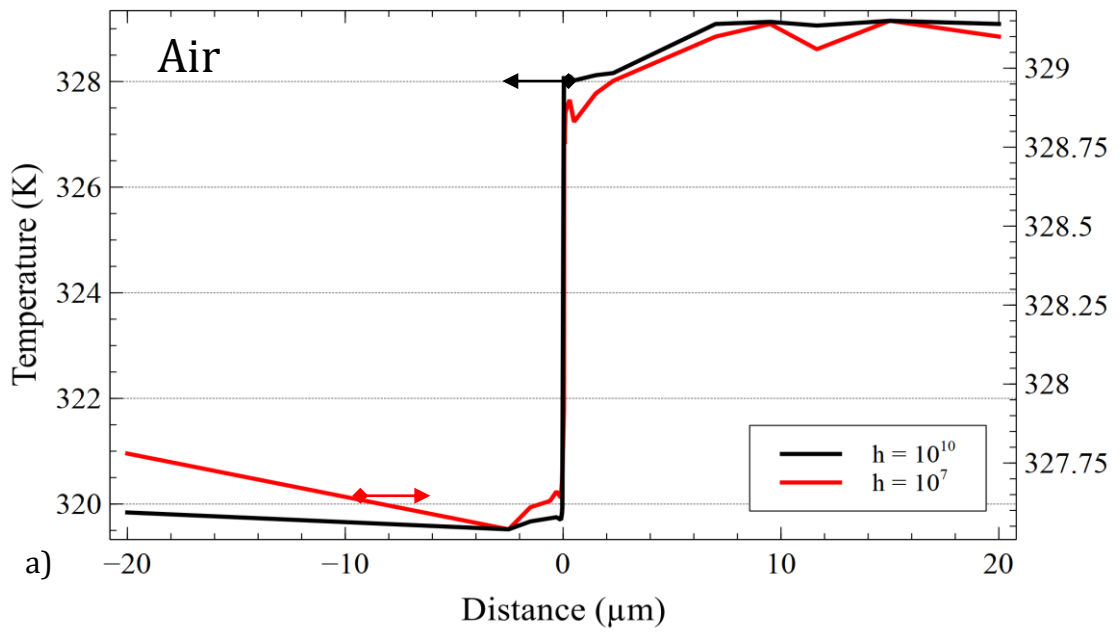


Figure 73 Plots of the average temperature of the probe during a line scan in the air (a) and in water (b) for the chosen solid/solid heat transfer coefficients ($h = 10^7 - 10^{10} \text{ W(m}^{-2}\text{K}^{-1})$). Arrows point the corresponding vertical axis.

To give an idea of how the temperature field is affected by the thermal conductivities of the different materials, three representative images of the simulated probe/sample temperature in water have been selected and shown in Figure 74 (in water). As expected, when the probe is located $20 \mu\text{m}$ from the Pt/Si₃N₄ interface on the Pt side (Figure 74a), the heat is better conducted through the sample lowering the tip's temperature. This is particularly evident by looking at the same results obtained in an air environment, shown in Figure

75a, where the area of the sample that is heated is very small. The temperature at the very apex of the tip in air is around 333 °C in comparison to the 300 °C seen in water. In addition, no significant increase in the sample surface temperature of the sample is observed, at the most 0.35 °C, a fact attributable to platinum’s high thermal conductivity. While approaching the interface (35 nm from it) as shown in Figure 74b, the heat spreads through the dissimilar materials and an increase in surface temperature is observed in the Si₃N₄ side.

Water

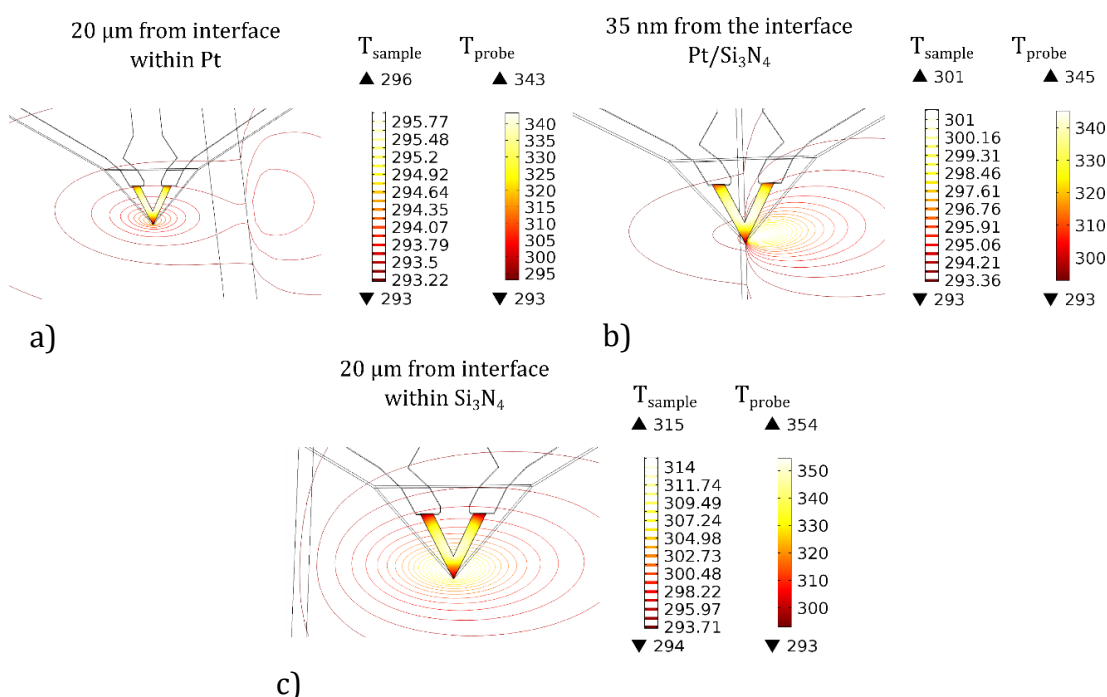


Figure 74 Temperature of the heater and sample during the simulated SThM scan of dissimilar materials at a) 20 μm , b) 35 nm and c) 20 μm from the interface in water.

In contrast, as depicted in Figure 75b, heat does not spread in air and still highly localised to the point of tip-sample contact, with the tip temperature remaining the same (333 °C).

Finally, when the tip is on the Si₃N₄ side (20 μm from the interface), as depicted by Figure 74c, the temperature is seen to increase for both tip and sample’s surface due to silicon nitride’s lower thermal conductivity when compared to Pt. This mirrors the in-air results shown in Figure 75c, where the sample temperature matches that predicted for the in-water system, although the probe temperature is still quite different, as expected for a probe surrounded by water

(discussed in detail in section 4.2). In all the cases shown it is also possible to see how the heated area of the sample is always larger in water than in air.

Air

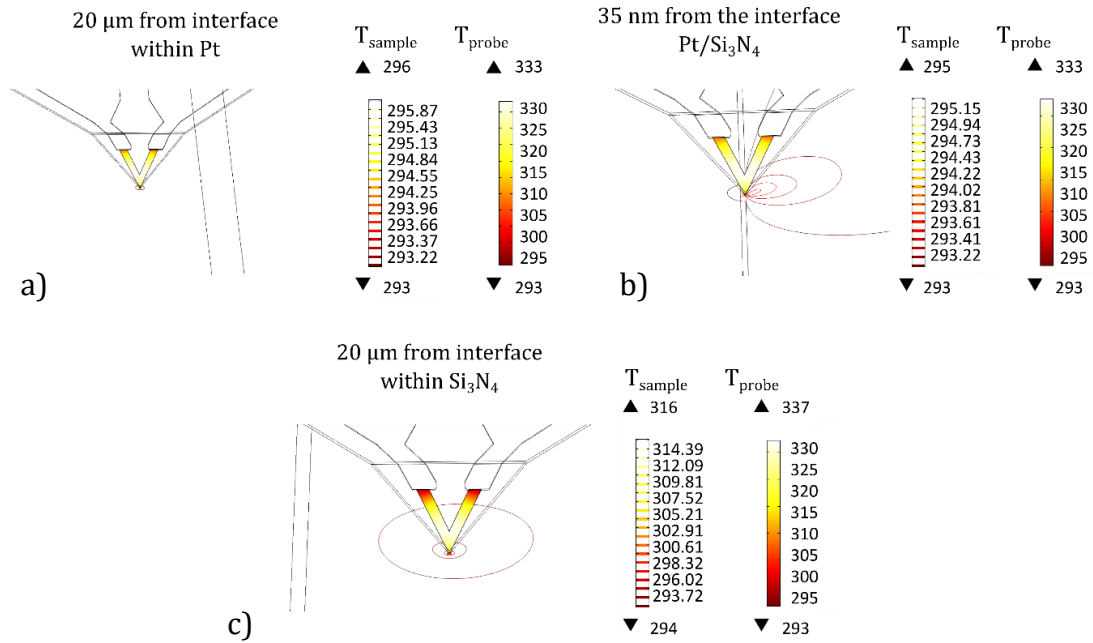


Figure 75 Temperature of the heater and sample during the simulated SThM scan of dissimilar materials at a) 20 μm , b) 35 nm and c) 20 μm from the interface in air.

To obtain the average temperature of the probe used in the plot of Figure 73, a simple but effective procedure was employed as shown in Figure 76.

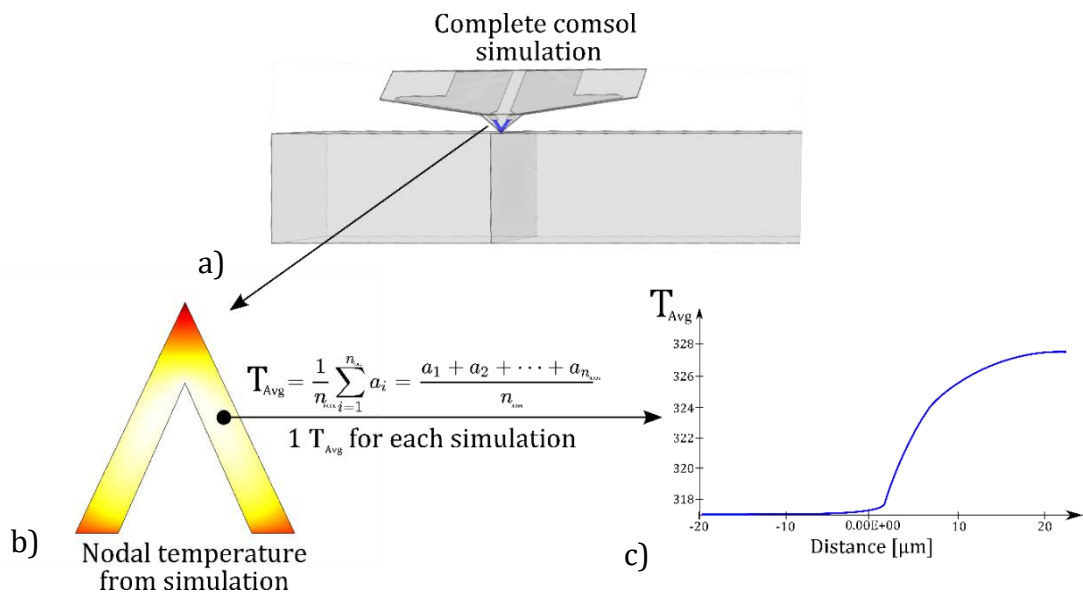


Figure 76 Schematic representation of methodology for average temperature calculation, a) finite element model in COMSOL, b) example of nodal temperature contour and c) the average temperature.

For each separate numerical analysis undertaken at a probe x-position (Figure 76a), the temperature from every node within the tip resistor was extracted and used to calculate the average as would be measured electrically (Figure 76b). This average temperature was then plotted against the distance from the interface (Figure 76c). This procedure was repeated for all twenty simulations and the plots produced for air and water environments.

It can be clearly seen that the two plots (Figure 73) exhibit significant differences between each other. First, in air, the magnitude of the probe temperature-jump strongly depends on solid-solid h , whereas in water it does not. In addition, the transition of the probe contact from one material to another results in an abrupt change in signal when in air, however in water the signal change is gradual. These observations can be mapped onto two characteristics expected of the experimental results:

1. Changes in the tip solid-solid contact material will result in significant variation of contact conductance, radically altering the magnitude of the signal in-air, while having a negligible effect in water (the where solid-solid tip-sample heat path is less significant than the solid-water-solid heat path). As a result, surface contamination that becomes adhered (or detached) to the surface or probe tip, will cause changes in the scan, but these changes will be much larger in air than in water.
2. Scanning across the transition between materials of dissimilar thermal conductivities will result in a much more abrupt signal change in air than in water.

Point 1 could explain the poor long-term thermal scan stability and noisy images that are observed in air but are absent in water, whereas point 2 suggests that a marked difference in resolution should be observable for in-air scans when compared to in-water. Point 1 will be considered below, whereas point 2 is explored in more detail in chapter 5.

Heat transfer between the tip and sample (sometimes considered as a purely solid-solid contact) has been found to be very complex due to the several factors that affect the thermal conductance between the two parts [240, 272]. Thermal contact conductance is the thermal conductivity of the interface between two contacting surfaces and is dependent on surface roughness, material properties, interface temperature, interface pressure and the presence of a water meniscus

that can fill gaps at the interface. This last factor is very relevant to this research. When conventional SThM is operated in air with normal levels of humidity a water meniscus is present at the tip-sample contact [69]. This water meniscus tends to appear during SThM scans due to the capillary condensation of humidity contained in the environment and is crucial in determining the thermal interaction between the sample and the probe. Figure 77 shows a schematic representation of a tip-sample contact and associated water meniscus, where R_a is the tip apex radius, w is the meniscus width and β is the ratio between the meniscus width and the tip apex diameter. These parameters are important for the calculation of the meniscus conductance as has been reported in [54].

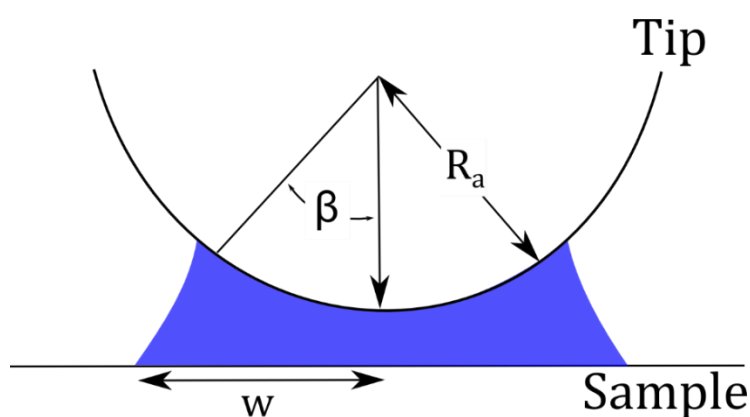


Figure 77 Schematic of the meniscus between the probe and sample [63].

Despite extensive research efforts, the magnitude of heat transfer across the water meniscus still a challenging topic, especially if the properties of water at such a small length scales are to be considered. Most importantly, it has been reported by Gomes et al [54] and Luo et al [88] that heat transfer through the water meniscus can dominate the other mechanisms present. Studies performed by Assy et al [63], demonstrated how the determination of tip-sample thermal conductance in the presence of the water meniscus can be complex, as its extent is intimately dependent on the type of surface analysed (hydrophilic or hydrophobic), the roughness of the surface and the humidity of the environment. As stated by Park *et al.* [240], hydrophilic interfaces are predicted to exhibit larger thermal conductance in comparison to the hydrophobic ones. This variability is addressed by the work in this thesis as, when the probe is completely immersed in an aqueous environment, the localised tip water meniscus does not exist anymore. Instead, an “infinite” water meniscus can be considered, remarkably simplifying the thermal interactions as its extent is

independent of the sample surface, temperature or humidity of the surrounding environment. In some ways this is analogous to the discovery by microscopists that AFM scanning under water provided a much gentler and more controllable environment than that found in air [181, 182]. Even if considered a solid-water - solid system (small amount of water trapped between probe and sample), the assumptions done above are still valid. In fact as it will be shown in next chapter, by looking at the temperature-distance curves in water (Figure 78, e), a few nm separation does not alter the signal significantly from hard contact. This is the reason why out-of-contact scans (see Chapter 5 lift-mode) are feasible.

When considering the thermal contrast exhibited in SThM scans within the two environments, the coefficients of thermal conductivity between the two media examined clearly play an important role. As reported Table 1 within the FE models two coefficients of thermal conductivity between the sample and the environment are considered depending on the use of air or water. Both the solid-fluid heat transfer coefficient and the thermal conductivity of water are larger than those exhibited by air. As a consequence, the presence of water not only homogenizes the tip-surface contact but also promotes solid-liquid heat transfer between the sample and the environment. This has the effect of minimising the rapid jump in signal (Figure 73, a) when the probe moves from a high conductive to a less conductive material. Similar results have been obtained by Ge et al [239], where the authors demonstrated that in an aqueous environment the thermal conductance of Au nanoparticles, chemically functionalised to be hydrophilic, do not exhibit abrupt changes during the measurement.

One interesting consequence of the impact of solid-solid heat transfer coefficient (h) on SThM images is that samples with two different thermal conductivities sometimes do not exhibit any contrast in their thermal images [1] when imaged in air. This can be the result of changes in heat transfer coefficient and material thermal conductivity cancelling each other out as the probe moves from contact with one surface to another. However, in water, the temperature of the probe looks to be largely tip-sample (solid-solid) h independent. This means that the contribution of h in water can be considered constant and the contrast does not vary with changes in tip-contact material, sample hydration or thin regions of surface contamination but is still sensitive to sample thermal conductivity.

4.5 CONCLUSIONS

Within this chapter, work was presented to demonstrate and understand the behaviour of SThM probes in an aqueous environment. The use of surrogate devices permitted the low-cost test and destruction of devices in three environments, air, flutec pp3 and DI water. In agreement with studies from other researchers, only the devices tested in DI water suffered failure. Analysis of the failure mode and comparison with the literature identified electrochemical corrosion of Nickel is the probable main cause. A solution to this problem, based on the electronic system described in Chapter 3, was then implemented and demonstrated to be successful.

In order to best interpret the data from the SThM scan, probes were calibrated, and the results compared to detailed finite element simulations in the same liquid environments (flutec pp3 and DI water). From the finite element simulations, a clear variation in thermal field changes was observed when operating in each environment. This was interpreted as being caused by the large difference in thermal conductivity between air, flutec pp3 and water. In water, the change in behavior was most significant, due to its higher thermal conductivity. Another consequence of water's high thermal conductivity was the prediction that it would facilitate better thermal coupling between the SThM tip and sample in comparison to air or Flutec.

These numerical results were backed-up by subsequent SThM scans of a solid sample (Pt/Si₃N₄). The scans were performed in air and water using the new liquid holder and instrumentation described in section 3.4. From the measurements the following points were demonstrated:

1. a-SThM can be operated safely in a liquid environment, attaining a maximum self-heating temperature of 65 °C, in line with that predicted by numerical analyses.
2. The electrochemistry-suppressing instrumentation used permitted stable, long-duration scans without probe failure or damage.
3. The overall thermal contrast exhibited by a-SThM was comparable to or better than traditional air scans.

4. When operating in water environments a better thermal coupling between sample and tip was achieved thanks to the larger thermal conductivity of water in comparison to air.
5. The enhanced thermal coupling allowed for better contrast and apparent improved stability, especially when scanning a surface that consisted of dissimilar materials, almost eliminating thermal artefacts which are present in conventional air scans.

In conclusion, the overall concept of aqueous SThM was fully demonstrated, and the potential limitations with respect to traditional SThM in air identified, demonstrating its readiness for more challenging applications.

CHAPTER 5: CONTACT AND NOT IN CONTACT a-SThM ON SOLID SAMPLES

5.1 INTRODUCTION AND MOTIVATION

To further explore the performance of under-water SThM beyond the topographic and thermal images discussed in Chapter 4, the effect of probe-sample separation together with the thermo-spatial resolution of contact scans was explored. One of the most interesting aspects of this new methodology is the possibility to obtain SThM images in non-contact mode. Results described in Chapter 4 suggest that the thermal coupling between the sample and the probe is enhanced by the water environment. This has been found to be very helpful in minimising artefacts and improving the stability of measurements made using the technique. This stems from the fact that the presence of water is expected to create an improved thermal connection between the probe's tip and the sample, beyond the solid-solid thermal contact normally present. When exploring this phenomenon, it is important to establish the impact of tip-sample separation on heat transfer in water. This includes the minimum distance required to obtain a signal at least comparable to in-air measurements, as well as the implication the phenomenon has on resolution when scanning different materials. This understanding is particularly important as, if proven, the approach could be used in a new SThM mode applicable to biological applications, where there are soft and delicate samples and gentle imaging is preferred. Specifically, a-SThM offers the possibility to exploit the large thermal conduction of water to establish good thermal coupling between the probe and the sample even in the absence of a solid-solid contact.

5.2 FEASIBILITY STUDY OF NON-CONTACT THERMAL MEASUREMENT

In order to investigate and demonstrate this aspect and to prove the impact of moving the SThM probe out of contact with the surface, simultaneous force-distance and temperature-distance curves can be generated. When considering these force-distance curves, carried out at a rate of 0.1 Hz and presented in Figure 78, a clear snap-into- and out-of-contact can be seen in the air (Figure 78a, d) for both mechanical and thermal signals. However, this feature is effectively eliminated underwater (Figure 78b, e).

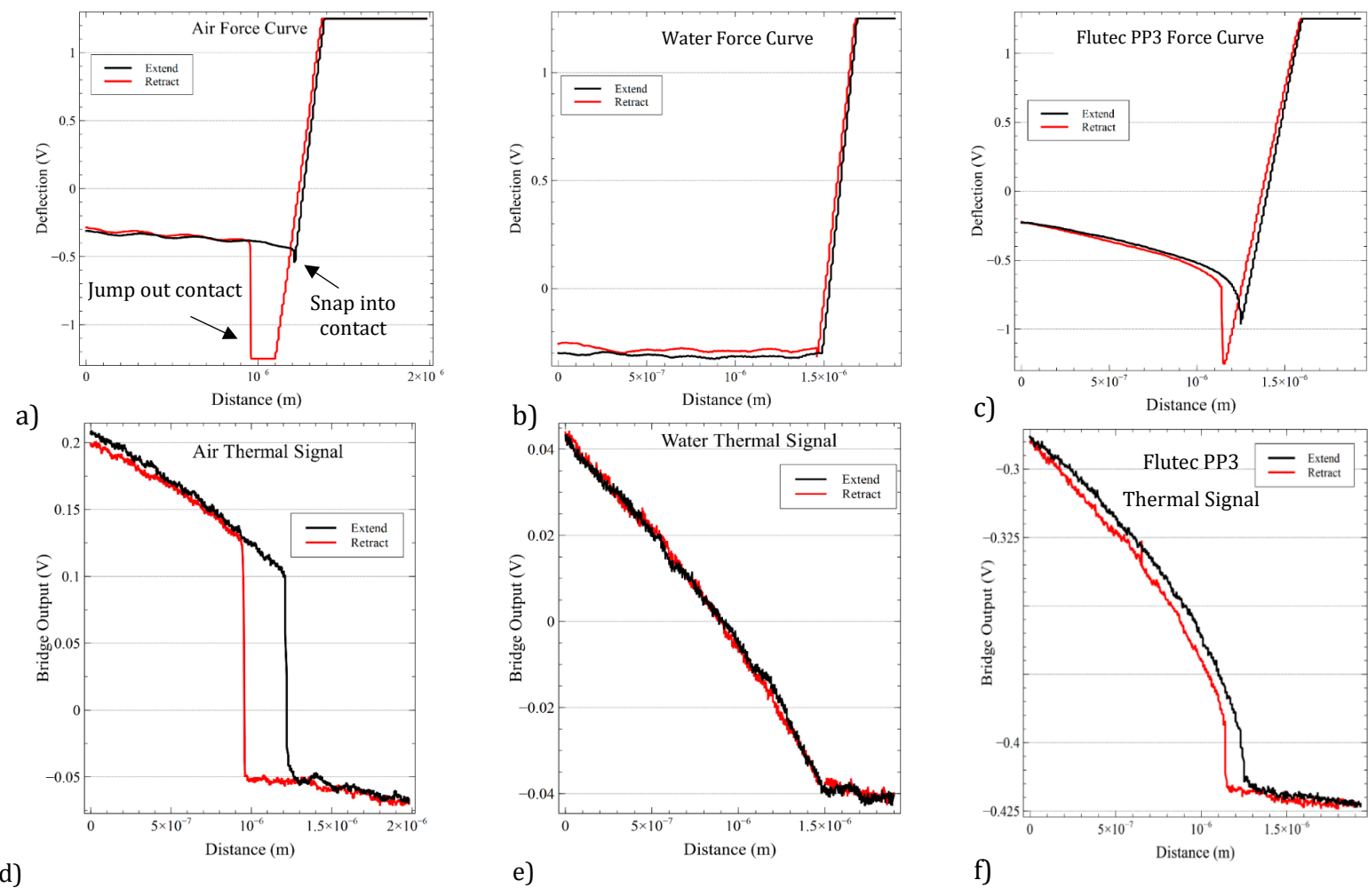


Figure 78 Comparison between SThM force curves (a), (b), (c) and thermal signals (d), (e), (f) over $\text{Si}_3\text{N}_4/\text{Pt}$ sample in air, in water and flutec PP3..

From a mechanical perspective, this is entirely consistent with the long-observed advantages of operating AFM underwater and is due to the absence of attractive capillary forces caused by the thin water film present when imaging in the air [182]. Although unsurprising, it should be noted this mechanical stability, even when the probe is extremely close to the sample, enables out-of-contact imaging with probe-sample separations of >100 nm. The absence of a sudden jump in the thermal signal can be attributed to the higher thermal conductivity of water in comparison to air, resulting in significant thermal coupling between tip and sample even when separated by a relatively large distance. This is important as it opens up the possibility of non-contact thermal scans, with strong tip-sample thermal coupling but zero mechanical interaction. One area where this could be particularly useful is the thermal imaging and manipulation of very soft samples (e.g. in biology) that could be damaged or distorted by tip-sample mechanical interactions.

To understand the role and importance of water, force-distance/temperature-distance plots were also acquired under flutec PP3 (Figure 78c, f). In flutec it is still possible to see a jump in contact (Figure 78, c), probably due to the continued presence of a thin water film on the surface (oily liquids such as flutec are immiscible in water). Consequently, a jump in the thermal signal response is also still visible (Figure 78, f). It should also be noted that in the flutec force curve, the horizontal approach-retract area (far from contact) is not flat but tends to curve. This is representative of the bimetallic SThM cantilever mechanical bending when the SThM probe is subjected to temperature changes, in this case, caused by it moving towards and away from the sample. To improve the thermal-mechanical stability different solutions have been proposed, Wenzler *et al.* [218] investigated the benefits of removing and redepositing the gold thin-film in conjunction with annealing steps. Conversely, others proposed complex cantilever designs with symmetrical supported torsion levers [273] or designing micromachined sample stages to reduce thermal drift [274]. Specifically, in this case, the probe is cooling down while approaching the surface, causing the probe's lower gold surface to contract more than the silicon nitride and the cantilever to deflect towards the surface. This mechanism is present during the measurements in both liquid environments. However, it is more evident in flutec, due to the higher (relative to water) cantilever temperature during self-heating.

This is caused by the lower thermal transport from the probe to the fluted environment and is explored in figure 51 of the previous chapter.

These experiments were also reproduced using the COMSOL model described in chapter 3. Figure 79 (a and b) shows the 3D temperature distribution of the self-heated probe tip, cantilever and the surface during contact between the Si_3N_4 sample and the probe. The main objective of these simulation is to numerically estimate the contribution of water environment on the conduction of heat between the tip and the sample.

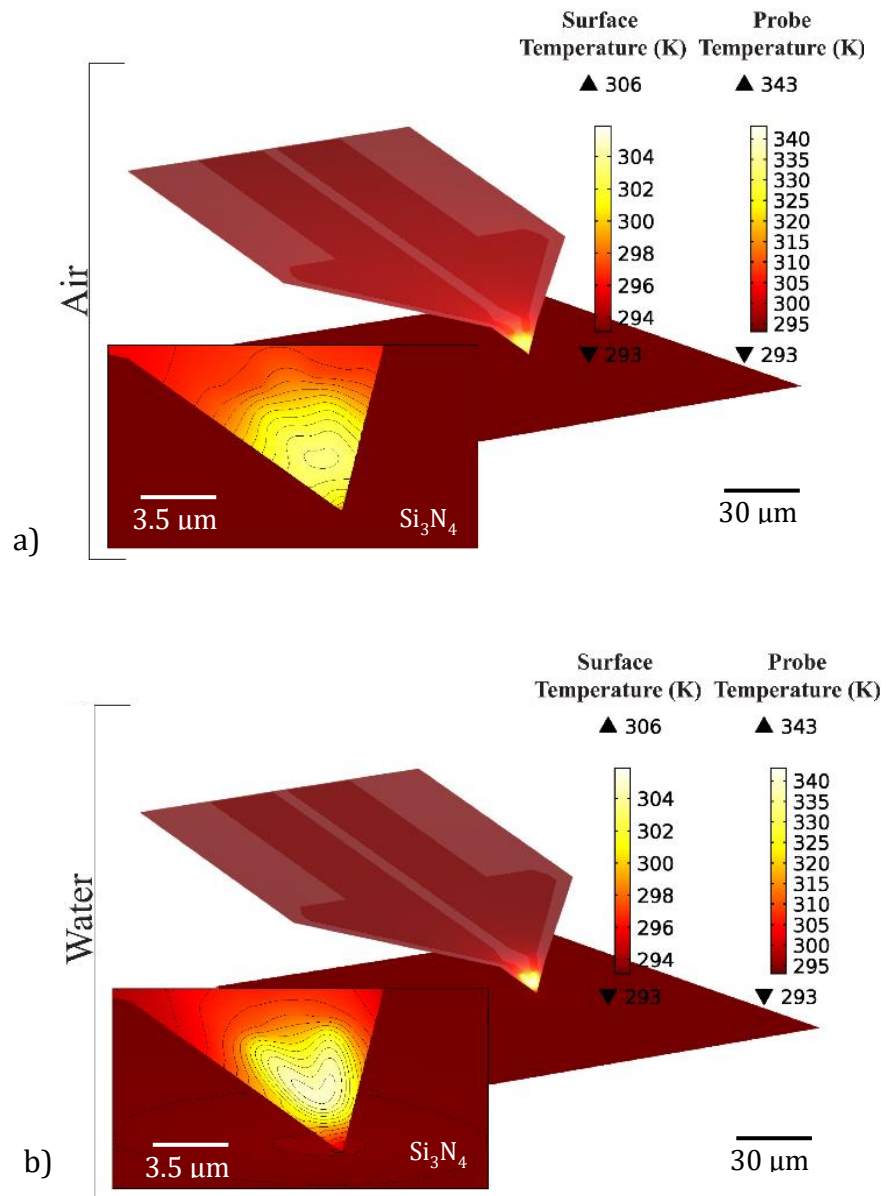


Figure 79 COMSOL MULTIPHYSICS 3D model of the probe in contact with Si_3N_4 sample. Increase of the temperature of the probe in contact with the sample and surface temperature distribution of Si_3N_4 in the air (a) and in water (b).

In air, the temperature distribution differs considerably to that seen in water. Again, this is due to the higher thermal conductivity of water allowing greater

heat transfer between the tip and the surface below, leading to a decrease in the tip temperature and in and a spatially wider increase in sample temperature. In order to further visualise the difference between scans in air and water when the probe is in contact, two numerical simulation were carried out and results are shown in Figure 80. The heat flux from the probe and the heated area in the two environments are shown.

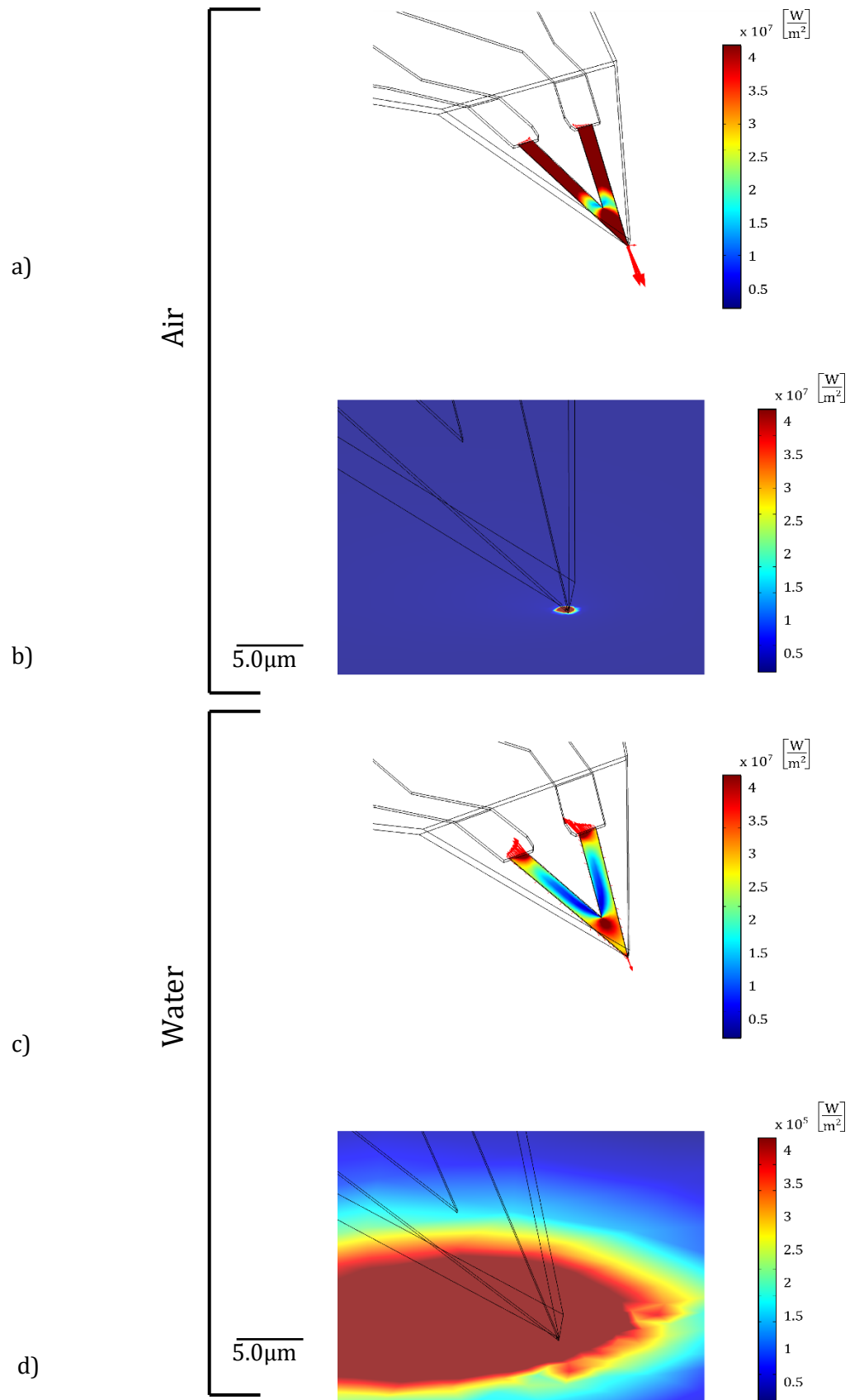


Figure 80 COMSOL MULTIPHYSICS 3D model of the probe in contact with Si_3N_4 sample. Total heat flux magnitude and heat flux vectors of the probe and the heated extension of the sample Si_3N_4 in the air (a-b) and in water (c-d) respectively (The vectors magnitude is **not** normalized to a single maximum value).

When operating in air (Figure 80a), the heat flux is very high on the probe, and it is predominantly at the tip apex. Most of the heat travels from the probe directly to the sample through the solid-solid tip contact, since the thermal resistance in this direction is minimal in comparison to other routes such as conduction to the air that is in contact with the probe. This is also clear in Figure 80b, where only a very localised area of the sample is heated. Conversely, when operating in water heat is also dissipated into the surrounding environment, with the heat flux directly into the sample significantly reduced in comparison to the in-air scenario (this can also be seen from the temperature plots in Figure 79b). The heat flux vectors (which are 1 order magnitude larger than those in air for display purposes) can be seen to predominantly point back along the cantilever, as well as out from the tip, however heat flux can also be seen all along the length of the heater (Figure 80c). As with the previous observations described above, the main effects of water are seen to reduce the temperature of the sample along with enlarging the area affected by the heat transfer (Figure 80d). This is one of the key differences of air, which despite showing higher heat flux at the tip apex than water, does not have the more even heat flux distribution all along the tip. However, it is also evident that the heat flux entering the surface is lower due to the dissipation in the surrounding environment, which is in line with the temperatures simulated and observed during experiments along this research work.

By repeating the simulations (above) for various probe Z positions, a plot of the averaged tip temperature (i.e. SThM measured signal) versus tip-sample separation (from 0 μm to 5 μm) was generated (Figure 81). The plot shows the same trend observed in Figure 82; with a gradual change of $\sim 2^\circ\text{C}$ in the tip temperature as it approaches the surface in water compared to the more sudden snap in/out of contact visible in air and flutec. This agreement of experiment and model suggests that the sample is still strongly thermally coupled to the tip in water, even when mechanical contact between the two is lost. However, the other two environments exhibit a much more abrupt decrease in thermal coupling as soon as the probe moves out of contact. It can also be seen that the probe temperature, both in and out of contact is much smaller in water than for the other two liquids. Again, this is consistent with the increased thermal conductivity of the water environment as described in the sections above.

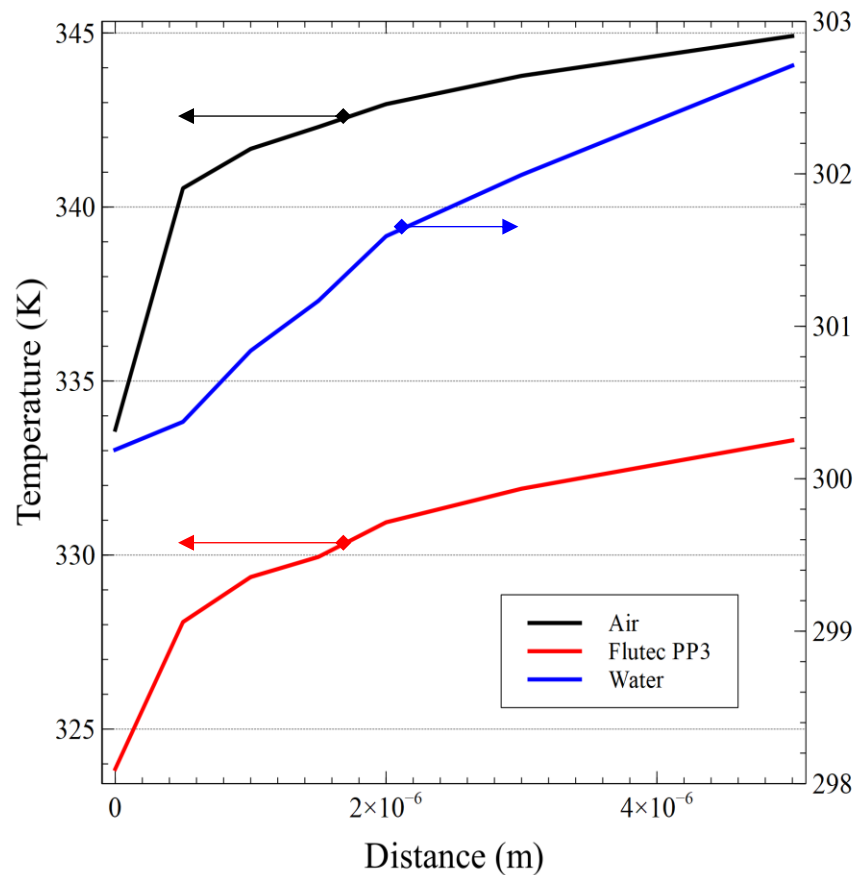


Figure 81 Plot of the average temperature of the probe versus its distance from Si in air, flutec PP3 and water (left vertical axis for Air and Flutec PP3 and right vertical axis for Water).

Experimental results were then compared to these COMSOL simulations. To better compare the results obtained from the different experiments, the temperature-distance signals in air, flutec and water were re-acquired using the same electrical gain in output and are plotted together in Figure 82. These curves represent from left to right on the X axis, the probe approaching and making contact with the sample. In agreement with the modelled data in Figure 81, the total variation in the measured thermal signal obtained in water is much smaller than that observed in the other two environments. Although flutec has some similarities with water (i.e. a more gradual temperature variation out of contact), its overall magnitude is more comparable to air. This matches the trend of thermal conductivities of each environment ($k_{\text{air}} = 0.025 \text{ W m}^{-1} \text{ K}^{-1}$, $k_{\text{flutec}} = 0.0611 \text{ W m}^{-1} \text{ K}^{-1}$ and $k_{\text{water}} = 0.563 \text{ W m}^{-1} \text{ K}^{-1}$) as well as the presence or absence of a thin water film as described previously.

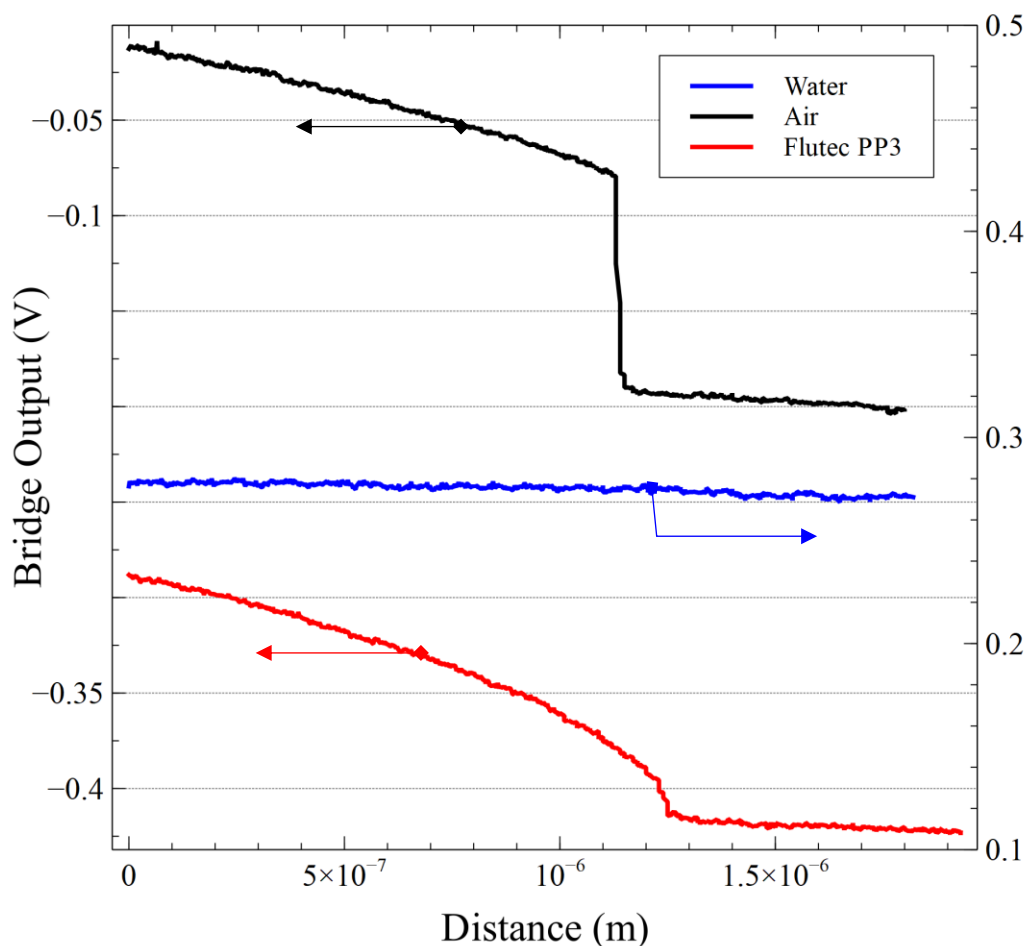


Figure 82 Plot of approach thermal signal of probe versus its distance from Si₃N₄/Pt sample in air, flutec PP3 and water (left vertical axis for Air and Flutec PP3 and right vertical axis for Water).

The absence of capillary induced snap-in and out of contact as also demonstrated in Figure 78b, d, shows that the SThM probe exhibits great mechanical stability and tip-sample thermal coupling with tip-sample separations >100 nm. This opens up the possibility to carry out non-contact nano-thermal studies of fragile samples such as biological material, suspended nanostructures or brittle and porous materials [94].

5.3 NON-CONTACT THERMAL MEASUREMENTS

The simplest way to implement non-contact thermal imaging, whilst ensuring a consistent tip-sample separation is to employ a technique built into the Multimode AFM called ‘lift mode’ [275]. In lift mode AFM, an image of the sample is generated in two passes, as shown in Figure 83. During the first pass (Main Trace) the tip is in contact with the surface, scanning a complete line and recording topography in the normal manner. Before starting the second line, the tip is lifted to the “Lift start height”, a large start height is typically used to ensure the tip is fully separated from the sample as necessitated if tip adhesion is

significant, a common occurrence when measuring soft samples. At this point topographic feedback is automatically turned off, the tip is positioned away from the surface by a pre-set distance (Lift Scan Height) and line scan is repeated (on the Lift Trace) with the tip following the topographic data recorded in the previous sweep. In this way, the probe records the topography of the sample when in contact and then uses this to scan the same line profile out of contact. It is possible to observe from Figure 83 that an angled feature will have a different separation from the tip. However, the temperature-distance curves (Figure 78) show that, in water, the variation of signal with separation does not have a steep gradient compared to the sudden jump seen in air (and to a lesser extent, flutec). In air, a 100 nm change in separation close to the surface jumps the signal by approximately 70% of the entire change seen in the 2 μm temperature-distance curve. In flutec, the same jump is around 20% of the entire change, in water it is less than 10%. Therefore, in water, small variations in distance will not significantly impact the probe signal.

In our experiment, this meant topography and thermal signals were recorded in contact and then a second thermal signal was recorded with the probe retracted from the surface.

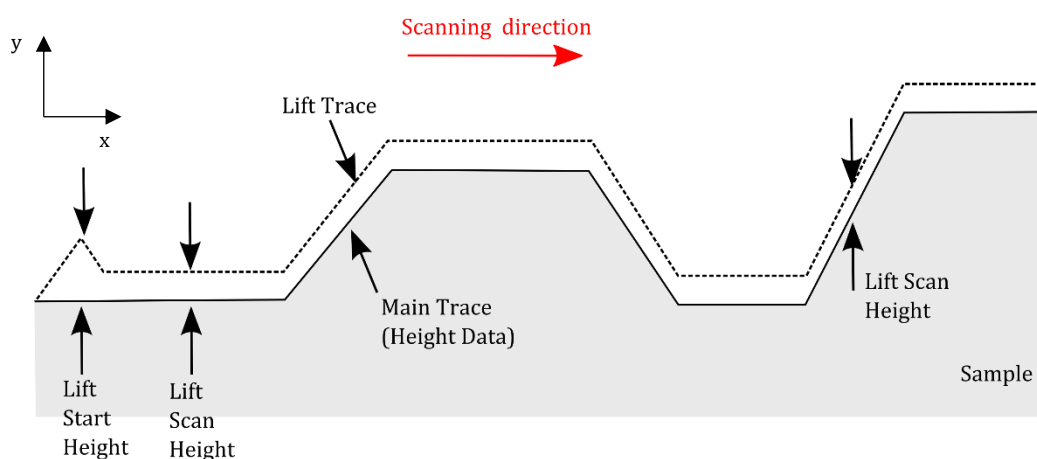


Figure 83 Lift mode profiles, where dashed line represents lift mode scan.

Figure 84 shows the results from AFM and SThM in water for two different separation heights (0.5 μm and 1.5 μm). From a first view of the results using AFM (Figure 84a, b, c and d, e, f), the measurement is viable although the signal can be seen to decrease when the height is increased to 1.5 μm . It can also be seen that the thermal signal in water is very stable both in and out of contact (Figure 84c and f).

In order to evaluate the significance of water in this result as opposed to any liquid in general, the experiment was also carried out under flutec pp3. As can be seen in Figure 85, the thermal images obtained under flutec exhibit inferior lift-mode thermal contrast when compared to water, even when the tip-sample separation is only 0.5 μm (Figure 85, c). This phenomenon is even more evident at 1.5 μm lift height, where the transition from Pt to Si_3N_4 is barely discernible under flutec (Figure 85, f), whilst still being clear under water (Figure 84, f). By comparing the non-contact scans obtained in these two liquids, it is evident how important the specific surrounding environment is in a liquid-SThM measurement.

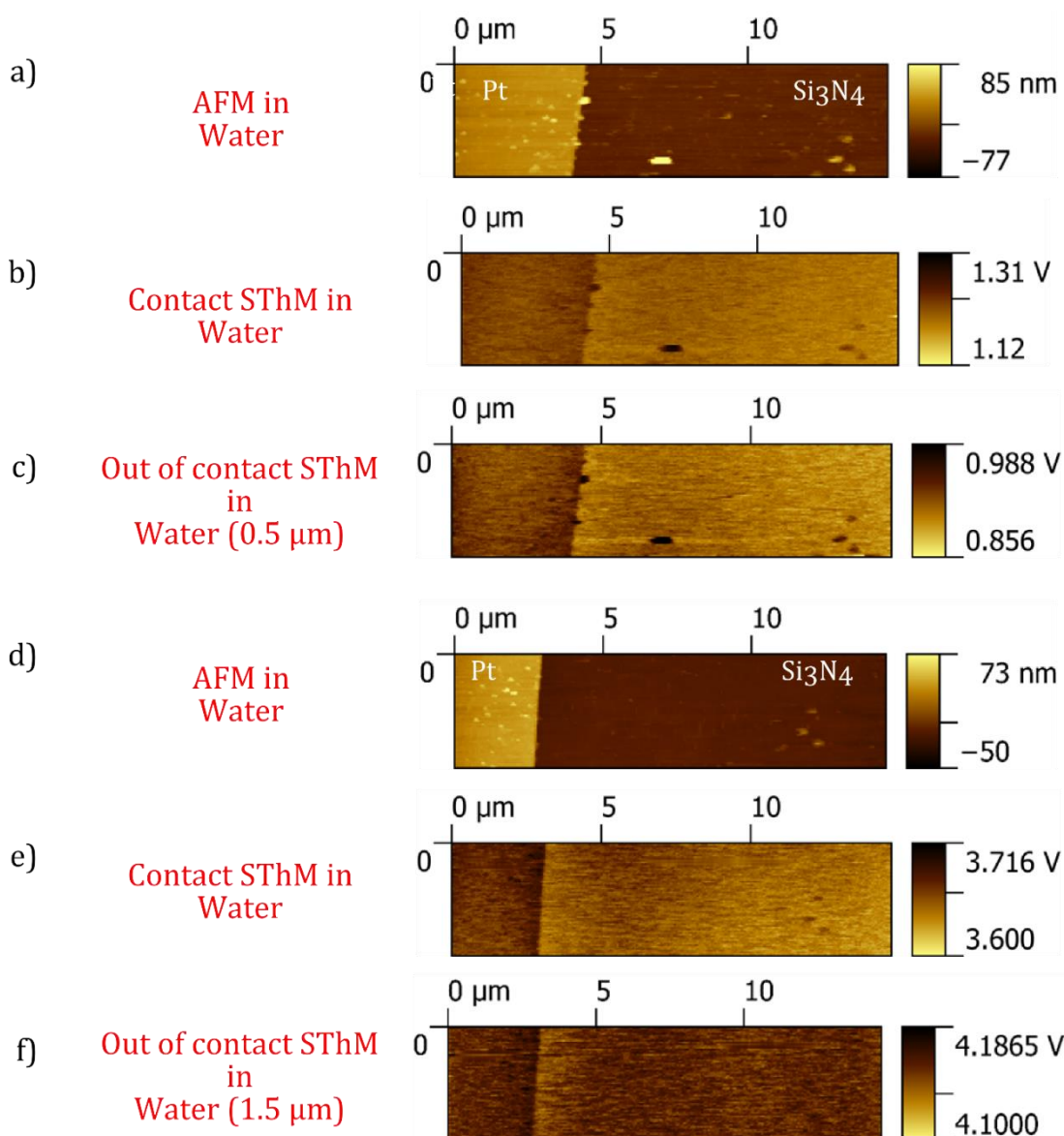


Figure 84 SThM of Pt on Si_3N_4 in water showing AFM height images (a-d), thermal images in contact (b-e) and thermal images out-of-contact (c-f) with probe distant from the surface of 0.5 μm and 1.5 μm .

As detailed in Chapter 4, this is primarily due to the difference in thermal conductivity of the two liquids: $k_{\text{water}} = 0.563 \text{ W m}^{-1} \text{ K}^{-1}$ respect to flutec, $k_{\text{flutec}} = 0.0611 \text{ W m}^{-1} \text{ K}^{-1}$. Following this observation, water can be clearly seen to be the most efficient, accessible environment for non-contact thermal imaging. Having said this, it should be noted that the thermal conductivity of flutec is still superior to air ($k_{\text{air}} = 0.025 \text{ W m}^{-1} \text{ K}^{-1}$), making non-contact imaging in flutec possible at small tip-sample separations, an important consideration if the sample is incompatible with water (e.g. due to solubility or chemistry).

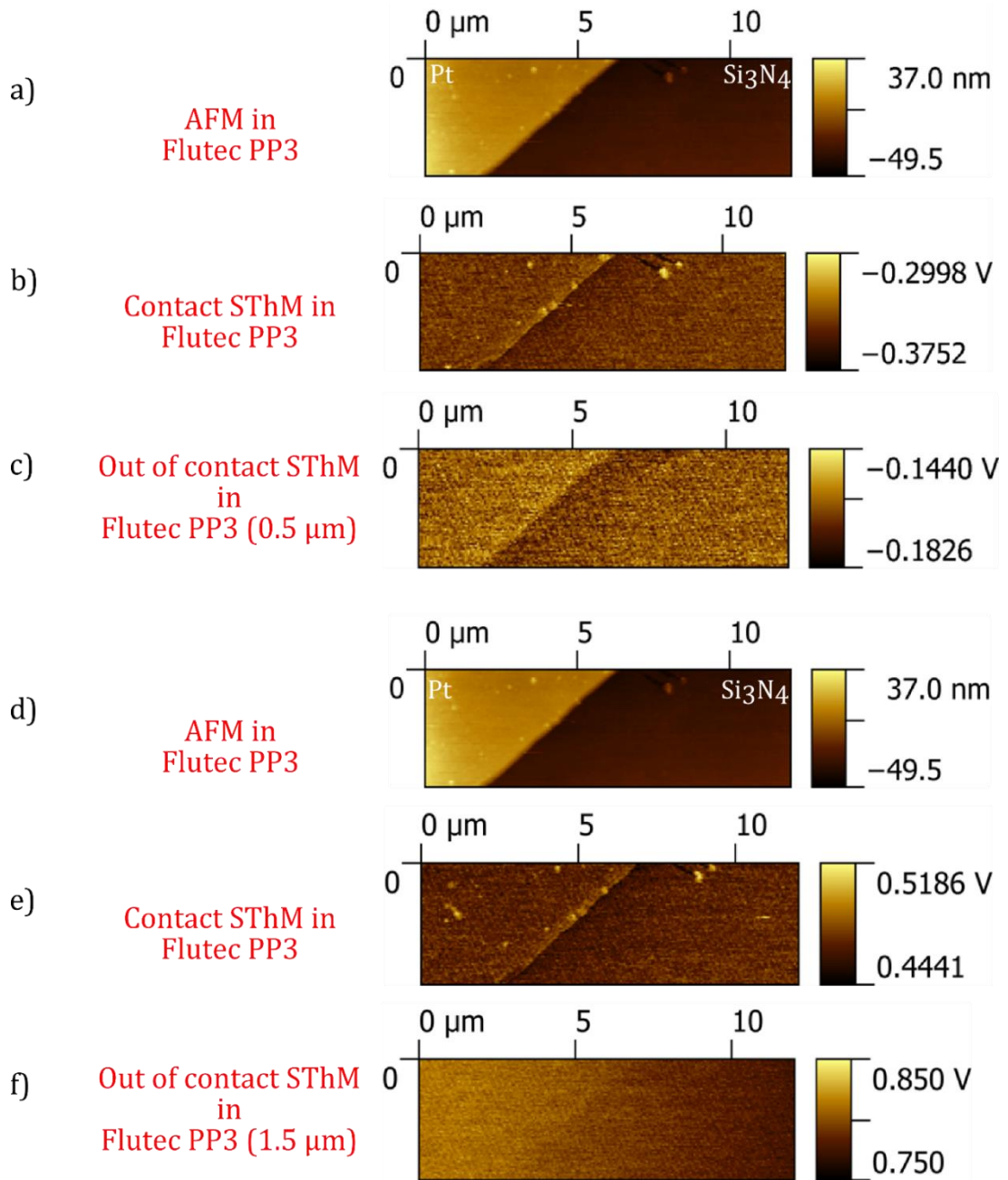


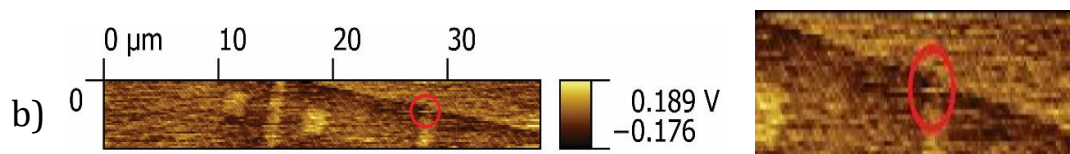
Figure 85 SThM of Pt on Si₃N₄ in flutec PP3 showing AFM height images (a-d), thermal images in contact (b-e) and thermal images out-of-contact (c-f) with probe distant from the surface of 0.5 μm and 1.5 μm .

To investigate non-contact thermal imaging of more complex samples, the same measurement was carried out on a Au/Si₃N₄ sample that will be described in more detail in Section 5.3. However, in brief, the sample consisted of various sized, thin film gold (Au 100 nm, NiCr 5 nm) features produced using e-beam lithography, metal evaporation and lift-off on a Si₃N₄ (50 nm thick) coated Si wafer. This time, SThM thermal images were acquired with the probe in contact and lifted 1.5 μm from the surface. Figure 86 shows topographic (a), contact SThM (b) and out-of-contact images (c) in water. The lifted thermal scan not only shows very good resolution with the probe 1.5 μm away from the surface but the topographic artefact, which is evident in the contact -mode thermal scan (red circles in Figure 86), is no longer visible out-of-contact.

Topography



In contact SThM



Out of contact SThM (1.5 μm)



Figure 86 SThM of Au on Si₃N₄ in water showing AFM height images (a), thermal images in contact (b) and thermal images out-of-contact with probe distant 1.5 μm from the surface (c) and zoom in of the associated picture within the red circle, showing a thermal artefact.

Thermal conductivity, as imaged by SThM, may not accurately reflect the true sample thermal conductivity due to artefacts originating from the tip-sample contact, for example those induced by sample surface roughness. These variations in thermal coupling between sample and probe alter the heat flux and therefore the measured temperature. This affects contrast in the thermal image and can occur during the scan, while the tip scans over changes in surface roughness, or when the tip-sample contact varies.

To better understand the mechanisms at play, Figure 87 shows a cross-section view of the 3D FE simulation results of an SThM probe in- and out- of contact with a high thermal conductivity sample (Si). In each case, the probe self-heating currents for each environment were different and selected to be probe-safe whilst resulting in similar operating probe temperatures as detailed in section 3.7. There are a number of important aspects that this data demonstrates: It is possible to see that, in air (Figure 87, b) and in flutec (Figure 87, c), the out-of-contact probe has almost the same tip temperature distribution along its length, with a significant tip temperature difference of several degrees between contact and out-of-contact.

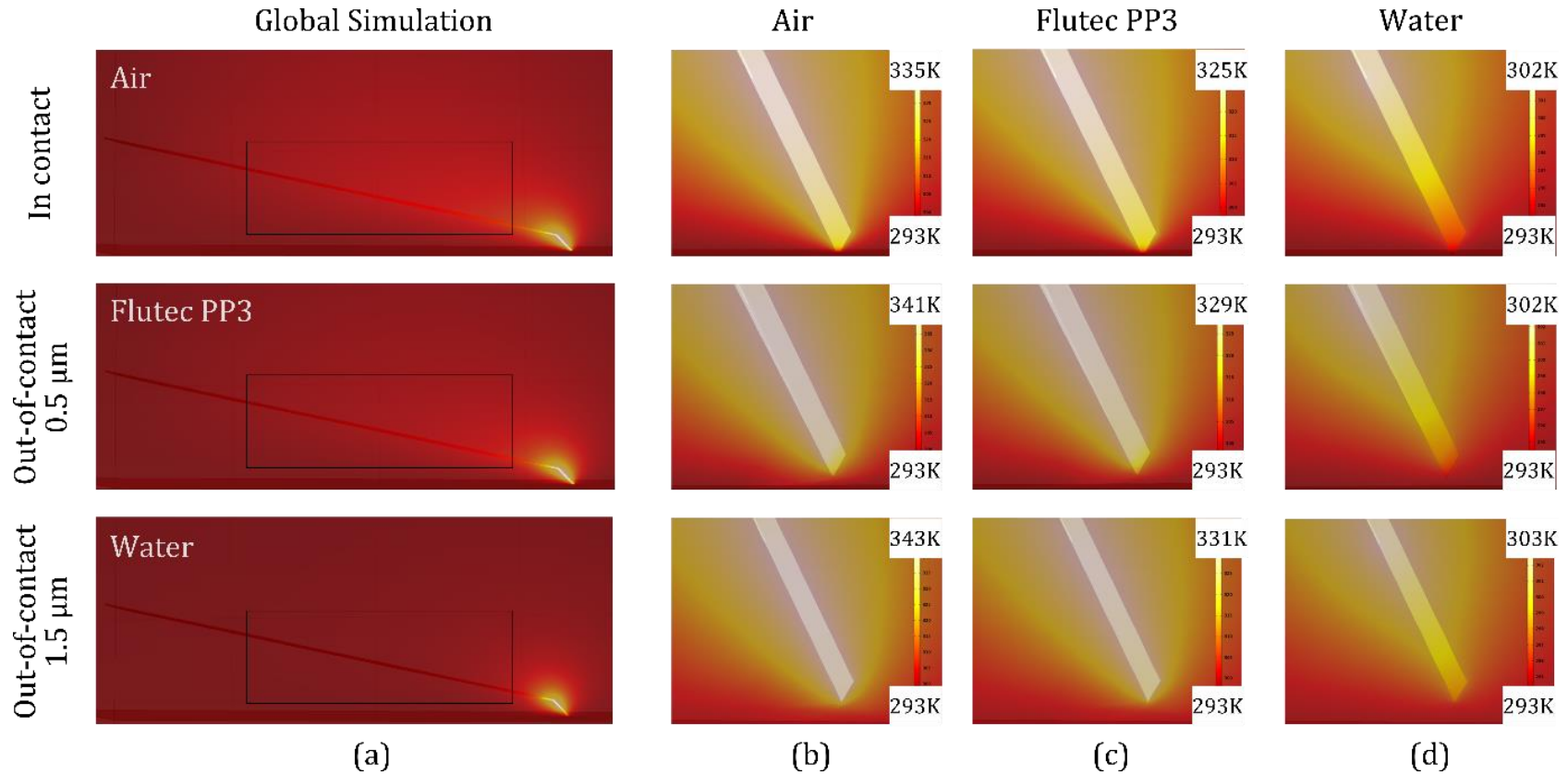


Figure 87 Cross sections through 3D FE simulation of typical Si_3N_4 cantilever with Au leads and Pt thermal sensing element heated by Joule Heating. The global simulation images (a) show the difference of cantilever temperature distribution (black rectangles) between water and the other two environments. Zoomed view of the tip in contact with Si and out-of-contact ($0.5\mu m$ and $1.5\mu m$) in air (b) flutec PP3 (c) and water (d).

It can also be seen from the plot that the tip temperature follows a similar trend in both environments, with a lower temperature at the apex of the tip. The main difference being the temperature magnitude which is a function of environment thermal conductivity and drive current. Although less easy to visualise, the same phenomenon can be seen in the maximum temperatures shown in the contours (Figure 87,b and c). However, in water (Figure 87, d) the temperature distribution shows a completely different trend, where significant apex cooling can be seen even 1.5 μm away from the surface. By comparing the results (Figure 87, d), for the contact and complete non-contact case, the temperature distribution in the area next to the tip changes more significantly. In order to better visualise the effect of contact and out of contact, temperature profiles along the probe apex are shown in Figure 88 and Figure 89 for air, flutec PP3 and water.

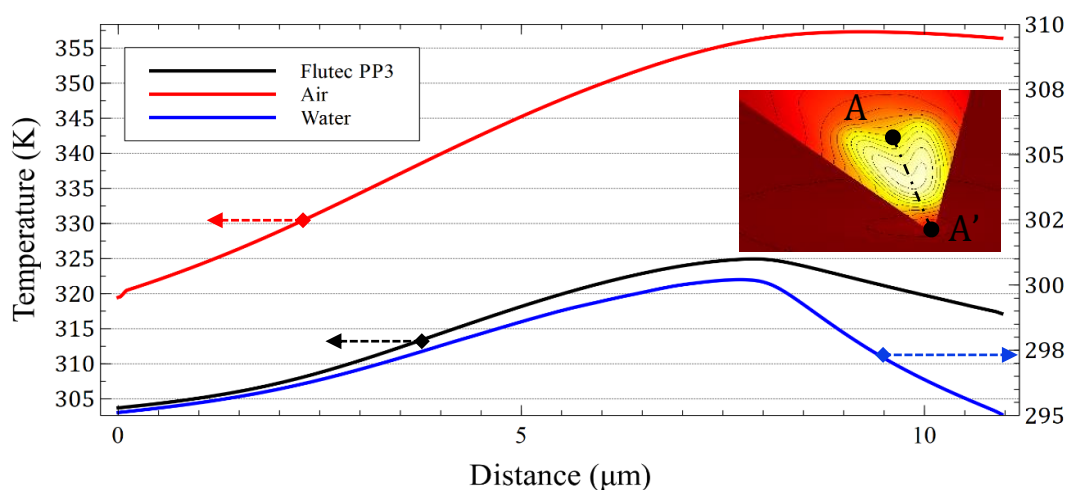


Figure 88 Temperature along the probe apex, on the path A-A', when performing SThM (simulation) in Air, Flutec PP (left vertical axis) 3 and water (right vertical axis) in out-of-contact at 1.5 μm from the sample.

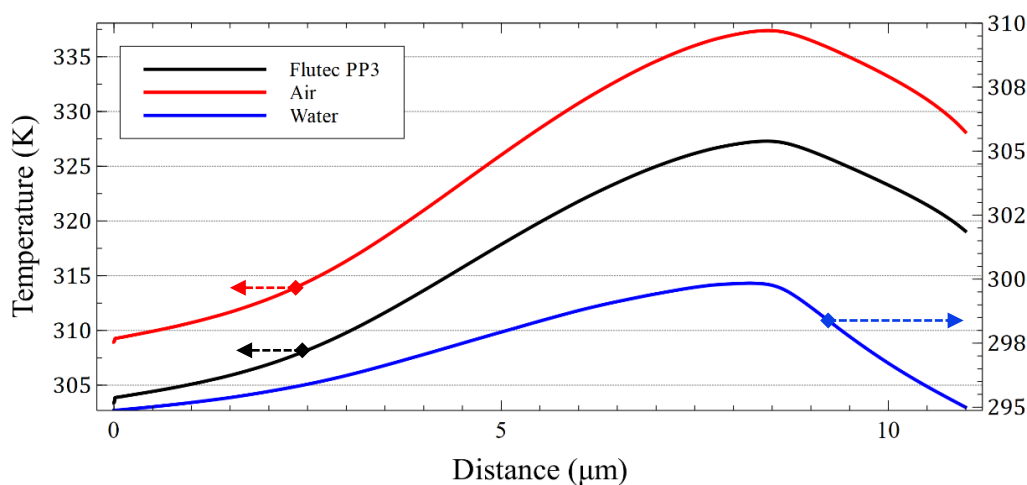


Figure 89 Temperature along the probe apex, on the path A-A', when performing SThM (simulation) in Air, Flutec PP (left vertical axis) 3 and water (right vertical axis) in-contact with the sample.

The main difference between contact and out of contact is in the temperature behaviour in the area close to the sample. When out of contact, the temperature stays constant in air and flutec pp3 (at the tip apex), but this decreases when the same simulation is performed in water. This suggests a better thermal coupling despite the presence of a physical gap between tip and sample. Conversely, a similar trend is observed when in contact. However, the temperature measured in water is always lower than the other two environments. In addition, a steeper temperature gradient is observed at the end of the tip, as shown in and Figure 89. Different visualisations of the results obtained from FE simulations are presented in Figure 90, where the probe (Figure 90a, b) and surface temperature (Figure 90c, d) are shown for the in-contact case within air (a, c) and water (b, d) environments respectively. As expected, the sample surface in the air (Figure 90c) experiences a higher maximum temperature than the sample in water (Figure 90d). It worth noting that although the peak surface temperature is lower underwater, the heated area extends over a larger area. This is consistent with the thermal-spatial resolution (section 4.4), temperature-distance coupling (section 5.1) and reduced self-heating (section 4.3) described in the previous sections and all ascribed to the better thermal coupling between the probe and the environment/sample achievable in water. Similar results were obtained for out of contact simulations and are shown in Figure 91. The temperature field across the probe is depicted in Figure 91a and Figure 91b, for air and water respectively. When operating in water the tip apex is colder than when operating in air. This localised drop in temperature is associated with the localised increase in sample temperature shown in Figure 91d. Conversely in air, as it is shown in Figure 91c, the temperature of the sample under the probe remains close to the ambient temperature. This result is not unexpected as the amount of heat travelling from the tip to the sample is significantly lower in air compared to the water environment. Finally, it can be seen in Figure 91d that in water, the area of the sample displaying an increase in temperature remains localised below the apex of the probe tip.

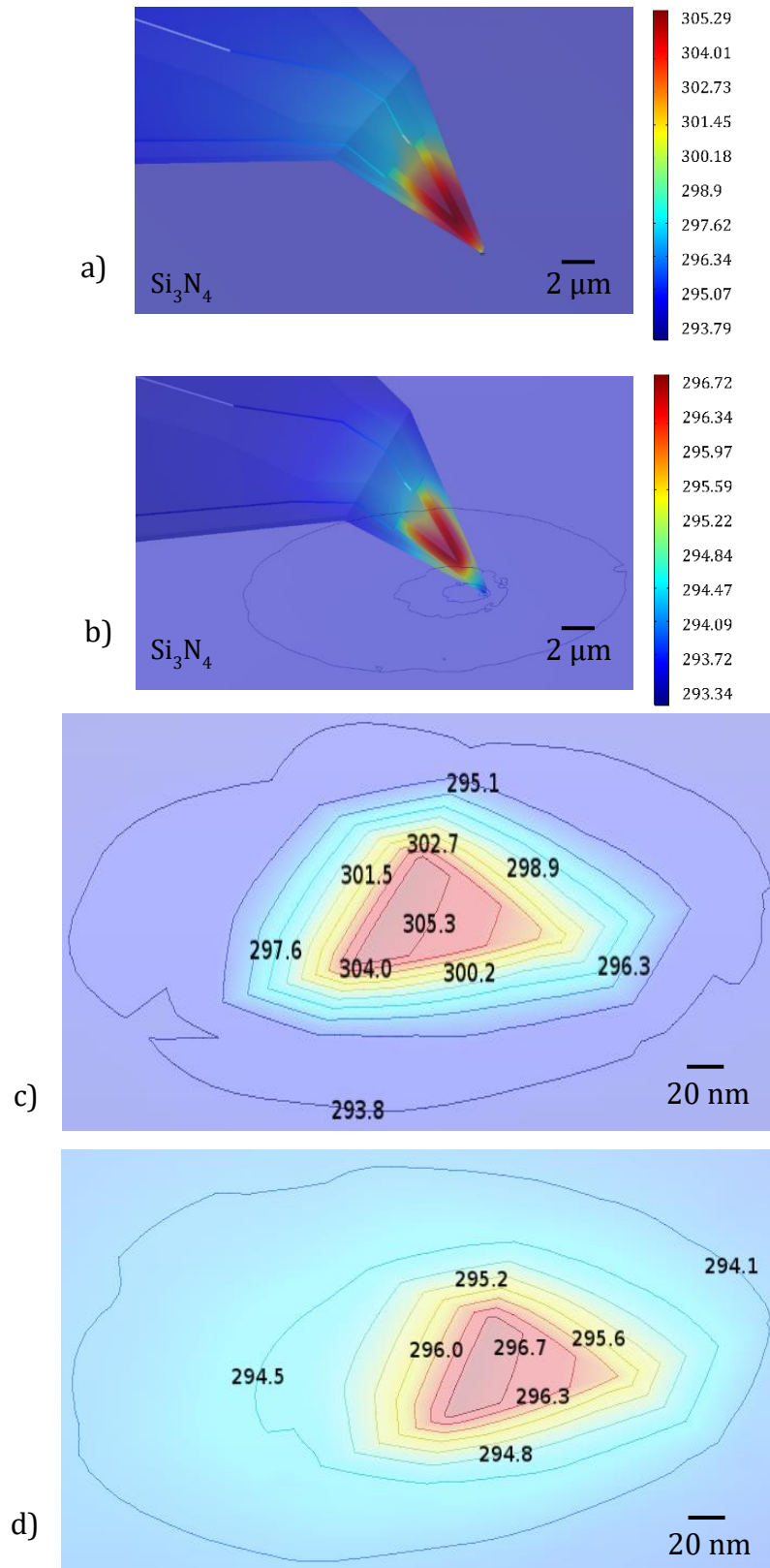


Figure 90 In contact SThM simulations results showing the probe temperature for air and water environment (a and b). The local temperature of the sample's surface is shown in c and d for air and water environments respectively.

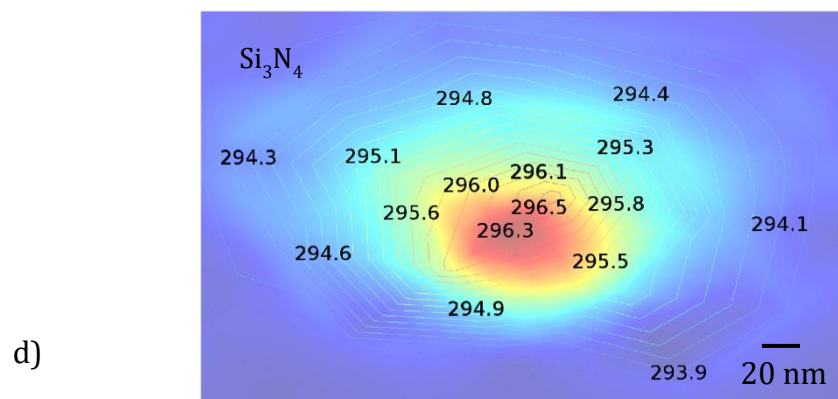
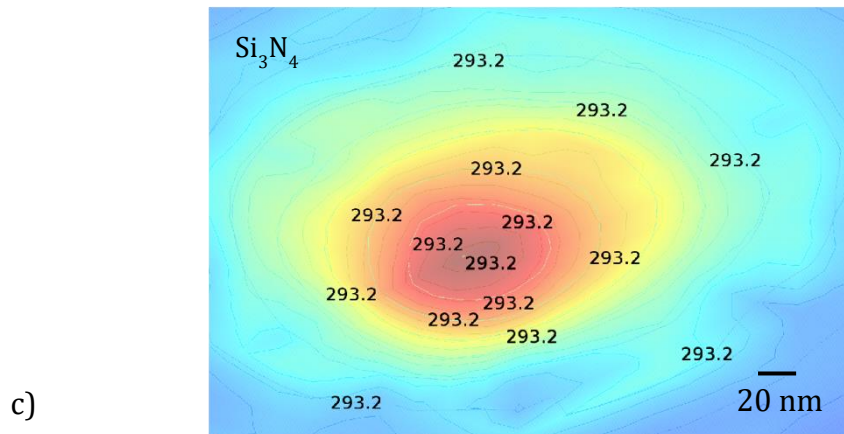
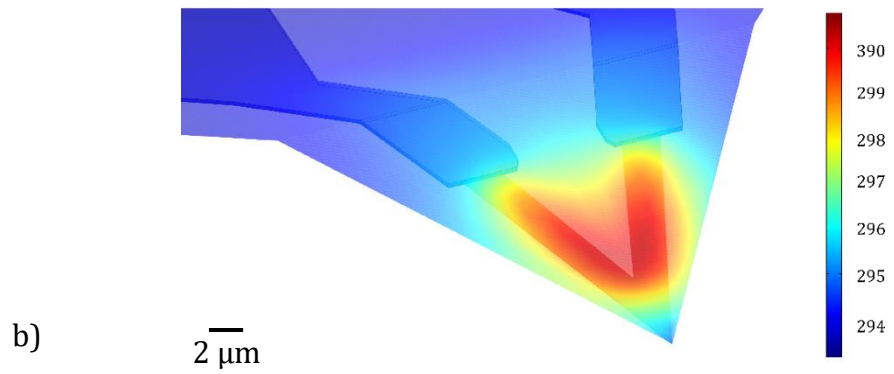
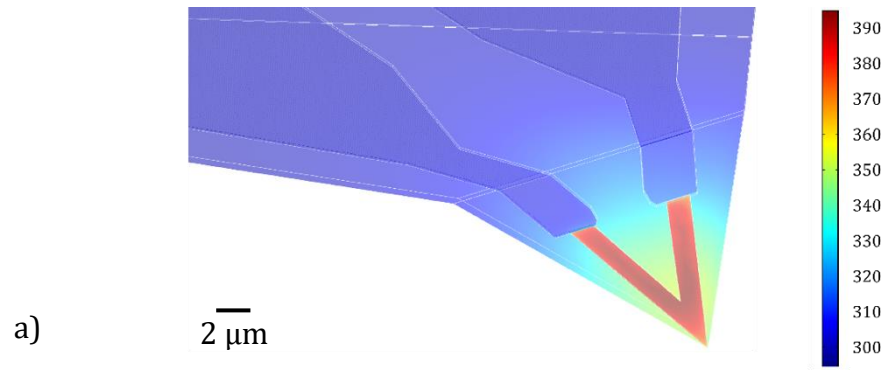


Figure 91 Out of contact SThM simulations results showing the probe temperature for air and water environment (a and b). The local temperature of the sample's surface is shown in c and d for air and water environments respectively.

The difference between air and water is highlighted by plotting the total heat flux magnitude of the heater and sample (separately). In Figure 92a and Figure 92c, the total heat flux generated within the heater during the simulation is shown alongside vectors. This magnitude is obtained by the combination of the heat fluxes in all the 3 normal directions (x-y-z). In air, Figure 92a, the magnitude of the heat flux is lower than that measured in water (Figure 92c). By comparing the path of the vectors, representing the heat flux coming from each node, it is also possible to observe how heat travels away from the probe to the sample and the environment. In this case the heat flux vectors for air have been magnified 10 times and those for water reduced of 10 times in order to produce a clear image. This was necessary due to the large difference in heat flux generated in the two environments. In air (Figure 92a) the heat travels predominantly back along the cantilever due to conduction as well as from the tip into the sample. Conversely, in water (Figure 92d) heat leaves the heater in a more uniform manner, both through conduction along the probe but also into the liquid environment due to the lower thermal resistance offered by the water/solid interface.

These observations are further strengthened by Figure 92b and Figure 92d, where the inward heat flux is shown for the sample surface. The difference between air and water of the heat flux flowing in the sample is significant. The use of water as a medium improves the thermal coupling between the probe and sample and, at the centre of the sample, the maximum heat flux is around $-1.02 \text{ E}^6 \text{ W/m}^2$ whereas in air it is $-4.14 \text{ E}^5 \text{ W/m}^2$. However, it worth mentioning that even in water, the heat flux vectors remain mainly within the silicon nitride of the probe as shown in Figure 92c. This is unsurprising, given that, despite water's relatively high thermal conductivity (0.563 W/mK), silicon nitride still has a much higher conductivity (3 W/mK).

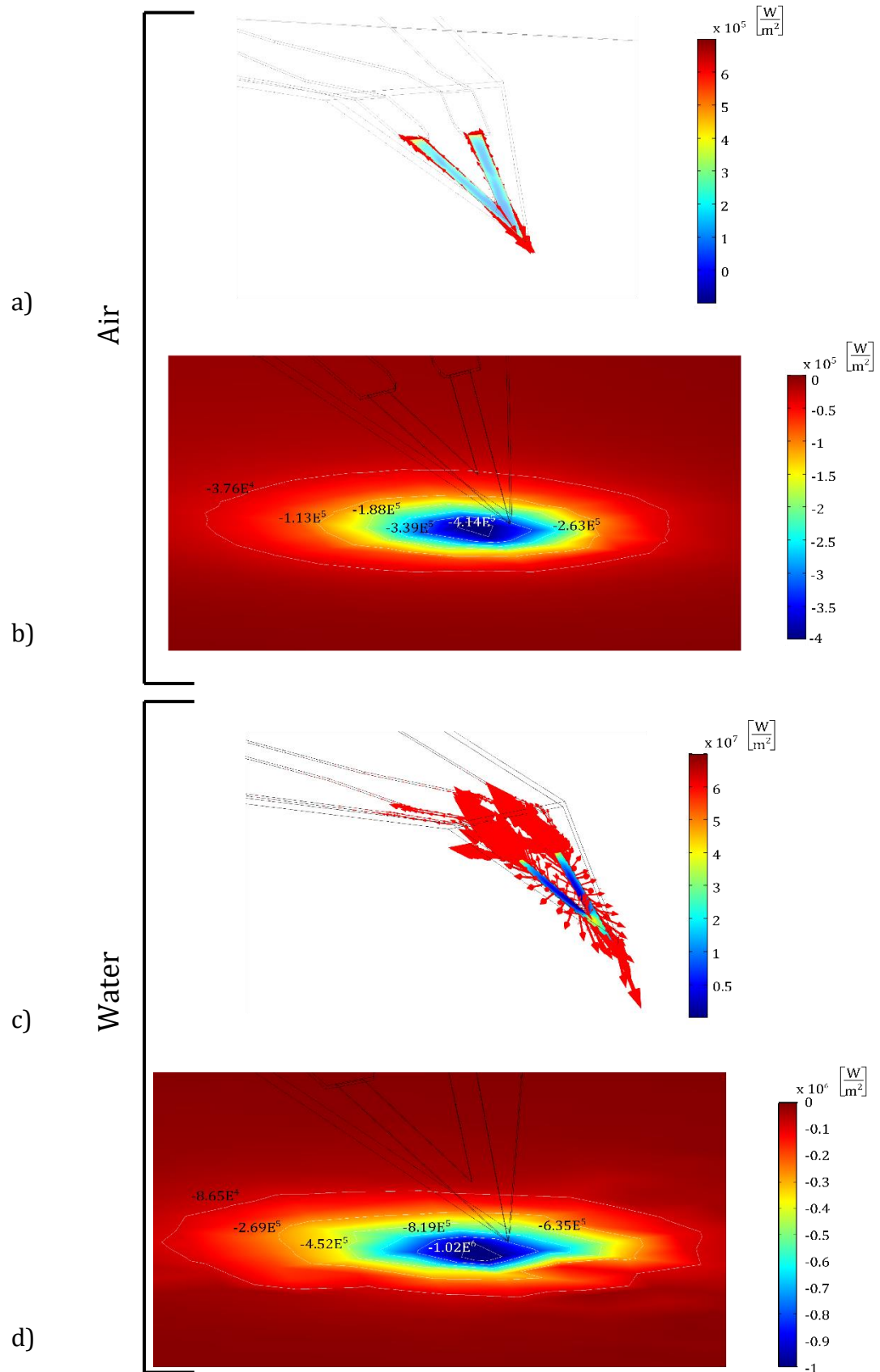


Figure 92 COMSOL MULTIPHYSICS 3D model of the probe in out of contact with Si_3N_4 sample. Total heat flux magnitude and heat flux vectors of the probe and the sample Si_3N_4 in the air (a-b) and in water (c-d) respectively.

The observation that, in water, the tip tends to cool down not only when in contact but also at distances of 0.5 and 1.5 microns is caused by the enhanced thermal coupling established between tip, sample and water environment. A similar but lower magnitude decrease in tip temperature can be observed also in Air and Flutec as shown in Figure 88. It can also be seen that, when looking at the global simulation results (Figure 87), the cantilever temperature distribution also differs between water and the other two environments (highlighted in the black rectangles of Figure 87, a). This gives a good indication of heat propagation within the system and how strongly the environment influences heat conduction away from the probe. From these models, thanks to the higher thermal conductivity of water, the heat is much more localised at the apex of the probe (location of the heater) when compared to air and flutec. One possible consequence of this that was not explored in this research due to time limitations, is that water will help minimise the problems associated with bimetallic bending of SThM cantilevers due to self-heating.

5.4 AIR/WATER RESOLUTION COMPARISON

The results above do lead to a clear question; what are the limiting factors for thermo-spatial resolution of SThM in aqueous environments? It is well established that the presence and nature of the surface water film that is naturally present on surfaces in ambient conditions impacts on the thermal-spatial resolution of SThM [54]. Therefore, it is a natural assumption that immersion of the probe and sample into an aqueous environment will alter the resolution limits of SThM. One obvious way to quantify this effect is by measuring thermal signals from features with ever-decreasing size. However, in this regard, it is crucial to recognise that thermal-spatial resolution is relatively complex as it measures the ability of an SThM probe to distinguish between two adjacent thermally contrasting regions of a surface, rather than simply identifying a single region. However, when using physically small features to explore thermal-spatial resolution, it is important to consider that their contrast is not only affected by their thermal conductivities, but also the dimensions of the features and the contact thermal resistance between the probe and both materials. This phenomenon was demonstrated in the work of Ge, et. al. [70] who altered the measured SThM signal obtained from a gold feature on a Si_3N_4 background by changing the dimensions of the feature. As a consequence, he proposed an

alternative approach, to quantify resolution, based around measuring the thermal response of a SThM probe scanning across an abrupt change in thermal resistance. Inspired by that work, a sample was fabricated (Figure 93 design (a) and sample (b)) that included large ‘pads’ acting as heatsinks at the end of narrow wires. This approach was employed by Ge, et al. who demonstrated that it permitted small gold features that still exhibited low thermal resistance, partially decoupling thermal resistance from wire dimensions, thereby simplifying interpretation of the SThM measurements. The samples were produced using e-beam lithography, metal evaporation and lift-off (Au 100 nm, NiCr 5 nm) on a Si₃N₄ (50 nm thick) coated Si wafer, with the same process steps as those detailed in section 4.1.

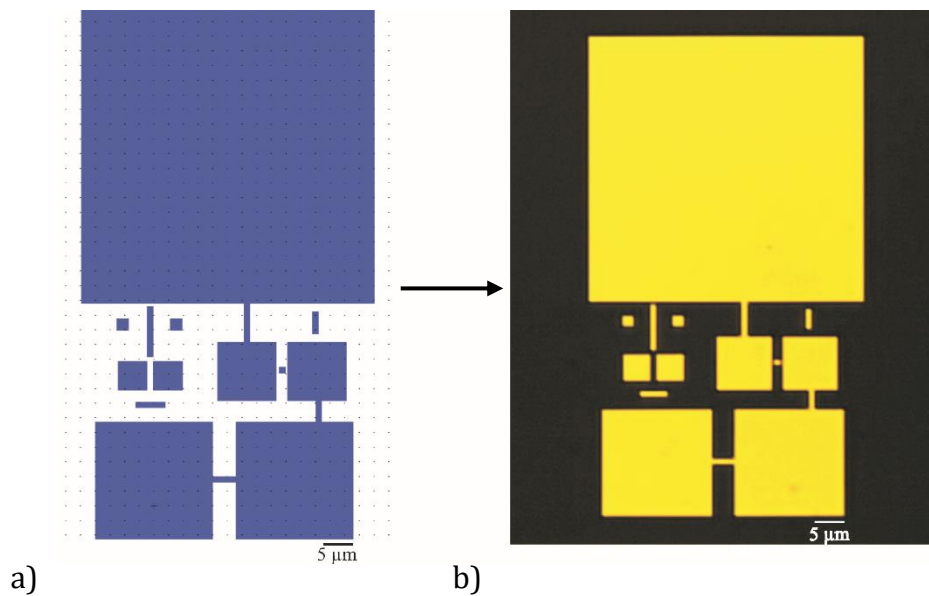


Figure 93 Design of the pattern (a) and optical microscope image of the Au/Si₃N₄ sample surface after lift-off (b).

Imaging was carried out using conventional SThM probes (Figure 94) driven using the instrumentation described in chapter 3 in a multimode AFM.

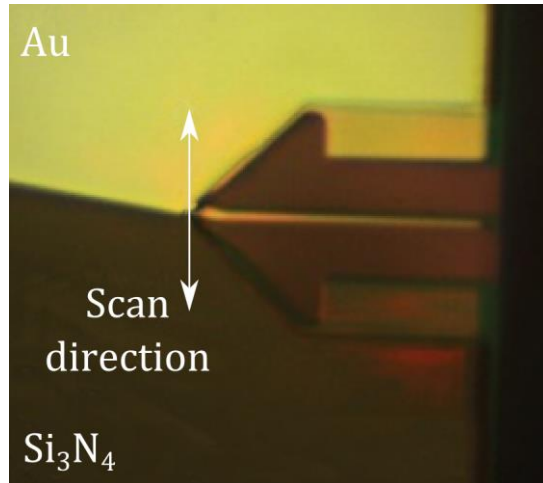


Figure 94 SThM cantilever on a sample and the scan direction highlighted by a white arrow.

The liquid used for this experiment was DI water, for which the probe has been fully characterised as in section 4.2. The images taken were 512 pixels per line with a scan rate of 0.5 Hz. This set of parameters is strongly related to the thermal equalization time. The thermal equalization time is the time required by two bodies, initially at a different temperature, to reach the equilibrium meaning no heat flux flows from a body to another. For SThM probes, the capability to measure this change is crucial to identify the response speed. If the probe is very responsive to changes in temperature it will reach equilibrium faster. The more time this process takes, the slower the local temperature measurement, which must be taken into account in the selected scan speed. To ensure reliable results the scanning speed should allow the probe to properly reach equilibrium at each pixel. If the scan speed is too high thermal artefacts and inaccurate measurements can be observed. It has been estimated that SThM probes used in this thesis take 2.4 ms to achieve a stable temperature [1]. Since the scan rate of the fast scan direction was controlled to be 0.5 Hz and 512 pixels, the probe has ~ 4 ms for each pixel and guarantees that the temperature of the thermal sensor can always be defined.

Topographic images (Figure 95, a, c, e and g) and thermal images (Figure 95, b, d, f and h) were obtained simultaneously during the scan. The most striking feature of the in-air scans is the poor contrast exhibited by the thermal features, making it difficult to assess the resolution of the image. For example, in Figure 95, b it is challenging to locate the different geometries of the Au features. The 5 μm wide gold pad (labelled 1 in Figure 83b) exhibits a signal that is largely indistinguishable from the background Si_3N_4 . Evidence that this is a geometric

effect can be seen from the improved contrast visible from the gold wire with a larger width (50 μm) in the same image (labelled 2 in Figure 95b). This trend continued when scanning a smaller area, (Figure 95, e and f), where the thermal signal of the small pad is nearly indistinguishable from the substrate.

Conversely, in water, as shown in Figure 95 both topography (c) and thermal (d) scans, show clear, easily distinguished features with a high contrast thermal signal. By comparing Figure 95b and d, it can be seen that the use of water results in clear contrast between the background Si_3N_4 and the Au pads. All the major geometries are clearly visible, and it is also possible to identify the smaller pads. In addition, results in water offer less streaking than air when the smallest scan area is considered (Figure 95, g and h). The contrast between the Au and Si_3N_4 is clear, even for the $1 \times 1 \mu\text{m}^2$ square (Figure 95, g and h). The topography signal is excellent, allowing both the gaps of the small pad to be identified in Figure 95 g. This should be compared to the results shown in Figure 95e where the pad appears connected to the rest of the structure due to scanning artefacts. The superior images in water also translate to the thermal scan where the pad is easily visible and one of the smallest gaps can be identified. This is a significant improvement over the equivalent in-air data (Figure 95, f), where the Au pad is almost indistinguishable from the background Si_3N_4 . From Figure 95, h it is possible to notice (see the red circle on the image) that the Si_3N_4 gaps on the right and left side of the $1 \times 1 \mu\text{m}^2$ Au pad are asymmetric; this could be an indication of the tip shape or rotation due to probe twisting in the scan direction.

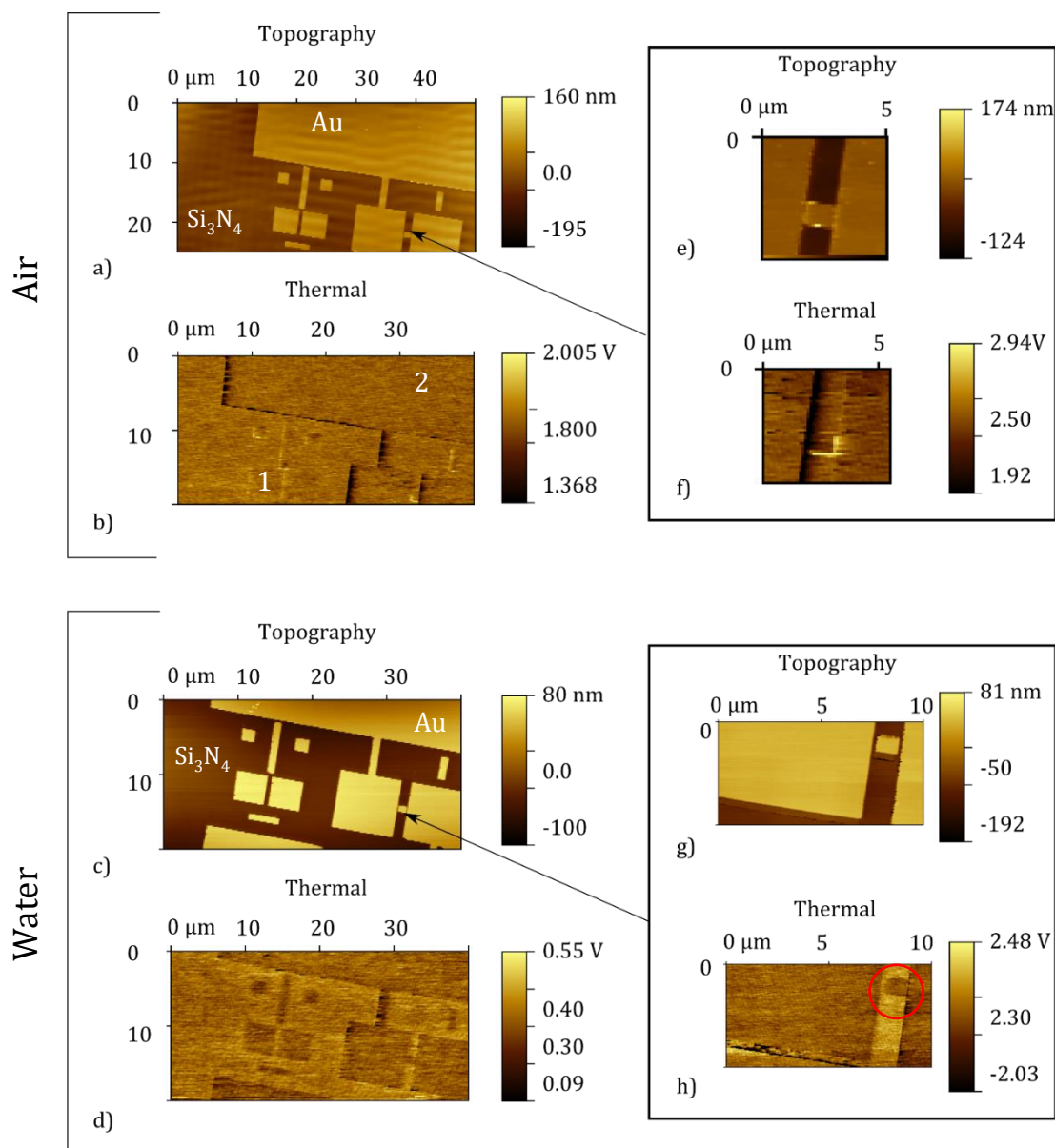


Figure 95 AFM topographic images and thermal images showing the same sample scanned by a standard SThM probe in air (a), (b) and water (c), (d). In the rectangle on the right is reported an enlarged topographic (e) and thermal (f) image in air and topographic (g) and thermal (h) under water and, where a $1 \times 1 \mu\text{m}^2$ square is clearly visible.

Figure 96 (a), (b) shows a direct comparison between the thermal signal intensities by looking at cross-sections of the data from the same sample region in air and water. The exact location of the cross sections are shown by the black and red lines on the inset thermal images on the bottom right of each plot. It is worth mentioning that in both cases the average signal is presented and was obtained by performing an average over the 20 pixel width of 20×40 px (width x length) lines, using the Gwyddion software tool. Each of the lines was drawn to encompass two Au features of different areas that were observed to give different contrast in the air scans: a pad of $50 \times 50 \mu\text{m}^2$ and a wire of $1 \times 8 \mu\text{m}^2$. From the

line plots in Figure 96 is possible to see that, although noisy, in air (plot a) the magnitude of the thermal signal from the pad is lower compared to the wire. This lower signal is indicative of a region with higher thermal resistance, closer to the background Si_3N_4 as discussed in the work by Ge, et. al [70]. However, in water, the magnitude of the thermal signal from the two features is very similar, as confirmed by the image where all geometries appear to have the same contrast.

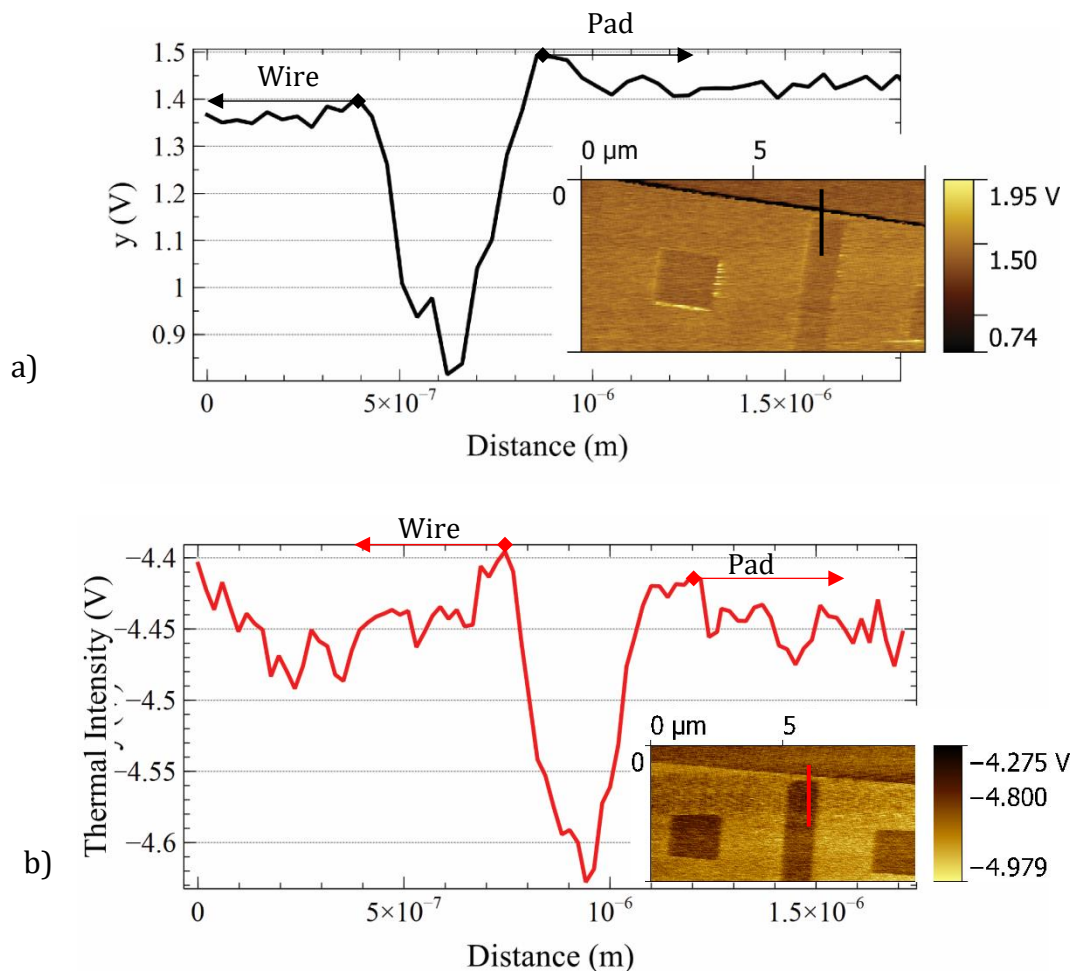


Figure 96 Thermal signal intensity in a) air and b) water along the path where the signal is taken.

Ge et al. [254] proposed a method to compare the thermal-spatial resolution of SThM probes by analysing the thermal response while scanning over an abrupt change in sample thermal resistance. Although this was intended for use on topography free samples that avoid the influence of topographic artefacts, it was employed here to give a qualitative comparison between air and water thermal responses. To achieve this, cross-sections were taken through the data along a line that crossed Au and Si_3N_4 features (Figure 97, a and b) in both air and water. From the plots in Figure 97 (c), it can be seen that the rate of change in probe temperature is similar in both air and in water if topographic artefacts, strongly

visible in air, are ignored. By plotting trace and retrace cross-sections, it is possible to notice that these artefacts depend on scan direction. In air, the probe twist combined with the changing contact points at the edges make the trace-retrace difference significant. In water, this is less visible, however probe twist probably impacts on the symmetry of the probe-sample interaction, where sharp corners or smooth corners swap when a change in scan direction is made.

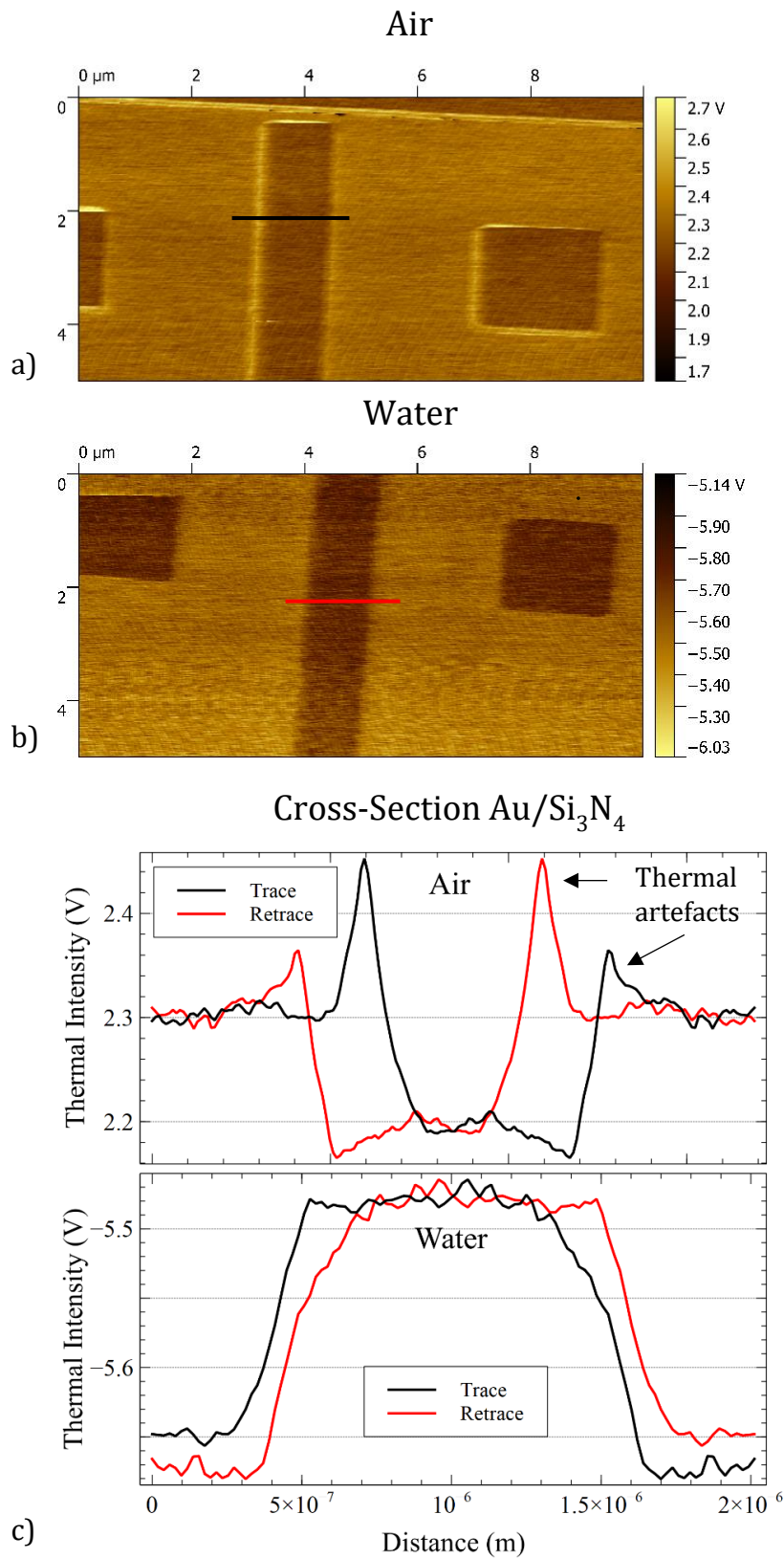


Figure 97 Thermal images of Au/Si₃N₄ sample in air (a) and water (b), obtained by averaging the signal over a 40x20 px area. Trace and retrace plot of the cross sections showing the differences in both the environments with the topographic artefact present in air (c).

In order to obtain a more accurate estimation of the thermal spatial resolution of a-SThM, the same approach reported in [1, 94] that employ a Boltzmann sigmoidal fit

$$f(x) = y1 + (y1 - y2)/(1 + \exp(x - x0/\Delta x)) \quad (21)$$

was used. A schematic representation of this fit, widely used in science, is shown in Figure 98.

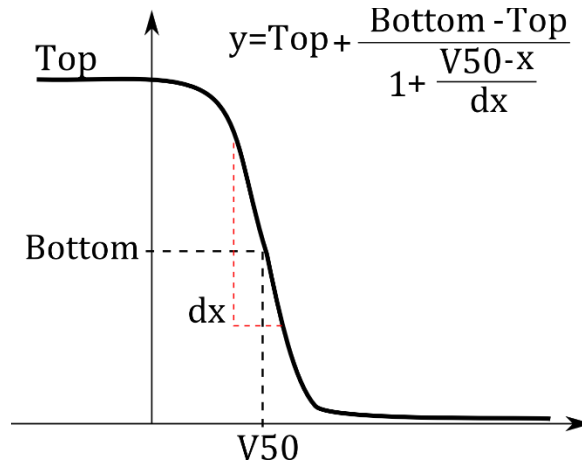


Figure 98 Boltzmann sigmoid function plot and parameters.

The key parameter is the “slope” that describes the increase of the function value while transitioning between low and high values. Since in this case there are two different materials with different thermal conductivities, a change in temperature at the interface is expected. The Boltzmann Sigmoid function, therefore, provides a simple way to describe the rate of change, as is depicted by dx in Figure 98.

Figure 99 shows half cross sections taken from the thermal scans in Figure 97. As discussed by Ge et. al [70], the value of $2 \times dx$ provides a good indication of the resolution, which in this case is 84 nm for water and 42 nm (if ignoring the thermal artefact) for the experiments in air (Figure 99) Despite the decrease in the thermal spatial resolution observed, the result achieved by a-SThM is well in line with scans obtained under ambient conditions as well as similar work done in non-conductive liquid environments [94], further demonstrating the usability of the technique. The second obvious difference that can be seen when comparing the in-water experimental (Figure 97, c) and simulated results (Figure 73, c) is the slope measured and predicted.

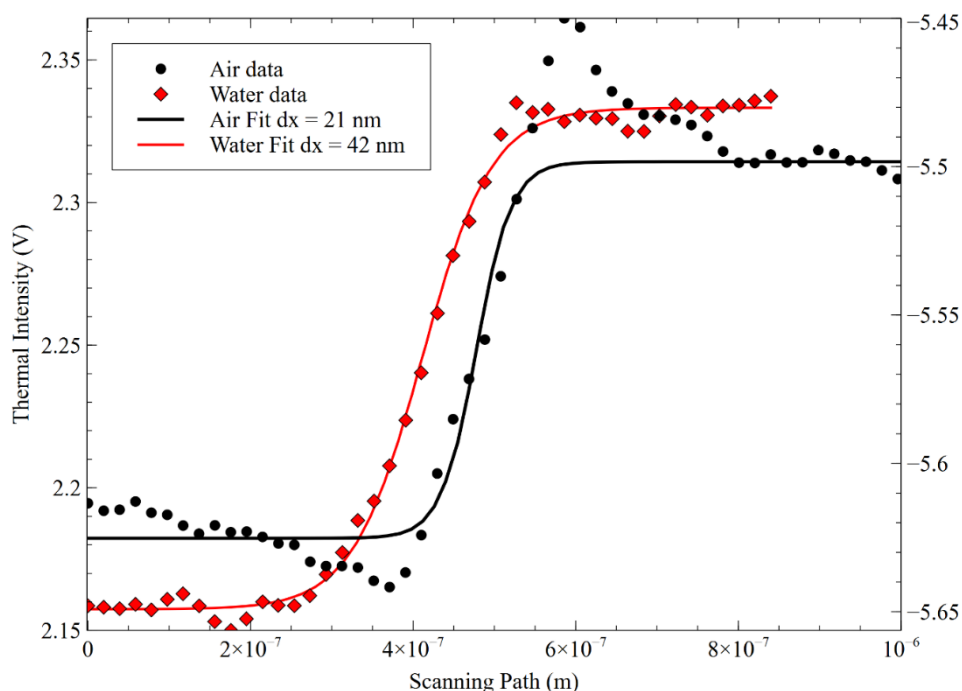


Figure 99 Comparison of experimentally measured curves of thermal intensity for SThM in air and in DI water across Au-Si₃N₄ boundary and associated fit ($R^2 = 0.99712$ for water and $R^2 = 0.93812$ for air).

The results shown in Figure 99 are interpolated and verified with the sigmoid fit, from which is possible to reliably extract an indication of the spatial resolution. This was obtained by using an Origin's proprietary non-linear fitting toolbox. The fit in water is straightforward since the signal is very smooth with no artefacts and minimal noise present. This can be seen from the excellent agreement between the fit and the data as shown by the values in Table 3.

Reduced Chi-Sqr	1.7E-5
Residual Sum of Squares	6.8E-4
Adj. R-Square	0.99712

Table 3 Fitting outcome for data in water

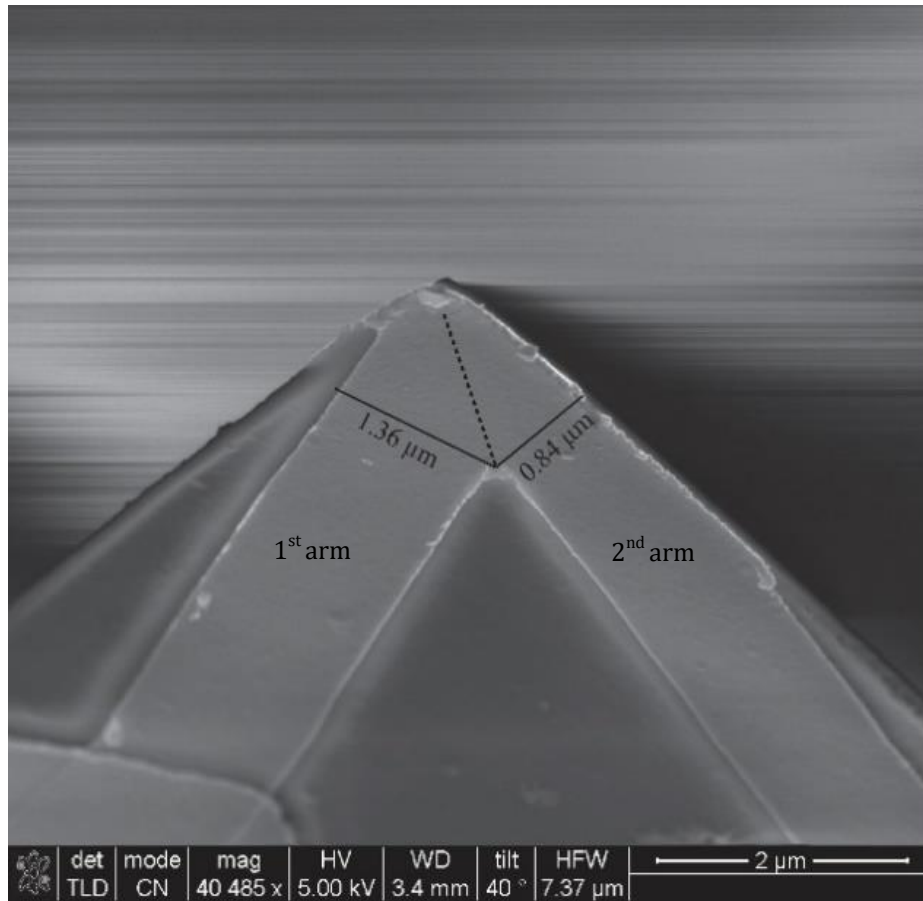
For the data obtained in air, there is an abrupt change in thermal conduction, caused by the artefact discussed previously. This overshoot has to be removed before performing the fit in order to obtain a reliable result. The data regarding the plot quality are reported in Table 4.

Reduced Chi-Sqr	2.4E-4
Residual Sum of Squares	0.017
Adj. R-Square	0.93812

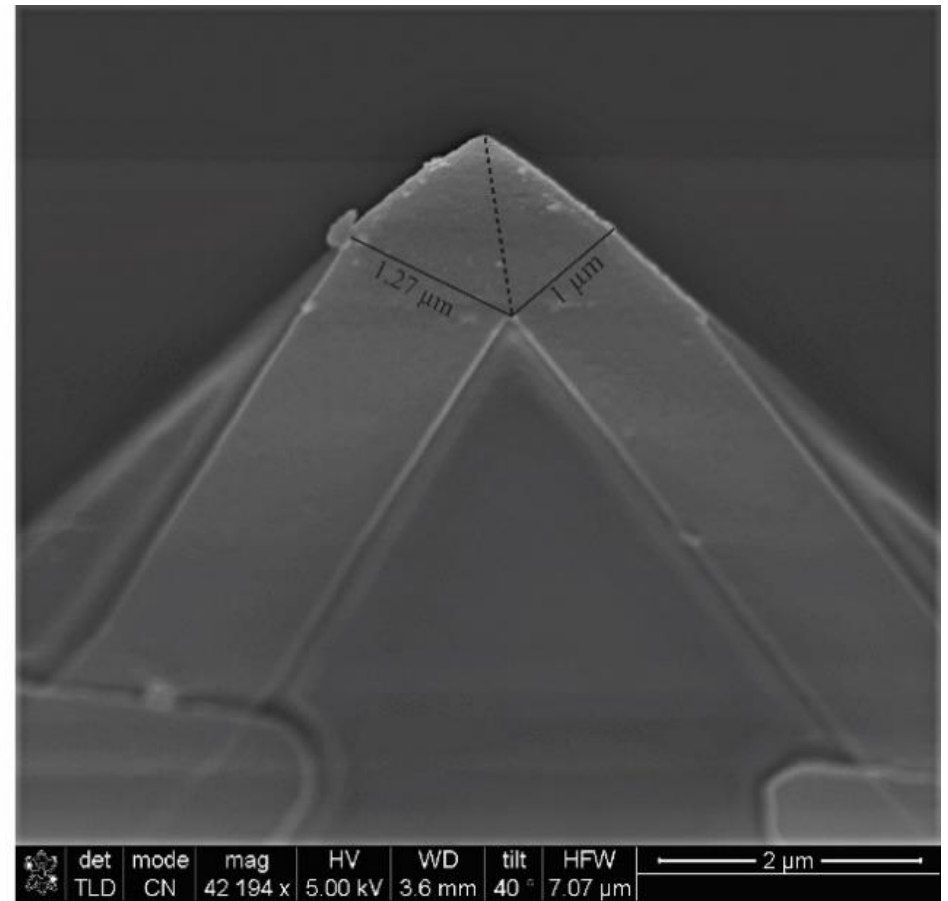
Table 4 Fitting outcome for data in air, with truncated data.

The values of dx obtained by the fit are in line with those available in literature [70, 94] and numerical model, and it is more reliable than analytical solutions that only consider the problem in a single dimension.

This difference in slope, which corresponds in a difference in resolution, can be tentatively explained by considering the fabrication process of a standard SThM probe. This is not considered in the finite element model, where the probe is perfect in terms of geometry. Figure 100(a) and (b) shows SEM images of a misaligned SThM probe Pt tip resistor and a correctly aligned one respectively. This misalignment represents a well-known issue of the ebeam lithography process employed for resistor definition when using non-ideal alignment marks [276], [277] as is the case during SThM probe production. Since the two arms constituting the heater do not have the same width and length, there will be an alteration of the resistance and hence Joule heating distribution of the probe, compared to the ideal behaviour. Consequently, the region of greatest heat (or temperature sensitivity) may not be located on the apex of the tip and, in the case of Figure 100(a), it would be expected to be along '2nd arm'. In addition to this, the presence of a thin arm can cause the premature failure of the probe by electromigration [256], [255]. By taking these results into account and considering the plots of Figure 97(c), it is possible to conclude that the probe's thermal-spatial resolution in water may be altered by variations in the Pd heater's geometry. This poses the problem that a variation in probe-to-probe performance may be expected. However, it also suggests a potentially superior new probe design, where the heat generated by the Joule effect is more concentrated at the end of the tip.



a)



b)

Figure 100 SEM images of a misaligned (a) and a standard (b) thermal heater of the probe.

To explore this concept through modelling, the Pt heater design was reduced in dimensions, with the CAD model as shown in Figure 101,a. A comparison of the simulated results in water ($I_{\text{applied}} = 0.0017 \text{ A}$) between the standard Pt resistor (Figure 101, b) and the newly designed one (Figure 101, c), is shown. An improvement in signal amplitude is visible between the two (Figure 101, d) with a minor improvement in thermal resolution of the new heater (black diamonds) compared to the standard one (blue square) using the Boltzmann sigmoidal fit discussed above.

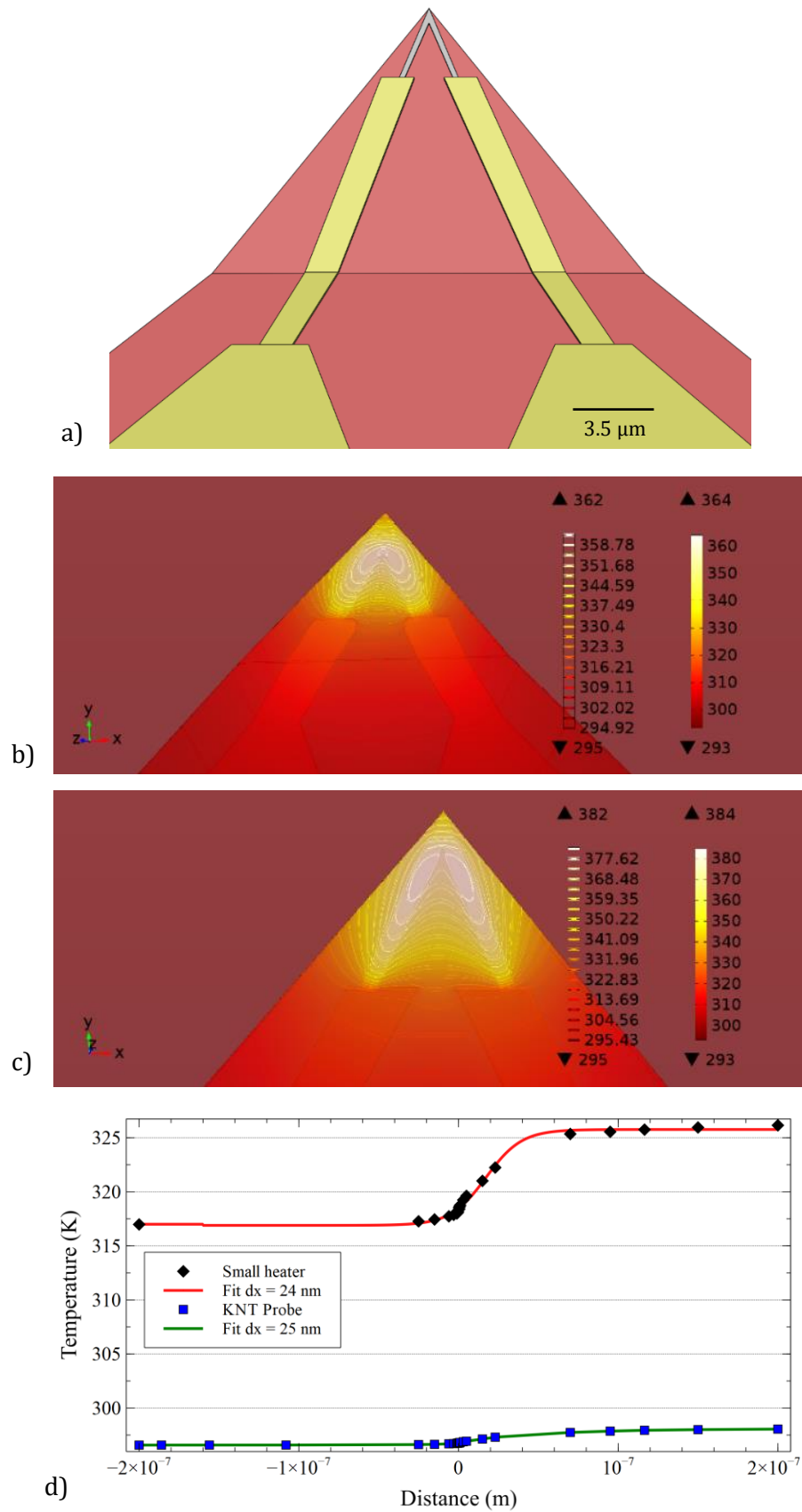


Figure 101 Probe 3D CAD model (a), thermal field for the standard KNT probe (b), the newly designed probe (c) and the simulated thermal scan achieved by using these two probes and the associated fit(d).

To further improve the underwater spatial resolution, making it as close as possible to air, changes in the cantilever have also been considered. The concept involves generating a cut-out in the cantilever, potentially increasing the performance of the probe since the heat generated has a reduced conduction path along the cantilever to the probe base. These changes to the cantilever can be seen in Figure 102, a, b and c. Three new designs with a cut-out in the cantilever region were considered. One with the cut out close to the tip (Figure 102, a), in the region between the Au connections (Figure 102, b) and in both areas (Figure 102, c). However, it is possible to see from the results (Figure 102, d, e, f, g), that these cut-outs only increase the temperature by few degrees (max temperature change is 4 K) when compared to the small heater with no cut-out. In theory with the introduction of the cut-out the resistance in the central area of the tip increases, leading to a subsequent increase in temperature. However, due to the fact that the cut-out is filled with water, a relatively good thermal conductor, during a-SThM the advantages it would offer in air or vacuum are not readily apparent and the temperature does not rise significantly.

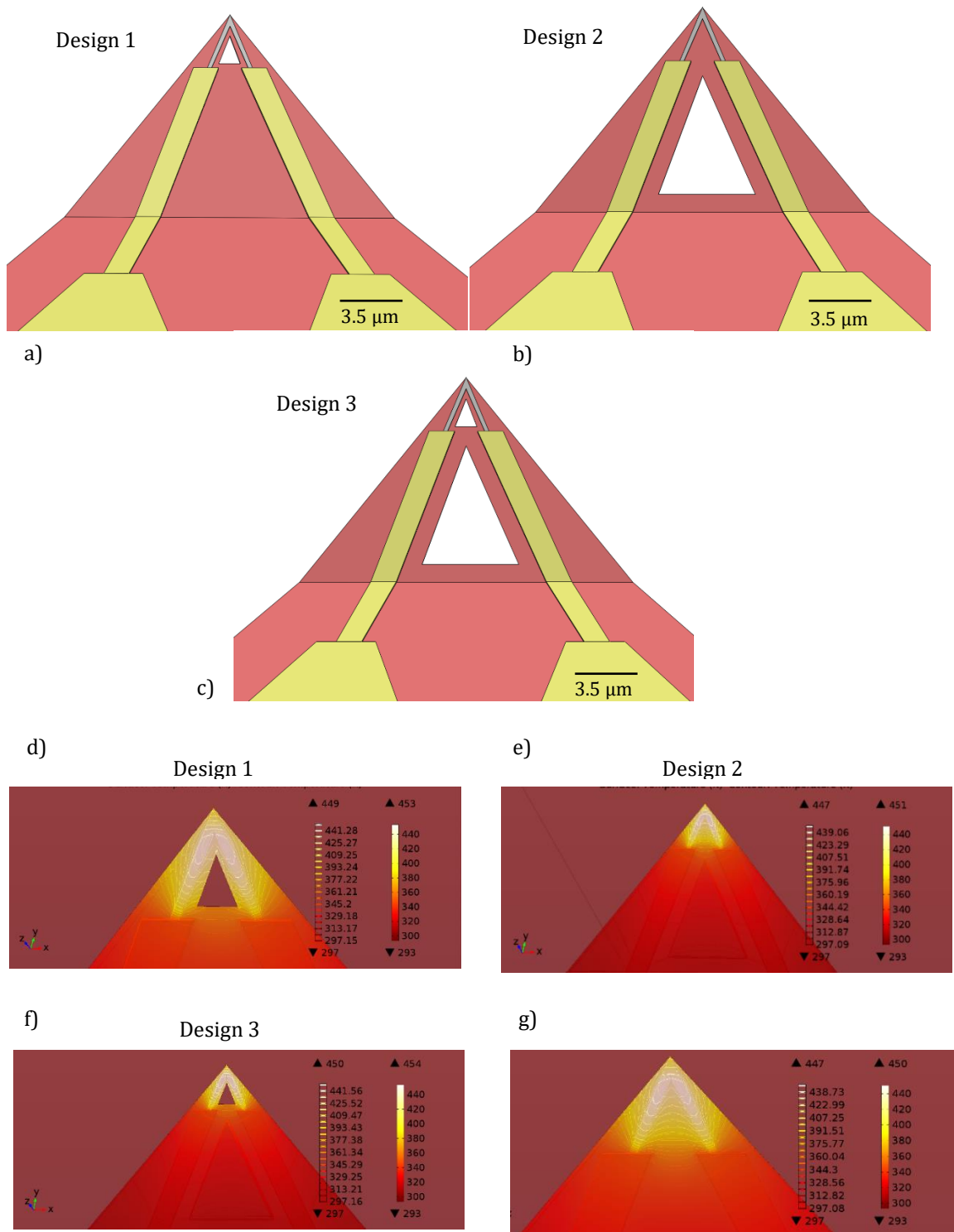


Figure 102 Different design attempts a, b, c and thermal fields for SThM probes with one cut-out at the heater level (d), at the cantilever level (e), in both the areas (f) and of the new design without any cut-out (g).

This leads to a final optimisation concept, with the use of a smaller thermal resistor that tapers as it approaches the tip (Figure 103, a).

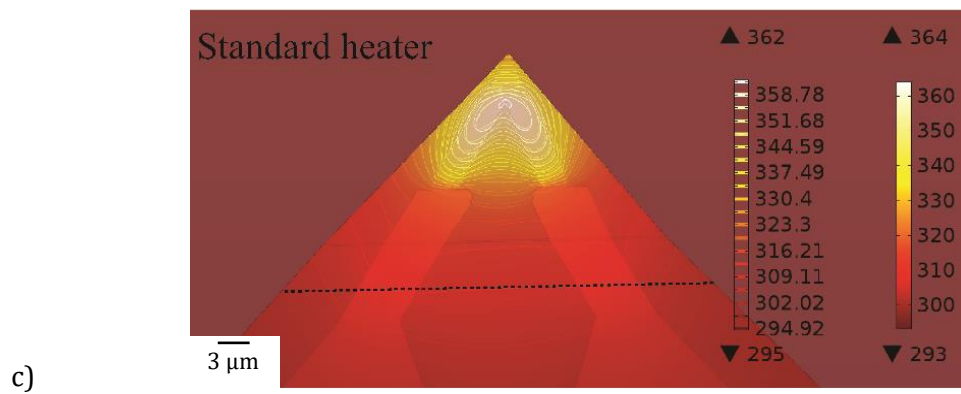
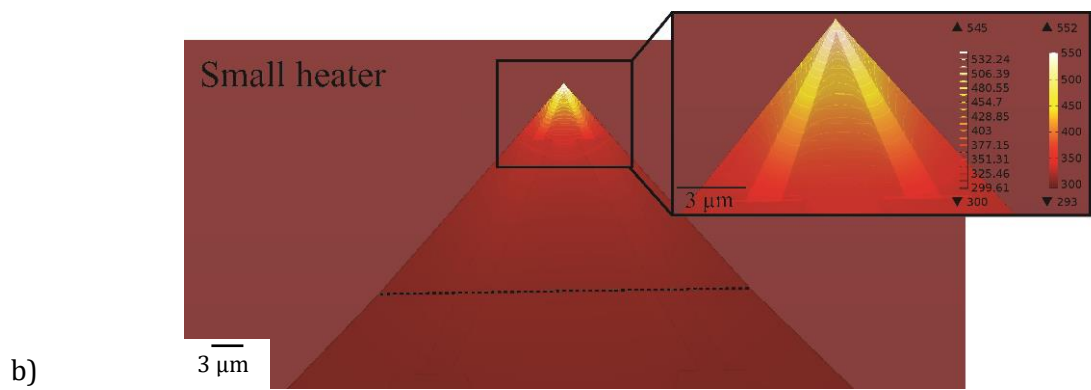
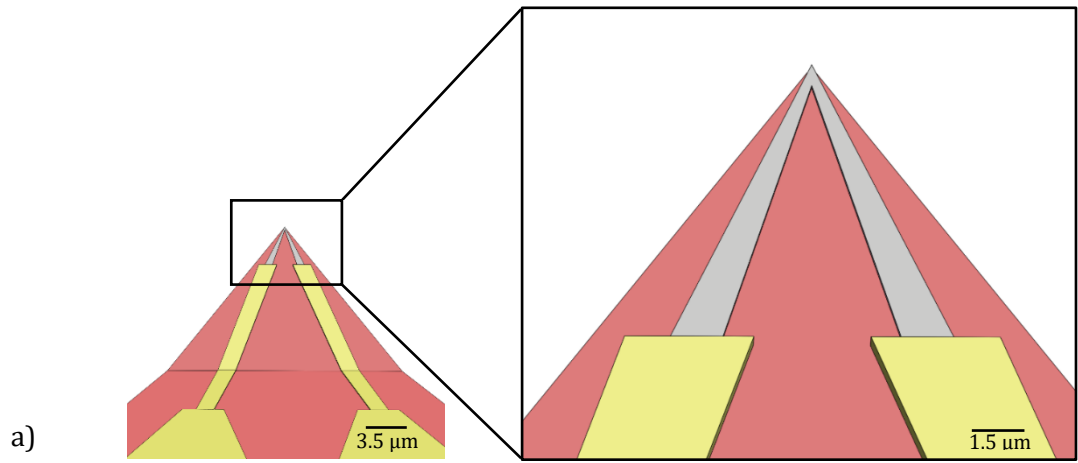


Figure 103 (a) CAD model of the newly designed probe, FEA temperature distribution of a thermal probe with a newly designed smaller heater (b) and with the standard heater (c).

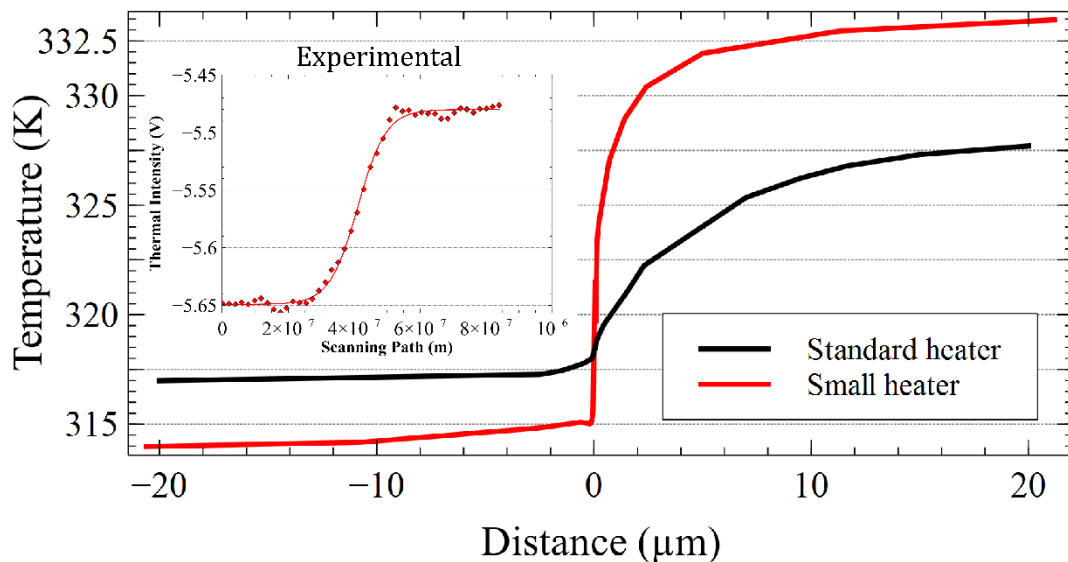


Figure 104 Plot achieved by the underwater simulations with these two probes scanning across a Pt/Si₃N₄ sample compared with the experimental curve.

Figure 104 shows the simulated temperature step for the standard KNT probe and the newly designed probe scanning across the Pt/Si₃N₄ boundary in a water environment. The simulated resolution response of this new, smaller heater looks closer to the observed behaviour in the experimental data. It can also be seen that the smaller tip may not only help to localise the heat at the very end of the tip (black square in Figure 103, b) and consequently to increase the resolution, but also the value of the maximum temperature achievable in water. This improvement is significant if compared with the standard probe in Figure 103, c. In addition, the maximum achievable probe temperature is dictated by the highest current density that the probe can tolerate. The proposed change in probe heater dimensions and geometry produces a change in its cross-section area, which reduces at the probe tip. This design choice increases the current density at the very end of the tip, leading to a very localised increase in temperature, whilst keeping the current density below the point electromigration occurs.

As a final demonstration of the possible improvement that could be obtained by adopting this new tapered tip design, the thermal contrast plot for KNT, small heater (with no cut-out) and small-tapered heater probes are shown in Figure 105. This data was obtained by following the same procedure described shown in Figure 75 on page 146 of section 4.4, with the only difference being the geometries of the different probe models used. Importantly, the same current was employed for all to aid comparison. The Boltzmann sigmoidal fit to the standard KNT design exhibits the lowest thermal contrast and overall

temperature when compared with the other two designs. From Figure 105 the best results are obtained from the SThM probe with the small and tapered heater, both in terms of temperature change and spatial resolution.

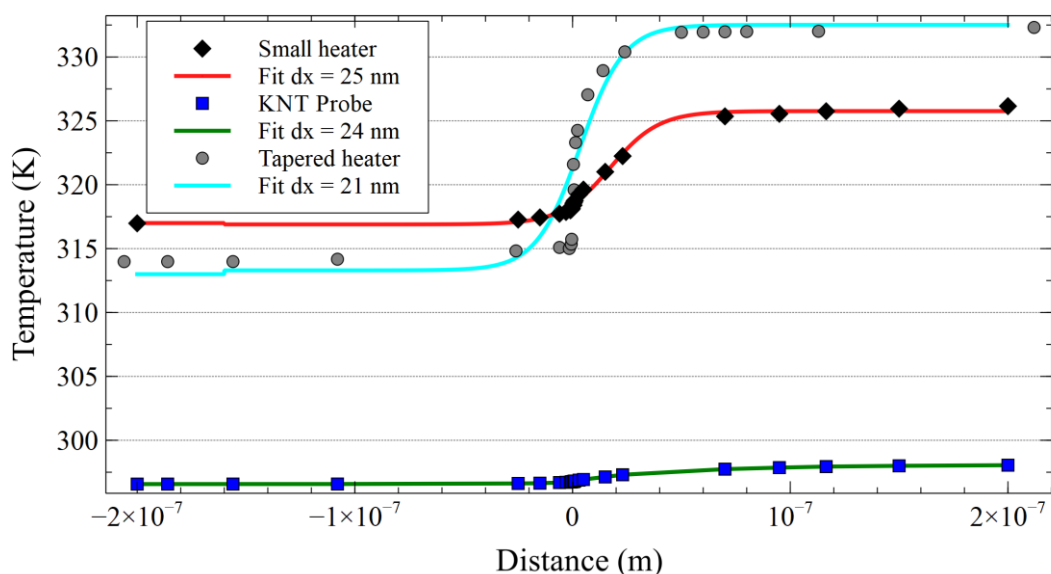


Figure 105 Simulated thermal scan plot for standard probe (green line), small heater (red) and the small-asymmetrical design (blue).

5.5 CONCLUSIONS

One of the key features of aqueous SThM identified in this thesis is its ability to perform thermal scans out of contact with the sample. This is a key capability that may be advantageous for several applications including cell manipulation and the study of delicate solid and biological samples. As is well-known, in-air out-of-contact scans are not possible since the thermal conductivity of air is too small to allow significant tip-sample thermal coupling at a tip-sample separation that is also mechanically stable (i.e. beyond the effect of the water meniscus).

In this chapter, the feasibility of out-of-contact thermal measurements was explored in flutec and water, further confirming the critical importance of environmental thermal conductivity on SThM measurements. When operating in water the improved tip-sample thermal coupling enabled effective SThM even when the gap between the sample and the tip was 1.5 microns. Similar, but lesser (lower resolution and contrast) results were achieved using flutec.

One important observation was that, by performing out-of-contact a-SThM, artefacts, that normally exist in AFM and SThM when in contact, can be avoided. An additional advantage shown experimentally when operating in out-of-contact mode was the extended operating stability of the probe. When in contact the probe tends to alter and degrade while scanning, producing a variable signal.

However, when out of contact this problem disappears for the obvious reasons, making long-term, repeatable scans more achievable.

Not surprisingly, it was also noted that the thermal-spatial resolution of a-SThM is lower than traditional SThM scans in air. This limitation, which doesn't necessarily impede its use, could be tackled in the future by redesigning the probe specifically targeting the heater. Modelling of a tampered heater design demonstrated very good performance, reaching a much higher temperature and offering better thermal spatial resolution than the traditional KNT design in the water. This represents an obvious step in the design of an aqueous SThM dedicated probe which would be a logical next stage as the probes used within this work were originally optimised for use in air or vacuum.

Both simulations and experiment demonstrate the advantages of a water environment, where a superior, more stable thermal contact exists between the SThM sensor and the surface. In this environment it is also possible to conduct true non-contact scanning, holding the tip 100's nanometres or more above the surface being thermally imaged. This allowed in-water SThM to be used to in the two-pass 'lift-mode' imaging technique, which requires double the time to obtain a dataset but works very well as water's thermal conductivity is enough to obtain good thermal contrast. This approach drastically reduces the risk of sample-distorting forces caused by tip-surface contact, opening the technique to biological studies where samples can be extremely delicate.

CHAPTER 6: BIOLOGICAL SAMPLES

6.1 INTRODUCTION AND MOTIVATION

Although the previous chapters have demonstrated the validity of a-SThM, as well as its advantages when investigating samples that could be scanned in air, its main potential lays with its suitability to investigate biological samples in their native environment. In this chapter, a-SThM is employed in two important scenarios – to interrogate the thermo-mechanical behaviour of a biomaterial (I-collagen) and to probe the response of live cells to localised heating.

6.2 I-COLLAGEN

Collagen is the most abundant protein in the human body, playing a significant role in dictating the mechanical properties of various tissues (e.g.: bone, tendon, skin). Three types of collagen form large fibrillar structures: type I (skin, tendon and bone), type II (cartilage), and type III (skin). This research will focus on Type I fibrillar collagen, due to its importance within the human body, where over the 90% of the tissues and organs are contain Type I collagen.

Type I-collagen consists of triple helical tropocollagen molecules that have highly conserved lengths of $L \sim 300$ nm, roughly 1.5 nm in diameter. The Staggered arrays of these collagen molecules form fibrils, which themselves arrange to form collagen fibres [278] as shown in Figure 106.

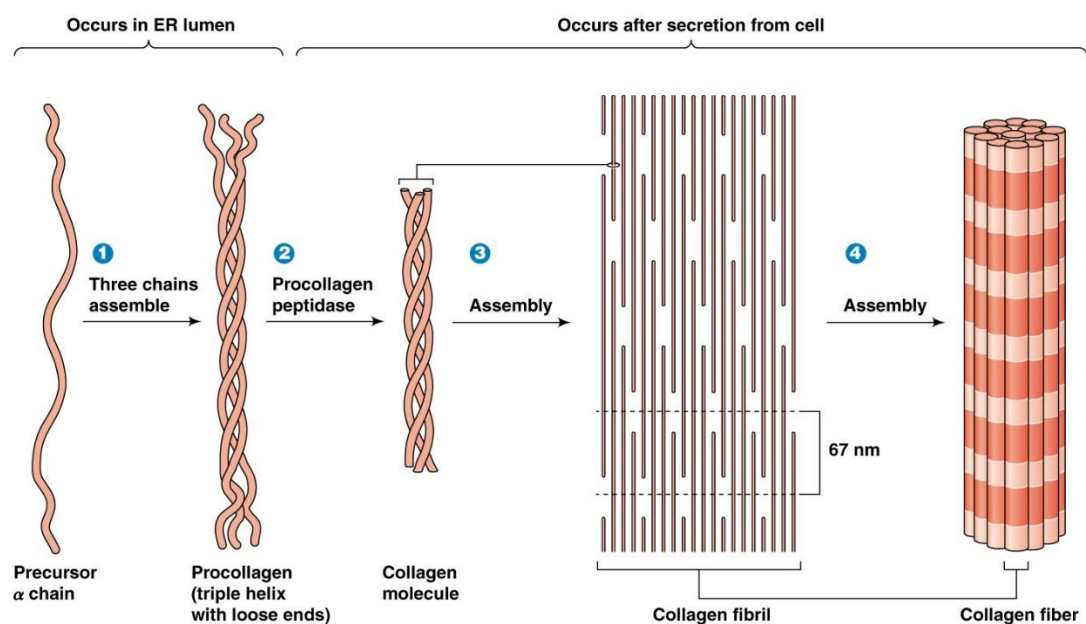


Figure 106 Evolution from a single chain precursor to the fibre [279].

In recent years, the phenomena associated with exposure of collagen to heat flow and varying temperature ranges have been accurately investigated [280-282].

Thermal transitions of type I-collagen fibrils have been studied using differential scanning calorimetry and spectrophotometry for a range of conditions [280]. This work demonstrated the presence of two heat absorption peaks around 45 and 55°C. This result is important because it offers more precise and repeatable insights into the curves of fibril denaturation. This was the first time that such a study was undertaken using scanning microcalorimeters, allowing the authors to investigate the self-association of collagen observing both fibril formation and denaturation. The study of denaturation is important to predict and characterise the physiological stability of collagen. In a more practical aspect, for example, the micro-scale destabilisation of type I-collagen is considered an important factor in osteogenesis imperfecta [283], which is a serious and potentially fatal illness associated to very fragile bones.

A very interesting aspect of studying I-Collagen is the clear change in material thermal properties when denaturation occurs. In particular, a change in the specific heat at constant pressure was observed. This difference was investigated by comparing the calorimetric curves under fibril-forming and non-forming conditions, showing that ΔC_p of fibril denaturation is caused by a decrease in the C_p of collagen at pre-melting temperatures [280].

In addition to its thermal characteristics, the mechanical properties of collagen are also strongly affected by the denaturation process [281, 284]. The elastic properties of collagen have been studied using standard mechanical tests (N.B. this is only applicable to large tissue samples, so it only gives an average of the respective properties) to obtain stress-strain relationship or, using nano-indentation and AFM.

For the aforementioned reasons, a-SThM could allow the simultaneous study of both thermal and mechanical properties of samples with very high resolution. This is in a similar vein to the way conventional AFM has been previously used to study collagen under physiological conditions [285].

Gutsmann *et al.* presented spectroscopic force measurements performed on rat tail collagen [286]. In this work, the mechanical properties of collagen fibrils were investigated using a new type of small cantilever (length <20 μm). By using this cantilever, it was possible to pull individual subunits of collagen fibers. The most important result obtained was the correlation between periodic patterns in the

topography of rat tail tendon collagen fibrils and the binding patterns observed in the force spectroscopy experiments on these molecules. The results also contained very complex and unique force-extension curves, which could not be fitted and extrapolated using a traditional material model. Expanding on this work, Bozec *et al.* [104] conducted the first analytical characterization of a biological system using a thermally controlled AFM probe on collagen fibers by employing a microthermal analysis (μ TA) approach [104],[56]. This technique, initially developed by Hammiche *et al.* [287, 288], can be used to perform dynamic and localized thermomechanical analysis, where a modulated stress is applied directly in a small area of interest of a surface. While the force is applied, a change in the local temperature is simultaneously imposed in a controlled way by a heating device that is not embedded in the AFM tip. This imposed localized temperature modulation is used to generate thermal expansion, which in turn generates mechanical strain.

This technique is realized by using a thermally active AFM probe (in early works a Wollaston probe) instead of a traditional AFM probe [56]. The key advantage in using an active probe is the ability to locally modulate the sample heating, which is associated with an equally modulated local thermal expansion of the materials. When compared to more conventional methods, this allows a more local and direct analysis of the sample over a region defined by the contact area between the probe and sample (around ~ 20 μm diameter for a Wollaston wire probe). However, difficulties can be experienced as the spatial resolution and contrast are directly dependent on the probe contact area. This specific issue is partially addressed by the current generation of SThM probes, which exhibit higher spatial resolution due to a smaller tip radius.

Extending the μ TA to biomaterials in their natural environment, Bozec *et al.* [104] recorded the thermo-mechanical behavior of a sample of hydrated collagen in contact with a hot thermal probe (Wollaston wire probe [104]). Using modern microthermal analysis instrumentation, they investigated the properties of collagen fibrils and gelatin, simultaneously producing both localized thermal measurements and topographic images of the resultant imprints. This approach allowed them to characterize the differing thermal response between native collagen fibrils and their denatured form, gelatin. The work demonstrated that substantial differences in terms of thermal transition are present. These

transitions were studied under two different conditions, hydrated and dry. The first condition exhibited a well-defined thermal transition at 65 ± 10 °C, which is associated with the process of gelatinization of collagen in a hydrated environment as the result of breaking internal cross-links [104]. Once this transition was passed the increasing temperature ultimately led to complete drying of the sample through evaporation. At this point the sample was considered dried and two further transitions were identified at 150 ± 10 °C and 220 ± 10 °C [104]. The first due to evaporation of residual H-bonded water contained within the sample that is recognized to be associated with the triple helix structural conformation of collagen macro-molecules. The second transition occurred in totally dry conditions and is associated with the shift from the classical triple helix structure to random coils. The authors [104] suggested that this difference in transition temperatures is related to the gelatinization process of the collagen fibrils.

Although Wollaston wire probe is considerably more robust than the thin-film Pd probe used in this thesis, it still suffers failure when used under aqueous solutions. Therefore, the probe could not be fully immersed in water and instead the sample was kept hydrated by employing humid air. Under these conditions, the interface between probe and sample is extremely complex, consisting of air, water film, probe and hydrated collagen. This had two fundamental consequences: mechanically, the thick water film and diffuse hydrated surface structure of the collagen/gelatin, which exists at the surface of collagen fibrils in aqueous environments, resulted in significant challenges achieving, maintaining and breaking contact with the sample surface. Thermally, tip temperatures exceeding 100°C caused rapid water evaporation and drying of the sample before any thermal events could be detected. Below 100°C, the temperature dependant water meniscus that existed between probe and sample made quantification of the tip-sample thermal contact near impossible. Finally, as highlighted above, probes were still prone to failure if the water film became too thick. As a consequence, this method developed by Bozec *et al.* [104] required an extremely challenging balancing act between sample hydration whilst simultaneously ensuring that the SThM probe did not become submerged in the water film.

The new method described in this thesis bypasses the majority of these challenges by eliminating air from the probe-water-sample system, greatly simplifying the experiment.

Since one of the major motivations for enabling SThM in water is its use in biology, gelatinized I-collagen was chosen for a first a-SThM test as, when in an aqueous environment, this material is soft, biologically relevant and easily prepared.

6.2.1 COLLAGEN GEL SAMPLE PREPARATION

During preparation, I-collagen can be held in solution with an acid pH, however, if this is neutralized, a jelly-like solid is obtained. Employing this behavior, a sample was prepared on top of a glass slide using the following steps:

- i. 1 part of NaOH was mixed with 1 part of 10 x polychlorinated biphenyls (PCBs) and 8 parts of 8.2 mg/ml collagen solution [289]. This process neutralised the (pH~3) collagen solution, resulting in I-collagen gel.
- ii. From the resulting solution, 5 μ l was taken and placed on a glass slide, taking care to spread the gel evenly on the glass.
- iii. The sample was then placed in an incubator at 37 °C until dry (~2 hour) to obtain the gel coated slide.

6.2.2 COLLAGEN GEL EXPERIMENT

The experiment was conducted by contacting the SThM probe tip on the sample with increasing probe heating power under DI water. In each case, the heated probe was left in contact with surface with constant force for a pre-determined period of time and heating power (2 minutes or 5 minutes; zero, half or full power). The probe was then moved to a different area of the sample and the process repeated until all conditions had been tested. Force-distance curves were compared at the end of each experiment and the results shown in Figure 107a) and b). From the deflection of the cantilever and its derivative, it is possible to see that the mechanical properties of gelatinized collagen changed both with time and power applied. The mechanical deflection showed the typical behaviour of a soft sample when a cold probe was used (black line in each plot), however by increasing the heating power, the gradient was seen to change. A key point of this experiment is that contacting the surface for up to 5 minutes with an unheated probe resulted in unchanged force-distance plots, with no changes visible in comparison to the initial (0 minute) plot. However, when employing a self-heated

probe in the same way, a progressive change of gradient was observed. This suggests that the sample-softening phenomenon is not due to pure mechanical indentation from the force applied over time but is related to probe temperature. Finally, as a control, the same SThM measurements were carried out on a glass slide and compared to those obtained on collagen (Figure 107 (c)). These force curves do not exhibit any effect due to increased heating, with all curves showing the same gradient independent of probe temperature. This demonstrates that the varying gradient is not caused by mechanical changes in the SThM probe itself as a result of sustained self-heating, but instead must be from changes in the sample.

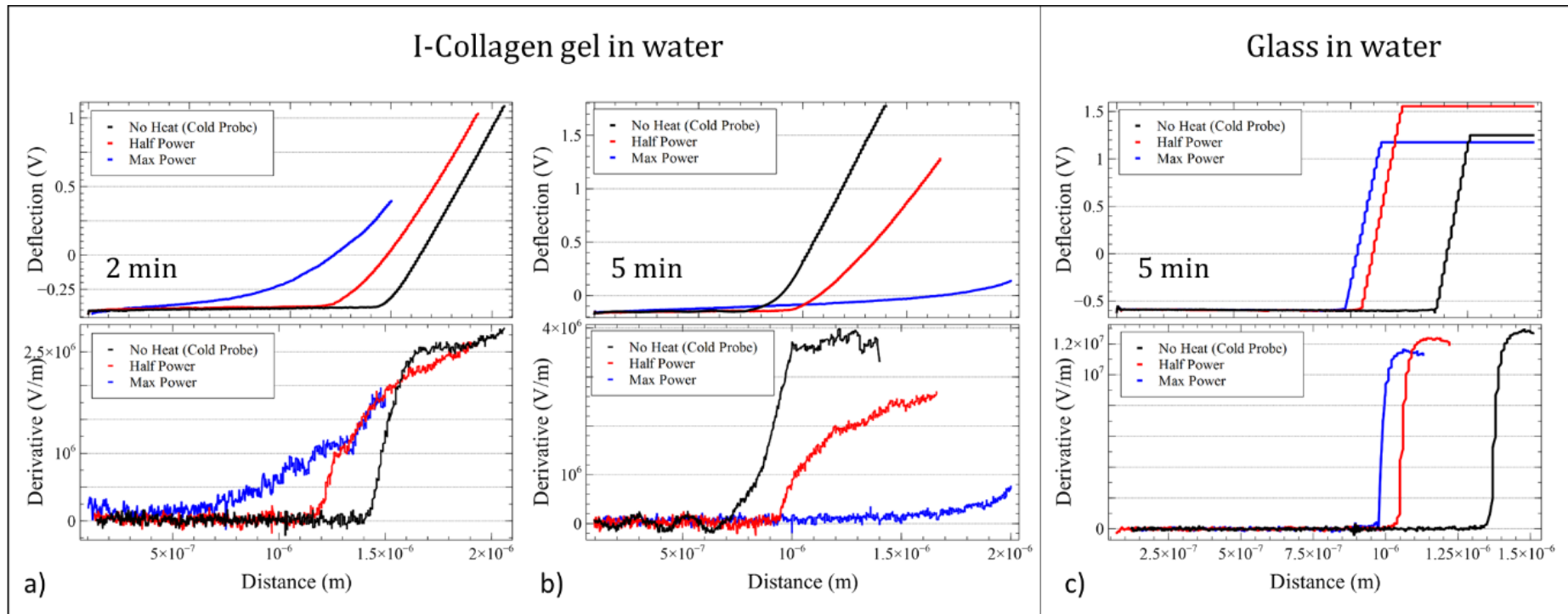


Figure 107 Force curves and their derivatives obtained when a hot probe touches I-collagen gel for 2 min (a) and 5 min (b). The curve are compared with those of a glass sample (c).

After removal from the SThM instrument, the I-collagen sample was imaged and several probe imprints, corresponding to 5 min probe at maximum applied heating power, were observed. Figure 108a shows the imprints imaged using an AFM that offers non-contact, high spatial resolution imaging (Bruker Icon, operating in PeakForce QNM mode [290]). Figure 108 (b) shows a topographic image of the full area (100 x100 μm^2) as well as detail of an imprint, together with their corresponding 3D plots. The imprint had a depth of $\sim 1 \mu\text{m}$ and a diameter of $\sim 14 \mu\text{m}$ which is much larger than the probe contact radius on a hard surface ($\sim 50 \text{ nm}$ [70]).

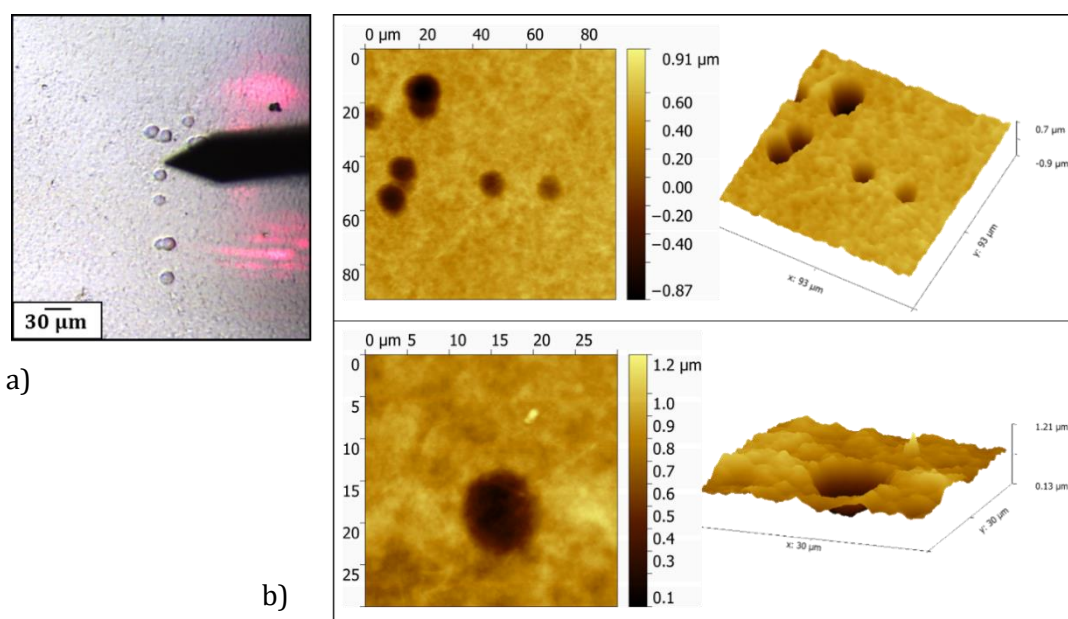


Figure 108 Icon AFM picture (a), topographic height images in tapping mode and 3-D plots of imprints left by a heated probe on gelatinized I-collagen on glass slide (b).

This can be explained by the presence of a constant force setpoint in the AFM control loop during the hot-probe experiment. This is a crucial parameter and it defines the desired voltage for the feedback loop (discussed in sub-section 2.6.1), hence it is directly related to the desired deflection of the cantilever. During the measurement the voltage associated to the setpoint is compared with the real time deflection of the cantilever, which is obtained from the photodiode voltage signal and any difference used to adjust the piezo position. This procedure ensures that the force generated between the tip and the sample (estimated using Hook's law), can be maintained at a constant value. The control loop achieves this by altering the AFM's Z piezo position to keep photodiode measured force and setpoint values as close to each other as possible. The response of the control loop

is dictated by control loop gains that can be altered by the user, requiring a certain level of skill. This is particularly important during imaging as, if the gains are too high, the piezo response will overshoot steep topographic features. Conversely, if the gains are small the piezo height will not change leaving the photodiode signal free to vary around the assigned setpoint, leading to the loss of tip force control. The accurate estimation of the force setpoint, in conjunction with cantilever stiffness is also crucial to determine the correct tip-sample force. This is particularly important with soft materials such as biological samples, that can often be very fragile and delicate. It is worth noting that the choice of setpoint and gains are influenced by other parameters such as scanning frequency and size. In this instance, because of the control loop maintaining constant tip-sample force, a hot tip in contact with an increasingly softening sample will continuously push into the sample, causing a significant footprint expansion. This is highlighted by the schematic depicted in Figure 109, where the tip-sample force is maintained at a constant during the indentation of the heated probe into the sample. In particular, the material softening caused by the elevated temperature results in a progressive increase in the deformation of the sample. It should be noted that, in this situation, the force is kept constant and the probe penetrates the sample with a progressively increase depth (and subsequently increased diameter due to the conical tip shape).

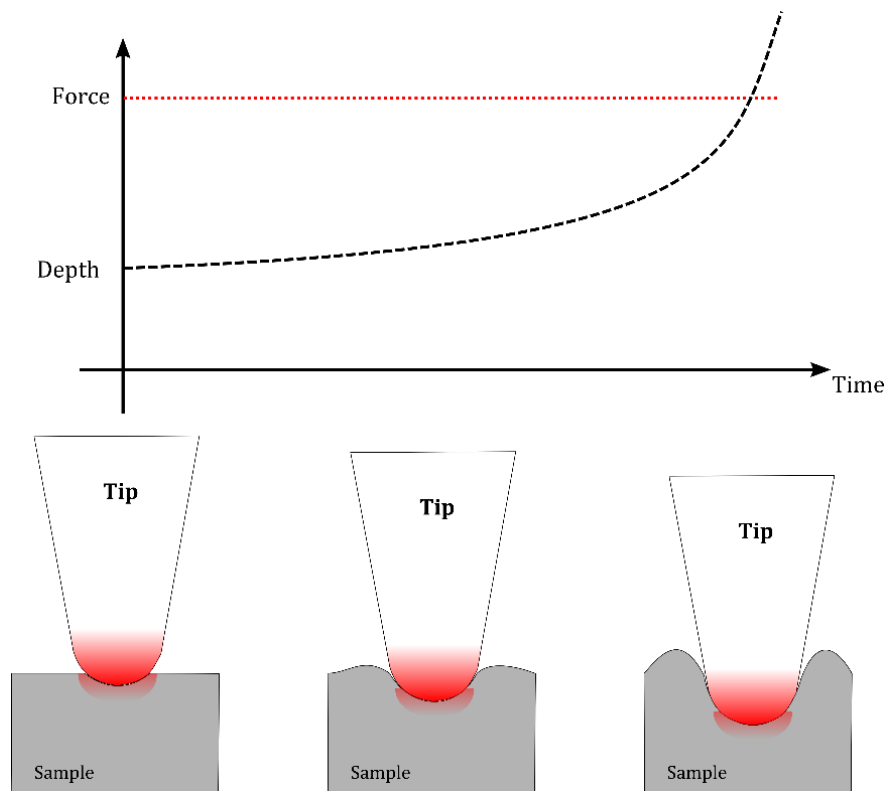


Figure 109 Schematic representation of the tip-sample interaction and subsequent material softening during a constant force indentation.

6.2.3 COLLAGEN FIBRILS PREPARATION AND RESULTS

A sample of I-Collagen fibrils was provided by Dr Laurent Bozec: Biomaterials and Tissue Engineering UCL, University College London [291]. The sample was supplied under DI water solution in the form of a piece of tissue (3 mm thick).

The basic structure of collagen fibrils consists of type I collagen molecules, which are composed of three polypeptide chains, each consisting of 1300–1700 amino acid residues. The collagen molecule is stabilized by extensive hydrogen bonds, many associated with hydroxyproline. Microfibrils, that compose each fibril, are assembled from 4 to 5 molecules and each of these has a characteristic periodicity of 67 nm. Fibrils are formed thanks to cross-linking that allows several micro fibrils to interconnect. These structures are the building blocks for collagen fibers, which are stabilized further by intra- and intermolecular cross-links.

In contrast to collagen fibrils, collagen gel is the result of a denaturation process of fibrils induced by temperature. Gels have a different microstructure, where very poor or no cross-linking is present. They consist of large entanglements of collagen fibers, which can have variable length and thickness. Gels have good fluid properties up to 25 °C but become more rigid at a temperature of around 37 °C.

Usually collagens fibrils, which have a very good crosslinking are present in most living tissues. Conversely, gels that exhibit poor cross linking are found far more rarely, for example in situations such as in wounds or in growing tissues. For this particular reasons gels have been widely investigated for their potential use in skin wound recovery [292] and drug delivery [293].

As our interest is in investigating the use of a-SThM to study biomaterials, collagen fibrils represent a useful first step in this direction. The main idea behind the experiment was to locally manipulate fibrils using the concentrated heat generated by the self-heating probe.

Engineering modified collagen:

- i. Rinse the supplied collagen in RO water, this washed the sample clean of the solution it was suspended in during storage.
- ii. Cut and stretch the sample on a glass slide (0.4mm thick), this process was crucial to allow good adhesion to the glass substrate. In addition it was fundamental that the sample was as flat as possible, since the probe must scan over it without sticking to any large asperity.
- iii. Leave in air until dry (20 min), this final process allowed the collagen to fully attach to the glass without the use of any adhesive. Once this step was concluded the sample was safely scanned using the AFM/SThM.

The I-collagen fibrils sample was placed under DI water and, once rehydrated (5 min), the same procedure was followed as for the gel sample (Section 6.2.2). This procedure of washing and rehydrating fibril collagen samples with purified water is a well-established technique and was employed to ensure valid comparison with the data of other researchers who employed the same sample preparation [294, 295].

From the deflection of the cantilever and the derivative of this data, it was observed that the mechanical properties of collagen fibrils changed with duration of exposure to the heated probe. This phenomenon can be further explored by employing a variation of the analysis developed for the well-established force-distance AFM technique, which can be used to extract information on sample mechanical properties.

Sets of integral equations have been developed that relate AFM force-deflection curves to the elastic material properties of soft materials when subjected to an effective pressure profile. When two cylindrical or spherical bodies enter into contact, it is intuitive to imagine that increasing stress is present at the interface between them, this is known as Hertzian contact stress. This stress is associated with the localised contact and deformation of the two bodies, which produces high tensile and compressive stresses in the materials involved. If the contact and the stresses are in the elastic regime of the materials, the point of contact can be considered as a circular area. A classic example used to show the concept of the cross area of contact is the case of two balls impacting one against the other. The two balls, shown in Figure 110, are placed into contact by a force F , each having a different radius (R_1 and R_2) and different elastic properties, Young's modulus (E_1 and E_2) and Poisson's ratio (ν_1 and ν_2).

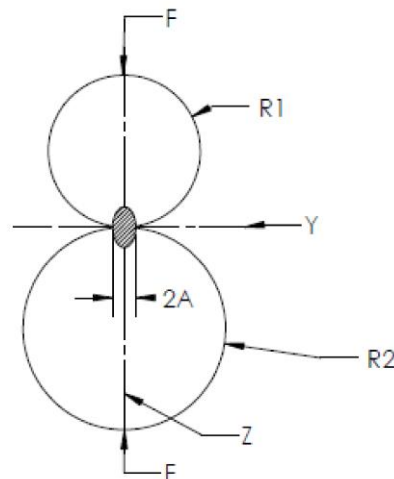


Figure 110 Contact stress at the area of contact between two spheres subjected to a force F .

The maximum pressure generated depends on the contact area and this can be estimated by:

$$A = \sqrt[3]{\frac{3F \left[\frac{1-\nu_1^2}{E_1} + \frac{1-\nu_2^2}{E_2} \right]}{4 \left(\frac{1}{R_1} + \frac{1}{R_2} \right)}} \quad (22)$$

By re-arranging equation 22 it is possible to obtain the force as function of the elastic modulus of the two spheres. When considering the interaction between the AFM tip and the sample one of elastic properties and dimensions are known. During an AFM scan the force and deflection are recorded and used to derive the elastic modulus of the substrate. In order to do this the force-deflection curve is

fitted using a mathematical formulation that relates the force and the deflection. An example of a mathematical solution has been provided by Dimitriadis et al. [296]. The following relationship relates the applied force F , the Young's modulus and Poisson's ratio of the soft sample and indentation depth on the vertical axis δ :

$$F = \frac{4E}{3(1-\nu^2)} R^{\frac{1}{2}} \delta^{\frac{3}{2}} \left[1 - \frac{2\alpha_0}{\pi} \chi + \frac{4\alpha_0^2}{\pi^2} \chi^2 - \frac{8}{\pi^3} \left(\alpha_0^3 + \frac{4\pi^2}{15} \beta_0 \right) \chi^3 + \frac{16\alpha_0}{\pi^4} \left(\alpha_0^3 + \frac{3\pi^2}{5} \beta_0 \right) \chi^4 \right] \quad (23)$$

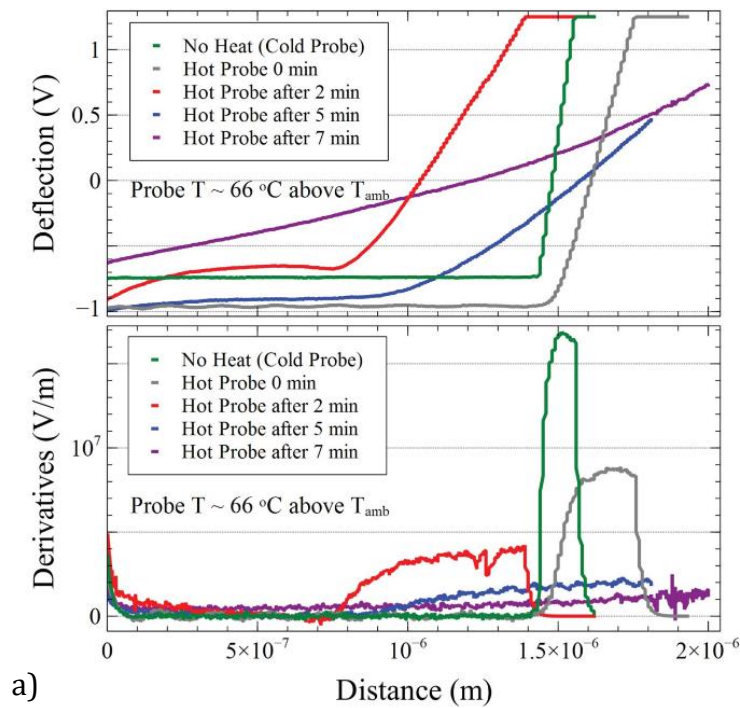
where $\chi = \sqrt{R\delta}/h$, and the constants α_0 and β_0 are functions of the material Poisson's ratio ν given below and the term outside the bracket represents the Hertz solution for the indentation of a semi-infinite solid. Beyond this, the terms within the bracket are terms that are required to consider the finite thickness of the sample. When h (height of the sample in a specific point) increases, χ decrease and theoretically can go to zero for very thick samples. However, when it decreases as the sample becomes thinner it increases the force required to attain a given indentation depth. This solution has the advantage of being applicable for a wide range of Poisson's ratio and allows calculation of the Young's modulus for incompressible material ($\nu=0.5$), a situation typical for biological samples that have a high-water content.

At the most basic level, the lower the force-distance gradient observed after probe-sample contact, the softer the sample is. In this work, the probe was set to either unheated (ambient temperature) or heated (66°C above ambient) as the force-distance curves were generated. In addition, given that the phase transition is not instantaneous, the heated probe was left in contact with the sample surface for various lengths of time (0, 2, 5 and 7 minutes) before the acquisition of the force-distance curves from the same location. Each measurement was made on a fresh region of collagen. From the deflection of the cantilever and the derivative of this data (Figure 111a), both probe temperature and contact time can be seen to have an influence on the mechanical properties of the collagen fibrils. The mechanical deflection shows typical behaviour of a soft sample when a cold probe was used. However, the use of the heated probe causes changes in the stiffness of the sample. The time dependent nature of the thermomechanical phenomenon is also clear as can be seen from the change in shape and slope of the deflection curves. The probe deflection can be seen to be relatively linear, with the derivative reaching a plateau for the cold probe, as well as a heating period of 0

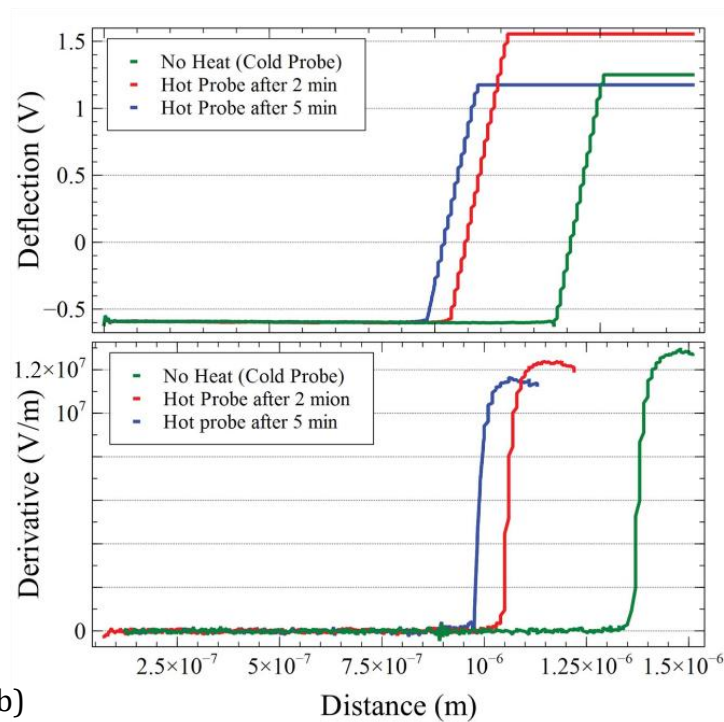
and 2 minutes; however, when the heating time was increased this trend disappeared and a non-linear trend is shown. In addition, the maximum deflection is lower than before and no signal saturation (typically caused by the laser spot entirely leaving the centre of the AFM's split-photodiode) occurred, indicating a lower force. This difference in behaviour is also highlighted by the derivatives (Figure 111a), where an increase in heating time is associated with a significant reduction of magnitude.

Finally, for comparison, the same SThM measurements were made on a glass slide (Figure 111b). As observed previously, force curves obtained on glass do not exhibit any effect due to heating with all curves showing the same gradient. This again proves that the varying gradient seen on collagen is not caused by mechanical changes in the SThM probe as a result of self-heating, but instead must be from the sample. This confirms that the phenomenon is a result of combined force and temperature applied by the SThM probe.

In order to calculate the stiffness of the samples a freely available piece of software developed by the University of Bremen was used [297]. This software uses similar principles to those described above, employing the Hertzian contact model for a sphere to interpolate the deflection-height curve. The user can set several parameters including probe radius, cantilever inclination angle respect with the sample and cantilever stiffness. A series of different force formulations are available for different types of indenting shape. In this instance, the most accurate one available is the one developed by Gavara et al.[298] for elastic moduli determination of cells by atomic force microscopy. A brief discussion of the software is included in Appendix D. This software uses the Levenberg-Marquardt algorithm to solve the problem in an iterative way, via an initial guess provided by the user, followed by a minimisation process. In this case the function to be minimised is the least square of the force-height fit. The user can also provide the initial guessed point of contact. This feature is very important because, due to the absence of any snap-in phenomenon (water environment), it is difficult for the software to find this point numerically.



a)



b)

Figure 111 Force curves and their derivatives obtain when a probe, cold at the beginning, touches I-collagen fibrils for 0 min, 2 min, 5 min and 7 min (a), compared with those of a glass sample (b).

The values of sample stiffness for the different experimental conditions are shown in Figure 112. The results suggest that, as expected, the heating has no effect on glass, but a significant decrease in stiffness is observed for the collagen fibrils sample. The value for 0 minutes of heating is around 20 MPa, which is in

line with similar experiments, without heating, carried out on collagen fibrils in a water environment [299]. When the heated probe was left on the sample the stiffness dropped rapidly, although this decrease was not linear, significantly slowing after 2 minutes (1.94 MPa), until at 7 minutes the stiffness was around 90 kPa.

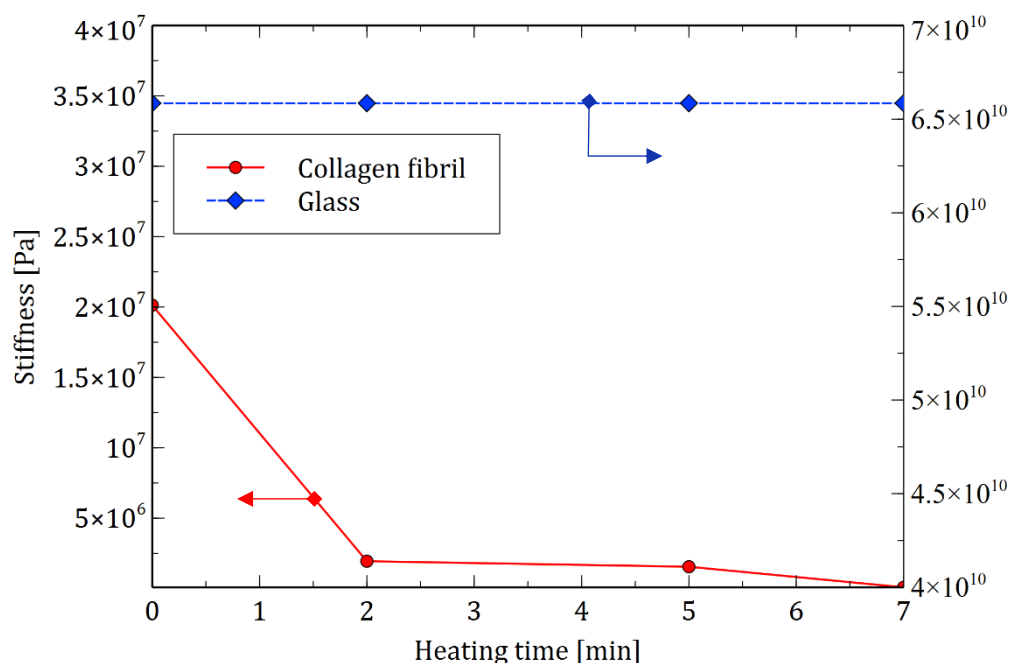


Figure 112 Stiffness curves for the glass and collagen against heating time in water.

Post-indentation images were obtained by moving the sample to the Bruker Icon AFM, operating in PeakForce QNM mode. Figure 113 shows topographic (a) and deflection (c) images of one site where the hot SThM probe was held in contact with the collagen surface. The area where the probe heated the sample is well-defined and exhibits a significant change in depth, similar to the result seen on collagen gel. In addition, from the scan it is possible to see the fibrous nature of the sample, but this is not visible where the heated probe made contact. The darker area in Figure 113a indicates a gradual change in height, underlining the thermal nature of the process that spreads from the point of contact to the surrounding area. This is in excellent agreement with the measurements made on collagen gel in section 6.2.2 above.

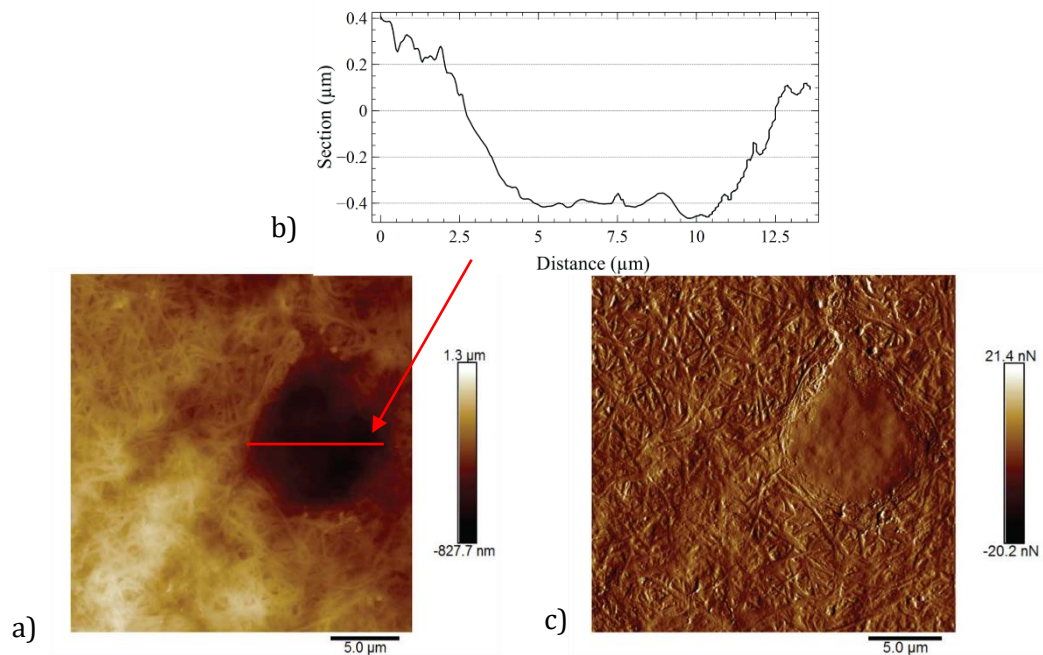


Figure 113 Icon AFM picture (a), topographic height image, (b) section plot on the highlighted path and (c) deflection image.

A cross-section of the indented feature shows that the imprint has a depth of $\sim 0.8 \mu\text{m}$ and a diameter of $\sim 10 \mu\text{m}$ (Figure 113, b), as with the collagen gel results described in the previous section, this is much larger than the tip radius of the SThM probe ($\sim 50 \text{ nm}$). This can be explained, once again, by considering indentation of the hot tip in contact with the heat-softened sample. The probe-sample contact was maintained with a constant force setpoint, resulting in the probe slowly pushing into the softening surface, causing a significant footprint expansion. Figure 113, c shows the deflection image of the same scan area. At the most basic level, this image can be considered to show the differential of the topographic image, therefore highlighting abrupt changes in topography. In this instance, this emphasises the small fibril structures even on gradients such as the edge of the indentation pit. Consequently, it clearly shows the change in the sample structure especially in the area where the heated probe was stationed. It can be seen that contact between the sample and heated probe resulted in alteration of the collagen, transforming it from fibrils to an amorphous structure. This is consistent with the study of hydrated collagen described above, where the start of fibril-gelatin transition was observed at 58°C ; which corresponds to the beginning of denaturation of collagen into gelatin caused by the rupture of internal cross-links [104].

It can be seen from our results that a clear, abrupt transition exists between the region exhibiting well-defined fibrils (Figure 114, a) and the amorphous region (Figure 114, b), suggesting a steep, well defined temperature gradient surrounds the probe. This observation can be explored by comparing the experimental result with the FEA model (introduced in Section 3.7) of a water-submerged probe in contact with a hydrated collagen sample.

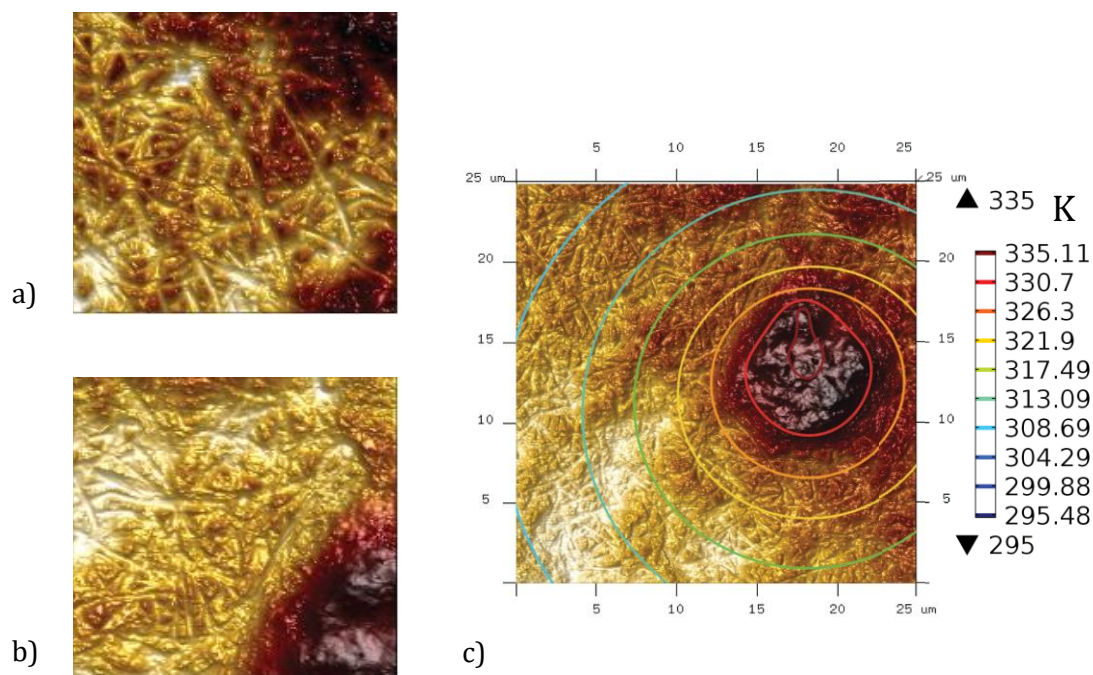


Figure 114 Topographic height (a) and deflection (b) images of an imprint left by a heated probe on I-collagen fibrils. 3-D plot with FE simulation of the surface temperature contour on top of the imprint (c).

The numerical analysis was carried out using the same conditions as the experiment, in terms of environment (fully immersed in water) and applied current to the probe. The collagen sample was modelled as a representative cluster of solid material, and importance was given to the thermal properties. Since the collagen sample was fully hydrated and experiments carried out submerged in water, it was assigned the thermal properties of water. A more detailed description of the geometry and boundary conditions of the model can be found in Chapter 3. It is worth underlining that the scope of this simulation was to predict the thermal field and not the mechanical response of collagen. However, within the bounds of this simplification, the model adopted can be considered a good approximation. The most significant result obtained from the simulation is the predicted extent and temperature of the thermal field. This can be compared with the experimentally measured imprint left by the SThM probe

on the sample. Figure 114(c) shows the collagen surface isothermal contour obtained from the FEA simulation overlaid at exactly the same scale on the topographic 3D AFM image of the collagen fibril sample imprinted by the heated SThM probe. The change in color in the AFM image corresponds to a change in depth, and the imprint is well-centered with the area where the sample temperature was predicted to be ~ 62 °C from the FEA model. Collagen appears to be completely amorphous in the center of the heated region, however, maintained its original form (fibrils) in the areas with low applied temperature. This is confirmed by looking at the temperature calculated by the simulation (Figure 114, c), where the boundary of the amorphous region is associated with a predicted temperature of ~ 58 °C which corresponds with the transition from fibril to amorphous observed in literature by Bozec *et al.* [104].

6.3 MG-63 LIVING CELLS

6.3.1 INTRODUCTION

Perhaps one of the most debated areas in biology regards the temperature distribution within living cells, a topic in which theoretical and experimental approaches still fail to agree on. This knowledge is of great interest because of the insights it could provide into cellular pathways and chemistry as well as to be a marker for diagnosing disease. The ability to measure the temperature of individual cells is currently an extremely challenging task for researchers [42, 300]. In recent years scientists have started to develop methods that can reveal temperature heterogeneity both between cells and within them. Several methods for measuring and mapping temperature in single cells [53], [201] have been used, from focused infrared laser beam to illuminated nanoparticles [301], [302], [303], [304], [305]. Other techniques have been exploited to record temperature variations in living cells in the absence of any exogenous heating source, in an attempt to scrutinize endogenous thermogenesis in single cells as well as fluorescent thermosensors [306], [307] or nanoscale thermometers [308].

A particularly innovative piece of research in this field was carried out by Johannessen *et al* [309]. The main objective of this research work was the accurate measurement of heat dissipated by cells as an estimate for the efficiency of the cellular system and to monitor their activity. The key achievement of this research was the creation of a micro calorimeter capable of analysing very small quantities of sample, in the order of 700 pL of culture solution. The system

demonstrated a temperature resolution of 0.125 mK, and a low heat capacity of 1.2 nJ [309]. In his work Johannessen was, for the first time, able to estimate cellular response by measuring temperature change and heat flux, relating these results with other indicators including oxygen consumption. However, the measurements obtained were not perfect, as they did not give the response of a single cell, but an average over the estimated number of cells contained in the sample. This poses limitations to the understanding of cell response to any treatment used in the micro calorimeter.

In living cells, all structurally important parameters such as binding rates of crosslinkers [310], molecular motor activity [311], or polymerization velocity of actin filaments [312] are known to be temperature sensitive and thus temperature directly affects cell molecular architecture and mechanical properties. It is therefore reasonable that temperature changes can alter the mechanical stability of a cell's cytoskeleton, which is a complex network of filamentous proteins, linkers and molecular motors that constantly assemble and disassemble [313]. In turn, cell mechanical properties have been identified as crucial for many cell functions, ranging from stem cell differentiation [314] to cancer progression [315]. In this regard, Kießling *et al.* showed how laser-induced heating could result in a drop of cell stiffness [316], and an increase of viscous deformation (creep) due to the elevated temperature (up to 37 °C) caused by the laser source. SThM under biologically benign conditions offers a novel way to model thermal therapies, in which body tissue is exposed to extremely localised high temperatures (up to 45 °C), in-vitro. a-SThM can selectively heat each cell individually within a biologically benign environment, providing specific indication on cellular mechanical response to the heat treatment. The resulting information could then be used to define the location, magnitude and duration of a thermal source required to kill a single cell. This is particularly relevant to groups who are investigating treatment of tumours via hyperthermia using deep penetrating near infrared (NIR) lasers with or without contrast enhancing agents (indocyanine green), that convert laser radiation in localised heat [317]. Thermal therapies that employ simple heating sources such as laser light [318], [319], [320], [321], focused ultrasound [322] and microwaves [323], [324], [324], [325], still have trouble discriminating between tumours and surrounding healthy tissues [326]. This is a concept that shows great promise,

although success with current systems has been modest [327], [328] making it an ideal candidate for study using a-SThM.

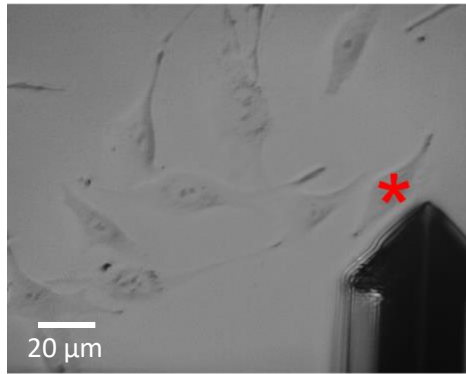
6.3.2 EXPERIMENTAL METHOD AND RESULTS

The aim of this experiment was to demonstrate, for the first time, real-time single cell-selective thermal manipulation under their liquid environment using a-SThM. The reason behind this has been discussed previously (Section 6.3.1) and resides in exploring the possibility to study the response of cells to various levels of heat flux and temperature. The samples used were MG63 living cells, provided by Prof Huabing Yin, Biomedical Engineering of the University of Glasgow. The steps required to prepare the sample for scanning using a-SThM are reported in Appendix E.

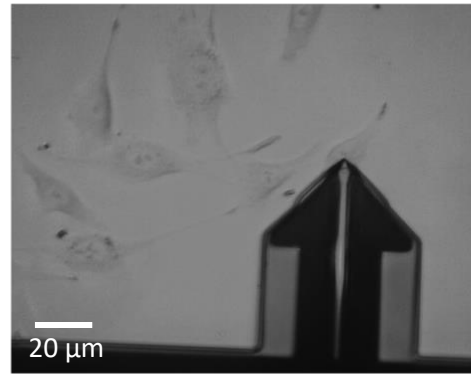
The experiment was conducted by heating up the thermal probe to 85°C and leaving it in contact with a single MG-63 cell for ~ 2 minutes; this was enough to kill the cell which became detached from the surface (Figure 115).

In order to determine whether cell death was simply caused by the mechanical force of the AFM probe or if heating played a role, the experiment was repeated on a different cell, this time employing an unheated probe. However, even after continuous contact for ~ 10 min, the cell remained alive and could not be removed from the substrate. This strongly suggests that cell death was caused by heating rather than the force generated by the SThM probe working in contact mode.

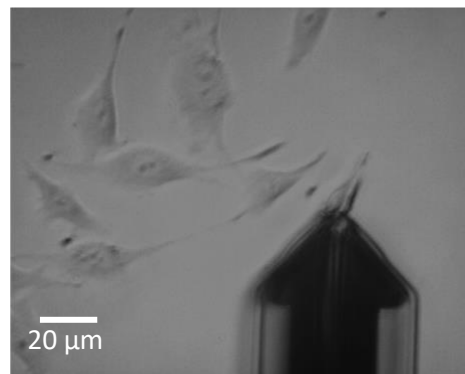
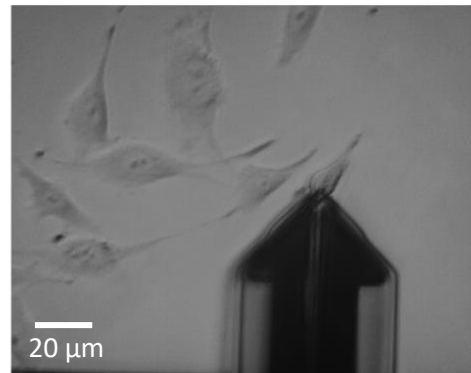
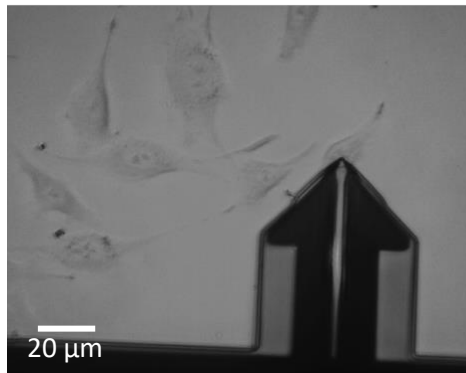
Before



In contact



After 2 minutes



*** Cell killed and removed by SThM probe**

Figure 115 Optical microscope images of a single MG63 cell left in contact with a hot SThM probe (2 min) and lifted up.

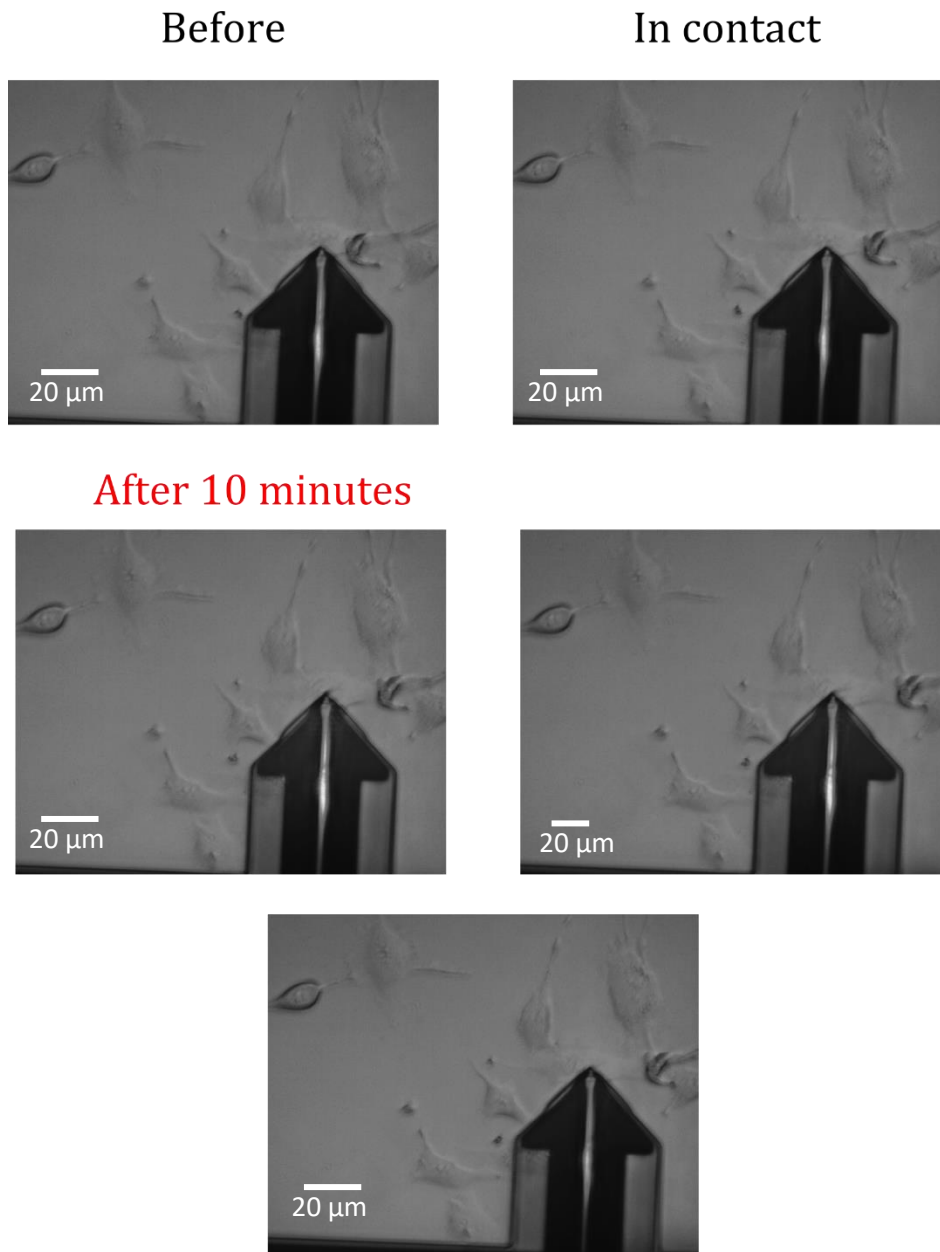


Figure 116 Optical microscope images of a single MG63 cell left in contact with a cold SThM probe (for 10 min) and lifted up.

The same finite element simulation approach employed for collagen fibrils (Section 6.1.4) was used to predict the temperature distribution experienced by the cell in contact with a self-heated SThM probe. The model was realised by simulating the probe in contact with a substrate representing a living cell (i.e. same dimensions and thermal properties) as shown in Figure 117 . The cell was discretised as an oval 3D shape (40 μm length, 4 μm thick) with a regular tetrahedral mesh matched to the substrate, that it was considered to be in perfect contact with. The probe was meshed with the same type of element with and heat transfer condition assigned as boundary condition at the interface. The heat flux could flow between the different bodies which were connected by nodal contact.

This allowed heat to flow between the probe tip and the cell/substrate. Heat transfer primarily occurred via this contact and via the surrounding water environment, which is not shown in the interests of clarity. Conduction was also considered between the cell and the substrate, by matching the nodes on the two meshes and assigning a common thermal boundary condition, allowing continuity in the calculation. Heat generation was simulated in the probe via Joule Heating by applying a current through the probe pads (0.0045 A) as described previously in Section 3.7. The external faces of the environment, not visible in Figure 117, were set to room temperature.

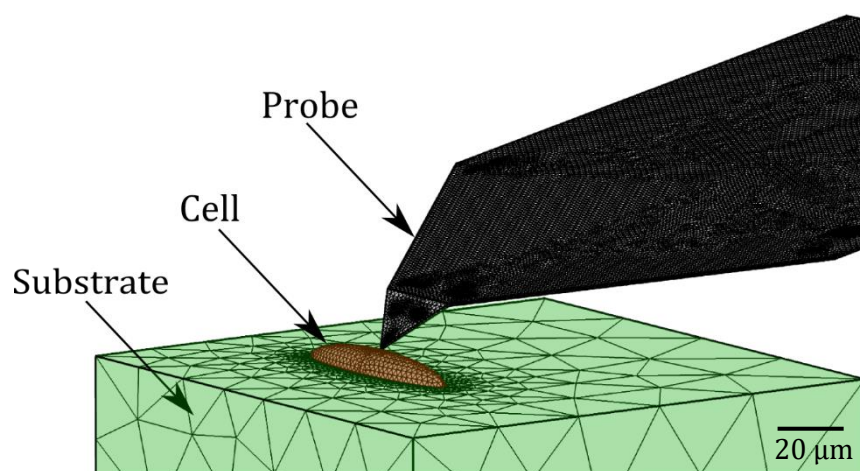


Figure 117 Finite element mesh of the probe/cell/substrate model, the surrounding environment is not shown for sake of clarity.

This finite element model was used to estimate the magnitude and the radius of the thermal field caused by the self-heated probe. The temperature contours, encompassing the probe, cell and substrate are shown in Figure 118. As expected, the highest temperature is located on the probe heater (site of maximum heat generation), which has a peak value of around 80 °C, while the apex of the tip has a decreased value due to lower heat generation in relation to loss from thermal coupling with the water environment and the cell. An advantage of the FEA result is that it allows various components of the system to be considered in isolation. This can be seen in the detailed view of Figure 118, where the temperature achieved on the cell surface alone is predicted to be around 50 °C. This temperature is highly localised to the area on and nearby the cell, rapidly dropping to around 30 °C in areas a few micrometres away from the tip. Although this model does contain assumptions necessary to simplify the model, for example, the thermal contact between the different parts is considered perfect

and no interfacial resistance to the flow is considered, the predictions are physically reasonable and match well with the experimental results.

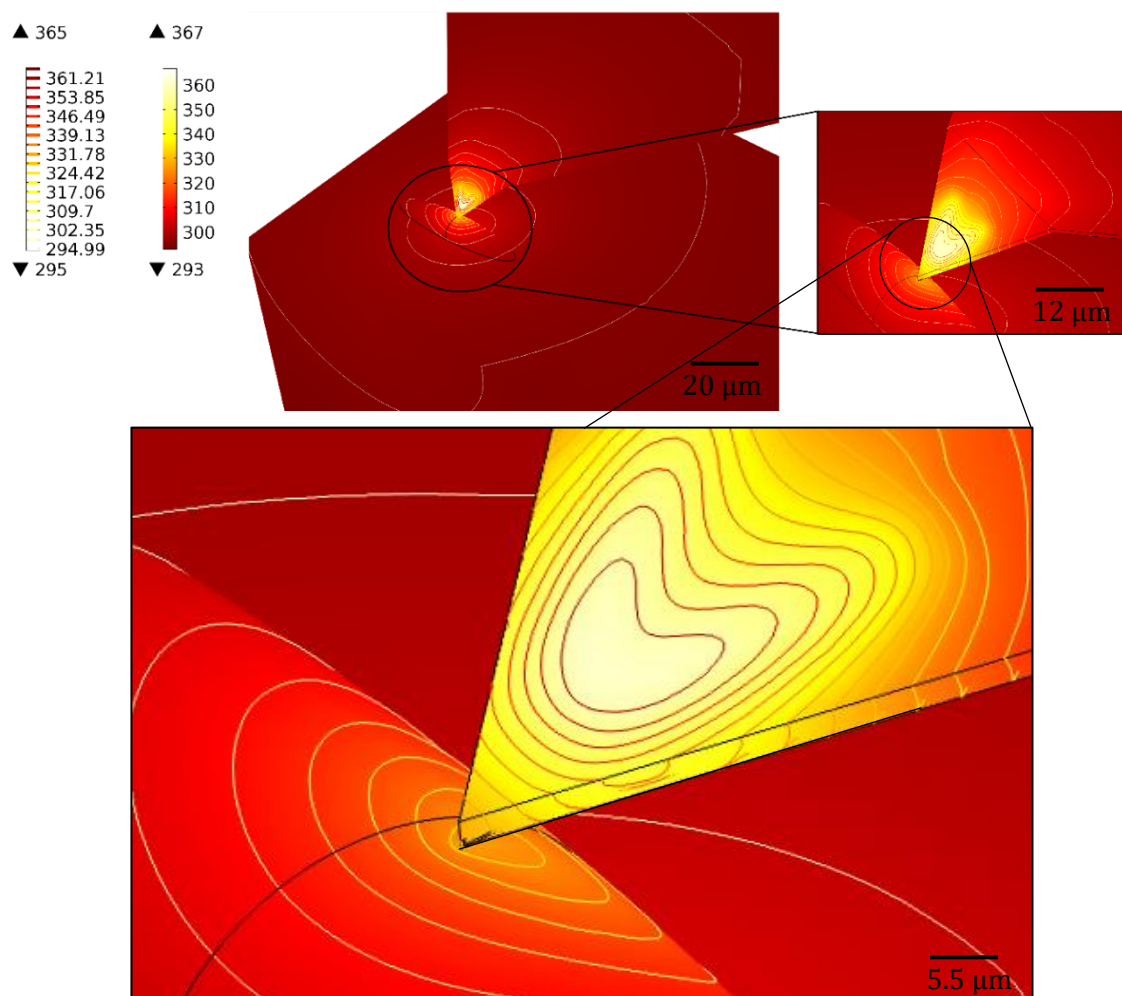


Figure 118 COMSOL Multiphysics analysis results showing the temperature generated by the probe using a current of 0.0047 A in a water environment.

To expand the analysis, the isothermal contour predicted to be experienced by the heated cell was then overlaid at the same scale on the optical microscope image taken during the experiment. Figure 119 shows the temperature profile superimposed on a MG63 cell ($\sim 50 \mu\text{m}$ diameter [329]) where a spherical volume of $\sim 200 \mu\text{m}^3$ (estimated from image) was predicted to be raised above $50 \text{ }^\circ\text{C}$ (323 K) by the self-heated SThM probe in contact. This volume was obtained from measurements of the contour plot within COMSOL assuming a perfect isotropic temperature propagation in space.

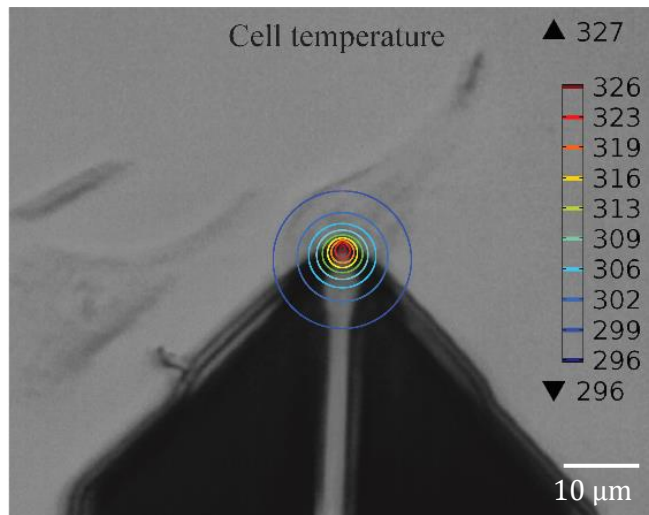


Figure 119 Temperature predicted by COMSOL MULTIPHYSICS joule heating simulations during the contact with a hot probe and extracted for MG63 cell.

This magnitude agrees with the literature which indicates a temperature range of 42-46°C is enough to kill cancer cells [330], [331], [332]. It should be clear from this image that, even with non-optimised commercial probes, significant heating is only predicted to occur in a region directly around the probe tip with a radius of less than 15 μm. Therefore, it is worth noting that, as shown in Figure 119, the surrounding medium and cells will not experience temperatures higher than 23 °C. This was held up by repeated measurements in which cell death was solely observed in cells directly in contact with the probe. Such highly localised heating matches that reported in recent work using optical [333] and particle-based [334] heating methods that demonstrate the sensitivity of cellular membranes to elevated temperature. It is important to point out that the most significant limitation of a-SThM for biological samples as reported here stems from the prototype instrument employed. The Multimode AFM is not well designed to perform biological measurements and future work will move to a system based around a more suitable optical microscope. For example, the integration of a competent inverted microscope would permit additional tests on cell behaviour using Trypan Blue dye [335], which can clearly identify dead cells.

However, despite their deficiencies, these results do illustrate the high precision and selectiveness of the a-SThM method, which permits a single cell (or even one region of a single cell) to be significantly heated whilst adjacent cells (or regions of the same cell) remain at ambient/moderate temperatures. Furthermore, it should be noted that the extent of the heated region is dictated by the size of the RTD heater on the probe and is not intrinsic to the proposed instrument.

Therefore, specifically modified a-SThM probes with smaller heaters, as discussed in Section 5.3, could be employed to heat a smaller region.

6.4 CONCLUSION

In this chapter, two novel experiments were employed to demonstrate the capability of the new a-SThM to modify biological samples in their native aqueous, electrically conductive environments.

The first experiment regarded I-collagen gel and fibrils, prepared and deposited on a transparent glass support. The KNT SThM probe was heated and used to modify the sample structure (from fibrils to amorphous collagen) by generating imprints on the sample. This demonstrated that a-SThM can produce very localised changes in mechanical properties of a biological sample, which is known to be sensitive to temperature.

To cross-validate the experimental results, an FE model was used to predict the thermal field experienced by the samples during the experiment. The results obtained showed very good agreement with the experiment and with the literature regarding the thermal degradation of I-Collagen. This experiment elegantly demonstrated the power of this new method and how the introduction of a-SThM could assist work on the thermo-mechanical behaviour of biological material and systems.

The second experiment involved the killing of individual, live cancer MG-63 cells. The a-SThM probe was used to heat up a single cell, and its behaviour was monitored. When the hot probe (80 °C) was left in contact with a constant force for 2 minutes, the cell died, detaching from the substrate. By comparing the experimental and numerical results it is clear that the heat was localised and the affected area very small. This demonstrates that the technique can be used for the selective killing of each cell adhered to a substrate, facilitating the study of parameters such as exposure time or temperature magnitude for each cell. In addition, the method was demonstrated to be very accurate in manipulating and altering only the cells in direct contact with the probe. This particular feature suggests that a-SThM could become a useful tool for the in-vitro study of thermal-mechanical behaviour on specific biological samples.

The most significant limitation in all experiments on biological systems was that multimode AFM employed as the base for the a-SThM instrument. This microscope, whilst capable of in-liquid measurements, is far from ideal when

employing live, biological samples. This is primarily due to the lack of thermostatic sample control alongside only having a basic optical microscope. An ideal instrument would incorporate both a competent, inverted optical microscope, capable of more advanced imaging, such as fluorescence, as well as the ability to maintain sample temperature, maximising the duration that cells remain viable for. Having said this, the measurements presented in this chapter clearly demonstrate the first-ever use of SThM on biological samples held in a benign aqueous environment.

CHAPTER 7: FINAL REMARKS

The first goal of this PhD was to enable SThM to work under aqueous environments (a-SThM). This was achieved by modifying the AFM instrumentation by means of a new probe holder and a new electronic system. The modified instrument was designed to prevent electrochemical reactions that were hypothesised as the reason for immediate SThM probe failure under-water. This hypothesis was proven, with clear evidence of the electrochemical nature of failure, through an extensive experimental testing campaign that employed sacrificial heater samples. The new tool was successfully tested and employed in the study of several samples. Thermal measurements achieved by scanning a $\text{Si}_3\text{N}_4/\text{PI}$ sample in water were in excellent agreement with COMSOL simulations, clearly showing the enormous potential of this technique in water. In addition, the measurements demonstrated very good stability and the possibility to conduct non-contact scans, extending SThM into previously inaccessible fields. These results were rigorously explored in a systematic study looking at the performance of SThM underwater, employing both experimental and numerical approaches to quantify the results. For this purpose, solid samples with well understood geometry and material properties were measured and compared to an equivalent FE models, with excellent agreement. The results obtained from both this experimental and numerical approach were then used to propose a new probe design better optimised to deliver maximum resolution in a water environment. Specifically, a smaller, asymmetric heater was identified as a good candidate to maximise the achievable temperature and increase thermal contrast, which is crucial when imaging dissimilar materials.

Finally, a major achievement of this work was to validate the technique by demonstrating its applicability to biological experiments. This was initially tested on a biologically relevant material, showing that the probe can be hot enough to alter the mechanical properties of soft I-collagen gel and I-collagen fibrils in their native environment, leaving imprints on the samples. The a-SThM apparatus was then employed to manipulate living MG-63 cells. The simple, but first of its kind, experiment consisted of the selective local heating of different cells. The result was the selective killing of only those cancer cells exposed to elevated temperatures at the point of contact, leading to detachment of the dead cell from the collagen substrate. In order to exclude the mechanical effects of the AFM

contact force, other cells were subjected to the same load from an unheated probe for longer periods, up to 10 minutes. However, no alteration of the sample was observed, demonstrating the direct impact of localised heat on cell behaviour.

7.1 SUMMARY AND CONCLUSIONS

From the perspective of biology and life science, nanoscale thermal measurement and manipulation are increasingly being recognised as a key tool in the study and control of cellular processes. This has resulted in the innovations and insights highlighted in the Introduction chapter, demonstrating how nano-thermal processes can allow researchers to study and manipulate fundamental biological processes that generate and utilise energy, an area which involves almost every activity of a living cell. However, current methodologies for measuring temperature in biological samples are often limited in their spatial resolution and sensitivity. Indeed, many common methodologies are based on large scale sample analyses, which do not consider single cells, but instead interrogate larger tissues. Therefore, despite their common use, these methods do not allow the study of behaviour exhibited by single cells. In addition, the large thermal mass of such samples and instruments results in a poor temporal response, another crucial aspect for real-time analyses. Excluding a-SThM, the new approach presented in this research, the most promising technique is DNA based thermometry. However, when compared to DNA based thermometry a-SThM, can be considered to be a much more ‘multipurpose’ tool, capable not only of thermal measurement but also of directly altering sample temperature in a highly selective manner, with a high spatial resolution of around 50 nm. This capability makes a-SThM a valid tool to overcome the gap that separates thermal manipulation and temperature measurement, expanding the toolset currently available for nanoscale thermal-biology research and minimising the technical barriers for new investigators entering the subject. Beyond this demonstration, the work has also highlighted interesting new approaches enabled by the instrument, for example, the possibility of out-of-contact measurements that are possible in a water environment. This may provide more reliable SThM imaging, even on conventional samples that could be imaged in air.

7.2 FUTURE WORK

Several methods are currently used for measuring and manipulating temperature in single cells [53], [201], from focused infrared lasers to illuminated nanoparticles [301], [302], [303], [304], [305], fluorescent thermosensors [306], [307] or nanoscale thermometers [308]. However, the measurements obtained are sometimes controversial and most techniques can be considered to be in their early stages [40]. Beyond this, methods that locally heat cells come with their own strengths and weaknesses, for example, laser approaches, whilst being relatively convenient, still have trouble discriminating between tumors and surrounding healthy tissues, often heating healthy tissue located between the source and the target site [326], [336]. Other methods such as magnetic fluid hyperthermia (MFH) which employs magnetic nanoparticles as heaters (MNHs) can be used to selectively kill cancer cells but present significant challenges in monitoring and controlling the temperature during treatment [331].

Even from these few examples, it can be seen that there is a real demand for the development of devices capable of accurate temperature determination for such processes, as well as the investigation of heat production and dissipation that they cause [337], [42]. The resulting information would be of great interest due to the insights it could provide into cellular pathways and chemistry as well as being a marker for diagnosing disease. For these reasons, a-SThM promises a new approach to provide additional data in this active area of research.

Three specific challenges can be identified to unlock the full potential of this technique. The first concerns continued development of its implementation, allowing more interesting and challenging samples to be studied, for example those that display different thermal-mechanical properties. This will employ our new understanding of probe-water-sample interaction, as well as improved instrumentation that can automate probe temperature ramps. Since it has been demonstrated that a hot probe can permanently deform soft samples, the possibility of heated-SPM lithography on biological samples should be explored. Most importantly, this same approach could also be deployed on live samples such as single cells, where the SThM probe could be used to selectively kill and remove them from specified areas of a substrate.

The second challenge relates to the instrumentation; the multimode AFM was adapted to work in water, generating very promising results. However, this

microscope is not well designed for aqueous/biological measurements. A more suitable AFM specifically designed for fragile and biological samples has been identified (JPK Nano-wizard AFM). Work will be undertaken to adapt this instrument for use as an a-SThM, permitting more challenging samples to be studied. In particular, non-contact and tapping mode imaging will be further investigated. Within the work presented in this thesis evidence of good SThM thermal resolution when out-of-contact has been provided for both flutec PP3 and for water environments. The larger thermal conductivity of water could potentially allow constant thermal signals to be obtained in tapping mode or PeakForce imaging thanks to the relatively low temperature-distance gradient displayed by SThM probes in aqueous environments. This technique would be a big step forward in SThM, especially for its application on biological samples.

The third challenge is presented by the probes themselves. As has been demonstrated in the presented COMSOL simulations, significant improvements could be made to the probe design. With the insights gained from this work, it will be possible to create new probe designs which are better suited for biological samples, improving the thermal-spatial resolution as well as the maximum attainable probe temperature under liquid. Once designed, these probes could be fabricated in the JWNC at Glasgow before being evaluated in the newly developed a-SThM systems.

APPENDICES

A. DESIGN OF PT/Si₃N₄ DEVICES

As mentioned above, the first part of this PhD concerns the fabrication of a device having material properties and dimensions comparable with the SThM probes used in Glasgow [80]. It was also decided, to assist in the familiarisation in basic microfabrication, to simplify the design as much as possible, minimising costs and fabrication time. Pursuing the goal to mimic the behaviour of a thermal AFM probe in a liquid environment, the platinum resistor at the extreme end of the cantilever can be approximated by a platinum heater connected to two pads through two wires. The width (hence cross-section) of the pads and the wires was maximized to provide them with the smallest possible resistance. Therefore, by applying a potential difference to the pads, Joule heating was primarily limited to the central, narrow heater. With this basic layout, three resistors with different lengths were produced. Figure 120 and Figure 121 show the relevant dimensions and the heater designs, the pads are 'hollow' triangles to maximise their extent for easy contact but reduce the Electron Beam Lithography (EBL) total writing time.

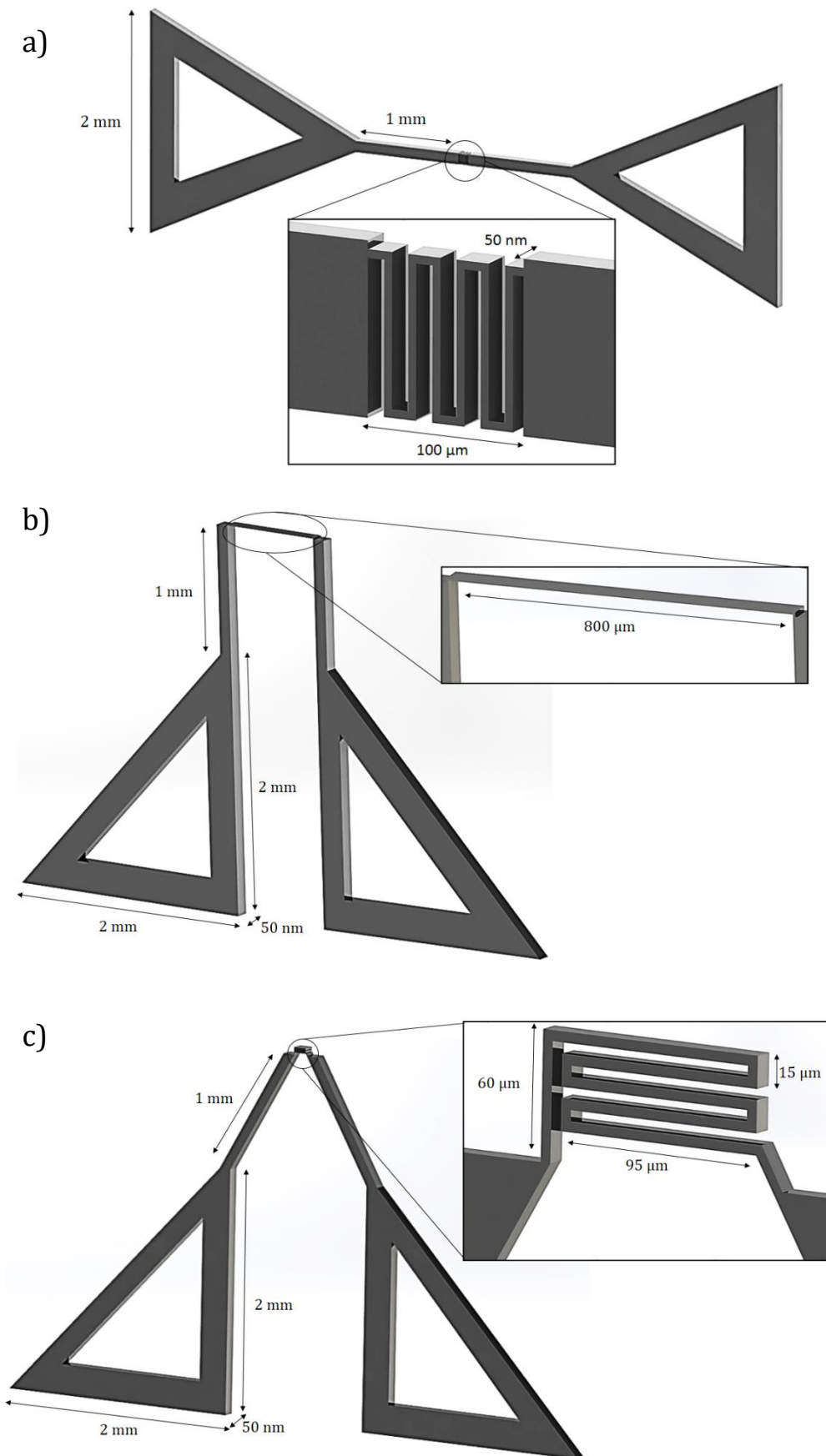


Figure 120 Resistors design. The total length (l) of the heaters is respectively (a) $l = 1290\ \mu\text{m}$, (b) $l = 1630\ \mu\text{m}$, and (c) $l = 1210\ \mu\text{m}$.

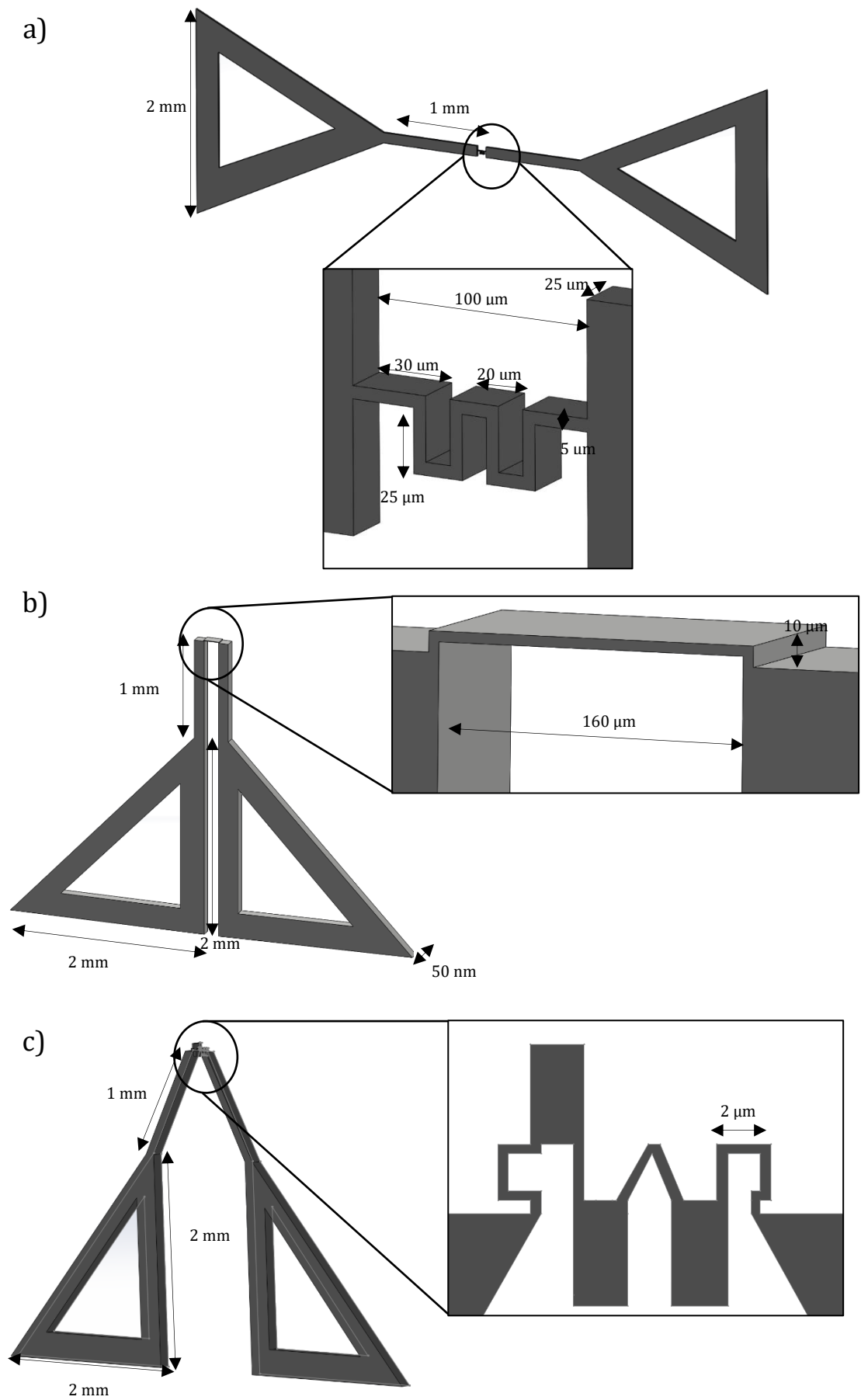


Figure 121 Resistors design. The total length (l) of the heaters is respectively (a) $l=410\mu\text{m}$, (b) $l=340\mu\text{m}$, and (c) $l=287\mu\text{m}$.

The resistors share the same thickness (50 nm) and the heaters have the same width (5 μm).

B. a-STHM ELECTRONIC SCHEMATIC AND CODE

The complete schematic of electronics required to operate SThM in liquid is shown in Figure 122. All the required components are included within the schematic, including the lock-in amplifier, the sinusoidal signal generator, the signal filtering, amplifying electronic board as well as the transformers and bridge with the resistances and the SThM probe.

The code shown below is used to control the electronics including the input output interface, the communication with the computer governing the Multimode AFM, and the signal processing. The code also manages the signal phase change and the comparison between output signal and reference signal [72].

```

#include "mbed.h"
#include "stdio.h"

DigitalOut led1(LED1);
DigitalOut led2(LED2);
DigitalOut led3(LED3);
DigitalOut led4(LED4);
BusOut digit(p30,p29,p28); //D1 (msdigit), D2, D3
BusOut segment(p26,p27,p21,p22,p23,p24,p25); //g,f,e,d,c,b,a
DigitalIn up90(p19); //Inputs for increasing and decreasing the phase
DigitalIn dn90(p18);
DigitalIn up10(p17);
DigitalIn dn10(p16);
DigitalIn up1(p15);
DigitalIn dn1(p14);
Serial pc(USBTX, USBRX);
SPI spi(p5, p6, p7); // mosi, miso, sclk
DigitalOut csrf(p8); // FSYNC for RF DDS
DigitalOut cslou(p9); //FSYNC for upper LO generator DDS
DigitalOut cslo1(p10); //FSYNC for lower LO generator DDS

float phasdeg = 111.0; //phase in degrees
int phasint; // Integer phase as degrees
int phasbin; //phase as binary
int deltaphas; //Has phase been changed?
char numconv[16]; //String to convert a number to characters into
int result; //return from subroutines
int disnum; //a single digit for display
int debouncectr; //counter to debounce switches
int foocount;
int phasword; //word containing the phase writing command to send to the RF oscillatoe

//int sevseg[10] = {0x7e, 0x30, 0x6d, 0x79, 0x33, 0x5b, 0x5f, 0x70, 0x7f, 0x7b}
//int sevseg[10] = {0x01, 0x4f, 0x12, 0x06, 0x4c, 0x24, 0x20, 0x0f, 0x00, 0x04}

int ddsinit()
{

//for (foocount =0; foocount <100000; foocount++)
//{

csrf = 1; // FSYNC for RF DDS disable
cslou = 1; //FSYNC for upper LO generator DDS disable
cslo1 = 1; //FSYNC for lower LO generator DDS disable

```

```

wait_ms(1);
//spi.write(0xffff); //dummy SPI output

csrf = 0;
spi.write(0x8000); //SELSRC = 0 so selected by pins not registers
csrf = 1;
csrf = 0; //FSYNC for RF DDS enable
spi.write(0xf800); //initialise RF channel
csrf = 1;
csrf = 0;
spi.write(0x3314);
csrf = 1;
csrf = 0;
spi.write(0x2200);
csrf = 1;
csrf = 0;
spi.write(0x3100);
csrf = 1;
csrf = 0;
spi.write(0x2000);
csrf = 1;
csrf = 0;
spi.write(0xC000);
csrf = 1;

```

```

cslou = 0;
spi.write(0xf800); //initialise ULO channel
cslou = 1;
cslou = 0;
spi.write(0x3313);
cslou = 1;
cslou = 0;
spi.write(0x2280);
cslou = 1;
cslou = 0;
spi.write(0x3100);
cslou = 1;
cslou = 0;
spi.write(0x2000);
cslou = 1;
cslou = 0;
spi.write(0xC000);
cslou = 1;

```

```

cslol = 0;
spi.write(0xf800); //initialise LLO channel
cslol = 1;
cslol = 0;
spi.write(0x3300);
cslol = 1;
cslol = 0;
spi.write(0x2280);
cslol = 1;

```

```

cslol = 0;
spi.write(0x3100);
cslol = 1;
cslol = 0;
spi.write(0x2000);
cslol = 1;
cslol = 0;
spi.write(0xC000);
cslol = 1;
//}
return 0;
}

int main() {
spi.format(16,2);
spi.frequency(100000);
result = ddsinit();

//disnum = 0;
while(1) {

//disnum = disnum +1;
//if (disnum == 10) disnum = disnum-10;

if (up90 == 0)
{
phasdeg = phasdeg + 90.0;
deltaphas = 1;
}
else if (dn90 == 0)
{
phasdeg = phasdeg - 90.0;
deltaphas = 1;
}
else if (up10 == 0)
{
phasdeg = phasdeg + 10.0;
deltaphas = 1;
}
else if (dn10 == 0)
{
phasdeg = phasdeg - 10.0;
deltaphas = 1;
}

else
{
}
// Limit phase to range 0 ... 360

//pc.printf("phasedeg is %f \t",phasdeg);

```

```

if (phasdeg < 0.0) phasdeg = phasdeg + 360.0;
if (phasdeg >= 360.0) phasdeg = phasdeg - 360;

//pc.printf("phasedeg is %f \n",phasdeg);
if (deltaphas ==1)
{
//update phase in DDS chip
phasbin = (int)(phasdeg / 360.0 * 4095.0);
pc.printf("phasbin is %i",phasbin);
phasword = 0x1900; //Command bits to write 4 MSB phase0 bits to phase defer register
phasword = phasword + (phasbin / 256);
pc.printf("phasword upper is %i",phasword);
csrf = 0;
spi.write(phasword);
csrf = 1;
phasword = 0x0800; //Command bits to write 8 MSB phase0 bits to phase register
phasword = phasword + phasbin - 256 * (phasbin / 256);
pc.printf("phasword lower is %i \n",phasword);
csrf = 0;
spi.write(phasword);
csrf = 1;
}
else
{
//led1 = 0;
}

deltaphas = 0;
//wait(0.3);
//Now display phase
for (debouncetr = 0; debouncetr < 100; debouncetr++)
{
phasint = phasdeg;
disnum = phasint / 100;
segment = sevseg[disnum];
//segment = sevseg[disnum[0]];
digit = 0x4;
wait(0.0005);
disnum = (phasint - disnum * 100) / 10;
segment = sevseg[disnum];
//segment = sevseg[disnum[1]];
digit = 0x2;
wait(0.0005);
disnum = phasint - 10 * (phasint / 10);
segment = sevseg[disnum];
//segment = sevseg[disnum[2]];
digit = 0x1;
wait(0.0005);
digit = 0x00;
if (up1 == 0)
{
phasdeg = phasdeg + 0.01;
deltaphas = 1;
}
}

```

```

else if (dn1 == 0)
{
phasdeg = phasdeg - 0.01;
deltaphas = 1;
}
else
{
}
}
/* digit = 0x3;
segment = 0x00;
wait(0.5);
digit = 0x5;
wait(0.5);
digit = 0x6;
wait(0.5);
*/
}
}

```

C. LIFT-OFF PROCESS

Lift-off is an additive process that is employed mainly in research for the creation of metallic interconnections. Within this methodology a series of structures are created using a sacrificial material, typically a resist, which is subsequently patterned. Once the patterned regions of resist are removed the desired metal is deposited in the gaps formed. This methodology is widely adopted when patterns are created by direct writing, for example through EBL. A schematic representation of the lift-off process is shown in Figure 123. In Figure 123 (1-2) the substrate is prepared and then covered by a resist like PMMA. Subsequently, the resist coating is exposed by e-beam to create a predefined pattern. The exposed resist is then developed and removed in a selective solvent bath in Figure 123 (3) leaving only the specified parts of the substrate uncovered and ready for metal deposition by evaporation (Figure 123 (4)). The final step of the lift-off process is accomplished by soaking the substrate in a general solvent bath (e.g., acetone for PMMA resist) to wash away the remaining resist and undesired material Figure 123 (5) [338].

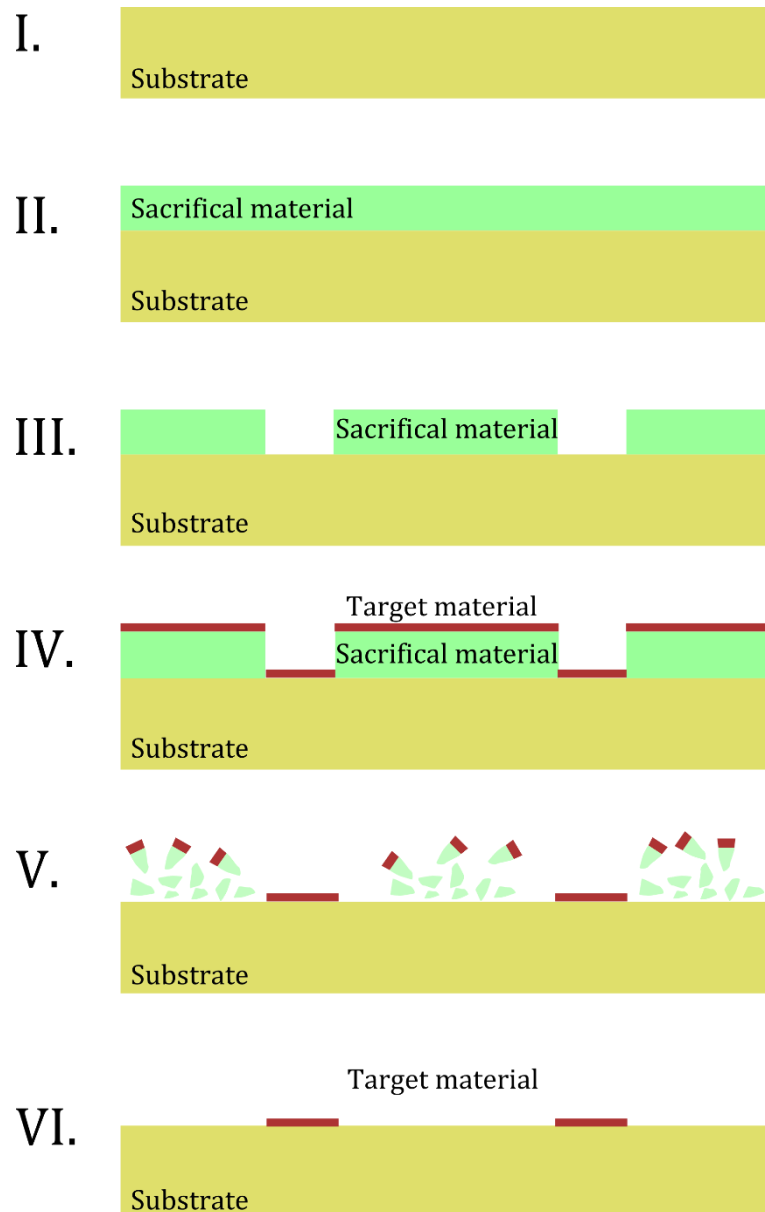


Figure 123 Lift-off process steps: I. Preparation of the substrate II. Deposition of the sacrificial stencil layer III. Patterning the sacrificial layer (ex. etching), creating an inverse pattern IV. Deposition of the target material V. Washing out the sacrificial layer together with the target material on its surface VI. Final pattern.

One of the key factors in this method is the adhesion between the metal and the substrate. When weak adhesion is present it is possible to also inadvertently remove the deposited metal during the soaking phase. A solution to this issue is presented by using an intermediate layer between the substrate that essentially acts as an adhesive layer. Common materials used for this purpose are metals that readily form surface oxides such as titanium, chromium and nickel/chromium that are referred to as 'sticky layers'.

The outcome of the lift-off process is also influenced by the overall thickness of resist, which impacts the highest resolution attainable with EBL. This is caused by scattering of electrons during exposure. To maximise the yield of the lift-off

process two layers of different resists are usually used. On the top of the main resist a very thin layer of more sensitive resist is deposited. During exposure to the e-beam the top layer is slightly underexposed, resulting in an overhanging resist profile. The effect of an underexposed resist layer is to produce less sharp edges. In addition, while the metallisation proceeds, evaporated metal could deposit on the overhanging resist leading to the premature closure of the feature. This issue is particularly common for those structures with an elevated height, where the metal gradually tapers with increasing layer thickness. Such a process leads to a non-straight growth of the metallic layer, which instead has sidewalls with a slope angle of between 70° and 80° to the substrate. Despite this, layer tapering is used as an advantage to manufacture devices like tips for STM or field emitters. Another critical characteristic that allows a successful lift-off is the discontinuity between the metal and resist, that is greatly assisted by a resist-overhang. Lift-off usually fails due to the absence of such discontinuities between the metal upon the resist and that directly on the substrate; in general, the vertices tend to fail first.

D. HERTZ FIT TOOL FOR ELASTIC MODULUS CALCULATIONS

The Hertz fit tool, downloaded freely from <http://www.biophysik.uni-bremen.de/start/radmacher-group/data-analysis/>, can be used to calculate the elastic modulus of a sample. This specific tool is especially designed for soft samples typical in biological applications. However, it is worth mentioning that it was designed for undertaking calculations on AFM measurements carried out in air.

The software does the following steps in order to compute the Young's modulus:

1. Subtract deflection offset by averaging first 10% of the data to be analysed
2. Use the threshold value to determine a first guess of the contact point
3. On the basis of this first guess for a contact point the force and indentation values are calculated at the two data points, where the deflection corresponds to Δ_1 or Δ_2 . The fit function is inverted for these two value pairs to obtain a new guess for the contact point and the elastic modulus.

4. These two values are the starting point for the Levenberg Marquard algorithm, which will result in new values for E and δ_0
5. On the basis of this new contact point δ_0 the indentation is calculated again and the Levenberg Marquard algorithm is started a second time.
6. The results of this second round are the final results
7. In addition to the numerical values, a theoretical force vs. indentation curve and a theoretical force curve are calculated and displayed.

An example of the final graphical outputs is shown in Figure 124.

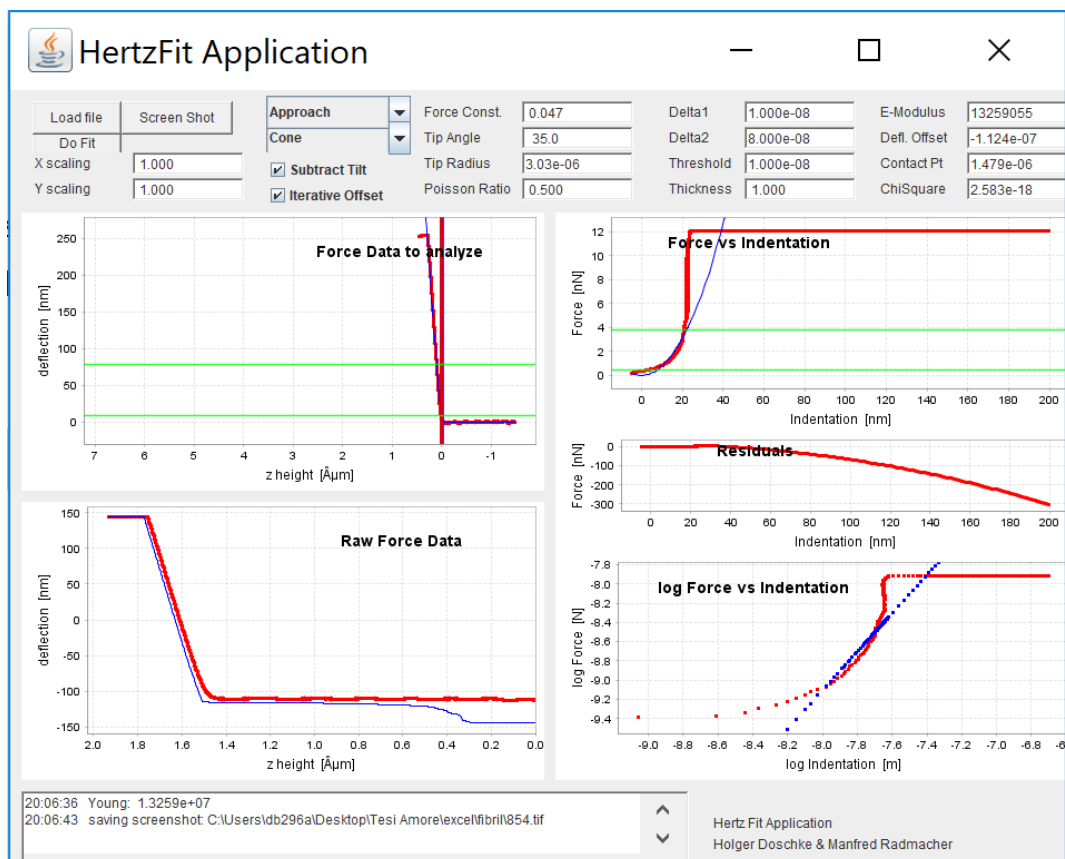


Figure 124 Hertz fit output example.

E. LIVING CELLS SAMPLE PREPARATION

- **Medium preparation**

Dulbecco's modified Eagles Medium (DMEM) – high glucose

Foetal Bovine Serum (FBS)

Medium 199

Penicillin-streptomycin (pen-strep)

Sodium pyruvate

100 ml of DMEM was removed from the bottle and replaced with 100 ml of Medium 199. To this, 50 ml (10 %) FBS, 5 ml (1 %) sodium pyruvate and 5 ml (1 %) pen-strep were added. The media was stored in a fridge at 4 °C until required and pre-heated to 37 °C for 15 minutes before use, as was also the case for PBS (phosphate-buffered serum) and trypsin.

- **Splitting cells**

Cells were washed twice in PBS (this removes any media that stops the trypsin from working and also removes any dead cells).

- i. Trypsin was added to the flask (2 ml in T25 or 5 ml in T75). (Trypsin cleaves the peptide chains holding the cells to the flasks at the carboxylic side of the amino acids lysine and arginine except when followed by proline).
- ii. The flask with trypsin was placed into an incubator at 37 °C for 4 minutes (longer than 4 minutes is not a problem as long as it does not exceed 15 minutes, anything longer and the cells will die). Cells were checked to have detached under an optical microscope, the sides of the flask were tapped if cells were not fully detached.
- iii. An equal amount of media was added to the trypsanised cells (2 ml in T25 of 5 ml in T75 flask). (This stops the trypsin from working. The liquid was then placed into a 15 ml falcon tube.
- iv. The falcon tube was centrifuged at 1200-1400 rpm for 4 minutes. This pellets the cells. Media was poured off, 1 ml of fresh media was added and the pellet was re-suspended.
- v. Cells were counted or split the into the new flask, labelled with name, cell type, passage number and then placed into a 37°C incubator until required.

- **Collagen sample**

- i. A slightly modified CellSeed recommended protocol was employed for collagen type I coating of the surface [339]. The modifications were intended to increase the concentration of collagen on the surface:
Collagen solution 800 µg/ml with 0.02 M acetic acid.

- ii. 20 μl of this diluted collagen solution was added to a glass slide (0.4 mm thick, 4 x 4 mm²) previously coated with a thin layer of gold (100 nm thick), covering the entire area.
- iii. The sample was incubated for 1 hour at 37°C incubator before being washed in PBS and air-dried.

The MG63 cells were added on top of the collagen solution coated slide to allow cells to adhere to the surface and grow more readily. The glass sample was coated with Au before the collagen solution to make collagen solution more stable on the surface but also to increase cell visibility on the Multimode AFM optical microscope. The overall assembly is shown in Figure 125 where the different substrate layers are schematically represented.

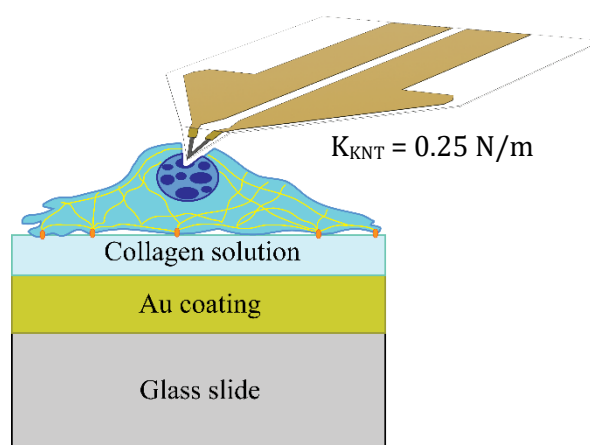


Figure 125 2D representation of the thermal probe pushing the cell nucleus on the prepared sample.

Once the cells were deposited on the slide, the sample was left in an incubator at 37 °C for 12 hours to ensure cells were completely attached on the slide and had started their growth process as shown in Figure 126. As experiments were conducted using the liquid holder of a conventional multimode AFM without an environmentally controlled stage, (described in Section 3.4) 40 ml of 1M HEPES solution was added to the normal 450 ml of medium to ensure a fixed pH of ~7.1 and the survival of the cells.

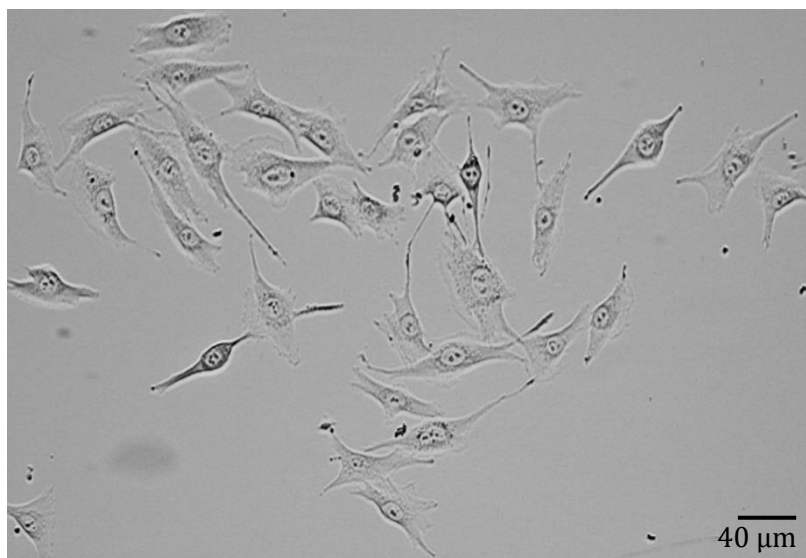


Figure 126 Optical microscope image of the deposited cell used during the experiment.

REFERENCES

1. Ge, Y., *Quantitative measurement using scanning thermal microscopy*. 2016, University of Glasgow.
2. Shallcross, D., *Fahrenheit and Celsius, Kelvin and Rankine*. Vinculum, 2008. **45**(3): p. 4.
3. Sadat, S., et al., *Nanoscale thermometry using point contact thermocouples*. Nano letters, 2010. **10**(7): p. 2613-2617.
4. Shi, L., et al., *Scanning thermal microscopy of carbon nanotubes using batch-fabricated probes*. Applied Physics Letters, 2000. **77**(26): p. 4295-4297.
5. Park, H., et al., *Fabrication of a microchannel integrated with inner sensors and the analysis of its laminar flow characteristics*. Sensors and Actuators A: Physical, 2003. **103**(3): p. 317-329.
6. Agarwal, A., et al., *Silicon nanowire sensor array using top-down CMOS technology*. Sensors and Actuators A: Physical, 2008. **145-146**: p. 207-213.
7. Zhou, J., et al., *Flexible piezotronic strain sensor*. Nano letters, 2008. **8**(9): p. 3035-3040.
8. Dekker, C., *Carbon nanotubes as molecular quantum wires*. Physics today, 1999. **52**: p. 22-30.
9. Mirza, M.M., et al., *Determining the electronic performance limitations in top-down-fabricated Si nanowires with mean widths down to 4 nm*. Nano letters, 2014. **14**(11): p. 6056-6060.
10. Hicks, L. and M.S. Dresselhaus, *Effect of quantum-well structures on the thermoelectric figure of merit*. Physical Review B, 1993. **47**(19): p. 12727.
11. Neto, A.C., et al., *The electronic properties of graphene*. Reviews of modern physics, 2009. **81**(1): p. 109.
12. Boukai, A.I., et al., *Silicon nanowires as efficient thermoelectric materials*. Nature, 2008. **451**(7175): p. 168-171.
13. Fan, S., et al., *Self-oriented regular arrays of carbon nanotubes and their field emission properties*. Science, 1999. **283**(5401): p. 512-514.
14. Zhu, Y., et al., *Graphene and graphene oxide: synthesis, properties, and applications*. Advanced materials, 2010. **22**(35): p. 3906-3924.
15. Dan, Y., et al., *Gas sensing properties of single conducting polymer nanowires and the effect of temperature*. Nanotechnology, 2009. **20**(43): p. 434014.

16. SHARMA, G., *Size, shape and temperature effect on nanomaterials*. Indian Journal of Pure & Applied Physics (IJPAP), 2015. **53**(11): p. 768-775.
17. Lim, J.R., et al., *Fabrication method for thermoelectric nanodevices*. Advanced materials, 2005. **17**(12): p. 1488-1492.
18. Cheng, C., et al., *Heat Transfer across the Interface between Nanoscale Solids and Gas*. ACS Nano, 2011. **5**(12): p. 10102-10107.
19. Thiery, L., et al., *Thermal contact calibration between a thermocouple probe and a microhotplate*. Journal of heat transfer, 2008. **130**(9): p. 091601.
20. Paulik, M.A., et al., *Development of infrared imaging to measure thermogenesis in cell culture: thermogenic effects of uncoupling protein-2, troglitazone, and β -adrenoceptor agonists*. Pharmaceutical research, 1998. **15**(6): p. 944-949.
21. Davis, K.L., et al., *Spatially resolved temperature measurements in electrophoresis capillaries by Raman thermometry*. Analytical chemistry, 1993. **65**(3): p. 293-298.
22. Fujii, T., et al., *Near-field fluorescence thermometry using highly efficient triple-tapered near-field optical fiber probe*. Review of Scientific Instruments, 2012. **83**(12): p. 124901.
23. Luerssen, D., et al., *Nanoscale thermorefectance with 10mK temperature resolution using stochastic resonance*. Semiconductor Thermal Measurement and Management Symposium, 2005 IEEE Twenty First Annual IEEE, 2005: p. 253-258.
24. David, R. and I.W. Hunter, *A liquid-in-glass thermometer read by an interferometer*. Sensors and Actuators A: Physical, 2005. **121**(1): p. 31-34.
25. Ring, E., *The discovery of infrared radiation in 1800*. The Imaging Science Journal, 2000. **48**(1): p. 1-8.
26. Henneke, E.G., K.L. Reifsnider, and W.W. Stinchcomb, *Thermography—an NDI method for damage detection*. JOM, 1979. **31**(9): p. 11-15.
27. Tattersall, G.J., *Infrared thermography: a non-invasive window into thermal physiology*. Comparative Biochemistry and Physiology Part A: Molecular & Integrative Physiology, 2016. **202**: p. 78-98.
28. Gade, R. and T.B. Moeslund, *Thermal cameras and applications: a survey*. Machine vision and applications, 2014. **25**(1): p. 245-262.

29. Richards, P., *Bolometers for infrared and millimeter waves*. Journal of Applied Physics, 1994. **76**(1): p. 1-24.
30. Peterson, B., *Infrared imaging video bolometer*. Review of Scientific Instruments, 2000. **71**(10): p. 3696-3701.
31. Raman, C.V. and K.S. Krishnan, *A new type of secondary radiation*. Nature, 1928. **121**(3048): p. 501-502.
32. Bumbrah, G.S. and R.M. Sharma, *Raman spectroscopy–Basic principle, instrumentation and selected applications for the characterization of drugs of abuse*. Egyptian Journal of Forensic Sciences, 2016. **6**(3): p. 209-215.
33. Harris, D.C. and M.D. Bertolucci, *Symmetry and spectroscopy: an introduction to vibrational and electronic spectroscopy*. 1989: Courier Corporation.
34. Turrell, G. and J. Corset, *Raman microscopy: developments and applications*. 1996: Academic Press.
35. Tuschel, D. *Raman thermometry*. 2016; Available from: <https://www.spectroscopyonline.com/view/raman-thermometry>.
36. Maher, R.C., et al., *Temperature-Dependent Anti-Stokes/Stokes Ratios under Surface-Enhanced Raman Scattering Conditions*. The Journal of Physical Chemistry B, 2006. **110**(13): p. 6797-6803.
37. Guilbault, G.G., *Practical fluorescence*. Vol. 3. 1990: CRC Press.
38. Auzel, F., *Upconversion and anti-stokes processes with f and d ions in solids*. Chemical reviews, 2004. **104**(1): p. 139-174.
39. Kip, B.J. and R.J. Meier, *Determination of the local temperature at a sample during Raman experiments using Stokes and anti-Stokes Raman bands*. Applied spectroscopy, 1990. **44**(4): p. 707-711.
40. Brites, C.D., et al., *Thermometry at the nanoscale*. Nanoscale, 2012. **4**(16): p. 4799-4829.
41. Albrecht, C., *Joseph R. Lakowicz: Principles of fluorescence spectroscopy*. Analytical and Bioanalytical chemistry, 2008. **390**(5): p. 1223-1224.
42. Okabe, K., et al., *Intracellular temperature mapping with a fluorescent polymeric thermometer and fluorescence lifetime imaging microscopy*. Nature communications, 2012. **3**: p. 705.
43. Kubin, R.F. and A.N. Fletcher, *Fluorescence quantum yields of some rhodamine dyes*. Journal of Luminescence, 1982. **27**(4): p. 455-462.

44. Allison, S. and G. Gillies, *Remote thermometry with thermographic phosphors: Instrumentation and applications*. Review of Scientific Instruments, 1997. **68**(7): p. 2615-2650.
45. Löw, P., et al., *High-Spatial-Resolution Surface-Temperature Mapping Using Fluorescent Thermometry*. Small, 2008. **4**(7): p. 908-914.
46. Wang, X.-d., O.S. Wolfbeis, and R.J. Meier, *Luminescent probes and sensors for temperature*. Chemical Society Reviews, 2013. **42**(19): p. 7834-7869.
47. Masters, B.R., *Principles of fluorescence spectroscopy*. Journal of Biomedical Optics, 2008. **13**(2): p. 029901.
48. Favaloro, T., J.-H. Bahk, and A. Shakouri, *Characterization of the temperature dependence of the thermorefectance coefficient for conductive thin films*. Review of Scientific Instruments, 2015. **86**(2): p. 024903.
49. Childs, P., J. Greenwood, and C. Long, *Review of temperature measurement*. Review of scientific instruments, 2000. **71**(8): p. 2959-2978.
50. Donnelly, V. and J. McCaulley, *Infrared-laser interferometric thermometry: A nonintrusive technique for measuring semiconductor wafer temperatures*. Journal of Vacuum Science & Technology A: Vacuum, Surfaces, and Films, 1990. **8**(1): p. 84-92.
51. Kasuya, T., *Electrical resistance of ferromagnetic metals*. Progress of Theoretical Physics, 1956. **16**(1): p. 58-63.
52. Preston-Thomas, H., *The international temperature scale of 1990 (ITS-90)*. metrologia, 1990. **27**(1): p. 3.
53. Kucsko, G., et al., *Nanometre-scale thermometry in a living cell*. Nature, 2013. **500**(7460): p. 54-58.
54. Gomès, S., A. Assy, and P.O. Chapuis, *Scanning thermal microscopy: A review*. physica status solidi (a), 2015. **212**(3): p. 477-494.
55. Majumdar, A., *Scanning thermal microscopy*. Annual review of materials science, 1999. **29**(1): p. 505-585.
56. Pollock, H. and A. Hammiche, *Micro-thermal analysis: techniques and applications*. Journal of Physics D: Applied Physics, 2001. **34**(9): p. R23.
57. Aubry, R., et al., *SThM temperature mapping and nonlinear thermal resistance evolution with bias on AlGaIn/GaN HEMT devices*. IEEE transactions on electron devices, 2007. **54**(3): p. 385-390.

58. Williams, C. and H. Wickramasinghe, *Scanning thermal profiler*. Applied Physics Letters, 1986. **49**(23): p. 1587-1589.
59. Weaver, J., L. Walpita, and H. Wickramasinghe, *Optical absorption microscopy and spectroscopy with nanometre resolution*. Nature, 1989. **342**(6251): p. 783-785.
60. Nonnenmacher, M. and H. Wickramasinghe, *Scanning probe microscopy of thermal conductivity and subsurface properties*. Applied Physics Letters, 1992. **61**(2): p. 168-170.
61. Majumdar, A., J. Carrejo, and J. Lai, *Thermal imaging using the atomic force microscope*. Applied Physics Letters, 1993. **62**(20): p. 2501-2503.
62. Pylkki, R.J., P.J. Moyer, and P.E. West, *Scanning near-field optical microscopy and scanning thermal microscopy*. Japanese journal of applied physics, 1994. **33**(6S): p. 3785.
63. Assy, A., et al., *Analysis of heat transfer in the water meniscus at the tip-sample contact in scanning thermal microscopy*. Journal of Physics D: Applied Physics, 2014. **47**(44): p. 442001.
64. Buzin, A.I., et al., *Application of a Wollaston wire probe for quantitative thermal analysis*. Thermochemica Acta, 2002. **381**(1): p. 9-18.
65. Nakabeppu, O., M. Igeta, and K. Hijikata, *Experimental study on point contact transport phenomena using the atomic force microscope*. Microscale Thermophysical Engineering, 1997. **1**(3): p. 201-213.
66. Zhou, H., et al., *Generic scanned-probe microscope sensors by combined micromachining and electron-beam lithography*. Journal of Vacuum Science & Technology B, 1998. **16**(1): p. 54-58.
67. Mills, G., et al., *Scanning thermal microscopy using batch fabricated thermocouple probes*. Applied physics letters, 1998. **72**(22): p. 2900-2902.
68. Cretin, B., et al., *Scanning thermal microscopy*. Microscale and nanoscale heat transfer, 2007: p. 181-238.
69. Ge, Y., et al., *Quantification of probe-sample interactions of a scanning thermal microscope using a nanofabricated calibration sample having programmable size*. Nanotechnology, 2016. **27**(32): p. 325503.
70. Ge, Y., et al., *Dimension-and shape-dependent thermal transport in nano-patterned thin films investigated by scanning thermal microscopy*. Nanotechnology, 2017. **28**(48): p. 485706.

71. Ho, P.S. and T. Kwok, *Electromigration in metals*. Reports on Progress in Physics, 1989. **52**(3): p. 301.
72. Dobson, P.S., J.M. Weaver, and G. Mills. *New methods for calibrated scanning thermal microscopy (SThM)*. in *Sensors, 2007 IEEE*. 2007. IEEE.
73. King, W.P., et al., *Atomic force microscope cantilevers for combined thermomechanical data writing and reading*. Applied Physics Letters, 2001. **78**(9): p. 1300-1302.
74. Vettiger, P., et al., *The "millipede"-nanotechnology entering data storage*. IEEE Transactions on nanotechnology, 2002. **99**(1): p. 39-55.
75. Vera-Londono, L., et al., *Advances in Scanning Thermal Microscopy Measurements for Thin Films*, in *Coatings and Thin-Film Technologies*. 2018, IntechOpen.
76. Nelson, B.A. and W.P. King, *Measuring material softening with nanoscale spatial resolution using heated silicon probes*. Review of scientific instruments, 2007. **78**(2): p. 023702.
77. Haeberle, W., M. Pantea, and J. Hoerber, *Nanometer-scale heat-conductivity measurements on biological samples*. Ultramicroscopy, 2006. **106**(8-9): p. 678-686.
78. Lee, D.-W. and I.-K. Oh, *Micro/nano-heater integrated cantilevers for micro/nano-lithography applications*. Microelectronic engineering, 2007. **84**(5): p. 1041-1044.
79. Nakabeppu, O., et al., *Scanning thermal imaging microscopy using composite cantilever probes*. Applied physics letters, 1995. **66**(6): p. 694-696.
80. Zhang, Y., P. Dobson, and J. Weaver, *High temperature imaging using a thermally compensated cantilever resistive probe for scanning thermal microscopy*. Journal of Vacuum Science & Technology B, 2012. **30**(1): p. 010601.
81. Cretin, B., et al., *Scanning thermal microscopy*, in *Microscale and nanoscale heat transfer*. 2007, Springer. p. 181-238.
82. Souidi, A., R.D. Dawson, and Y. Gu, *Quantitative heat dissipation characteristics in current-carrying GaN nanowires probed by combining scanning thermal microscopy and spatially resolved Raman spectroscopy*. Acs Nano, 2010. **5**(1): p. 255-262.

83. Royall, P.G., et al., *An investigation into the use of micro-thermal analysis for the solid state characterisation of an HPMC tablet formulation*. International journal of pharmaceutics, 1999. **192**(1): p. 97-103.
84. Six, K., et al., *Identification of phase separation in solid dispersions of itraconazole and Eudragit® E100 using microthermal analysis*. Pharmaceutical research, 2003. **20**(1): p. 135-138.
85. Cahill, D.G., K. Goodson, and A. Majumdar, *Thermometry and thermal transport in micro/nanoscale solid-state devices and structures*. Journal of Heat Transfer, 2002. **124**(2): p. 223-241.
86. Harding, L., et al., *Two-and three-dimensional imaging of multicomponent systems using scanning thermal microscopy and localized thermomechanical analysis*. Analytical chemistry, 2007. **79**(1): p. 129-139.
87. Menges, F., et al., *Temperature mapping of operating nanoscale devices by scanning probe thermometry*. Nature communications, 2016. **7**(1): p. 1-6.
88. Luo, K., et al., *Sensor nanofabrication, performance, and conduction mechanisms in scanning thermal microscopy*. Journal of Vacuum Science & Technology B: Microelectronics and Nanometer Structures Processing, Measurement, and Phenomena, 1997. **15**(2): p. 349-360.
89. Gotsmann, B. and M. Lantz, *Quantized thermal transport across contacts of rough surfaces*. Nature materials, 2013. **12**(1): p. 59-65.
90. Dobson, P., G. Mills, and J. Weaver, *Microfabricated temperature standard based on Johnson noise measurement for the calibration of micro-and nano-thermometers*. Review of scientific instruments, 2005. **76**(5): p. 054901.
91. Kim, K., et al., *Quantitative scanning thermal microscopy using double scan technique*. Applied Physics Letters, 2008. **93**(20): p. 203115.
92. Somnath, S. and W.P. King, *An investigation of heat transfer between a microcantilever and a substrate for improved thermal topography imaging*. Nanotechnology, 2014. **25**(36): p. 365501.
93. Kim, K., et al., *Ultra-high vacuum scanning thermal microscopy for nanometer resolution quantitative thermometry*. Acs Nano, 2012. **6**(5): p. 4248-4257.
94. Tovee, P.D. and O.V. Kolosov, *Mapping nanoscale thermal transfer in-liquid environment—immersion scanning thermal microscopy*. Nanotechnology, 2013. **24**(46): p. 465706.

95. Duvigneau, J., H. Schönherr, and G.J. Vancso, *Nanoscale thermal AFM of polymers: transient heat flow effects*. ACS nano, 2010. **4**(11): p. 6932-6940.
96. Arrhenius, S., *Über die Dissociationswärme und den Einfluss der Temperatur auf den Dissociationsgrad der Elektrolyte*, in *Zeitschrift für Physikalische Chemie*. 1889. p. 96.
97. Wang, X., X. Chen, and Y. Yang, *Spatiotemporal control of gene expression by a light-switchable transgene system*. Nature methods, 2012. **9**(3): p. 266-269.
98. Lowell, B.B. and B.M. Spiegelman, *Towards a molecular understanding of adaptive thermogenesis*. Nature, 2000. **404**(6778): p. 652-660.
99. Rolfe, D. and G.C. Brown, *Cellular energy utilization and molecular origin of standard metabolic rate in mammals*. Physiological reviews, 1997. **77**(3): p. 731-758.
100. Chatterjee, D.K., P. Diagaradjane, and S. Krishnan, *Nanoparticle-mediated hyperthermia in cancer therapy*. Therapeutic delivery, 2011. **2**(8): p. 1001-1014.
101. Lucchetta, E.M., et al., *Dynamics of Drosophila embryonic patterning network perturbed in space and time using microfluidics*. Nature, 2005. **434**(7037): p. 1134-1138.
102. Kumar, S.V. and P.A. Wigge, *H2A. Z-containing nucleosomes mediate the thermosensory response in Arabidopsis*. Cell, 2010. **140**(1): p. 136-147.
103. Sunyer, R., et al., *The temperature dependence of cell mechanics measured by atomic force microscopy*. Physical biology, 2009. **6**(2): p. 025009.
104. Bozec, L. and M. Odlyha, *Thermal denaturation studies of collagen by microthermal analysis and atomic force microscopy*. Biophysical journal, 2011. **101**(1): p. 228-236.
105. Buchholz, A.C. and D.A. Schoeller, *Is a calorie a calorie?* The American journal of clinical nutrition, 2004. **79**(5): p. 899S-906S.
106. Van Wylen, G.J., R.E. Sonntag, and C. Borgnakke, *Fundamentals of classical thermodynamics*. Vol. 1. 1994: John Wiley & Sons.
107. Needham, D. and M.W. Dewhirst, *The development and testing of a new temperature-sensitive drug delivery system for the treatment of solid tumors*. Advanced drug delivery reviews, 2001. **53**(3): p. 285-305.

108. He, X., et al., *In situ thermal denaturation of proteins in dunning AT-1 prostate cancer cells: implication for hyperthermic cell injury*. Annals of biomedical engineering, 2004. **32**(10): p. 1384-1398.
109. Pradhan, P., et al., *Targeted temperature sensitive magnetic liposomes for thermo-chemotherapy*. Journal of Controlled Release, 2010. **142**(1): p. 108-121.
110. Roti Roti, J.L., *Cellular responses to hyperthermia (40–46 C): Cell killing and molecular events*. International Journal of hyperthermia, 2008. **24**(1): p. 3-15.
111. Jelesarov, I. and H.R. Bosshard, *Isothermal titration calorimetry and differential scanning calorimetry as complementary tools to investigate the energetics of biomolecular recognition*. Journal of molecular recognition, 1999. **12**(1): p. 3-18.
112. Millot, N., et al., *Rapid determination of enantiomeric excess using infrared thermography*. Organic process research & development, 2002. **6**(4): p. 463-470.
113. Terentyuk, G.S., et al., *Laser-induced tissue hyperthermia mediated by gold nanoparticles: toward cancer phototherapy*. Journal of biomedical optics, 2009. **14**(2): p. 021016.
114. Downing, H.D. and D. Williams, *Optical constants of water in the infrared*. Journal of Geophysical Research, 1975. **80**(12): p. 1656-1661.
115. Horwitz, J.W., *Water at the ice point: a useful quasi-blackbody infrared calibration source*. Applied optics, 1999. **38**(19): p. 4053-4057.
116. Bower, S., J. Kou, and J. Saylor, *A method for the temperature calibration of an infrared camera using water as a radiative source*. Review of Scientific Instruments, 2009. **80**(9): p. 095107.
117. Usamentiaga, R., et al., *Infrared Thermography for Temperature Measurement and Non-Destructive Testing*. Sensors, 2014. **14**(7): p. 12305.
118. Jaeger, M.S., et al., *Contact-free single-cell cultivation by negative dielectrophoresis*. Journal of Physics D: Applied Physics, 2008. **41**(17): p. 175502.
119. Chelladurai, V., D. Jayas, and N. White, *Thermal imaging for detecting fungal infection in stored wheat*. Journal of Stored Products Research, 2010. **46**(3): p. 174-179.

120. Leung, D., S.O. Kang, and E.V. Anslyn, *Rapid determination of enantiomeric excess: a focus on optical approaches*. Chemical Society Reviews, 2012. **41**(1): p. 448-479.
121. Kuriyama, R. and Y. Sato, *Two-wavelength Raman imaging for non-intrusive monitoring of transient temperature in microfluidic devices*. Measurement Science and Technology, 2014. **25**(9): p. 095203.
122. Kim, S.H., et al., *Micro-Raman thermometry for measuring the temperature distribution inside the microchannel of a polymerase chain reaction chip*. Journal of Micromechanics and Microengineering, 2006. **16**(3): p. 526.
123. Anisimov, A., et al., *Optical thermometry based on level anticrossing in silicon carbide*. Scientific reports, 2016. **6**: p. 33301.
124. Wilson, E.B., J.C. Decius, and P.C. Cross, *Molecular vibrations: the theory of infrared and Raman vibrational spectra*. 1980: Courier Corporation.
125. Benninger, R.K., et al., *Quantitative 3D mapping of fluidic temperatures within microchannel networks using fluorescence lifetime imaging*. Analytical chemistry, 2006. **78**(7): p. 2272-2278.
126. Kortmann, J. and F. Narberhaus, *Bacterial RNA thermometers: molecular zippers and switches*. Nature Reviews Microbiology, 2012. **10**(4): p. 255.
127. Yamaguchi, S., et al., *Dibenzoborole-Containing π -Electron Systems: Remarkable Fluorescence Change Based on the "On/Off" Control of the $p\pi-\pi^*$ Conjugation*. Journal of the American Chemical Society, 2002. **124**(30): p. 8816-8817.
128. Pais, V.F., et al., *Organic fluorescent thermometers based on borylated arylisoquinoline dyes*. Chemistry—A European Journal, 2014. **20**(25): p. 7638-7645.
129. Someya, S., et al., *Combined measurement of velocity and temperature distributions in oil based on the luminescent lifetimes of seeded particles*. Measurement Science and Technology, 2009. **20**(2): p. 025403.
130. Basu, B.B.J. and N. Vasantharajan, *Temperature dependence of the luminescence lifetime of a europium complex immobilized in different polymer matrices*. Journal of Luminescence, 2008. **128**(10): p. 1701-1708.
131. Demchenko, A.P., *Photobleaching of organic fluorophores: quantitative characterization, mechanisms, protection*. Methods and Applications in Fluorescence, 2020. **8**(2): p. 022001.

132. Samy, R., T. Glawdel, and C.L. Ren, *Method for microfluidic whole-chip temperature measurement using thin-film poly (dimethylsiloxane)/Rhodamine B*. Analytical chemistry, 2008. **80**(2): p. 369-375.
133. Jaque, D. and F. Vetrone, *Luminescence nanothermometry*. Nanoscale, 2012. **4**(15): p. 4301-4326.
134. Jung, W., et al., *Microscale surface thermometry using SU8/Rhodamine-B thin layer*. Sensors and Actuators A: Physical, 2011. **171**(2): p. 228-232.
135. Lahmani, F., et al., *Intramolecular charge transfer properties in the excited state of para-disubstituted biaryls*. Journal of Photochemistry and Photobiology A: Chemistry, 1993. **70**(1): p. 39-49.
136. Disney, M.D., et al., *Detection of bacteria with carbohydrate-functionalized fluorescent polymers*. Journal of the American Chemical Society, 2004. **126**(41): p. 13343-13346.
137. Arai, S., et al., *Mitochondria-targeted fluorescent thermometer monitors intracellular temperature gradient*. Chemical Communications, 2015. **51**(38): p. 8044-8047.
138. Liang, R., et al., *A temperature sensor based on CdTe quantum dots-layered double hydroxide ultrathin films via layer-by-layer assembly*. Chemical Communications, 2013. **49**(10): p. 969-971.
139. Wittwer, C.T., et al., *Continuous fluorescence monitoring of rapid cycle DNA amplification*. Biotechniques, 1997. **22**(1): p. 130-139.
140. Yamamoto, S., S. Park, and H. Sugiyama, *Development of a visible nanothermometer with a highly emissive 2'-O-methylated guanosine analogue*. RSC Advances, 2015. **5**(126): p. 104601-104605.
141. Tashiro, R. and H. Sugiyama, *Biomolecule-based switching devices that respond inversely to thermal stimuli*. Journal of the American Chemical Society, 2005. **127**(7): p. 2094-2097.
142. Yang, J.-M., H. Yang, and L. Lin, *Quantum dot nano thermometers reveal heterogeneous local thermogenesis in living cells*. ACS nano, 2011. **5**(6): p. 5067-5071.
143. Bontempi, A., et al., *Scanning thermal microscopy based on a quartz tuning fork and a micro-thermocouple in active mode (2 ω method)*. Review of Scientific Instruments, 2016. **87**(6): p. 063702.

144. Nguyen, T.P., et al., *Recent improvements on micro-thermocouple based SThM*. Journal of Physics: Conference Series, 2017. **785**(1): p. 012005.
145. Park, J.-H. and T. Sudarshan, *Chemical vapor deposition*. Vol. 2. 2001: ASM international.
146. Geschke, O., H. Klank, and P. Telleman, *Microsystem Engineering of Lab-on-a-chip Devices*. 2004: John Wiley & Sons.
147. Fletcher, P.D., et al., *Micro reactors: principles and applications in organic synthesis*. Tetrahedron, 2002. **58**(24): p. 4735-4757.
148. Suzuki, M., et al., *Microscopic detection of thermogenesis in a single HeLa cell*. Biophysical journal, 2007. **92**(6): p. L46-L48.
149. Shrestha, R., et al., *A High-Precision Micropipette Sensor for Cellular-Level Real-Time Thermal Characterization*. Sensors, 2011. **11**(9): p. 8826-8835.
150. Fish, G., et al., *Ultrafast response micropipette-based submicrometer thermocouple*. Review of scientific instruments, 1995. **66**(5): p. 3300-3306.
151. Watanabe, M., et al. *Micro-thermocouple probe for measurement of cellular thermal responses*. in *Engineering in Medicine and Biology Society, 2005. IEEE-EMBS 2005. 27th Annual International Conference of the*. 2006. IEEE.
152. Arata, H.F., et al., *Temperature alternation by an on-chip microheater to reveal enzymatic activity of β -galactosidase at high temperatures*. Analytical chemistry, 2005. **77**(15): p. 4810-4814.
153. Poehler, E., et al., *Microchamber arrays with an integrated long luminescence lifetime pH sensor*. Analytical and Bioanalytical Chemistry, 2016. **408**(11): p. 2927-2935.
154. Yu, S., et al., *A novel polyimide based micro heater with high temperature uniformity*. Sensors and Actuators A: Physical, 2017. **257**: p. 58-64.
155. Wang, S., et al., *Micro-differential scanning calorimeter for liquid biological samples*. Review of Scientific Instruments, 2016. **87**(10): p. 105005.
156. Balčytis, A., et al., *Micro-thermocouple on nano-membrane: thermometer for nanoscale measurements*. Scientific reports, 2018. **8**(1): p. 6324.
157. Arata, H.F., et al., *Temperature distribution measurement on microfabricated thermodevice for single biomolecular observation using fluorescent dye*. Sensors and Actuators B: Chemical, 2006. **117**(2): p. 339-345.

158. Balčytis, A., et al., *Micro-thermocouple on nano-membrane: thermometer for nanoscale measurements*. Scientific reports, 2018. **8**(1): p. 1-6.
159. Kawata, Y., Y. Nawa, and W. Inami, *High resolution fluorescent bio-imaging with electron beam excitation*. Microscopy, 2014. **63**(suppl_1): p. i16-i16.
160. Daeinabi, K. and M.H. Korayem, *Indentation analysis of nano-particle using nano-contact mechanics models during nano-manipulation based on atomic force microscopy*. Journal of Nanoparticle Research, 2011. **13**(3): p. 1075-1091.
161. Sitti, M. and H. Hashimoto, *Teleoperated touch feedback from the surfaces at the nanoscale: modeling and experiments*. IEEE/ASME transactions on mechatronics, 2003. **8**(2): p. 287-298.
162. Patil, S., et al., *Force microscopy imaging of individual protein molecules with sub-pico Newton force sensitivity*. Journal of Molecular Recognition, 2007. **20**(6): p. 516-523.
163. Gross, L., et al., *The chemical structure of a molecule resolved by atomic force microscopy*. Science, 2009. **325**(5944): p. 1110-1114.
164. Dinelli, F., et al., *Measurements of stiff-material compliance on the nanoscale using ultrasonic force microscopy*. Physical Review B, 2000. **61**(20): p. 13995.
165. Dinelli, F., et al., *Mapping surface elastic properties of stiff and compliant materials on the nanoscale using ultrasonic force microscopy*. Philosophical Magazine A, 2000. **80**(10): p. 2299-2323.
166. Kolosov, O. and K. Yamanaka, *Nonlinear detection of ultrasonic vibrations in an atomic force microscope*. Japanese journal of applied physics, 1993. **32**(8A): p. L1095.
167. Rugar, D., et al., *Single spin detection by magnetic resonance force microscopy*. Nature, 2004. **430**(6997): p. 329-332.
168. Hammiche, A., et al., *Localized thermal analysis using a miniaturized resistive probe*. Review of Scientific Instruments, 1996. **67**(12): p. 4268-4274.
169. Tsukruk, V.V., V.V. Gorbunov, and N. Fuchigami, *Microthermal analysis of polymeric materials*. Thermochemica Acta, 2002. **395**(1): p. 151-158.
170. Binnig, G. and H. Rohrer, *Scanning tunneling microscopy*. Surface science, 1983. **126**(1): p. 236-244.

171. Binnig, G., C.F. Quate, and C. Gerber, *Atomic force microscope*. Physical review letters, 1986. **56**(9): p. 930.
172. Butt, H.-J., B. Cappella, and M. Kappl, *Force measurements with the atomic force microscope: Technique, interpretation and applications*. Surface science reports, 2005. **59**(1): p. 1-152.
173. Tovee, P.D., *Nanoscale Resolution Scanning Thermal Microscopy of Highly Thermally Conductive Materials in Different Environments*. 2013: p. 182.
174. Zhong, Q., et al., *Fractured polymer/silica fiber surface studied by tapping mode atomic force microscopy*. Surface Science Letters, 1993. **290**(1-2): p. L688-L692.
175. Nair, S.S., C. Wang, and K.J. Wynne, *AFM Peakforce QNM mode for measurement of nanosurface mechanical properties of Pt-cured silicones*. Progress in Organic Coatings, 2019. **126**: p. 119-128.
176. Adamcik, J., A. Berquand, and R. Mezzenga, *Single-step direct measurement of amyloid fibrils stiffness by peak force quantitative nanomechanical atomic force microscopy*. Applied Physics Letters, 2011. **98**(19): p. 193701.
177. Sun, S., et al., *Nanomechanical mapping of a deformed elastomer: visualizing a self-reinforcement mechanism*. ACS Macro Letters, 2016. **5**(7): p. 839-843.
178. Heu, C., et al., *Glyphosate-induced stiffening of HaCaT keratinocytes, a Peak Force Tapping study on living cells*. Journal of structural biology, 2012. **178**(1): p. 1-7.
179. Zhao, B., et al., *Mechanical mapping of nanobubbles by PeakForce atomic force microscopy*. Soft Matter, 2013. **9**(37): p. 8837-8843.
180. Cheng, X., et al., *Characterization of local elastic modulus in confined polymer films via AFM indentation*. Macromolecular rapid communications, 2015. **36**(4): p. 391-397.
181. Drake, B., et al., *Imaging crystals, polymers, and processes in water with the atomic force microscope*. Science, 1989. **243**(4898): p. 1586-1589.
182. Weisenhorn, A., et al., *Forces in atomic force microscopy in air and water*. Applied Physics Letters, 1989. **54**(26): p. 2651-2653.
183. Lyubchenko, Y., et al., *Atomic force microscopy of DNA and bacteriophage in air, water and propanol: the role of adhesion forces*. Nucleic acids research, 1993. **21**(5): p. 1117-1123.

184. Hoh, J.H. and P.K. Hansma, *Atomic force microscopy for high-resolution imaging in cell biology*. Trends in Cell Biology, 1992. **2**(7): p. 208-213.
185. McPhee, G., et al., *Can common adhesion molecules and microtopography affect cellular elasticity? A combined atomic force microscopy and optical study*. Medical & biological engineering & computing, 2010. **48**(10): p. 1043-1053.
186. Tittmann, B. and X. Xi, *Imaging and quantitative data acquisition of biological cell walls with Atomic Force Microscopy and Scanning Acoustic Microscopy*. 2014, Energy Frontier Research Centers; Center for Lignocellulose Structure and Formation (CLSF).
187. Butt, H.-J., et al., *Imaging cells with the atomic force microscope*. Journal of structural biology, 1990. **105**(1): p. 54-61.
188. Weisenhorn, A., et al., *Measuring adhesion, attraction, and repulsion between surfaces in liquids with an atomic-force microscope*. Physical Review B, 1992. **45**(19): p. 11226.
189. Davydov, A., et al., *Anodic Behavior of Nickel-Chromium Alloys in Sodium Chloride Solutions: Pitting and Transpassivity*. Russian Journal of Electrochemistry, 2005. **41**(10): p. 1032-1037.
190. Li, M.-H. and Y. Gianchandani, *Applications of a low contact force polyimide shank bolometer probe for chemical and biological diagnostics*. Sensors and Actuators A: Physical, 2003. **104**(3): p. 236-245.
191. Shi, L. and A. Majumdar, *Thermal transport mechanisms at nanoscale point contacts*. Journal of heat transfer, 2002. **124**(2): p. 329-337.
192. Lefèvre, S., S. Volz, and P.-O. Chapuis, *Nanoscale heat transfer at contact between a hot tip and a substrate*. International journal of heat and mass transfer, 2006. **49**(1): p. 251-258.
193. Pettes, M.T. and L. Shi, *A reexamination of phonon transport through a nanoscale point contact in vacuum*. Journal of Heat Transfer, 2014. **136**(3): p. 032401.
194. Shi, L. and A. Majumdar, *Micro-nano scale thermal imaging using scanning probe microscopy*, in *Applied Scanning Probe Methods*. 2004, Springer. p. 327-362.

195. Gomès, S., N. Trannoy, and P. Grossel, *DC thermal microscopy: study of the thermal exchange between a probe and a sample*. Measurement Science and Technology, 1999. **10**(9): p. 805.
196. Hinz, M., et al., *High resolution vacuum scanning thermal microscopy of Hf O 2 and Si O 2*. Applied Physics Letters, 2008. **92**(4): p. 043122.
197. Gomes, S., et al., *Application of scanning thermal microscopy for thermal conductivity measurements on meso-porous silicon thin films*. Journal of Physics D: Applied Physics, 2007. **40**(21): p. 6677.
198. Kolosov, O. and B. Robinson. *Immersion scanning thermal microscopy: probing nanoscale heat transport in liquid environments*. in *2nd International Conference on Fluid Flow, Heat and Mass Transfer 2015*. Ottawa, Ontario, Canada, May 2015
199. Tian, W., et al., *A high precision apparatus for intracellular thermal response at single-cell level*. Nanotechnology, 2015. **26**(35): p. 355501.
200. Huang, J., et al., *Ultrafast thermal analysis of surface functionalized gold nanorods in aqueous solution*. ACS nano, 2013. **7**(1): p. 589-597.
201. Baffou, G., et al., *A critique of methods for temperature imaging in single cells*. Nature methods, 2014. **11**(9): p. 899-901.
202. Kiyonaka, S., et al., *Validating subcellular thermal changes revealed by fluorescent thermosensors*. Nature methods, 2015. **12**(9): p. 801-802.
203. Suzuki, M., et al., *The 105 gap issue between calculation and measurement in single-cell thermometry*. Nature methods, 2015. **12**(9): p. 802-803.
204. Baffou, G., et al., *Reply to*. Nature methods, 2015. **12**(9): p. 803-803.
205. Okabe, K., et al., *Intracellular thermometry with fluorescent sensors for thermal biology*. Pflügers Archiv - European Journal of Physiology, 2018. **470**(5): p. 717-731.
206. Nigam, S. and D. Bahadur, *Dendrimer-conjugated iron oxide nanoparticles as stimuli-responsive drug carriers for thermally-activated chemotherapy of cancer*. Colloids and Surfaces B: Biointerfaces, 2017. **155**: p. 182-192.
207. Bai, L.-Z., et al., *Inductive heating property of graphene oxide-Fe₃O₄ nanoparticles hybrid in an AC magnetic field for localized hyperthermia*. Materials letters, 2012. **68**: p. 399-401.

208. Moroz, P., S.K. Jones, and B.N. Gray, *Magnetically mediated hyperthermia: Current status and future directions*. International Journal of Hyperthermia, 2002. **18**(4): p. 267-284.
209. Goodman, A.M., et al., *Near-infrared remotely triggered drug-release strategies for cancer treatment*. Proceedings of the National Academy of Sciences, 2017. **114**(47): p. 12419-12424.
210. Tong, L., et al., *Gold nanorods mediate tumor cell death by compromising membrane integrity*. Advanced Materials, 2007. **19**(20): p. 3136-3141.
211. Tsai, P.C., et al., *Measuring Nanoscale Thermostability of Cell Membranes with Single Gold–Diamond Nanohybrids*. Angewandte Chemie International Edition, 2017. **56**(11): p. 3025-3030.
212. Pérez-Hernández, M., et al., *Dissecting the molecular mechanism of apoptosis during photothermal therapy using gold nanoprisms*. ACS nano, 2014. **9**(1): p. 52-61.
213. Li, M.H. and Y.B. Gianchandani, *Applications of a low contact force polyimide shank bolometer probe for chemical and biological diagnostics*. Sensors and Actuators A: Physical, 2003. **104**(3): p. 236-245.
214. Prasher, R., *Predicting the thermal resistance of nanosized constrictions*. Nano letters, 2005. **5**(11): p. 2155-2159.
215. Stoner, R. and H. Maris, *Kapitza conductance and heat flow between solids at temperatures from 50 to 300 K*. Physical Review B, 1993. **48**(22): p. 16373.
216. Margulies, S., *Force on a dielectric slab inserted into a parallel-plate capacitor*. American Journal of Physics, 1984. **52**(6): p. 515-518.
217. Zhang, Y., P. Dobson, and J. Weaver, *High temperature imaging using a thermally compensated cantilever resistive probe for scanning thermal microscopy*. Journal of Vacuum Science & Technology B, Nanotechnology and Microelectronics: Materials, Processing, Measurement, and Phenomena, 2012. **30**(1): p. 010601.
218. Wenzler, L., G. Moyes, and T. Beebe Jr, *Improvements to atomic force microscopy cantilevers for increased stability*. Review of scientific instruments, 1996. **67**(12): p. 4191-4197.

219. Hickling, A., *Studies in electrode polarisation. Part IV.—The automatic control of the potential of a working electrode*. Transactions of the Faraday Society, 1942. **38**(0): p. 27-33.
220. Flechsig, G.U. and A. Walter, *Electrically Heated Electrodes: Practical Aspects and New Developments*. Electroanalysis, 2012. **24**(1): p. 23-31.
221. Wachholz, F., et al., *A compact and versatile instrument for radio frequency heating in nonisothermal electrochemical studies*. Electroanalysis, 2007. **19**(5): p. 535-540.
222. Bruker AFM Probes. 2020; Available from: <https://www.brukerafmprobes.com/p-3530-mmtmec.aspx>.
223. Stratasys 3D-printers. 2020; Available from: <http://www.stratasys.com/3d-printers/design-series/objet30-prime>.
224. Stratasys transparent materials. 2020; Available from: <http://www.stratasys.com/materials/material-safety-data-sheets/polyjet/transparent-materials>.
225. Scanning probes. 2019; Available from: http://www.kelvinnanotechnology.com/products/products_scanning_probes.html.
226. Loctite adhesive. 2020; Available from: http://www.loctite.co.uk/news-4082_adhesive-at-the-double-6239_UKE_HTML.htm.
227. Electrolube silver paint. 2019; Available from: http://www.electrolube.com/products/maintenance-service-aids/scp/paints_and_paint_removers/.
228. Chui, B., et al., *Low-stiffness silicon cantilevers for thermal writing and piezoresistive readback with the atomic force microscope*. Applied Physics Letters, 1996. **69**(18): p. 2767-2769.
229. Tovee, P., et al., *Nanoscale spatial resolution probes for scanning thermal microscopy of solid state materials*. Journal of Applied Physics, 2012. **112**(11): p. 114317.
230. Kim, K.J. and W.P. King, *Thermal conduction between a heated microcantilever and a surrounding air environment*. Applied Thermal Engineering, 2009. **29**(8-9): p. 1631-1641.

231. Cahill, D.G., K. Goodson, and A. Majumdar, *Thermometry and Thermal Transport in Micro/Nanoscale Solid-State Devices and Structures*. Journal of Heat Transfer, 2001. **124**(2): p. 223-241.
232. Sondheimer, E.H., *The mean free path of electrons in metals*. Advances in physics, 1952. **1**(1): p. 1-42.
233. Cussler, E.L., *Diffusion: mass transfer in fluid systems*. 2009: Cambridge university press.
234. Alvarez, F., D. Jou, and A. Sellitto, *Phonon hydrodynamics and phonon-boundary scattering in nanosystems*. Journal of Applied Physics, 2009. **105**(1): p. 014317.
235. Fischer, G., H. Hoffmann, and J. Vancea, *Mean free path and density of conductance electrons in platinum determined by the size effect in extremely thin films*. Physical Review B, 1980. **22**(12): p. 6065-6073.
236. Bodzenta, J., et al., *Quantitative thermal microscopy measurement with thermal probe driven by dc+ ac current*. International Journal of Thermophysics, 2016. **37**(7): p. 73.
237. Timofeeva, M., et al., *Scanning thermal microscopy with heat conductive nanowire probes*. Ultramicroscopy, 2016. **162**: p. 42-51.
238. Wang, H., et al., *Computation of interfacial thermal resistance by phonon diffuse mismatch model*. Materials transactions, 2007. **48**(9): p. 2349-2352.
239. Ge, Z., D.G. Cahill, and P.V. Braun, *Thermal conductance of hydrophilic and hydrophobic interfaces*. Physical review letters, 2006. **96**(18): p. 186101.
240. Park, J. and D.G. Cahill, *Plasmonic Sensing of Heat Transport at Solid-Liquid Interfaces*. The Journal of Physical Chemistry C, 2016. **120**(5): p. 2814-2821.
241. Gundrum, B.C., D.G. Cahill, and R.S. Averback, *Thermal conductance of metal-metal interfaces*. Physical Review B, 2005. **72**(24): p. 245426.
242. Mahan, G. and M. Bartkowiak, *Wiedemann-Franz law at boundaries*. Applied physics letters, 1999. **74**(7): p. 953-954.
243. Cahill, D.G., et al., *Nanoscale thermal transport*. Journal of Applied Physics, 2003. **93**(2): p. 793-818.

244. Gao, J., et al., *Thermal characterization of microscale heat convection in rare-gas environment by a steady-state "hot wire" method*. Applied Physics Express, 2018. **11**(6): p. 066601.
245. Schafft, H.A., J.S. Suehle, and P.G.A. Mirel. *Thermal conductivity measurements of thin-film silicon dioxide*. in *Proceedings of the 1989 International Conference on Microelectronic Test Structures*. 1989.
246. Goodson, K. and M. Flik, *Electron and phonon thermal conduction in epitaxial high-Tc superconducting films*. Journal of Heat Transfer, 1993. **115**(1): p. 17-25.
247. Goodson, K.E. and M.I. Flik, *Solid layer thermal-conductivity measurement techniques*. Applied Mechanics Reviews, 1994. **47**(3): p. 101-112.
248. Valdes, L.B., *Resistivity measurements on germanium for transistors*. Proceedings of the IRE, 1954. **42**(2): p. 420-427.
249. Cardenas, C., et al., *Thermoreflectance measurement of temperature and thermal resistance of thin film gold*. Journal of Heat Transfer, 2012. **134**(11): p. 111401.
250. Ftouni, H., et al., *Thermal conductivity of silicon nitride membranes is not sensitive to stress*. Physical Review B, 2015. **92**(12): p. 125439.
251. Franssila, S., *Introduction to microfabrication*. 2010: John Wiley & Sons.
252. Wu, T.-T., et al. *Electrical properties of micro-heaters using sputtered NiCr thin film*. in *Nano/Micro Engineered and Molecular Systems (NEMS), 2013 8th IEEE International Conference on*. 2013. IEEE.
253. Flutec pp3. 2019; Available from: <http://f2chemicals.com/electricapps.html>.
254. Ge, Y., et al., *Topography-free sample for thermal spatial response measurement of scanning thermal microscopy*. Journal of Vacuum Science & Technology B, Nanotechnology and Microelectronics: Materials, Processing, Measurement, and Phenomena, 2015. **33**(6): p. 06FA03.
255. Lloyd, J., *Electromigration in thin film conductors*. Semiconductor science and technology, 1997. **12**(10): p. 1177.
256. Wu, W., et al., *Electromigration subjected to Joule heating under pulsed DC stress*. Solid-State Electronics, 2001. **45**(12): p. 2051-2056.
257. Lienig, J. and M. Thiele, *The Pressing Need for Electromigration-Aware Physical Design*. migration, 2018. **4**: p. 5.

258. Lienig, J. *Introduction to electromigration-aware physical design*. in *Proceedings of the 2006 international symposium on Physical design*. 2006. ACM.
259. Black, J.R., *Electromigration—A brief survey and some recent results*. *Electron Devices, IEEE Transactions on*, 1969. **16**(4): p. 338-347.
260. Tilley, R.J. and R. Tilley, *Understanding solids: the science of materials*. 2013: Wiley Online Library.
261. Rossmeisl, J., et al., *Electrolysis of water on oxide surfaces*. *Journal of Electroanalytical Chemistry*, 2007. **607**(1): p. 83-89.
262. Agrawal, B.K., *Introduction to engineering materials*. 1988: Tata McGraw-Hill Education.
263. Lin, L., A. Pisano, and V. Carey, *Thermal bubble formation on polysilicon micro resistors*. *Journal of Heat Transfer*, 1998. **120**(3): p. 735-742.
264. Davis, J.R., *Corrosion: Understanding the basics*. 2000: ASM International.
265. *Corrosion Definition*. 2020; Available from: <http://www.corrosionpedia.com/definition/661/immunity>.
266. Cook, W.G. and R.P. Olive, *Pourbaix diagrams for the nickel-water system extended to high-subcritical and low-supercritical conditions*. *Corrosion Science*, 2012. **58**: p. 284-290.
267. Hewitt, G.F., G.L. Shires, and T.R. Bott, *Process heat transfer*. Vol. 113. 1994: CRC press Boca Raton, FL.
268. Zadavec, M., M. Hriberšek, and L. Škerget, *Natural convection of micropolar fluid in an enclosure with boundary element method*. *Engineering Analysis with Boundary Elements*, 2009. **33**(4): p. 485-492.
269. Klapetek, P., I. Ohlídal, and J. Buršík, *Applications of scanning thermal microscopy in the analysis of the geometry of patterned structures*. *Surface and Interface Analysis: An International Journal devoted to the development and application of techniques for the analysis of surfaces, interfaces and thin films*, 2006. **38**(4): p. 383-387.
270. Umatova, Z., *A sensitive device for SThM quantification*. 2018, University of Glasgow.
271. Killgore, J.P., R.H. Geiss, and D.C. Hurley, *Continuous measurement of atomic force microscope tip wear by contact resonance force microscopy*. *Small*, 2011. **7**(8): p. 1018-1022.

272. Cahill, D.G., et al., *Nanoscale thermal transport. II. 2003–2012*. Applied Physics Reviews, 2014. **1**(1): p. 011305.
273. Beyder, A., C. Spagnoli, and F. Sachs, *Reducing probe dependent drift in atomic force microscope with symmetrically supported torsion levers*. Review of scientific instruments, 2006. **77**(5): p. 056105.
274. Sevim, S., S. Tolunay, and H. Torun, *Micromachined sample stages to reduce thermal drift in atomic force microscopy*. Microsystem Technologies, 2015. **21**(7): p. 1559-1566.
275. Kim, K., et al. *Quantitative Scanning Thermal microscopy with double scan technique*. in *ASME 2008 First International Conference on Micro/Nanoscale Heat Transfer*. 2008. American Society of Mechanical Engineers.
276. Thoms, S., Y. Zhang, and J.M. Weaver, *Improved alignment algorithm for electron beam lithography*. Journal of Vacuum Science & Technology B, Nanotechnology and Microelectronics: Materials, Processing, Measurement, and Phenomena, 2014. **32**(6): p. 06F509.
277. Thoms, S., et al., *Alignment verification for electron beam lithography*. Microelectronic Engineering, 2014. **123**: p. 9-12.
278. Wess, T., *Collagen fibril form and function*. Advances in protein chemistry, 2005. **70**: p. 341-374.
279. Friedrichs, J., *Analyzing Interactions Between Cells And Extracellular Matrix By Atomic Force Microscopy*. 2009.
280. Tiktopulo, E.I. and A.V. Kajava, *Denaturation of type I collagen fibrils is an endothermic process accompanied by a noticeable change in the partial heat capacity*. Biochemistry, 1998. **37**(22): p. 8147-8152.
281. Wall, M.S., et al., *Thermal modification of collagen*. Journal of shoulder and elbow surgery, 1999. **8**(4): p. 339-344.
282. Matteini, P., et al., *Thermal transitions of fibrillar collagen unveiled by second-harmonic generation microscopy of corneal stroma*. Biophysical journal, 2012. **103**(6): p. 1179-1187.
283. Beck, K., et al., *Destabilization of osteogenesis imperfecta collagen-like model peptides correlates with the identity of the residue replacing glycine*. Proceedings of the National Academy of Sciences, 2000. **97**(8): p. 4273-4278.

284. Wang, X., et al., *Effects of Collagen Unwinding and Cleavage on the Mechanical Integrity of the Collagen Network in Bone*. Vol. 71. 2002. 186-192.
285. Chernoff, E.A. and D.A. Chernoff, *Atomic force microscope images of collagen fibers*. Journal of Vacuum Science & Technology A, 1992. **10**(4): p. 596-599.
286. Gutschmann, T., et al., *Force spectroscopy of collagen fibers to investigate their mechanical properties and structural organization*. Biophysical journal, 2004. **86**(5): p. 3186-3193.
287. Hammiche, A., et al., *Two new microscopical variants of thermomechanical modulation: scanning thermal expansion microscopy and dynamic localized thermomechanical analysis*. Journal of microscopy, 2000. **199**(3): p. 180-190.
288. Hammiche, A., et al., *Scanning thermal microscopy: Subsurface imaging, thermal mapping of polymer blends, and localized calorimetry*. Journal of Vacuum Science & Technology B: Microelectronics and Nanometer Structures Processing, Measurement, and Phenomena, 1996. **14**(2): p. 1486-1491.
289. *Collagen solution*. 2020; Available from: <https://www.sigmaaldrich.com/catalog/product/sigma/c4243?lang=en®ion=GB>
290. *Bruker peakforce*. 2020; Available from: <https://www.bruker.com/products/surface-and-dimensional-analysis/atomic-force-microscopes/modes/modes/imaging-modes/peakforce-qnm.html>.
291. Neel, E.A.A., et al., *Collagen—emerging collagen based therapies hit the patient*. Advanced drug delivery reviews, 2013. **65**(4): p. 429-456.
292. Wallace, D.G. and J. Rosenblatt, *Collagen gel systems for sustained delivery and tissue engineering*. Advanced drug delivery reviews, 2003. **55**(12): p. 1631-1649.
293. Lee, C.H., A. Singla, and Y. Lee, *Biomedical applications of collagen*. International journal of pharmaceutics, 2001. **221**(1-2): p. 1-22.

294. Balooch, M., et al., *Mechanical properties of mineralized collagen fibrils as influenced by demineralization*. Journal of Structural Biology, 2008. **162**(3): p. 404-410.
295. Bembey, A.K., et al., *Hydration effects on the micro-mechanical properties of bone*. Journal of Materials Research, 2006. **21**(8): p. 1962-1968.
296. Dimitriadis, E.K., et al., *Determination of Elastic Moduli of Thin Layers of Soft Material Using the Atomic Force Microscope*. Biophysical Journal, 2002. **82**(5): p. 2798-2810.
297. *Stiffness calculation software*. 2020; Available from: <http://www.biophysik.uni-bremen.de/start/radmacher-group/data-analysis/>.
298. Gavara, N. and R.S. Chadwick, *Determination of the elastic moduli of thin samples and adherent cells using conical atomic force microscope tips*. Nature nanotechnology, 2012. **7**(11): p. 733.
299. Grant, C.A., et al., *Effects of hydration on the mechanical response of individual collagen fibrils*. Applied Physics Letters, 2008. **92**(23): p. 233902.
300. Graham, E.M., et al., *Quantitative mapping of aqueous microfluidic temperature with sub-degree resolution using fluorescence lifetime imaging microscopy*. Lab on a Chip, 2010. **10**(10): p. 1267-1273.
301. Zeeb, V., M. Suzuki, and S.i. Ishiwata, *A novel method of thermal activation and temperature measurement in the microscopic region around single living cells*. Journal of neuroscience methods, 2004. **139**(1): p. 69-77.
302. Donner, J.S., et al., *Mapping intracellular temperature using green fluorescent protein*. Nano letters, 2012. **12**(4): p. 2107-2111.
303. Maestro, L.M., et al., *CdSe quantum dots for two-photon fluorescence thermal imaging*. Nano letters, 2010. **10**(12): p. 5109-5115.
304. Tsuji, T., et al., *Cationic fluorescent polymeric thermometers with the ability to enter yeast and mammalian cells for practical intracellular temperature measurements*. Analytical chemistry, 2013. **85**(20): p. 9815-9823.
305. Ximendes, E.C., et al., *Unveiling in vivo subcutaneous thermal dynamics by infrared luminescent nanothermometers*. Nano letters, 2016. **16**(3): p. 1695-1703.

306. Kiyonaka, S., et al., *Genetically encoded fluorescent thermosensors visualize subcellular thermoregulation in living cells*. *Nature methods*, 2013. **10**(12): p. 1232-1238.
307. Gota, C., et al., *Hydrophilic fluorescent nanogel thermometer for intracellular thermometry*. *Journal of the American Chemical Society*, 2009. **131**(8): p. 2766-2767.
308. Yang, L., et al., *Luminescent Ru (bpy) 3 2+-doped silica nanoparticles for imaging of intracellular temperature*. *Microchimica Acta*, 2014. **181**(7-8): p. 743-749.
309. Johannessen, E.A., et al., *Micromachined Nanocalorimetric Sensor for Ultra-Low-Volume Cell-Based Assays*. *Analytical Chemistry*, 2002. **74**(9): p. 2190-2197.
310. Xu, J., D. Wirtz, and T.D. Pollard, *Dynamic cross-linking by α -actinin determines the mechanical properties of actin filament networks*. *Journal of Biological Chemistry*, 1998. **273**(16): p. 9570-9576.
311. Anson, M., *Temperature dependence and Arrhenius activation energy of F-actin velocity generated in vitro by skeletal myosin*. *Journal of molecular biology*, 1992. **224**(4): p. 1029-1038.
312. Zimmerle, C.T. and C. Frieden, *Effect of temperature on the mechanism of actin polymerization*. *Biochemistry*, 1986. **25**(21): p. 6432-6438.
313. Pollard, T.D. and G.G. Borisy, *Cellular motility driven by assembly and disassembly of actin filaments*. *Cell*, 2003. **112**(4): p. 453-465.
314. Guilak, F., et al., *Control of stem cell fate by physical interactions with the extracellular matrix*. *Cell stem cell*, 2009. **5**(1): p. 17-26.
315. Fritsch, A., et al., *Are biomechanical changes necessary for tumour progression?* *Nature Physics*, 2010. **6**(10): p. 730-732.
316. Kießling, T.R., et al., *Thermorheology of living cells—impact of temperature variations on cell mechanics*. *New Journal of Physics*, 2013. **15**(4): p. 045026.
317. Shafirstein, G., et al., *Indocyanine green enhanced near-infrared laser treatment of murine mammary carcinoma*. *International journal of cancer*, 2012. **130**(5): p. 1208-1215.
318. Chen, W.R., et al., *Laser-photosensitizer assisted immunotherapy: a novel modality for cancer treatment*. *Cancer letters*, 1997. **115**(1): p. 25-30.

319. Castrén-Persons, M., et al., *Contact Nd: YAG laser potentiates the tumor cell killing effect of hyperthermia*. *Lasers in surgery and medicine*, 1991. **11**(6): p. 595-600.
320. Waldow, S.M., P.R. Morrison, and L.I. Grossweiner, *Nd: YAG laser-induced hyperthermia in a mouse tumor model*. *Lasers in surgery and medicine*, 1988. **8**(5): p. 510-514.
321. Philipp, C.M., E. Rohde, and H.P. Berlien. *Nd: YAG laser procedures in tumor treatment*. in *Seminars in surgical oncology*. 1995. Wiley Online Library.
322. Jolesz, F.A. and K. Hynynen, *Magnetic resonance image-guided focused ultrasound surgery*. *Cancer journal (Sudbury, Mass.)*, 2002. **8**: p. S100-12.
323. Gazelle, G.S., et al., *Tumor ablation with radio-frequency energy*. *Radiology*, 2000. **217**(3): p. 633-646.
324. Mirza, A.N., et al., *Radiofrequency ablation of solid tumors*. *Cancer journal (Sudbury, Mass.)*, 2001. **7**(2): p. 95-102.
325. Seki, T., et al., *Percutaneous microwave coagulation therapy for patients with small hepatocellular carcinoma: comparison with percutaneous ethanol injection therapy*. *Cancer: Interdisciplinary International Journal of the American Cancer Society*, 1999. **85**(8): p. 1694-1702.
326. O'Neal, D.P., et al., *Photo-thermal tumor ablation in mice using near infrared-absorbing nanoparticles*. *Cancer letters*, 2004. **209**(2): p. 171-176.
327. Prudhomme, M., et al., *Interstitial diode laser hyperthermia in the treatment of subcutaneous tumor*. *Lasers in Surgery and Medicine: The Official Journal of the American Society for Laser Medicine and Surgery*, 1996. **19**(4): p. 445-450.
328. Chen, W.R., et al., *Photothermal effects on murine mammary tumors using indocyanine green and an 808-nm diode laser: an in vivo efficacy study*. *Cancer letters*, 1996. **98**(2): p. 169-173.
329. Docheva, D., et al., *Researching into the cellular shape, volume and elasticity of mesenchymal stem cells, osteoblasts and osteosarcoma cells by atomic force microscopy*. *Journal of cellular and molecular medicine*, 2008. **12**(2): p. 537-552.

330. Creixell, M., et al., *EGFR-targeted magnetic nanoparticle heaters kill cancer cells without a perceptible temperature rise*. ACS nano, 2011. **5**(9): p. 7124-7129.
331. Latorre, M. and C. Rinaldi, *Applications of magnetic nanoparticles in medicine: magnetic fluid hyperthermia*. Puerto Rico health sciences journal, 2009. **28**(3).
332. Rodríguez-Luccioni, H.L., et al., *Enhanced reduction in cell viability by hyperthermia induced by magnetic nanoparticles*. International journal of nanomedicine, 2011. **6**: p. 373.
333. Drobczyński, S., et al., *Toward Controlled Photothermal Treatment of Single Cell: Optically Induced Heating and Remote Temperature Monitoring In Vitro through Double Wavelength Optical Tweezers*. ACS Photonics, 2017. **4**(8): p. 1993-2002.
334. Espinosa, A., et al., *Duality of iron oxide nanoparticles in cancer therapy: amplification of heating efficiency by magnetic hyperthermia and photothermal bimodal treatment*. ACS nano, 2016. **10**(2): p. 2436-2446.
335. Tennant, J.R., *Evaluation of the trypan blue technique for determination of cell viability*. Transplantation, 1964. **2**(6): p. 685-694.
336. Ximendes, E.C., et al., *Unveiling in vivo subcutaneous thermal dynamics by infrared luminescent nanothermometers*. Nano letters, 2016. **16**(3): p. 1695-1703.
337. Wang, C., et al., *Determining intracellular temperature at single-cell level by a novel thermocouple method*. Cell research, 2011. **21**(10): p. 1517.
338. Tseng, A.A., et al., *Electron beam lithography in nanoscale fabrication: recent development*. IEEE Transactions on electronics packaging manufacturing, 2003. **26**(2): p. 141-149.
339. Yuan, X., et al., *A novel culture system for modulating single cell geometry in 3D*. Acta biomaterialia, 2015. **24**: p. 228-240.